MAGNETIC RELAXATION DYNAMICS AND PROCESSES IN MONO- AND DINUCLEAR LANTHANIDE SINGLE-MOLECULE MAGNETS

KATIE LOIS MARIE HARRIMAN

A thesis submitted to the University of Ottawa
in partial fulfillment of the requirements for the
Doctorate in Philosophy Chemistry

Department of Chemistry and Biomolecular Sciences
Faculty of Science
University of Ottawa

Abstract

Single-molecule magnets (SMMs) have been lauded for their application in next generation devices for their enhanced information storage capabilities, increased processing speeds, and increased storage densities compared to bulk magnets. However, the success of SMMs in such applications and their technological readiness is hindered by their operation temperatures and memory lifetimes. SMMs are molecular species that possess a bistable ground state and magnetic anisotropy, which together result in an energy barrier to the reorientation of the magnetic moment. The magnetic memory response relies on its ability to retain magnetization in the absence of an external field. To this end, lanthanide ions with their large inherent magnetic anisotropy combined with well-defined crystal field microstates are attractive candidates for eliciting higher operation temperatures and lifetimes. This dissertation focuses on the use of lanthanide ions in the development of high barrier SMMs with a close emphasis on the magnetic anisotropy and crystal field manipulation through geometry, design, and modification.

In the pursuit of lanthanide (Ln)-based SMMs, two cyclooctatetraenyl (COT^{2-}) complexes of the non-Kramers ion, Tm^{III}, $[Tm^{III}(\eta^8\text{-COT})I(THF)_2]$ and $[K(18\text{-C-}6)(THF)_2][Tm^{III}(\eta^8\text{-COT})_2]$, were isolated. As an ion that possess an integer angular momentum projection ($J = 6$), it was vital that a highly symmetric local environment was utilized to observe field-induced slow magnetic relaxation. The static and dynamic properties of $Tm^{III}(\eta^8\text{-COT})I(THF)_2]$ and $[K(18\text{-C-}6)(THF)_2][Tm^{III}(\eta^8\text{-COT})_2]$ were characterized revealing U_{eff} of 7.93 K and 53.3 K, respectively. More importantly, the effect of increased symmetry was observed on the rate of quantum tunneling of the magnetization (QTM), where the rate was two orders of magnitude faster in the heteroleptic complex. This emphasized the importance of local symmetry for non-Kramers ions and contributed to the rare class of Tm^{III} SMMs.

Due to the prevalent role of QTM in Ln-based SMMs, a common strategy is to induce magnetic communication between Ln ions to overcome its detrimental effects. To this end, bridging units should be sufficiently small enough to bring the Ln ions close in proximity, yet the surrounding environment of the metal center should still promote uniaxial magnetic anisotropy. We compared the effect of ancillary ligands on the magnetic properties of two dinuclear Dy^{III} compounds with the same $\{\mu\text{-Cl}\}_2$ core bridge. The complexes $[Dy^{III}\{N(SiMe_3)_2\}_2(\mu\text{-Cl})(THF)]_2$ and $[Dy^{III}(\eta^8\text{-COT})(\mu\text{-Cl})(THF)]_2$ were characterized with static and dynamic magnetic measurements. The well-matched ligand field of the silyl amide ligands with the Dy^{III} ion, precluded the observation of zero field tunneling. While both complexes are characterized by antiferromagnetic coupling, it is evident that peripheral ligands also play a vital role in determining the performance of multinuclear SMMs.

Magnetic coupling between 4f centers is classically weak; however, the use of ligands with diffuse electron clouds may penetrate the shielded 4f orbitals to effectively promote communication. One such ligand that had not previously been investigated for its ability to couple the magnetic moment of Ln ions was the trianionic cycloheptatrienyl. Utilizing Ln silyl amides, *in situ* deprotonation afforded the dinuclear complexes $[\mathrm{KLn^{III}}_2(\eta^7\text{-}\mathrm{C_7H_7})\{\mathrm{N(SiMe_3)_2}\}_4]$ (Ln = $\mathrm{Gd^{III}}$, $\mathrm{Dy^{III}}$, $\mathrm{Er^{III}}$). The static and dynamic magnetic characterization revealed rare and highly sought-after ferromagnetic coupling in a Ln-based system. The ancillary silyl amide ligands were a necessity for the isolation of these dinuclear species yet did not provide a synergistic ligand field for the Ln ions when combined with the cycloheptatrienyl bridge, ultimately preventing the observation of slow relaxation in some of the variants studied.

Pseudo-linear complexes, those molecules with strong axial donors have shown immense promise in the design of highly efficient SMMs. Our work has shown that amides are effective in directing the anisotropy of the Ln ions, thus the removal of the central organometallic bridge from the previous compounds would effectively create a highly anisotropic complex. This was achieved in our study of a formally five-coordinate complex of a ferrocene diamide ligated $\mathrm{Dy^{III}}$ ion, $[(\mathrm{NN^{TBS}})\mathrm{Dy^{III}I(THF)_2}]$. The static and dynamic magnetic properties were characterized, yielding $U_{\mathrm{eff}} = 771$ K with open magnetization hysteresis loops at zero-field, due in part to the axial disposition of the nitrogen atoms of the diamide ligand. Computational analysis of the parent compound and its fragments was completed. Our results indicated that the presence of equatorially coordinated solvent molecules such as THF, influence the axiality in the crystal field microstates more significantly than the coordinated halide.

The removal of coordinated solvent such as THF, is imperative to improve the performance of $\mathrm{Dy^{III}}$ SMMs. By way of a bulky bisanilide ligand that precludes the approach of solvent to the metal center, combined with a large bite angle, $[\mathrm{K(DME)_n}][\mathrm{L^{Ar}Dy^{III}(X)_2}]$, a formally four coordinate complex, was investigated. In contrast to the complex of the ferrocene diamide ligand, retention of the magnetic moment was not observed at zero-field, despite the fact that the slow relaxation dynamics occurred over a greater temperature range for which $U_{\mathrm{eff}} = 1278\text{-}1334$ K. In addition, variants of the bound halide (X = Cl, I) were examined for their effect on the static and dynamic magnetic properties, revealing zero field relaxation times that were on average 5.6x longer for the heavier congener.

The collective results of the findings presented herein are being utilized to synthesize new low-coordinate Ln-based SMMs. Combining divalent and redox chemistries with bulky amido ligands will ideally elicit even larger energy barriers to spin reversal and higher blocking temperatures, supporting the push towards Ln-based SMMs with increased technological readiness.

Dedicated to Adam and Rebecca

May you achieve great things.

No pressure, no diamonds.

– Thomas Carlyle

Acknowledgments

These are perhaps the hardest pages to write of my thesis; partly because it signifies the end of an era but also because this era of my life has been supported by so many people that truly mean a lot to me. In the words of Winnie the Pooh, *how lucky I am to have something that makes saying goodbye hard.*

First, I am so grateful to have had the opportunity to work under my supervisor, Prof. Muralee Murugesu, and even more grateful that he took a chance on me when I was just an undergraduate co-op student. I cannot express my gratitude enough to Muralee, he has taught me many life lessons (and metaphors) and created a safe place for me to freely express my concerns and worries for chemistry and life. His blind faith in my synthetic abilities and skills allowed us to dream of the most idealized systems together and motivated me when synthetic roadblocks were met. Muralee's desire for the next-big thing was the perfect match for my competitive spirit. He provided access to the best equipment and collaborators; for a grad student working on molecular magnets, it was like being a kid in the candy shop. I will always cherish the trust Muralee had for me and my work, being able to explore my ideas in a supportive environment is a privilege I do not take lightly. You pushed me, you challenged me, and you directed me to this point; with the utmost gratitude and appreciation, thank you for this experience and opportunity.

I am also incredibly grateful for the support and guidance I received from Prof. Jaclyn Brusso, who was not only my undergraduate thesis supervisor, but also a strong female mentor throughout my graduate studies and much of my undergrad. I attribute my great love of chemistry to Jaclyn who showed and taught me the fascinating world of materials and without whom, I probably would not have pursued a PhD. She has an impeccable eye for detail which was hugely helpful on all the projects we worked on together. I cannot express my appreciation for Jaclyn enough, I am honoured to have been a Brusso Bunch member.

I am also very appreciative of the time, effort, and participation from my thesis advisory committee: Prof. R. Tom Baker and Prof. Eva Hemmer. They have been with me on this PhD journey since the beginning, evaluating my requirements, offering their chemistry insight, and challenging me to think deeper at each of the checkpoints. Prof. Baker and Prof. Hemmer have played very special roles throughout my PhD; Prof. Baker has strongly supported many applications for me, and I was a contributor on a joint project between the Hemmer and Murugesu groups, which resulted in a publication. I am truly grateful for their presence throughout my PhD.

During my doctoral studies I was very fortunate to complete research under the supervision of Prof. William Evans at the University of California Irvine. The wonder and enthusiasm for chemistry that Prof. Evans has is seen and felt in everyone who gets the chance to work in his lab. I am so appreciative of all the discussions I got to have with Prof. Evans and the lessons I learned while in his lab. Additionally, I would like acknowledge Joseph Ziller, he is an outstanding crystallographer and was always willing to try to get the best data possible out of my crystals. While I did not get the chance to stay long, the Evan's lab truly made me feel like one of them; from hunting down the mysterious source of water in the SPS solvents, to using the Geiger counter on every surface, and the many lunches in the sun together. A special thank you to Austin Ryan, Dan Huh, Megan Dumas, Sam Moehring, and Tenner Jenkins who took the time to show me the ins and outs of the lab, to work on projects with me, and to share a pint or two with me.

In addition, much of the work presented herein would not have been possible without the contributions of many collaborators. First, I would like to thank Prof. Liviu Ungur for his efforts in many of the projects herein; his computational work was truly instrumental in understanding many of the systems we worked on together. I would also like to acknowledge Jason Brsomer and Prof. Paula Diaconescu for their synthetic work on the ferrocene diamide project; and a special thank you to Prof. Diaconescu for writing support letters and inviting me to present at the Southern California Organometallics Meetup, thank you for such an incredible experience! Additionally, I want to thank Jesse Murillo and Prof. Skye Fortier, for their truly outstanding synthetic work and structural elucidations on the bisanilide project; it was an incredible experience to work with you on that project and many others. Together, we even secured a fun front cover piece! Thank you to Prof. Elizaveta Suturina; her computational work was instrumental in the project with Jesse and Prof. Fortier. I am so appreciative of her willingness to jump on a call and talk out magnets and electronic structure with me, I have learned so much from her through those sessions.

Also, I would like to recognize the University of Ottawa crystallographers that I have had the chance to work with over the years; Ilia Korobkov, taught me how to use the diffractometers, and shared his wealth of 4f and 5f synthetic knowledge and crystal growing tricks with me, but more importantly he always challenged me to be a better chemist – thank you. Bulat Gabidullin, was always willing to go above and beyond for a structure solution for me, he even came back to us years after leaving the university with a structure of ours that he finally cracked, thank you for your efforts.

I would like to acknowledge Siena Wong (BSc. 2018) for her contributions to this work. Siena worked with me in the lab as an undergraduate researcher for nearly two years at the start of my PhD. We worked closely together trying new synthetic routes and dreaming of the next big SMM. Her dedication to chemistry and degassing solvents was bar none, and I am happy that we got to Zumba together on occasion.

Also, it does not go without saying that my colleagues in the Murugesu group over the years are the most supportive (and crazy) people I have ever met, and they have truly made my experience in the lab so much more pleasant. Fatemah Habib, Rebecca Holmberg, and Jennifer Le Roy took me under their wings when I first joined, and these women are total powerhouses! They each had their own special set of skills and I knew that I would have BIG shoes to fill. I am so honoured to have been able to work alongside them. While I must admit, they were intimidating, I am happy that they became friends along the way. I will always cherish the time I had with them both inside and out of the lab, yes even sky diving…

To the current Murugesu group: Paul Richardson, Dylan Errulat, Chris Bamforth, Niki Mavaragani, Darren Herweyer, Roberto Diaz-Rodriguez, Diogo Galico, Walace Doti do Pim, and Alex Kitos; first and foremost, always remember rule #1. At some point during my time in the Murugesu group, we went from a research group to a research cult, at least that is what is the "others" say. Maybe it was winning one-too-many pumpkin carving contests, or that our volleyball team was just that good. Either way, I am very happy to have spent the majority of my days (nights and weekends) with all of you! I am not sure what I will miss more, Paul loudly singing shantis, Chris' French press (shh…), or the duck quacks that filled the lab. I will certainly cherish the memories of our group potlucks turned Quiplash tourneys and the summer nights at La Maison with all of you.

I would also like to acknowledge past Murugesu group members who have truly made my time in the group a positive experience: Gabriel Brunet, Maykon Lemes, Thomas Lacelle, Elena Sebastiao, Yuting Jiang, Yixin Zhang, Adam Sun, Daniel Martins, I will forever be thankful for the laughs and chemistry we shared together. I also had the pleasure of working closely on projects with visiting students, Valerie Paprocki of Prof. Holger Braunschweig's group at the University of Würzburg and Will Blackaby of Prof. Michael Whittlesey's group at the University of Bath. I hope that I did the world of molecular magnetism just and that the squid and all its plotting did not scare you! I really enjoyed our time together even if it was brief. In addition, I would like to acknowledge Tomasz Witkowski, who was such a special soul and chemist, I have never seen anyone more in love with their craft. Thank you for always looking out for me and involving me in your crazy chemistry ideas.

To my chemistry department friends: Alicea Leitch, Frank Magnan, Tom Charlton, Terry McCallum, Kelsey Fournier, Julia Meyer, Meredith Allen, Dilan Polat, Josh Derasp, and many others, thank you for helping shape some of the best memories (or lack thereof) I have of grad school. On any given day, you would find one if not several of these amazing people at La Maison, ready to talk, cry, or laugh. And of course, I could not forget the chemistry girls' taco nights! What started off as a crazy idea between Dilan, Meredith and myself, and our desire for a chemistry grad student sorority (jokingly of course…) turned into one great tradition with girls from all different research groups. I am happy to have held down the spot as the resident inorganic chemist, and I hope that the next generation of women in the chemistry department carry this on.

Another large part of my experience at the University of Ottawa, was the staff; Dave Needham, Dave Armstrong, Annette Campeau, Josée Rouleau, Ian Myers, Max Beaulieu, Mike Murphy, Hervé Beaudoin, Olivier Demers, Lee Sorensen, and Pierre Bisson. It was always such a pleasure to see all your smiling faces around campus and to share a laugh. I am thankful for all your help from fixing instrumentation in a hurry (and I mean very, very, quickly…) to supporting moving projects, purchasing, and the shipment of (very sensitive!) samples; thank you for making the university a great place to be!

My dear friend Nathan, I think it is truly time for both of us to go home. Your energy and enthusiasm for chemistry is so infectious and you are without a doubt a key reason I am at the end of this degree writing this thesis. On a chance, our paths crossed in our first years of undergrad and I had no idea what was headed my way. I don't have the words to thank you enough for pushing me into the office of Jaclyn Brusso when I was so scared and unsure of what to do; you sparked one of the greatest journeys that I would ever embark on, thank you.

Arianne Bérubé-Lavoie, my personal trainer, who I gave what little I had of my graduate student stipend to. She is a large reason why I have made it this far in this journey. While she busted my butt in the gym to release all the stressors of grad school, she also worked my mind; her unbiased perspectives and questions that triggered critical thought pushed me to be a better person. I am so beyond grateful for all the time that she devoted to me and my well-being. Thank you for being more than a personal trainer, thank you for being my friend when I needed it the most.

The Lady Squad, my dearest friends, you have been the most understanding and supportive friends anyone would ever need. Your constant love and support fueled me on the toughest days. I am so appreciative of all times you checked in on me and made the trek to Ottawa, and even more so the forgiveness you showed when I had to run to the squid mid-visit. Thank you all for being bright lights during this journey.

To my family, thank you for your love and support throughout this journey, the Harriman Clang, yes that is clan with a "g", is a force to be reckoned with. Near or far, coast to coast, the support and cheerleading was always felt. And a special thank you to my dear aunts and second mothers, Karen and Linda, your love, support, constant encouragement, and positivity kept me going when things got challenging.

Lastly, to my mom, thank you for fiercely supporting me in all my endeavours. Who knew that all those years of skating would prepare me (and you) for a PhD? (the similarities are truly uncanny). Reflecting on my time in the lab, I think it is fair to say that you spent more than your fair share of time at the lab too. Your visits to Ottawa were often filled with driving me to and from the lab at crazy hours (yup… like skating) just to ensure that experiments were still running or to change a squid sample, or even sitting at my desk with me while I finished marking final exams on Christmas Eve. I even recall a time that you attended one of my conference talks during your holidays. You were always there, with a coffee in one hand and a big smile on your face saying “head up Katie-girl” (yup… still like skating); thank you Mumsie – we did it.

Table of Contents

Chapter 4 Utilizing Amides to Elicit Magnetic Relaxation within Organometallic Bridged Complexes 83

Chapter 5 Influence of Equatorial Ligands in a Highly Axial Bis-Amide Single-Molecule Magnet… 116

List of Figures

List of Tables

List of Abbreviations

a	Crystallographic unit cell axis
AC	Alternating current
AFM	Antiferromagnetic
Anal. Calcd	Analysis calculated
Å	Angstrom
b	Crystallographic unit cell axis
br	Broad (NMR/IR peak descriptor)
$\mathbf{cm^{-1}}$	Wavenumber
c	Crystallographic unit cell axis
C	Curie constant; fitting parameter
CASSCF	Complete active space self-consistent field
CF	Crystal field
CNT	Carbon nanotube
Cp*	Pentamethylcyclopentadienyl
COT	Cyclooctatetraenyl
d	Doublet (NMR)
D	Axial magnetic anisotropy parameter
DC	Direct current
DME	1,2-Dimethoxyethane
E	Energy; transverse anisotropy parameter
EMF	Endohedral metallofullerene
FC	Field cooled
FM	Ferromagnetic
FTIR	Fourier-transform infrared spectroscopy
g	g-factor
h	Hour; Planck’s constant
H	Magnetic field
$\mathcal{H}$	Hamiltonian
IR	Infrared
J	Coupling constant; total angular momentum quantum number
J_{dip}	Coupling constant; dipolar
J_{exch}	Coupling constant; exchange
K	Kelvin
KD	Kramers doublet
k_{B}	Boltzmann constant

LF	Ligand field
Ln	Lanthanide
LT	Low-temperature
m	Medium (IR); multiplet (NMR)
m_s	Second spin quantum number
m_J	Angular momentum quantum number
M	Magnetization; molar
M_{sat}	Magnetization, saturation
M_R	Magnetization, remnant
nm	Nanometer
NMR	Nuclear magnetic resonance
Oe	Oersted
PXRD	Powder X-ray diffraction
QTM	Quantum tunnelling of the magnetization
RASSI	Restricted active space state interaction
RT	Room temperature
s	Strong (IR); singlet (NMR)
s	Spin quantum number
S	Total spin quantum number
SCXRD	Single-crystal X-ray diffraction
SMM	Single-molecule magnet
SIM	Single-ion magnet
SOC	Spin-orbit coupling
SQUID	Superconducting quantum interference device
t	Time
T	Tesla
T	Temperature
T_B	Blocking temperature
TA-QTM	Thermally activated quantum tunneling of the magnetization
THF	Tetrahydrofuran
U_{eff}	Anisotropy barrier, effective
w	Weak (IR)
Z	Number of asymmetric units per unit cell
ZFC	Zero-field cooled
ZFS	Zero field splitting
α	Unit cell angle; distribution parameter
β	Unit cell angle
γ	Unit cell angle

δ	Chemical shift (NMR)
λ	Wavelength
μ	Magnetic moment
μ_{eff}	Magnetic moment, effective
μ_{B}	Bohr magneton
ν	Frequency, linear
τ	Relaxation time
τ^{-1}	Relaxation rate
τ_0	Attempt time
θ	Angle; Weiss constant
χ	Magnetic susceptibility
χ'	In-phase magnetic susceptibility
χ''	Out-of-phase magnetic susceptibility
χ_{S}	Adiabatic susceptibility
χ_{T}	Isothermal susceptibility
ω	Angular frequency

Compounds by Chapter with Chemical Formulas and Abbreviated Names

Chapter 2

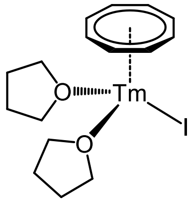

(**1-Tm**)

$[Tm^{III}(\eta^8\text{-COT})I(THF)_2]$ (**1-Tm**)

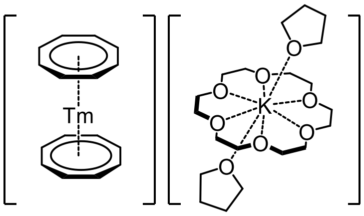

(**2-Tm**)

$[K(18\text{-}C\text{-}6)(THF)_2][Tm^{III}(\eta^8\text{-COT})_2]$ (**2-Tm**)

Chapter 3

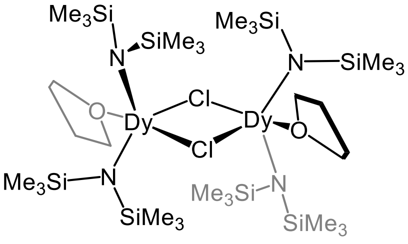

(**3-Dy**)

$[Dy^{III}\{N(SiMe_3)_2\}_2(\mu\text{-}Cl)(THF)]_2$ (**3-Dy**)

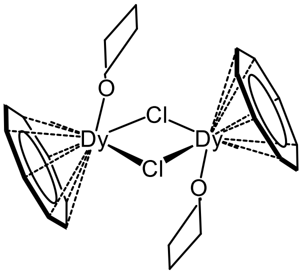

(**4-Dy**)

$[Dy^{III}(\eta^8\text{-COT})(\mu\text{-}Cl)(THF)]_2$ (**4-Dy**)

Chapter 4

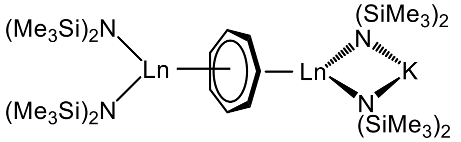

Ln = Gd (**5-Gd**), Dy (**5-Dy**), Er (**5-Er**)

$[\mathrm{KGd^{III}_2}(\eta^7\text{-}\mathrm{C_7H_7})\{\mathrm{N(SiMe_3)_2}\}_4]$ (**5-Gd**)
$[\mathrm{KDy^{III}_2}(\eta^7\text{-}\mathrm{C_7H_7})\{\mathrm{N(SiMe_3)_2}\}_4]$ (**5-Dy**)
$[\mathrm{KEr^{III}_2}(\eta^7\text{-}\mathrm{C_7H_7})\{\mathrm{N(SiMe_3)_2}\}_4]$ (**5-Er**)

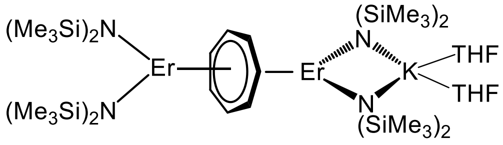

(**6-Er**)

$[\mathrm{K(THF)_2Er^{III}_2}(\eta^7\text{-}\mathrm{C_7H_7})\{\mathrm{N(SiMe_3)_2}\}_4]$ (**6-Er**)

Chapter 5

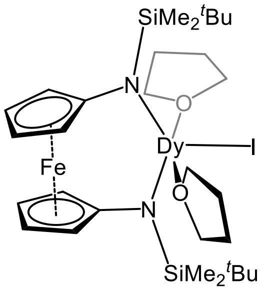

(**7-Dy**)

$[(\mathrm{NN^{TBS}})\mathrm{Dy^{III}I(THF)_2}]$ (**7-Dy**)

Chapter 6

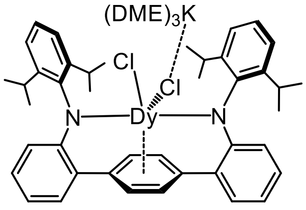

(**8-Dy**)

$[\mathrm{K(DME)_3}][\mathrm{L^{Ar}Dy^{III}Cl_2}]$ (**8-Dy**)

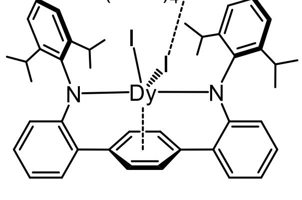

(**9-Dy**)

$[\mathrm{K(DME)_4}][\mathrm{L^{Ar}Dy^{III}I_2}]$ (**9-Dy**)

Chapter 7

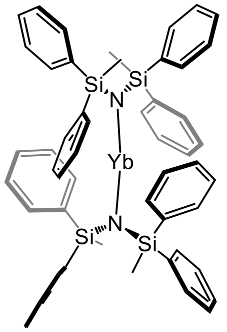

(**10-Yb**)

[Yb^{II}\{N(SiMePh$_2$)$_2$\}$_2$] (**10-Yb**)

Contributors

This work was supervised by a dissertation committee consisting of Professor Muralee Murugesu (P.I.), Professor Eva Hemmer, and Professor R. Tom Baker of the Department of Chemistry and Biomolecular Sciences at the University of Ottawa.

The X-ray structures for compounds **1-Tm**, **2-Tm**, **5-Gd**, **5-Dy**, **5-Er**, and **6-Er** were collected and solved by Dr. Ilia Korobkov of the Faculty of Science at the University of Ottawa. The X-ray structures for **3-Dy** and **4-Dy** were solved by Dr. Bulat Gabidullin of the Department of Chemistry and Biomolecular Sciences at the University of Ottawa.

Jason L. Brosmer and Professor Paula L. Diaconescu of the Chemistry and Biochemistry Department at the University of California Los Angeles performed the synthesis of **7-Dy** in Chapter 5. Jesse Murillo and Professor Skye Fortier of the Department of Chemistry and Biochemistry at the University of Texas at El Paso performed the syntheses and structural determinations of **8-Dy** and **9-Dy** in Chapter 6. *Ab initio* calculations and analysis on compounds **3-Dy** and **4-Dy** of Chapter 3; **5-Gd**, **5-Dy**, **5-Er**, and **6-Er** of Chapter 4; and **7-Dy** of Chapter 5 were performed by Professor Liviu Ungur of the Department of Chemistry at the National University of Singapore. *Ab initio* calculations and analysis on compounds **8-Dy** and **9-Dy** of Chapter 6 were performed by Professor Elizaveta A. Suturina of the Department of Chemistry at the University of Bath.

Siena Wong from the Department of Chemistry and Biomolecular Sciences contributed to the syntheses of **3-Dy** and **4-Dy** in Chapter 3. Dr. Jennifer J. Le Roy of the Department of Chemistry and Biomolecular Sciences contributed to the syntheses and magnetic data collection of **5-Gd**, **5-Dy**, **5-Er**, and **6-Er** in Chapter 4. Dr. Rebecca J. Holmberg of the Department of Chemistry and Biomolecular Sciences performed powder X-ray diffraction analysis on compounds **5-Gd**, **5-Dy**, **5-Er**, and **6-Er** in Chapter 4.

The results from Chapter 2 in this dissertation have been published in Harriman, K. L. M.; Korobkov, I. and Murugesu, M. *Organometallics*, **2017**, 36, 4515. Chapter 4 of this dissertation has been published in Harriman, K. L. M.; Le Roy, J. J.; Ungur, L.; Holmberg, R. J.; Korbkov, I. and Murugesu, M. *Chem. Sci.*, **2017**, 8, 231. Chapter 5 of this dissertation has been published in Harriman, K. L. M.; Brosmer, J. L.; Ungur, L.; Diaconescu, P. L. and Murugesu, M. *J. Am. Chem. Soc.*, **2017**, 39,1420. Chapter 6 of this dissertation have been published in Harriman, K. L. M.; Murillo, J.; Suturina, E. A.; Murugesu, M. and Fortier S. *Inorg. Chem. Front.*, **2020**, 7, 4805.

All other work in this dissertation was completed by the student under the supervision and advisement of Professor Muralee Murugesu of the Department of Chemistry and Biomolecular Sciences.

Contributions

Peer-Reviewed Contributions:

† Equal contributions to the presented work

1. **Harriman, K. L. M**.; Murillo, J.; Suturina, E. A.; Murugesu, M.* and Fortier S.* "*Relaxation dynamics in see-saw shaped Dy(III) single-molecule magnets*" *Inorg. Chem. Front.*, **2020**, 7, 4805-4812.
2. Paprocki, V.; Hrobárik, P.; **Harriman, K. L. M**.; Luff, M. S.; Kupfer, T.; Kaupp, M.*; Murugesu, M. and Braunschweig, H.* "*Stable actinide π complexes of neutral 1,4-diborabenzene." Angew. Chem. Int. Ed*, **2020,** 10.1002/anie.202004501.
3. **Harriman, K. L. M**.†; Errulat, D.† and Murugesu, M.* "*Magnetic axiality: Design principles from molecules to materials.*" *Trends in Chemistry*, **2019,** 1, 425-439.
4. Errulat, D.; Marin, R.; Galico, D. A.; **Harriman, K. L. M**.; Pialat, A.; Gabidullin, B.; Iikawa, F.; Couto Junior, O. D. D.; Moilanen, J.; Hemmer, E.*; Sigoli, F. A.* and Murugesu, M.* "*A luminescent thermometer exhibiting slow relaxation of the magnetization: towards self-monitored building blocks for next-generation opto-magnetic devices." ACS Cent. Sci.,* **2019**, 5, 7, 1187-1198.
5. Castañeda, R.; **Harriman, K. L. M**.; Wong, J. W. L.; Gabidullin, B.; Murugesu, M.* and Brusso, J. L.* "*Rational design of tetranuclear complexes employing N-imidoylamidine based ligands.*" *Eur. J. Inorg. Chem.*, **2019,** 963-972.
6. Zhang, Y.; **Harriman, K. L. M**.; Brunet, G.; Pialat, A.; Gabidullin, B. and Murugesu, M.* "*Reversible redox, spin crossover and superexchange coupling in 3d transition metal complexes of bis-azinyl analogues of 2,2':6',2''-terpyridine." Eur. J. Inorg. Chem.,* **2018**, 10, 1212.
7. **Harriman, K. L. M**.; Korobkov, I. and Murugesu, M. "*From a piano-stool to a sandwich: A stepwise route for improving the slow magnetic relaxation properties of thulium.*" *Organometallics*, **2017**, 36, 4515.
8. **Harriman, K. L. M**.; Brosmer, J. L.; Ungur, L.; Diaconescu, P. L. and Murugesu, M. "*Pursuit of record breaking energy barriers: A study of magnetic axiality in diamide ligated single-molecule magnets.*" *J. Am. Chem. Soc.,* **2017**, 39,1420.
9. **Harriman, K. L. M**.†; Le Roy, J. J.†; Ungur, L.; Holmberg, R. J.; Korbkov, I. and Murugesu, M.* "*Cycloheptatrienyl trianion: An elusive bridge in the search of exchange coupled dinuclear organolanthanide single-molecule magnets.*" *Chem. Sci.*, **2017**, 8, 231
10. **Harriman, K. L. M.** and Murugesu, M.* "*An organolanthanide building block approach to single-molecule magnets.*" *Acc. Chem. Res.*, **2016**, 49, 1158.
11. **Harriman, K. L. M**.; Kuhne, I. A.; Leitch, A. A.; Korobkov, I.; Murugesu, M.* and Brusso, J. L.* "*Halide influence on molecular amd supramolecular arrangements of iron complexes with a 3,5-bis(2-pyridyl)-1,2,4,6-thiatriazine ligand.*" *Inorg. Chem.*, **2016**, 55, 5376.

12. Frost, J. M.; **Harriman, K. L. M.** and Murugesu, M.* "*The rise of 3-d single-ion magnets in molecular magnetism: Towards materials from molecules?*" *Chem. Sci.*, **2016**, 7, 2470.
13. **Harriman, K. L. M**.; Leitch, A. A.; Stoian, S. A.; Habib, F.; Kneebone, J. L.; Gorelsky, S. I.; Korobkov, I.; Desgreniers, S.; Neidig, M. L.; Hill, S.; Murugesu, M.* and Brusso, J. L.* "*Ambivalent binding between a radical based pincer ligand and iron*." *Dalton Trans.*, **2015**, 44, 10516.

Forthcoming Contributions:

† Equal contributions to the presented work

1. Errulat, D.[†]; **Harriman, K. L. M.**[†]; Gálico, D. A.; Ovens, J. S.; Luff, M. S.; Mansikkamäki, A.* and Murugesu, M.* "*Aufbau vs, non-Aufbau ground states in two coordinate d^7 single-molecule magnets.*" *Angew. Chem. Int. Ed.*, Submitted (202106538).
2. Murillo, J.; Rani, R.; **Harriman, K. L. M.**; Gomez-Torres, A.; Wright, J.; Meulenberg, R.; Metta-Magana, A.; Murugesu, M.; Vlaisavljevich, B.* and Fortier, S.* "*Actinide arene-metalates: Ion pairing effects on the electronic structure of the first unsupported uranium-arene sandwich complexes.*" *Chem. Sci*., Submitted (SC-EDG-05-2021-002473).
3. **Harriman, K. L. M**.; Wong, S.; Gabidullin, B.; Ungur, L. and Murugesu, M.* "*Temperature and field dependent magnetic relaxation in $Dy_2(\mu\text{-}Cl_2)$ single-molecule magnets.*" Manuscript in preparation.
4. Gálico, D. A.; **Harriman, K. L. M**.; Mansikkamäki, A.; Moilanen, J. and Murugesu, M. "*Molecular distancing?*" Manuscript in preparation.

MAGNETIC RELAXATION DYNAMICS AND PROCESSES IN MONO- AND DINUCLEAR LANTHANIDE SINGLE-MOLECULE MAGNETS

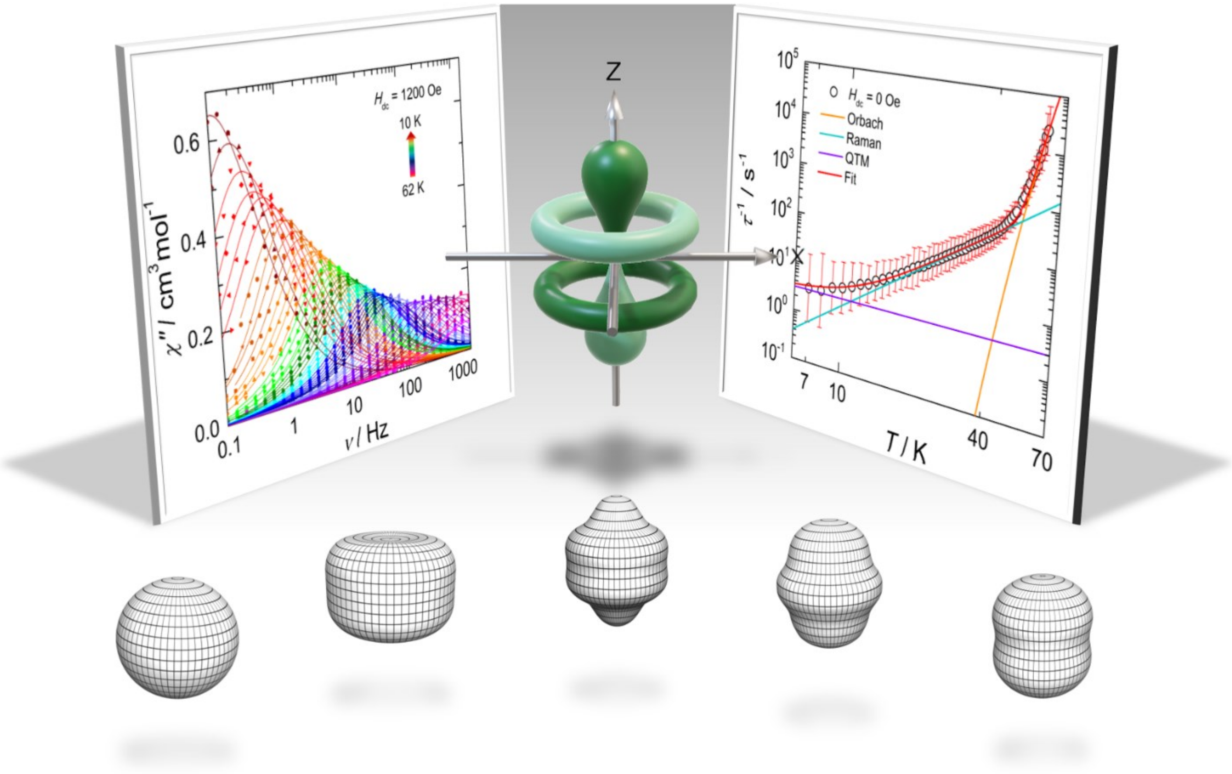

Chapter 1

Introduction to Lanthanide Single-Molecule Magnets

1.1 Opening remarks

In the early 90s, a pinnacle discovery was made; a molecular transition metal complex could retain magnetization for long periods of time, at liquid-helium temperatures, in the absence of an external magnetic field.[1,2] This molecule, the infamous multinuclear manganese cluster, $[\mathrm{Mn^{III}_4Mn^{IV}_8O_{12}(OAc)_{16}(H_2O)_4}]$ ($\mathrm{Mn_{12}Ac}$), had initiated the field of single-molecule magnets (SMMs).[3] This fundamental discovery sparked great interest and excitement for SMMs and for their potential to be incorporated into, and developed for new technological devices. Akin to traditional bulk ferromagnets, such as neodymium-iron boride magnets that are currently used for information storage and processing,[4] SMMs are considered to be their molecular counterparts and hold great potential for these types of applications. Perhaps more noteworthy, is that the scale and molecular nature of SMMs may afford enhanced capabilities for information storage and processing, including increased processing speeds and increased storage densities compared to bulk magnets.[5,6]

Within bulk magnets, the magnetic memory is domain dependent. Meaning that within spatial regions of these materials, individual spins are aligned; these distinct regions are separated by domain walls. Magnetic memory is observed in these types of materials because there is an energy cost associated with breaking or reorganizing these domain walls.[7] Thus, the magnetization persists for an extended period of time. Conversely, in SMMs the spins are not confined by magnetic domains, instead each molecule behaves as its own independent “domain”. SMMs are paramagnetic molecules characterized by a bistable magnetic ground state and magnetic anisotropy. Collectively, these features give rise to an energy barrier, U_{eff}, for the reorientation of their molecular spins.[3,8] When subjected to an external magnetic field, the spins of the molecule align with the magnetic field, which represents the most energetically favourable orientation. Thus, when the field is removed the magnetic moment persists in that orientation for a given amount of time. Fundamentally, when the energy barrier is significantly large enough, the rate for the reorientation of the moment becomes sufficiently slow. It is this feature that gives rise to a magnetic memory response in SMMs below a certain blocking temperature, T_{B}.

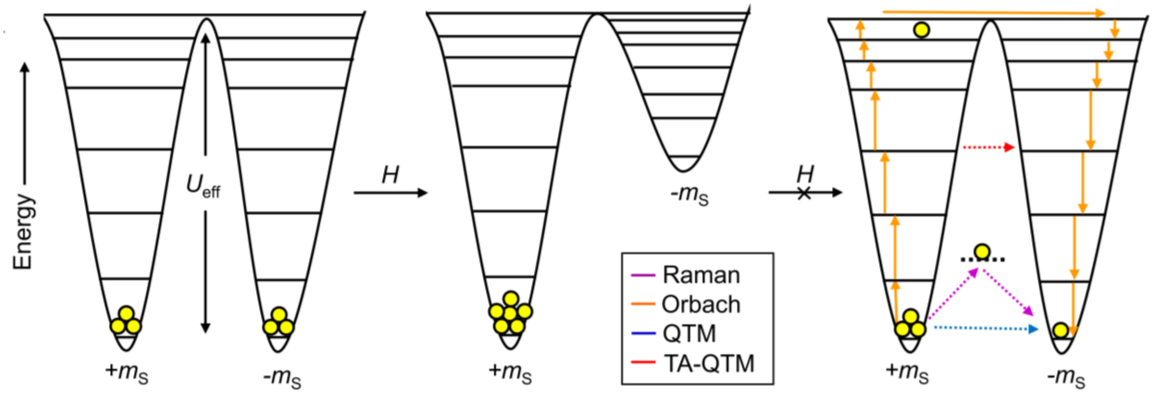

Figure 1.1 The magnetization and relaxation processes at the spin quantum number (M_s) level for single-molecule magnets. Adapted from ref. 105.

The magnitude of the barrier is closely linked to the anisotropy of an ion or system which is the result of zero-field splitting (ZFS). In a system with a total spin (S), there are $2S+1$ possible spin states, each with a spin quantum number (M_s), that is the sum of the individual spin quantum numbers of the unpaired electrons (m_s). Thus, a system with S total spin, can have M_s states that range from S to $-S$, where each state corresponds to the relative orientation of the spin, i.e., "spin up" or "spin down". Here, ZFS acts by removing the degeneracy in the M_s states, yielding an energy spectrum of $\pm M_s$ states characterized by a double well potential (Figure 1.1). Effectively, the spins will populate one of the low-energy M_s states/wells (+ or -); whichever one is most energetically favourable with the applied magnetic field. To achieve an equilibrated state, the spins must traverse the energy barrier through higher excited M_s states. For many SMMs, there is an energetically favorable direction for the magnetic moment to align, this is known as the anisotropy axis. Thus, the extent of the transverse anisotropy in these states directly relates to the time scale of the relaxation decay and time with which information can be retained on devices.

For most SMMs (i.e., transition metal SMMs), the properties which are highly applicable and desirable are only achievable at liquid helium temperatures, and for much of the last decade efforts have been focused on improving this variable. There are now modern SMMs based on lanthanide ions which have achieved this goal,[9] however several challenges regarding the physics still remain in order to make SMMs technologically relevant.[10,11] The high-level interest in lanthanide-based SMMs, and in particular mononuclear SMMs or single-ion magnets (SIMs), originates from (1) the stronger intrinsic magnetic anisotropy than transition metals and (2) the weaker spin-phonon interactions. Collectively, the result is longer relaxation times and longer magnetization lifetimes than their transition metal counterparts.

1.2 Electronic Structure of Lanthanides

The origin of SMM properties in lanthanide-based compounds is more complicated owing to spin-orbit coupling, thus the double well containing ± M_S numbers is no longer accurate for lanthanides. As a consequence of Russell-Saunders coupling, the spin (S) couples to the orbital moment (L) resulting in total angular momenta (J), meaning that an $^{2S+1}L_J$ term must be used instead of S as is for transition metals. The spin-orbit interaction splits the ^{2S+1}L state into well separated multiplets with different J (Figure 1.2). Typically, at room temperature and without an external bias, such as light, the spins will only populate the lowest lying, or ground state $^{2S+1}L_J$ as the states are very well separated by several thousands of wavenumbers (*ca.* 10^4 cm^{-1}).

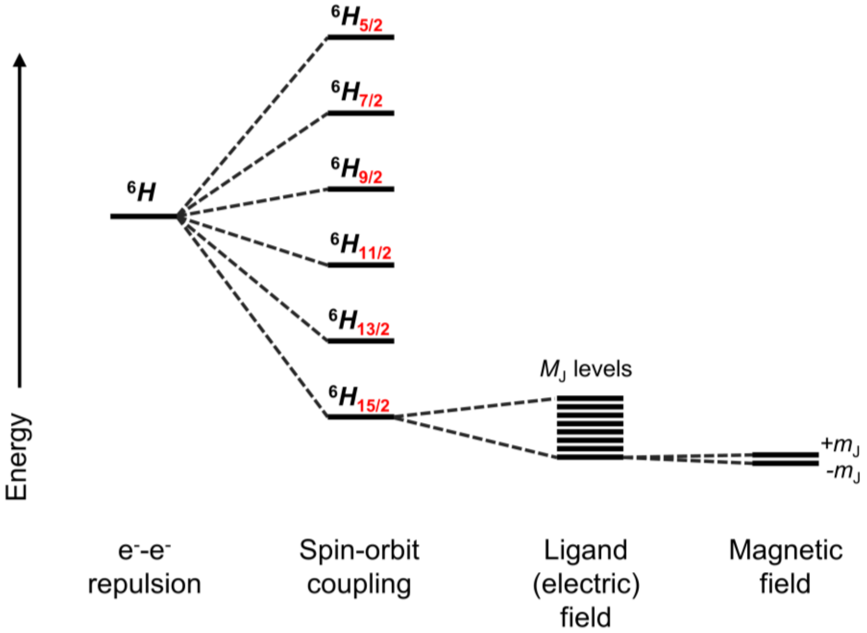

Figure 1.2 Schematic representation of the electronic structure of a lanthanide ion with a $^6H_{15/2}$ ground state term, such as Dy^{III}. The energy axis is not drawn to scale. Not all of the spin-orbit coupled states are depicted. The Stark sublevels are represented as 8 Kramers doublets of m_J states. Adapted from ref. 76.

When the lanthanide ion is placed within an electric field provided by surrounding ligands, the spin-orbit term is further split into 2J+1 Stark sublevels; for which each sublevel possess a M_J quantum number as opposed to an M_s number.[12,13] The LF acts to remove the degeneracy of these M_J states (spanning *ca.* 10^2-10^3 cm^{-1}), which is a direct consequence of magnetic anisotropy. And thus, there is a directional component for the magnetic moment in each of these states. As a result, the largest M_J projection is not guaranteed to be the most stabilized, or lowest in energy. It is widely understood that different Ln ions exhibit different magnetic anisotropies when subjected the same LF;[14,15] this means that the order and relative energies of the M_J states are both metal and ligand dependent. Nevertheless, the LF splitting of the multiplets usually occurs over a much larger energy range than transition metals, meaning that the potential energy barriers that could be achieved for Ln-based SMMs are fundamentally larger.

1.3 Relaxation of the Magnetization

In the presence of an external magnetic field the M_J states, or crystal field microstates as is for mononuclear SMMs, are split into respective $-m_J$ and $+m_J$ states. There is an energy difference between these "up" and "down" states, albeit small in magnitude (*ca.* 10^1 cm^{-1}), thus it is necessary for the system (i.e., the compound) to exchange energy with the environment (i.e., the crystalline lattice) as magnetic relaxation occurs. This exchange of energy is effectively termed spin-lattice relaxation.[16,17] Transitions between the $\pm m_J$ states are facilitated by the available phonons of the crystalline lattice, thus requiring phonons of a specific energy to allow for the relaxation through certain m_J states. For example, when phonons of the appropriate energy are not available in the system, the relaxation pathway effectively becomes "blocked". There are a number of mechanisms in which thermodynamic equilibrium between these states and the vibrational modes of the surroundings (i.e., lattice phonons) may be reached. Each process has a characteristic temperature and/or field dependence on the relaxation times (τ) or more specifically, the relaxation rates (τ^{-1}) that are obtained from the alternating current magnetic (ac) susceptibility (Equations 1.1-1.2).

$$\tau(T,H)^{-1} = \tau_{QTM}(T,H)^{-1} + \tau_{Orbach}(T)^{-1} + \tau_{Raman}(T)^{-1} + \tau_{Direct}(T,H)^{-1} \tag{1.1}$$

$$\tau^{-1} = \frac{B_1}{1+B_2H^2} + \tau_0^{-1}\exp\left(-\frac{U_{\mathrm{eff}}}{k_{\mathrm{B}}T}\right) + C\frac{1+C_1H^2}{1+C_2H^2}T^n + ATH^4 \tag{1.2}$$

These unique processes are usually dominant over specific temperature regimes; meaning that the relaxation occurs through the most efficient pathway or fastest route. As such, the expression is often simplified to consider only the temperature (in)dependent portions (Equation 1.3).

$$\tau^{-1} = \tau_{QTM}^{-1} + \tau_0^{-1}\exp\left(-\frac{U_{\mathrm{eff}}}{k_{\mathrm{B}}T}\right) + CT^n \tag{1.3}$$

Ideally an efficient SMM will use as many excited m_J states as possible before relaxing to the other spin state *via* one of the spin-lattice mechanisms. To achieve this, magnetic anisotropy must be maintained in the ground state and each of the higher excited states (i.e., $g_z >>> g_y, g_x$). The molecular geometry, strength of the electric/ligand field, and the magnitude of the transverse anisotropy will dictate the axiality in each doublet. In the absence of a perfectly axial crystal field, mixing between the m_j states occurs, it is therefore of the utmost importance to ensure that off-axis contributions to the crystal field are minimized to preserve the purity of the m_J states and promote their sequential ordering. Additionally, the electrical field about the metal ion, may be influenced by several factors within a crystalline lattice; that which are not limited to the charges of the bound ligands, but also solvent molecules and counter ions. These peripheral interactions result in changes in the energies of the m_j states and may be reflected in the relaxation pathways.

1.3.1 Quantum Tunneling of Magnetization

Quantum tunneling of the magnetization (QTM) is perhaps the most prevalent mechanism in Ln-based SMMs, and it is often viewed as a nuisance as it limits the relaxation times of a system typically at low temperatures. This relaxation mechanism does not require the spin to surmount an energy barrier and it is an effective means for relaxation from the $-m_J$ to $+m_J$ states without requiring any thermal activation. Thus, this process is also referred to as a through-barrier relaxation pathway. Specifically, the rate of QTM in a sample should be very slow such that the internal magnetic field of the crystalline sample is sufficient to bring the $\pm m_J$ states out of resonance with one another.[18,19] Conversely, this may also be modulated with the application of an external static applied field, acting to remove the degeneracy of the ground state doublet. However, the applied field should not be so great that the direct relaxation process becomes operable (*vide infra*), this commonly happens when the applied external field is significantly larger than the internal field of the crystal.[20] If slow relaxation dynamics are observed in this case, the system is therefore a field-induced SMM. An applied external field may also help with the observation of slow relaxation in systems that have integer angular momenta (non-Kramers ions), as ground state QTM is not formally forbidden, as per Kramers theorem.[21] If, however, the angular momenta is half-integer (Kramers ions), the strict double degeneracy of the ground state should preclude any QTM from occurring, however in practice this is rarely the case. When QTM occurs in the ground state doublet, the effect on the relaxation time is temperature independent. However, if this resonant tunneling occurs at higher excited state doublets, the processes are temperature and frequency dependent. This mechanism is termed thermally assisted quantum tunneling of the magnetization (TA-QTM). Only when the rate of the tunneling exceeds the rate of the thermally activated processes is the height of the barrier defined.

1.3.2 Spin-Phonon Interactions

When the temperature of the system is sufficiently high enough, other relaxation mechanisms may become operable; for example, the Orbach process at higher temperatures and the second-order Raman processes at intermediary temperatures. The Orbach process is a two-phonon energy transfer process that occurs *via* an intermediate excited state. For simplicity, the spin system will be assumed to already be in the excited state (Figure 1.3). Under these conditions, a phonon of energy equal to the difference between |3> and |2>

is first absorbed, followed by the emission of a second phonon equal to the energy difference for which magnetic relaxation is occurring ($h\omega_{3\rightarrow1}$).

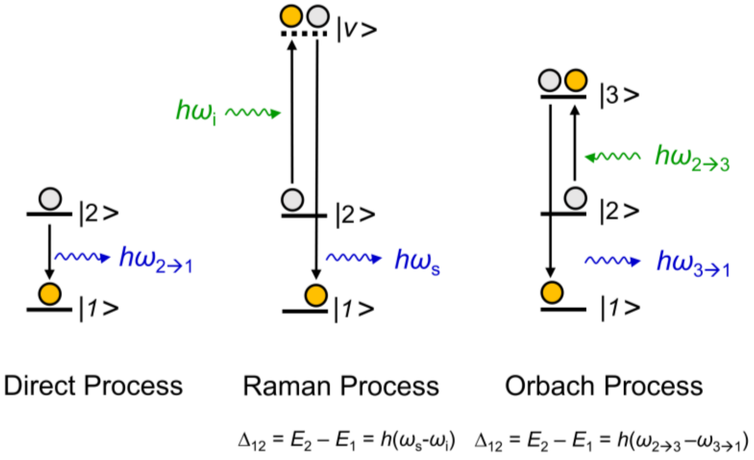

Figure 1.3 Schematic overview of the common spin-lattice relaxation processes observed in lanthanide-based SMMs: direct, Raman, and Orbach. The grey circles represent the initial states, and the orange circles represent the final state of the transition, assuming that the spin system is already in an excited state. Transitions are depicted as black arrows. Adapted from ref. 106.

The Orbach process has an exponential dependence on temperature (Figure 1.4). As a result, it will appear in the linear high temperature region of an Arrhenius plot, ln(τ) *vs.* T^{-1}, where the slope corresponds to the energy barrier to spin reversal (U_{eff}) and the *y*-intercept is the attempt time, or pre-exponential factor (τ_0). Often for thermal relaxation, τ_0 is expected in the range $10^{-9} - 10^{-12}$ s,[22] although smaller times are frequently obtained in high-barrier lanthanide SMMs ($U_{\mathrm{eff}} > 1000$ K).[23] On the contrary, larger attempt times are typically correlated with relaxation contributions from other pathways (i.e., not thermally activated pathways); likely pathways include QTM.[22]

The second order, two-phonon Raman process occurs in a similar manner as the Orbach process. Again, assuming that the spin system is already in the excited state, relaxation occurs v*ia* absorption of an incident phonon ($h\omega_i$) to a short lived virtual excited state, and subsequent emission of a second phonon ($h\omega_s$). The difference in energy between these two phonons is equal to the energy difference for which the magnetic relaxation is occurring. This process follows a power law dependence on temperature, meaning that when the relaxation times are plotted on log-log scale, the Raman relaxation regime will appear as a straight line (Figure 1.4). This is an excellent handle for quickly determining if a compound relaxes *via* this mechanism. To remain physically reasonable, the exponent (n) can only be values of 1-9 and should approximate to $n = 7$ for a non-Kramers ion (integer J) but should tend to $n = 9$ for a Kramers ion (half integer J).[24] However, regular deviations from these expected values occur; and while the origin for which is not fully understood some of the high-barrier SMMs frequently produce smaller n values.

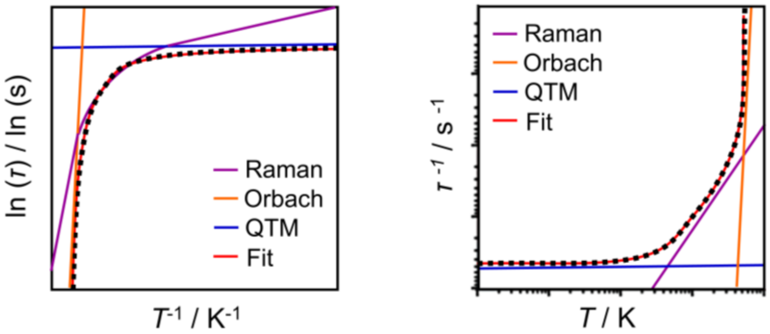

Figure 1.4 Schematic representation of the temperature dependence of the magnetic relaxation time (τ) represented on an Arrhenius plot (left) and (b) log-log scales (right). The dashed line represents hypothetical relaxation data and the solid lines correspond to the relative profiles and temperature regimes of Raman (purple), Orbach (orange), and QTM (blue) pathways. The red line corresponds to the sum of the individual processes.

Unlike the Orbach and Raman processes, the direct process is a single-phonon process, where the energy of this spin transition is equal to that of the lattice phonon energy. The spin system emits a phonon of energy equal to the difference in states upon relaxation from, i.e. |2> → |1>.The direct process is both field and temperature dependent and often requires the use of a static field to be observed owing to the very small energy different between the ground states. Thus, the direct process becomes much more evident at larger applied fields. Fitting for this process must occur *via* field dependent data or data which is collected under an applied static field, without this the entire term will tend to zero. Like the exponent parameter in the Raman term, the exponent parameter in the direct term has expected values for non-Kramers and Kramers ions of 2 and 4, respectively. In high-performance SMMs, the Orbach and Raman relaxation mechanisms may be sufficiently suppressed for transitions between $+m_J$ and $-m_J$ states thus the direct process can then facilitate subsequent transitions between M_J and $M_J + 1$ states. This sequential climbing of the M_J states will occur until tunneling rate exceeds it; therefore, the dynamics still abide by the Arrhenius law in this case.[3,25]

1.4 Magnetic Characterization of SMMs

The magnetic properties of SMMs are often evaluated with the use of a superconducting quantum interference device (SQUID). This sensitive instrument has the capabilities to detect very small changes in magnetic flux densities, detecting magnetic fields as small as 10^{-15} T.[26] As a result the magnetic moment of a sample can be determined with great accuracy. In practice, a SQUID converts small changes in magnetic flux into a voltage. A bias current is supplied to a superconducting ring with two Josephson junctions (i.e., a weak superconductor) in parallel. If this bias is larger than the maximum current that can flow through the junctions, a voltage is created across the SQUID coil/ring. A magnetic field disrupts the flow of electrons through the junctions on the coil; specifically, the field results in quantum mechanical interference between the two junctions. Any changes to the magnetic flux (increase or decrease) within the coil, by way of a sample, changes the quantum mechanical phase difference across the junctions, affecting the current flow through the SQUID coil.[26] The change in voltage across the coil is detected with conventional electronics. Although simplified, this is the basis for obtaining two types of SQUID measurements (1) direct current magnetometry and (2) alternating current magnetometry, both of which will be discussed in more detail below.

1.4.1 Direct Current Magnetic Measurements

The static magnetic properties of a sample are determined *via* direct current (dc) magnetic measurements. The movement of a sample through the SQUID coils while a constant static field is applied will elicit a magnetic response as per Equation 1.4.

$$\chi_{dc} = \frac{M}{H} \qquad \textbf{(1.4)}$$

In the case of a paramagnetic sample, with no magnetic interactions, the magnetic susceptibility will follow the Curie law (Equation 1.5) and would appear as a constant value across the measured temperature range. Typically, a deviation from this behavior, at low temperatures, would be indicative of ferromagnetic (increase) or antiferromagnetic (decrease) interactions within the sample.

$$\chi_{dc} = \frac{M}{H} = \frac{Ng^2\mu_B^2}{3k_BT}J(J+1) \qquad \textbf{(1.5)}$$

As a consequence of the Russell-Saunders coupling scheme in Ln ions, the ${}^{2S+1}L_J$ term can be used to determine the Landé *g*-factor as per Equation 1.6, and then subbed into the Curie Law to determine the free ion susceptibility. It should be noted that this only applies when the ground *J* term is well isolated from the excited states.[27]

$$g_J = \frac{3}{2} + \frac{S(S+1) - L(L+1)}{2J(J+1)} \tag{1.6}$$

In practice, the experimental room temperature susceptibility of a 4f sample is usually consistent with, or slightly smaller than the predicted value from the Curie law. This is due in part to the splitting imposed by the crystal field.[28] Additionally, a gradual decrease in the susceptibility often occurs as the temperature is sweeped lower. It should be noted that in the case of a 4f ion, this decrease in susceptibility is not necessarily a consequence of antiferromagnetic interactions. Often, depopulation of higher energy levels may account for this gradual reduction in susceptibility. In the case of highly anisotropic ions, more precipitous decreases are very frequently observed at low temperatures. This is indicative of magnetic blocking, where the magnetic moment becomes pinned along the anisotropy axis. For these reasons, a traditional Currie-Weiss (Equation 1.7) treatment of the susceptibility data to quantify magnetic interactions (θ) is not appropriate for Ln ions as the low temperature susceptibility does not describe solely ferromagnetic or antiferromagnetic interactions. Thus, one must consider the crystal field splitting of the microstates to accurately determine the magnetic interactions in an anisotropic Ln ion system, for which this requires *ab initio* calculations.[29]

$$\chi_{dc} = \frac{M}{H} = \frac{Ng^2\mu_B^2 S(S+1)}{3k_B T} \cdot \frac{1}{T - \theta} \tag{1.7}$$

The dependence of the magnetization on the applied field (H) and the reduced applied field (HT^{-1}) are often measured at low temperatures. The shapes of the curves can provide valuable insight into the ground state of the complex and also serve as a means for evaluating the presence of magnetic anisotropy in a sample. In a system with perfect uniaxial anisotropy (i.e., pure $\pm m_J$ states) the isothermal curves in the reduced magnetization plot, M *vs* HT^{-1} should overlap. However, this is rarely obtained, thus, small separations between the isothermal curves are indicative of magnetic anisotropy as the magnetization is a function of the effective *g*-tensor. Another point of comparison in the magnetization data is the saturation value (M_{sat}); typically, in the absence of angular momenta M_{sat} is directly proportional to the product of the total spin and the *g*-factor. However, with highly efficient Ln SMMs, the saturation value is both dependent on the ground state m_J and the effective *g*-tensor for that state, given by the relationship in Equation 1.8. For example, a magnetization saturation value of *ca.* 5 μ_B is expected for a Dy^{III} ion with a $\pm m_J = 15/2$ ground state that has an effective *g*-tensor of *ca.* 20.00 (with perfectly axial anisotropy).

$$M_{sat} = \frac{1}{4} g_{eff} N \mu_B \tag{1.8}$$

Moreover, due to the large anisotropies that Ln ions possess they are predisposed to an experimental phenomenon, magnetic torquing. This means, that in the presence of a large magnetic field, such as in the high field limit (7 T in a conventional magnetometer), as the moment approaches saturation, the crystallites in the sample may physically move to align in a preferred orientation. In practice, the sample must be sufficiently restrained in a matrix, usually of grease or eicosane to prevent this movement. The movement of crystallites will create artificial artefacts in the magnetization data.

1.4.2 Alternating Current Magnetic Measurements

Alternating current (ac) magnetic susceptibility measurements can be used evaluate the presence of slow magnetic relaxation, which is a dynamic process and therefore time dependent (Equation 1.9). Such measurements monitor the change in magnetic response of a material with respect to an oscillating field of minimal field strength (*ca.* 2-4 Oe). More importantly, these measurements allow for the quantification of relaxation rates which provide valuable insight into the relaxation dynamics of a particular system.

$$\chi_{ac} = \frac{\partial M}{\partial H} \tag{1.9}$$

These measurements are much more sensitive to the changes in the magnetic response to an applied field as the magnetization does not vary linearly like in the case of dc measurements. As a result, there is a phase shift of the magnetization signal with respect to the drive signal (φ) and both the amplitude and the phase of the magnetization is recorded by the instrument (Figure 1.5). χ_{ac} therefore has two components (Equation 1.10), the real or in-phase (χ') component (Equation 1.11) and the imaginary or out-of-phase (χ") component (Equation 1.12).

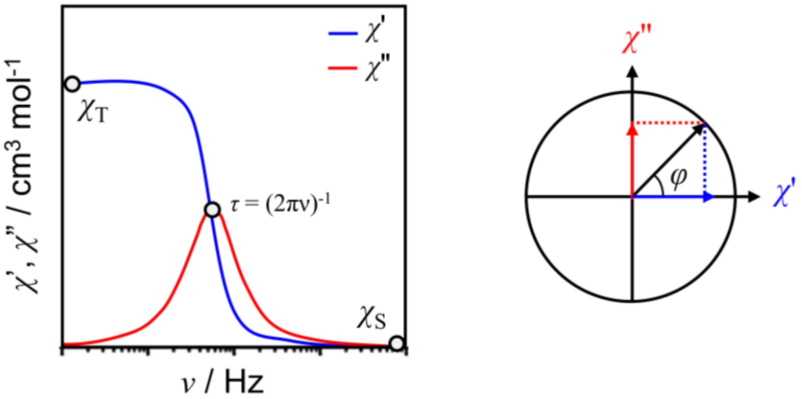

Figure 1.5 *Left:* Schematic representation of the frequency dependence of the in-phase (χ') and out-of-phase (χ") ac magnetic susceptibility. The isothermal (χ_T) and adiabatic (χ_S) susceptibilities are shown on the graph. *Right:* The amplitude and phase (φ) of the measured susceptibility broken down into χ' and χ" susceptibilities. Adapted from ref. 28.

$$\chi_{ac} = \sqrt{\chi'^2 + \chi''^2} \tag{1.10}$$

$$\chi' = \chi\cos(\varphi) \tag{1.11}$$

$$\chi'' = \chi\sin(\varphi) \tag{1.12}$$

Under thermal equilibrium conditions, i.e., the low frequency limit, the equilibrium magnetization will be the same as the static magnetic properties. At high frequency, the rearrangement of the magnetic moment may be slower than the driving field, this results in an increase in the χ" signal and a simultaneous decrease in the χ' signal (Figure 1.5), prompting differences between the magnetization of the sample and the equilibrium magnetization value. When this occurs, the system will achieve thermal equilibrium again by relaxing *via* one of the spin-phonon mechanisms discussed above in Section 1.3. More importantly, as the frequency of the driving field becomes much larger, the sample will eventually no longer be responsive to the oscillations in the field, and the χ" signal will decrease. A peak maximum of the χ" signal then effectively corresponds to the resonance where the frequency matches the relaxation time as described by Equation 1.13; where υ represents the linear ac frequency.

$$\tau = (2\pi\upsilon)^{-1} \tag{1.13}$$

When the phase shift in the magnetization becomes unchanged with respect to decreasing temperature, the relaxation time becomes constant; the result is overlapping peak maxima that is commonly associated with QTM.

Traditionally, the resonance frequencies were determined from Gaussian or Logistic fits of the experimental data and then later fit to the Arrhenius law (on a plot of ln(τ) *vs.* T^{-1}) to extract the corresponding U_{eff} and τ_0 values. This treatment to obtain the resonance frequency assumes that there is a single relaxation time to characterize the magnetization at a given temperature. In practice, this assumption can be an oversimplification, as a distribution of relaxation times may exists. To account for this, the generalized Debye model is invoked, introducing a distribution parameter (α). To remain physically reasonable, this α-value can take on a value between 0 and 1. When the α-value is any value other than 0, a distribution of relaxation times exists. Using the expressions for the generalized Debye model, the individual components of the ac susceptibility χ' (Equation 1.14) and χ" (Equation 1.15) can be fit independently and the parameters may be compared. Here, χ_T is the isothermal susceptibility and χ_S is the adiabatic susceptibility as shown in Figure 1.5.

$$\chi' = \chi_S + \frac{(\chi_T - \chi_S)\left[1 + (2\pi\upsilon\tau)^{1-\alpha}\sin\left(\frac{\pi\alpha}{2}\right)\right]}{1 + 2(2\pi\upsilon\tau)^{1-\alpha}\sin\left(\frac{\pi\alpha}{2}\right) + (2\pi\upsilon\tau)^{2(1-\alpha)}} \tag{1.14}$$

$$\chi" = \frac{(\chi_T - \chi_S)\left[1 + (2\pi\upsilon\tau)^{1-\alpha}\cos\left(\frac{\pi\alpha}{2}\right)\right]}{1 + 2(2\pi\upsilon\tau)^{1-\alpha}\sin\left(\frac{\pi\alpha}{2}\right) + (2\pi\upsilon\tau)^{2(1-\alpha)}} \tag{1.15}$$

While this treatment of the data works well when there exists a distribution of the relaxation times at a given temperature; if there are two distinct relaxation profiles (i.e., a bimodal out-of-phase signal), the independent relaxation times can be obtained through the summation of the individual generalized Debye models; effectively resulting in a deconvolution of the relaxation times.

It is important to note that the relaxation times should only be fit and obtained from the frequency dependent ac susceptibility data, not temperature dependent ac susceptibility data. There are two key reasons: (1) Tails in the low temperature region of the ac susceptibility can prevent the elucidation of resonance frequencies in the low frequency limit. An increase in the χ' and χ" signals at low temperature is a consequence of QTM. (2) Asymmetry in the peak shape can be induced when an applied static field is used in conjunction with the ac field. Static fields are often employed to eliminate the presence of ground state QTM, providing a clearer picture of the relaxation mechanisms. Unfortunately, the remaining dominant mechanisms are thus temperature dependent, and may have a region in which they are both operable (i.e., Raman and Orbach). The result is an asymmetric peak, and a resonance frequency which differs from the true value, eliciting inconsistences in the reported relaxation times and rates. For these reasons, it is crucial to obtain the relaxation rates solely from frequency dependent ac susceptibility measurements.

1.4.3 Magnetic Hysteresis and ZFC/FC Magnetization

Fundamentally, magnetic hysteresis measurements and zero-field cooled/field cooled (ZFC/FC) magnetization measurements are static field measurements (i.e., direct current magnetic susceptibility measurements), but, more importantly, they also provide crucial information regarding the viability of a SMM and its ability to retain information. These measurements provide insights into some of the different temperatures for blocking temperature (T_B). Hysteresis measurements are those where the temperature is kept constant, and the field is varied at a specified rate. These loops are cycled through positive and negative applied static fields, producing symmetric loops (Figure 1.16). Openings in the hysteresis loops will be the largest at low temperatures owing to longer relaxation times. However, this is not the case in systems that experience significant QTM effects. When the temperature is increased in each successive measurement, the loops will gradually decrease until there is no longer an opening, even at larger fields. From these measurements, the blocking temperature is defined by the highest temperature at which open hysteresis loops at $H = 0$ Oe are observed. Conversely, when there is no retention of the magnetic moment when the field is removed, the remnant magnetization (M_R) is zero, and the spins of the sample will simply follow the direction of the applied field passing through $H = 0$ Oe. There are significant challenges with quantifying a vital parameter such as T_B in this manner, more will be discussed in the following section.

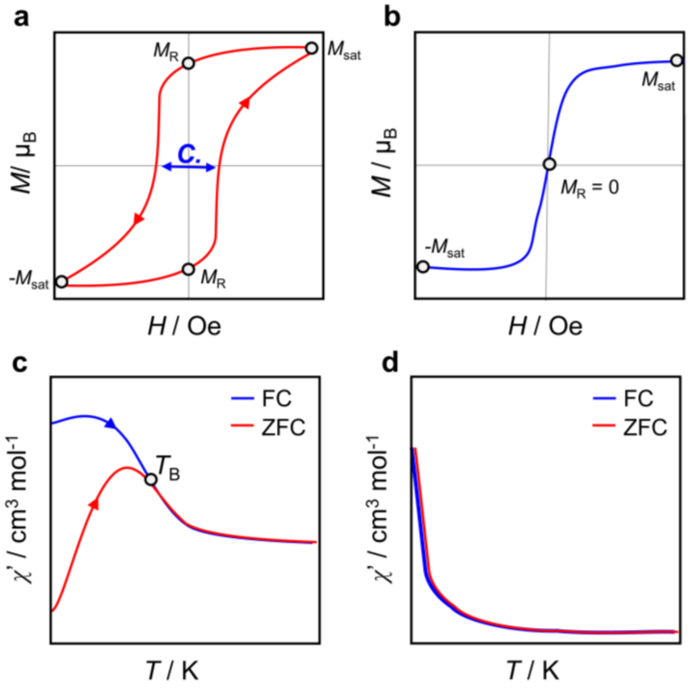

Figure 1.6 Schematic hysteresis curve (*M vs. H*) for (a) a superparamagnetic material or SMM below its blocking temperature and (b) for a paramagnetic material or SMM above its blocking temperature. M_R represents the remnant magnetization; the residual magnetization when the field is turned off ($H = 0$ Oe). M_{sat} represents the saturation magnetization value. The coercivity is represented by ***C***. Schematic ZFC-FC curves for (a) superparamagnetic material and (b) for a paramagnetic material.

Zero-field cooled, field-cooled (ZFC-FC) magnetization measurements involve cooling a sample in the absence of an applied magnetic field, then the magnetization of the sample is recorded upon increasing temperature (ZFC). This process is then repeated, where the sample is cooled in the presence of an applied magnetic field (FC). If the sample has the ability to retain magnetization, the two curves will differ. When the sample is cooled with the applied field, the spins will remain aligned with the applied field. However, in the zero-field cooled case, the spins do not have any preferential orientation upon cooling, thus when the field is applied to begin measuring in the warming mode, the spins will retain their random orientation until a specific temperature, that is the blocking temperature. From this measurement, the blocking temperature is defined by the temperature at which the two ZFC and FC curves bifurcate. This measurement is also sweep rate dependent. Ideally, both methods would be utilized, and the results compared for the characterization of T_B in an SMM.

1.5 The Challenges with Comparing SMMs

Historically, early SMMs often had large contributions from QTM, this would make obtaining a blocking temperature near impossible, as such many researchers frequently used U_{eff} as figure for merit for assessing the quality of an SMM. Virtually all molecules that exhibited an out-of-phase signal in their ac susceptibility were treated with the Arrhenius law. This equation assumes that there is some-kind of thermal equilibrium at play that allows for the spins of molecules to surmount a barrier before relaxing. However, now with a greater understanding of the various relaxation pathways accessible to Ln ions, this assumption that all molecules relax *via* the Orbach mechanism is an oversimplification at best. Even the highest performing SMMs to date, have shown contributions to their slow relaxation from other pathways such as Raman, direct, and QTM (although there are many more less studied mechanisms). This means that are some molecules that do not necessarily have an Orbach relaxation yet have U_{eff} values reported for them in literature. Further to this, the amount of data points utilized to determine the U_{eff} also presents errors, where points that are not strictly linear or apart of the Orbach relaxation are utilized, resulting in overlap with other relaxation processes, namely Raman. This can both inflate and decrease the U_{eff} value. As such, there are substantial challenges in correlating the performance of SMMs with their U_{eff}; despite this there have been significant milestones achieved, pushing the field of Ln-based SMMs to new heights (*vide infra*). Unfortunately, this difficulty in comparison also arises for other figures of merit, such as the blocking temperature (T_B).

A number of definitions exist in the literature for blocking temperature. Fundamentally it is agreed upon that it represents the temperature at which the magnetic moment becomes blocked to spin reversal, i.e., this is the highest temperature at which magnetization persists in the absence of an applied field. Yet there are many ways to characterize this figure of merit. The most abundantly used methods are (1) *M vs. H* hysteresis measurements; (2) ZFC-FC measurements; and to a lesser extent (3) the 100 s relaxation time. Importantly, many of the measurements are temperature and/or field dependent and direct comparisons to reported values can be inaccurate due to different sweeping rates, and different methods used.

In the literature there is a large discrepancy in the sweep rates used to complete hysteresis measurements (10 Oe s^{-1} – 500 Oe s^{-1}).[30] For research groups with access to a Physical Property

Measurement System, the continuous sweeping mode allows for very fast sweeping rates, as high as 500 Oe s^{-1}. Not only are sweeping rates of this magnitude not obtainable with a conventional SQUID magnetometer, a constant sweeping speed is difficult, if not impossible, to achieve over the entirety of the measurement. This can have significant effects on the observed magnetization profile; for example, quickly sweeping the applied magnetic field near the zero-field region of a magnetic hysteresis loop (*M* vs. *H*) may indicate retention of the magnetic moment, when in fact there is no retention. Thus, these discrepancies often lead to inflation in the reported T_B values from traditional *M vs. H* hysteresis measurements. ZFC-FC measurements have also become popular for approximating the blocking temperature, however this value is also highly dependent on the user and the way in which the measurement is executed. The metric identified from this measurement is T_{irrev}, which is the temperature at which the independent ZFC and FC curves bifurcate. This is sometimes used as an approximation of the blocking temperature. Unlike hysteresis measurements, it is not yet commonplace to disclose the sweep rate of the temperature used for ZFC-FC measurements in the literature, making the comparison much more difficult. Like hysteresis measurements, increasing sweeping speeds will artificially increase the observed T_B. In an effort to standardize the determination and reporting of T_B values and to eliminate the sweep rate dependence, the 100 s relaxation time alternative was introduced.[31] This interpretation of T_B is not applicable to all SMMs as a relaxation time of 100 s must be measurable and not extracted from the relaxation dynamics. There is also the challenge that not all SMMs exhibit the same relaxation dynamics over the same temperature range or at the same rate. Thus, this limits the comparison of SMMs to those that are high performing and structurally similar.

1.6 Significant Milestones and Lessons learned from 4f SMMs

From the concepts discussed above, a staggering amount of 4f SMMs have been synthesized and studied, with the most abundant ion being Dy^{III}. This is largely a result of the half-integer angular momenta projection of the $^6H_{15/2}$ ground state of Dy^{III}, which ensures that the ground state will at least be doubly degenerate in a field.[21] Thus, slow relaxation of the magnetization has been observed in Dy^{III}-based systems that are not strictly axial, or of high symmetry. These systems provide valuable insight into the fundamentals that govern the slow relaxation in 4f SMMs, revealing the influential aspects of ligand design, molecular structure, crystalline structure, and electronic structure on the overall slow relaxation dynamics. For the synthetic chemist, the examples that follow serve as lessons towards the development of new high-performing magnets with the intention of developing compounds that are technologically relevant for future devices.

1.6.1 Early Ln SMMs

The first Ln-based SMMs contained only a single metal center, despite much of the work, at the time, in the synthesis of SMMs being focused on multinuclear transition metal clusters.[32–35] These seminal 4f-SMMs were of the general formula $[\mathrm{LnPc_2}]^n$ (Ln = $\mathrm{Tb^{III}}$, $\mathrm{Dy^{III}}$, $\mathrm{Ho^{III}}$, Pc = phthalocyanide, n = -1, 0, +1), and they had D_4d local symmetry (Figure 1.7).[36,37] The slow relaxation performance of these molecules (U_{eff} = 330 K) surpassed the performance of their transition metal counterparts at the time of their discovery.[38,39] This finding paved the way for several key achievements in the field of Ln-based SMMs; not only did it demonstrate the viability of Ln SMMs, it simultaneously showed that a single metal center was sufficient for the observation of magnetic relaxation.

Moreover, within the ligand field provided by the phthalocyanide, the magnetic axiality of the $\mathrm{Tb^{III}}$ derivative was greater than the $\mathrm{Dy^{III}}$ compound; meaning that a larger m_J projection was stabilized in the case of $\mathrm{Tb^{III}}$ over $\mathrm{Dy^{III}}$ ($m_J = \pm 6$ for $\mathrm{Tb^{III}}$ and $m_J = 13/2$ for $\mathrm{Dy^{III}}$). This elicited greater SMM performance from $[\mathrm{Tb^{III}Pc_2}]$[TBA] (TBA = tetrabutylammonium) than $[\mathrm{Dy^{III}Pc_2}]$[TBA]; U_{eff} = 330 K *vs.* 40 K. This energy barrier was obtained from the fit of the experimental data to the Arrhenius law, and had assumed complete relaxation through the first excited state on account of the correlation between the ac magnetic susceptibility measurements and the doublet states that were determined from dc measurements and NMR.[40]

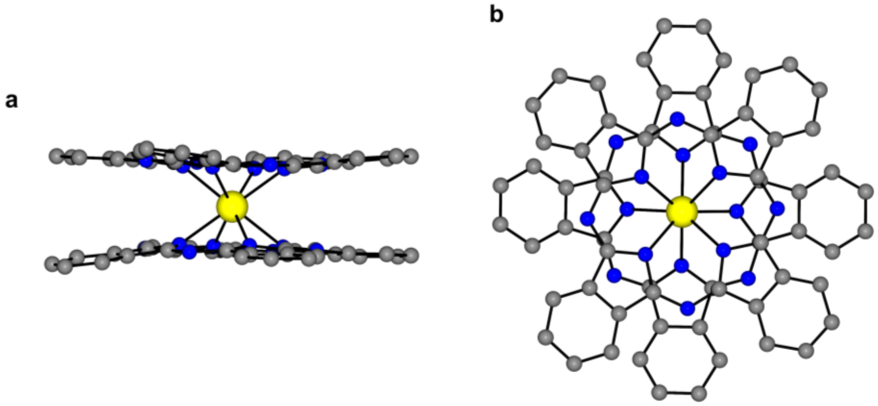

Figure 1.7 Solid state molecular structure of $[\mathrm{Tb^{III}Pc_2}]$ viewed from (a) the side and (b) from the top/above depicting its square antiprismatic (D_4d) local environment.[36] Colour code: Yellow (Tb), blue (N), grey (C). Hydrogen atoms have been removed for clarity.

However, in a later study it was found that QTM plays a significant role in the relaxation dynamics of this compound.[41] Magnetic hysteresis measurements revealed a classic stair-case structure associated with tunneling between degenerate crystal field microstates.[1,42] Furthermore, a recent report on the slow relaxation dynamics of $[Tb^{III}Pc_2]^-$ has revealed the field dependence of the magnetic relaxation (i.e. relaxation *via* the direct mechanism may be possible);[41] providing further evidence that relaxation dynamics are much more complicated than initially offered in 2003.[36,37]

The discovery of slow magnetic relaxation in $[LnPc_2]^n$ was followed by the polyoxometalates, $Na[Ln(W_5O_{18})_2]$ (Ln = Tb^{III}, Dy^{III}, Ho^{III}, Er^{III}), which similarly possessed D_4d local symmetry about the metal center (Figure 1.8).[43] Comparatively, the Er^{III} derivative had superior SMM properties out of all the prepared lanthanide congeners. Notably, despite both Er^{III} and Dy^{III} having $m_J = \pm$ 15/2 ground states, the directional dependence of the magnetic moment of these states is drastically different, i.e., the $m_J = \pm$ 15/2 state for Er^{III} is prolate, whereas the $m_J = \pm$ 15/2 state of Dy^{III} is oblate; requiring differing ligand fields to stabilize the large magnetic moment of this spin-orbit coupled ground state. Ultimately, $Na[Dy^{III}(W_5O_{18})_2]$ did not exhibit any SMM properties. With respect to $Na[Er^{III}(W_5O_{18})_2]$, the $m_J = \pm$ 13/2 was the most stabilized, which afforded the observation of the slow relaxation dynamics. This is in stark contrast to $[Er^{III}Pc_2]$, where the CF state with the largest magnetic moment was significantly destabilized, resulting in a $m_J = \pm 1/2$ ground state, despite both molecules having local D_4d symmetry.[40,43] Consequently, the origin for this behaviour is best described by the structural differences of the molecules imposed by the coordinating ligands. Here, the zenith angle (ϕ), the angle of the main rotational axis of the molecule, the metal ion, and a coordinating atom of the ligand, describes how axial or equatorial a LF is, for which larger angles are representative of a more equatorial LF. For the polyoxometalates, the ϕ angle is 58.5° and for the phthalocyanides this angle is slightly more acute at 54.5°.[44] This is particularly important when discussing the stabilization of certain m_J projections in these molecules with D_4d symmetry.

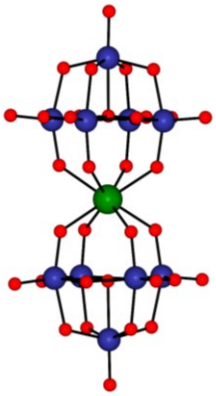

Figure 1.8 Solid state molecular structure for $[Ln(W_5O_{18})_2]^-$, depicting its square antiprismatic (D_4d) local environment.[43]Colour code: Green (Er), dark blue (W), red (O). Sodium cations have been removed for clarity.

It is thus crucial that the placement of coordinating atoms about the metal center are in energetically favourable positions so as to minimize any electronic repulsions and elicit stabilization of the largest m_J projection. Failure to do so, often results in the stabilization of small m_J states and loss of purity of the m_J states. Regardless, the relaxation, if any at all, is often characterized by fast ground state QTM in this case.

1.6.2 SMMs with Equatorial Ligand Fields

Following the success of the early Ln SMMs, organometallic SMMs (i.e., those with metal-carbon bonding interactions) became increasingly popular. The first report of an organometallic Ln SMM was in 2010, and the N-bridged dinuclear dysprosium molecule, $[\{Cp_2Dy^{III}(\mu\text{-bta})\}_2]$ (Cp = cyclopentadienyl, btaH = 1*H*-1,2,3-benzotrazole), utilized cyclopentadienyl ligands,[45] which was the first in several uses of aromatic carbocyclic ligands in the field of SMMs (Figure 1.9).[46]

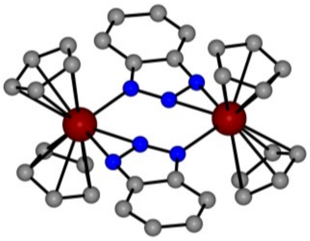

Figure 1.9 Solid state molecular structure of $[\{Cp_2Dy^{III}(\mu\text{-bta})\}_2]$, the first organometallic SMM reported in 2010.[45] Colour code: Dark red (Dy), blue (N), grey (C). Hydrogen atoms have been omitted for clarity.

Carbocyclic ligands, such as cyclooctatetraenyl (COT^{2-}) have been utilized widely in the field of SMMs, because metallocenes, or sandwich complexes, impart a particularly well suited LF for harnessing the maximum magnetic anisotropy of certain 4f ions.[14] In this regard, the first organometallic sandwich complex was reported by Gao in 2011,[47] this molecule, $[(\eta^5\text{-Cp*})Ln(\eta^8\text{-COT})]$ (Cp* = pentamethylcyclopentadienyl, Ln = Tb^{III}, Dy^{III}, Ho^{III}, Er^{III}, Tm^{III}), possessed an overall bent molecular structure with C_s point symmetry (Figure 1.10). The mirror plane bisects the centroids of the two aromatic rings and the metal center. The most pronounced SMM properties were observed in the Er^{III} derivative, with two thermally activated processes being identified with U_{eff} = 322 K and 197 K, and magnetic hysteresis below 5 K. Of the remaining 4f ions, only Dy^{III} and Ho^{III} produced an out-of-phase signal in the ac susceptibility when placed within a diamagnetic matrix, and yet, the barriers obtained are at best an entire order of magnitude smaller than those for $[(\eta^5\text{-Cp*})Er^{III}(\eta^8\text{-COT})]$.

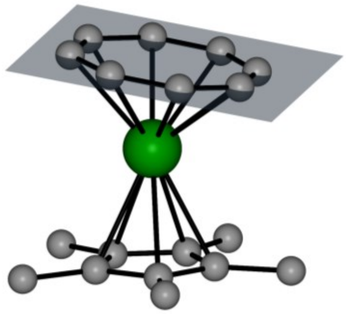

Figure 1.10 Solid state molecular structure for [(η^5-Cp*)Er^{III}(η^8-COT)], the first organometallic sandwich complex based on the COT ligand.[47] Transparent grey plane bisects the carbon atoms of the COT ligand, depicting the tilt angle. Colour code: Green (Er), grey (C). Hydrogen atoms have been omitted for clarity.

The bend in the molecular structure of [(η^5-Cp*)Ln(η^8-COT)] was believed to be the contributing factor towards QTM that inhibited the relaxation dynamics in this series of molecules. As such replacing one of the aromatic ligands became a desirable approach for increasing the local symmetry and improving the overall slow relaxation dynamics. Substituted COT frameworks were explored as a means for providing steric protection and increased stability to the resulting complexes. Homoleptic 4f complexes of COT^{2-} require counterions, usually alkali metal ions from the synthesis to yield an electrically neutral molecule. In the metallocene [Dy^{III}(COT")$_2$Li(THF)(DME)] (COT" = 1,4-bis(trimethylsilyl)cyclooctatetraene),[48–50] one of the COT" ligands acts as a bridge between the Dy^{III} ion and the Li ion, resulting in a longer Dy-centroid distance, ultimately yielding an unsymmetrical compound (Figure 1.11a). While a modest U_{eff} of 43 K was obtained, the multimodal ac susceptibility of this complex revealed the presence of multiple relaxation processes.[50] This compound demonstrated the complexity of 4f single-ion magnetism, yet also provided a platform for which the magnetic properties of 4f ions could be investigated as a function of the peripheral structural modifications; that is, finite tailoring of the ligand substituents and alkali metal ion interactions. The gradual deviations from ideal symmetry, which result as a consequence of the external silyl substituents, diminish the axiality and are responsible for the prevalent QTM observed in [Dy^{III}(COT")$_2$Li(THF)(DME)].

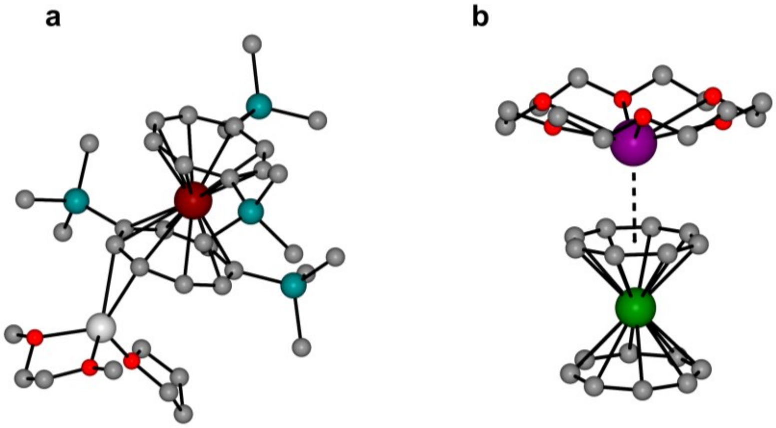

Figure 1.11 Solid state molecular structure of (a) [Dy^{III}(COT")$_2$Li(THF)(DME)] and (b) [K(18-crown-6][Er^{III}(COT)$_2$].[50,53] Colour code: Dark red (Dy), green (Er), purple (K), white (Li), teal (Si), red (O), grey (C). Hydrogen atoms have been removed for clarity.

To improve upon the magnetic properties, the ion-separated complex, [Li(DME)$_3$][Ln^{III}(COT")$_2$] (Ln = Dy^{III}, Er^{III}) was prepared and studied. The discrete Dy^{III} metallocene had a Li-C$_{COT}$ distance nearly double that observed for [Dy^{III}(COT")$_2$Li(THF)(DME)] and equivalent Dy-centroid distances; yet, prominent QTM was still present, resulting in a U_{eff} of 25 K, with no hysteretic behaviour.[51] *Ab initio* calculations on this compound determined the orientation of the ground state magnetic axis to be tilted away from the centroid-Dy-centroid axis, aligning with the silyl substituents. The ground state Kramers doublet (KD) is described by the $m_J = \pm 1/2$, whereas the highest energy doublet state was comprised by the $m_J = \pm 15/2$ state and was highly axial ($g_z = 19.9927$), suggesting that the replacement of Dy^{III} with Er^{III} would give significantly improved relaxation dynamics. Indeed, switching the ion resulted in open hysteresis loops with a blocking temperature of 8 K, and efficient thermal relaxation which only displayed Orbach-like (U_{eff} = 187 K) dynamics over the entire temperature range studied.[52] While no formal QTM regime was observed in the ac magnetic susceptibilities, a prominent step at zero field in the hysteresis curves of [Er^{III}(COT")$_2$]$^-$ is indicative of tunneling in the ground state of this complex. Moreover, removal of the silyl groups to afford [K(18-crown-6][Ln(COT)$_2$] (Ln = Dy^{III}, Er^{III}) did not improve the magnetic properties of Dy^{III} despite preserving the 8-fold symmetry in the molecule (Figure 1.11b).[53] The low-lying energy spectrum of [Dy^{III}(COT)$_2$]$^-$ is dense, with the ground state doublet corresponding to the $m_J = \pm 9/2$, with the next highest excited states corresponding to $m_J = \pm 11/2$ and $\pm 7/2$. Not only are the relative energies of the m_J states out of order, the anisotropy axes in the ground state and first excited KDs are perpendicular to one another. Contrary to this, [Er^{III}(COT)$_2$]$^-$ has exceptional slow relaxation dynamics, such that below 12 K a signal in the ac susceptibility could not be observed as the relaxation time is longer than 10 s. Overall an effective barrier of 286 K is achieved which corresponds to thermal relaxation *via* the second excited state. Further supporting this, is the co-axial alignment of the anisotropy axes in these Kramers doublets.

Given the prolate shape of the $m_J = \pm 15/2$ state of Er^{III}, even larger aromatic carbocyclic rings have been investigated. The complex $[Er^{III}(COT)(CNT)]$ (CNT = cyclononatetraenyl; $C_9H_9^-$), utilizes the 9-membered aromatic ring to provide a larger equatorial LF, with the goal of stabilizing the $m_J = \pm 15/2$.[54] The experimental U_{eff} of 361 K correlates well with the *ab initio* predicted barrier of 385 K through the $m_J = \pm 1/2$ state, with low lying doublet ordering of $m_J = \pm 15/2, \pm 13/2$, and $\pm 1/2$. Moreover, it may be possible to improve upon the properties of $[Er^{III}(COT)(CNT)]$ with substitution of the COT ligand with another CNT to afford the homoleptic species. Indeed, the synthesis of divalent homoleptic $[Ln^{II}(CNT)_2]$ (Ln = Sm^{II}, Eu^{II}, Tm^{II}, Yb^{II}) complexes has already been reported.[55]

A fundamental understanding of the effects of the ligand field on the orientation of the main magnetic axis was achieved through the above studies and molecules. Importantly, comparisons between Er^{III} and Dy^{III} complexes of COT provided pivotal evidence that the ligand field imposed by the COT ligand did not yield the desired orientation of the anisotropy for Dy^{III} ions. This difference in the spheroid shape of the $m_J = \pm 15/2$ for Dy^{III} and Er^{III} (i.e., prolate *vs.* oblate), combined with the lack of an axial LF for Dy^{III} was crucial in explaining and understanding the inferior SMM performance of this ion.

1.6.3 SMMs with Axial Ligand Fields

Despite the large CF splittings that are obtainable for Dy^{III} in the LF provided by the COT ligand, stabilization of the largest spin-orbit state with the largest magnetic moment is not possible owing to its oblate electron density. Thus, efforts to tailor the LF to this ion have elicited different synthetic and design approaches for maximizing the axial contributions of the LF, while simultaneously minimizing any off-axis contributions. This ideology has been supported by *ab initio* studies on relatively simple molecular frameworks, $[Dy^{III}O]^+$ and $[Dy^{III}F_2]^+$ for which efficient multi-step magnetic relaxation is predicted.[56,57] Unfortunately, these molecules are not trivial to synthesize,[58] but the sequential ordering of their m_J states, in combination with the large energy splitting of the Kramers doublets have provided ample inspiration for synthetic chemists. There are now several examples of magnetic relaxation in Dy^{III}-based SMMs in which relaxation utilizes several excited state Kramers doublets through employing an axially dominant LF.[59–62]

Molecules with D_5h point symmetry have become increasingly sought after as SMMs because a true D_5h point group does not have transverse CF terms and perfect axiality can be achieved in every Kramers doublet.[37,56] This means that magnetic relaxation should occur *via* multiple steps as the angle between the anisotropic axes of each doublet state will be very small or negligible. In reality, obtaining perfect D_5h symmetry is not easy but the angle between axes of different doublets can be minimized with strong dominant axial LF and CF components,[63] or by imparting symmetry axes such as C_2, C_3 and C_5.[64,65] Thus, even molecules with near perfect D_5h symmetry have shown notable anisotropy enhancements leading to large U_{eff} and T_B values. Prominent examples of such molecules include [Dy^{III}(bbpen)Br] (Figure 1.12a; H_2bbpen = *N*,*N*'-bis(2-hydroxybenzyl)-*N*,*N*'-bis(methylpyridyl)ethylenediamine))[66] and [Dy^{III}(Cy_3PO)$_2$(H_2O)$_5$]Br_3 (Figure 1.12b; Cy_3PO = tricylohexyl phosphine oxide)[67]; at the time of their discovery, they respectively held the records for largest U_{eff} (1025 K) and largest T_B (20 K). While [Dy^{III}(bbpen)Br] had the largest U_{eff} value, it possessed waist-restricted hysteresis, and conversely, [Dy^{III}(Cy_3PO)$_2$(H_2O)$_5$]Br_3 had a modest U_{eff} of 543 K despite displaying zero-field coercivity up to 20 K. The stark contrast in performance of these two molecules is suggested to be a consequence of different coordinating atoms in the equatorial plane of the molecule, causing a deviation in the relative orientation of the main magnetic axis with respect to the perceived C_5 axis.

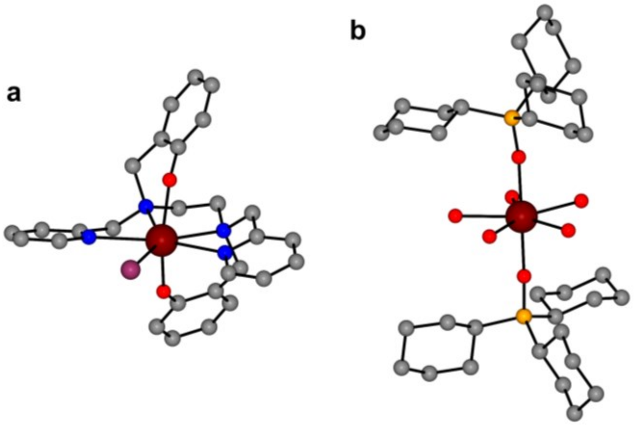

Figure 1.12 Solid state molecular structures of (a) [Dy^{III}(bbpen)Br] (H_2bbpen = *N*,*N*'-bis(2-hydroxybenzyl)-*N*,*N*'-bis(methylpyridyl)ethylenediamine)) and (b) [Dy^{III}(Cy_3PO)$_2$(H_2O)$_5$]Br_3 (Cy_3PO = tricylohexyl phosphineoxide).[66,67] Colour code: Dark red (Dy), orange (P), plum (Br), red (O), blue (N), and grey (C). Hydrogen atoms and counterions have been omitted for clarity.

It is evident that the atoms in the equatorial position of pentagonal bipyramidal Dy^{III} have a significant effect on the ensuing magnetic properties. In a later work, the effect of the axial position on the relaxation dynamics was investigated by way of comparison for [Dy^{III}(OR)X(L)$_5$]$^{3+}$ and [Dy^{III}(OR)$_2$(L)$_5$]$^{3+}$ (X = Cl, Br; OR = $^-OCMe_3$, $^-OSiMe_3$, ^-OPh; L = THF, pyridine, 4-methylpyridine).[68] By systematically varying the ligands in the axial positions, a correlation between the spin reversal barrier and the blocking temperature was achieved. Additionally, compounds with one halide in the axial position characteristically exhibited a QTM regime, whereas those compounds with the same axial ligand did not. Aside from slight variations in the height of the energy barriers among the studied compounds, a marked change in the relaxation rate at which the Raman process becomes dominant over the Orbach relaxation occurred more quickly and at higher temperatures for the asymmetric derivatives. Unfortunately, these findings are very specific to the geometry about the metal-center, and more magneto-structural correlation studies are needed to fully understand the effects of through barrier relaxation processes.

Another approach for imposing a highly axial ligand field is by use of cyclopentadienyl ligands. The smaller ring size of the cyclopentadienyl anion affords a greater concentration of electronic density in a localized area compared to the larger carbocyclic rings such as COT and CNT which impose more of an equatorial LF. To illustrate this, Cp ligands have much smaller centroid-Dy-C_{ring} angles (*ca.* 27°) compared to COT (*ca.* 44°),[53,69,70] yielding greater axiality (i.e., it describes how small the tunneling gap between doublets is).[71] *Ab initio* studies on $[(Cp^*)_2Dy^{III}]^+$ predicted very small tunneling gaps in the 3rd and 4th Kramers doublets, which would yield a high-performing SMM.[72] Unfortunately, the synthesis and isolation of this species is challenging owing to (1) the highly electropositive Dy^{III} ion and (2) the relatively small size of the Cp*. However, a family of $[(Cp^R)_2Ln]^+$ compounds has been reported in which substituents on the Cp ring block the approach of other ligands and solvents from the equatorial positions of the 4f ion, although minimal short-contacts with ligand substituents and the metal occur in some bulky variants of the Cp ligand. As a consequence, the orientation of the main magnetic axis deviates in higher excited states as these interactions would begin to introduce transverse components to the CF; indeed, there are already studies which have begun to look at this relationship.[73]

The bulky Cp-based ligand, Cp^{ttt} ($C_5H_2{}^tBu_3$-1,2,4; ${}^tBu = C(CH_3)_3$) was utilized in the synthesis of the first dysprosocenium cationic complex $[(Cp^{ttt})_2Dy^{III}][B(C_6F_5)_4]$.[69,70] Access to this homoleptic species was afforded by halide abstraction from $[(Cp^{ttt})_2Dy^{III}(Cl)]$ (Figure 1.13a); for which negligible slow relaxation properties were observed.[70,74] For $[(Cp^{ttt})_2Dy^{III}][B(C_6F_5)_4]$, the two Cp^{ttt} rings are fairly linear with a centroid-Dy-centroid angle of *ca.* 153° (Figure 1.13b). The *ab initio* calculations revealed highly ordered and pure Kramers doublets with superimposed orientations for the main magnetic axis, characterized by $m_J = \pm 15/2, \pm 13/2, \pm 11/2, \pm 9/2, \pm 7/2$, and $\pm 5/2$. Only in the highest two Kramers doublets is the purity lost and the mixing elicits anisotropy axes that are perpendicular to the other six Kramers doublets.[69] Overall, this leads to an astonishing U_{eff} of 1760 K/1837 K, with notable contributions from the Raman relaxation process. The Raman process becomes dominant at 60 K and this temperature is consistent with the blocking temperature obtained from hysteresis measurements as well as the ZFC-FC measurements. Combined *ab initio* calculations and experimental measurements suggest that the vibrations of the C-H bonds on the Cp^{ttt} ligand facilitate the transition between the ground and first excited state doublet. It is suggested that fine tuning the ligand and its substituents to impose greater molecular rigidity can increase the energy of the vibrations and optical phonons, shifting it out of resonance with the CF microstates, while simultaneously ensuring the population of the ground state through ligand design.

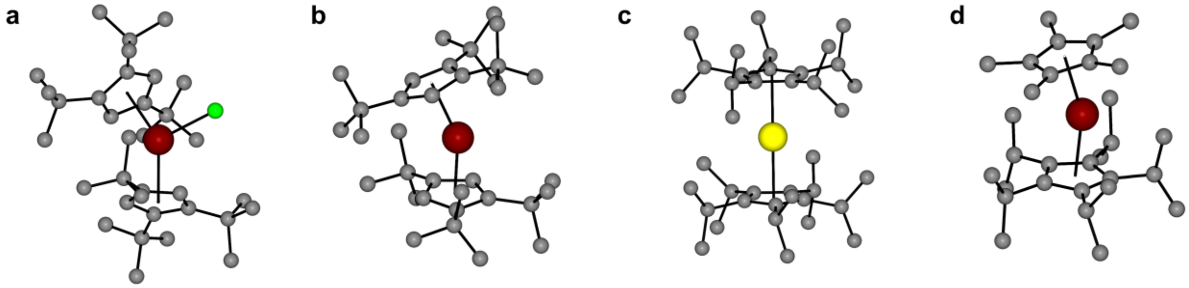

Figure 1.13 Solid state structures of (a) $[(Cp^{ttt})_2Dy^{III}(Cl)]$, (b) $[(Cp^{ttt})_2Dy^{III}]^+$, (c) $[(Cp^{iPr5})_2Tb^{II}]$, (d) $[(Cp^*)Dy^{III}(Cp^{iPr5})]^+$.[9,69,70,75] Colour code: Dark red (Dy), yellow (Tb), green (Cl), grey (C). Hydrogen atoms and counter anions have been omitted for clarity.

Divalent metallocenes of Cp-based ligands have also been prepared. The complexes, $[(Cp^{iPr5})_2Ln]$ ($Cp^{iPr5} = C_5{}^iPr_5$; Ln = Tb^{II}, Dy^{II}), are prepared from the reduction of $[(Cp^{iPr5})_2Ln^{III}(I)]$ yielding a perfectly linear divalent complex (Figure 1.13c).[75] The resulting electronic configurations for the reduced species are $4f^85d^1$ (Tb^{II}) and $4f^95d^1$ (Dy^{II}), and they are representative of Kramers and non-Kramers systems, respectively. Thus, the divalent Tb complex acts a model system for the isolation of a highly symmetrized Dy^{III} ion in a linear metallocene environment. While it is difficult to compare because the 5d orbital is occupied in $[(Cp^{iPr5})_2Tb^{II}]$, the U_{eff} of 1734 K and 100 s T_B of 52 K demonstrates the significance of a highly linear and symmetrical coordination environment in the development of new Dy^{III}-based SMMs. In addition to the symmetry effects, the physical placement of ligands about the metal center may also have drastic effects on the magnetic properties. Magneto-structural correlations on the family $[(Cp^{iPr4R})_2Dy^{III}][B(C_6F_5)_4]$ (R = H, Me, Et, *i*Pr) have shown the inter-complementary role of the centroid-Dy-centroid angle and the Dy-centroid distance. Ideally large angles, that approach 180° and short Dy-centroid distances should be sought; however this is incredibly difficult to achieve. Bulky substituents will promote a more linear angle yet increase the Dy-centroid distance, thus lacking a strong metal-ligand interaction for directing the anisotropy axis. A recent example has found a balance between these requirements. $[(Cp^*)Dy^{III}(Cp^{iPr5})][B(C_6F_5)_4]$ utilizes two different Cp ligands to obtain a staggering U_{eff} of 2217 K and a hysteresis blocking temperature of 80 K (Figure 1.13d).[9] The steric bulk provided by Cp^{iPr5} shields the equatorial positions of the Dy^{III}, and the smaller Cp* ligand reduces ligand-ligand repulsions and affords a smaller Dy-centroid distance. Interestingly, while the first dysproscenium ion, $[(Cp^{ttt})_2Dy^{III}]^+$, relaxes *via* the 6th Kramers doublet,[69] the thermal barrier in $[(Cp^*)Dy^{III}(Cp^{iPr5})]^+$ is defined by the 5th Kramers doublet despite the overall crystal field splitting occurring over a larger energy range. Moreover, the out-of-plane vibrations of the Cp* ligand (632.9 cm^{-1} and 640.5 cm^{-1}) are postulated to mediate the transition from the ground state to the first excited state (ΔE = 672 cm^{-1}); the energies of which are in good agreement with this hypothesis.

It is evident that optical and acoustic phonons play a significant role in determining the accessibility of higher excited states for magnetic relaxation in the $[(Cp^R)_2Dy^{III}]^+$ family. This class of SMMs have brought forth new considerations for the performance of SMMs and they must be understood and addressed to be effectively used in future devices. Many of these concerns related to the vibrational modes of the surrounding and the phonon density of states have been discussed in the context of solid-state materials for magnetic memory and devices,[76] but remain a challenge for the synthetic chemist to address.

1.6.4 Materials from Molecules: Low coordinate, high symmetry

The incorporation and use of SMMs in future devices will require them to be combined with other functional materials so that individual molecules may be addressed (i.e., for read and write applications) and this has resulted in several different approaches for the immobilization of SMMs. Some of these include both the surface functionalization and internal deposition of SMMs on, and in, carbon nanotubes (CNTs),[77,78] and graphene,[79] as well as the encapsulation of SMMs into the pores of metal-organic frameworks (MOFs).[80] Encapsulating SMMs is a way to impart a physical barrier between the SMM and the substrates by minimizing intermolecular interactions that are known to be deleterious to the spin reversal barrier as well as the coercivity. Typically, when deposited onto the surface of substrates, SMMs have lost these functionalities; the results of which have been largely attributed to the phonon bath of the substrate and the vibrational modes of the molecules being in resonance with one another.[81]

The encapsulation of 4f SMMs in CNTs is a desirable approach for incorporating SMMs as the CNT provides a buffer from other surfaces and phonons. Unfortunately, the encapsulation and confinement of $[Dy^{III}(acac)_3(H_2O)_2]$ (acac = acetylacetonate) in CNTs did not elicit the same (or any) relaxation dynamics as the SMM on its own (U_{eff} = 0 K *vs.* U_{eff} = 66 K).[82,83] The lack of organizational control represents a hurdle for maintaining and controlling the magnetic axiality. In this regard, endohedral metallo-fullerenes (EMFs) are able to control the symmetry,[84] as well as the exchange and dipolar interactions more precisely. EMFs are also easily sublimed, making them attractive for device fabrication techniques, and EMFs also have increased stability towards moisture and oxygen.[85] Specifically, the use of nitride-based EMFs $Ln^{III}_3N@C_{80}$ have become increasingly popular owing in part to their interesting magnetic properties, some of which include frustrated paramagnetism ($Ho^{III}_3N@C_{80}$ and $Tb^{III}_3N@C_{80}$),[86] ferromagnetism ($Gd^{III}_3N@C_{80}$),[87] and waist-restricted hysteresis ($Dy^{III}Sc^{III}_2N@C_{80}$).[88]

The hallmark example, $Dy^{III}Sc^{III}_2N@C_{80}$, possessed a single paramagnetic Dy^{III} ion and two diamagnetic Sc^{III} ions (Figure 1.14). This SMM has been the subject of numerous studies including an investigation on the effects of different diamagnetic matrices on QTM,[89] and in a separate study the effects of varying the number of spins within the EMF was also investigated (i.e., altering the relative proportions of Dy^{III} and Sc^{III} ions).[90] In both studies, QTM steps in the hysteresis curves were reduced, or eliminated, when either the EMF was suspended in a polystyrene matrix (i.e., magnetic dilution) or when a second Dy^{III} ion was introduced into the core of the fullerene (i.e., ferromagnetic coupling). In the latter case, the introduction of the third paramagnetic center to give $Dy^{III}_3N@C_{80}$ did not result in retention of the magnetic moment at any field in the hysteresis; this is a consequence of a frustrated ground state with competing ferromagnetic and antiferromagnetic interactions.

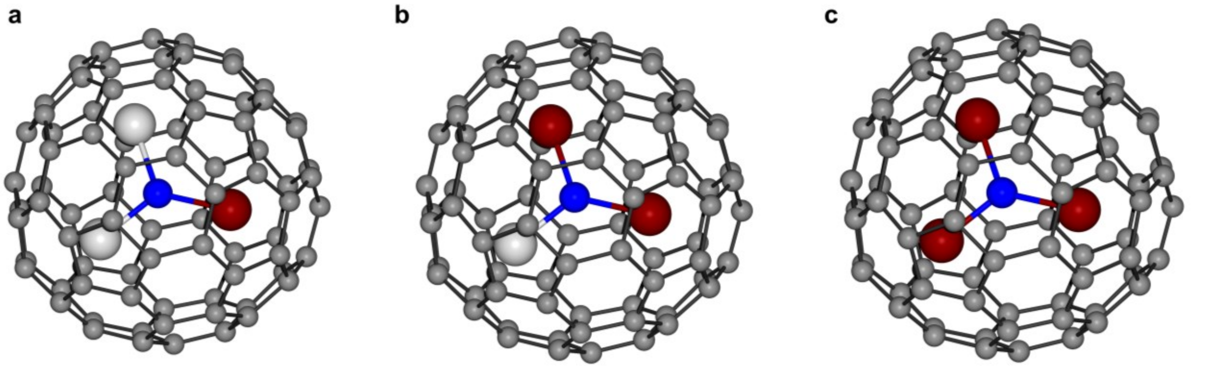

Figure 1.14 Solid state molecular structures of (a) $Dy^{III}Sc^{III}_2N@C_{80}$, (b) $Dy^{III}_2Sc^{III}N@C_{80}$, and (c) $Dy^{III}_3N@C_{80}$.[89,90] Colour code: Dark red (Dy), white (Sc), blue (N), grey (C). Counter ions omitted for clarity.

The utilization of radical-based ligands for coupling the spins of paramagnetic ions, and specifically 4f ions, is a well-established approach for increasing the magnetic communication between otherwise weakly interacting 4f ions.[91] Thus, the use of radical fullerenes can enhance the coupling between the encapsulated 4f ions and reduce fast zero-field tunneling. Incredibly strong coupling was achieved in $Gd^{III}_2@C_{79}N$, with 4f-radical coupling of -350 cm^{-1} (Figure 1.15a).[92] Remarkably, this is an order of magnitude larger than the previous benchmark complex $[K(18\text{-crown-6})](\{(Me_3Si)_2N\}_2(THF)Gd^{III})_2(\mu\text{-}\eta^2:\eta^2\text{-}N_2)$, J = -27 cm^{-1} (Figure 1.15b).[93] Despite the strong metal-radical interaction, the metal-metal coupling was characteristically weak (-0.4 cm^{-1}).[84] *Ab initio* calculations on the Dy^{III} analog of this complex ($Dy^{III}_2@C_{79}N$) predicted a highly axial ground state $m_J = \pm 15/2$ doublet with a minimal transverse magnetic moment, < 0.001 μ_B.[94] While this compound is expected to be an exceptional SMM, it remains elusive synthetically. Thus, a closely related compound, $Dy^{III}_2@C_{80}(CH_2Ph)$, has been prepared and studied (Figure 1.15c).[94] Here, the metal-radical coupling is considerably smaller (+32 cm^{-1}), yet relaxation through the exchange coupled states is still viable, producing a U_{eff} of 613 K. The benzyl adduct of $Dy^{III}_2@C_{80}(CH_2Ph)$ is anticipated to play a prominent role in the relaxation dynamics and pathways, because the fullerene is far too rigid to assist with relaxation *via* vibrational coupling.

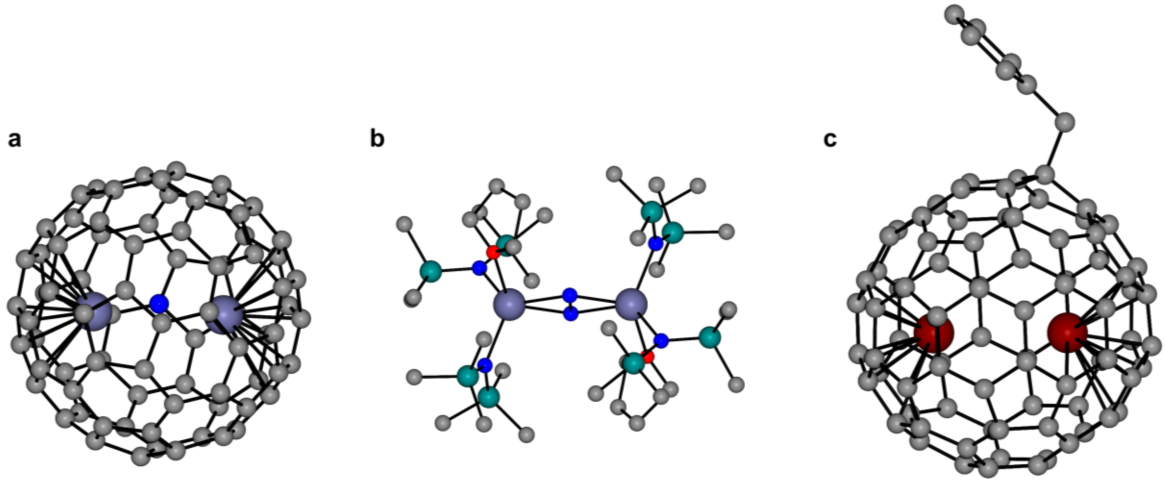

Figure 1.15 Solid state molecular structure of (a) $Gd^{III}_2@C_{79}N$, (b) $[K(18\text{-crown-}6)](\{(Me_3Si)_2N\}_2(THF)Gd^{III})_2(\mu\text{-}\eta^2{:}\eta^2\text{-}N_2)$, and (c) $Dy^{III}_2@C_{80}(CH_2Ph)$.[92-94] Colour code: Blue-grey (Gd), dark red (Dy), teal (Si), blue (N), red (O), grey (C). Hydrogen atoms, cations, and disorder have been removed for clarity.

A common theme throughout these Ln-based SMM milestones, is that the magnetic moment of a SMM is restricted to the orientation of the J quantum number (i.e., the m_J states, or CF microstates), and the energies, ordering, and relative purity of these states is largely dictated by the ligands surrounding the 4f ion. Likewise, the relative environment of a single-atom magnet adsorbed onto a substrate will also respond in a similar way, and the immediate surrounding atoms will behave as the LF dictating the ordering and relative energies of the atom's m_J states. An unsuccessful attempt at showcasing this with Ho^{III} ions on a Pt(111) surface,[95,96] was followed by the discovery of a single-atom Ho^{III} magnet.[97] The combination of the symmetry-protected position of the Ho^{III} ion (C_4v) with an insulating MgO layer afforded magnetic hysteresis with remanence and coercivity up to 30 K and 1 T, and a lifetime of 1500 s at 10 K for the magnetic moment. The MgO layer plays a vital role in the success of this system, as it acts by decoupling the magnetic moment of the Ho^{III} from the phonon and conduction bands of the Ag(100) substrate on which the device is built. This is a necessity for limiting the through barrier relaxation mechanisms, and the long-term maintenance of the magnetic moment. Overall, these are very challenging systems as the magnetic moment of single atoms is readily destabilized by interactions with the surface electrons, nuclear spins, and the lattice vibrations of the substrate on which they are deposited.[98–100] Often, the lifetime of the magnetic moment in such systems is less than a millisecond, even when subjected to large external applied fields;[100,101] thus further demonstrating the significance of achieving bistability, and maintenance of the magnetic moment for 1500 s at 10 K.

The success of surface adsorbed single-atom magnets is dependent on the properties of the substrate (i.e., the phonon density of the material) and not solely the symmetry or strength of the LF. In the previous example, the MgO layer was chosen specifically for its lower phonon density compared to that of the conductive substrate, Ag(100), thereby limiting potential vibrational modes that could shortcut the energy barrier.[97] Moreover, the bonding interactions with the substrate orbitals also significantly affect the ground state of the surface adsorbed 4f ion.[102] When subjected to different substrates, namely Pt(111) and Cu(111), the relative stabilization of the m_J projections of an adsorbed Er^{III} ion was different. The largest m_J state (± 15/2; *oblate*) was stabilized on the Pt(111) surface, owing in part to the more diffuse 5*d* orbitals of Pt, whereas the smallest m_J (± 1/2; *prolate*), of opposing spherical projection, was stabilized on the Cu(111) substrate; meaning that an efficient Er^{III} SMM is more likely when deposited on Pt(111). Lastly, beyond single-atom systems, *ab initio* studies have investigated the effects of surface adsorbed HoO^+ and DyO^+ diatomic units.[57] These theoretical diatomics are of significance to the field of 4f SMMs, as the Dy^{III} congener was first theorized to have a CF splitting of >2100 cm^{-1}, with an expected U_{eff} greater than 3000 K, although it remains synthetically elusive.[56] This system showcased the abilities of new computational methods for predicting the CF of Ln-based SMMs, namely multiconfigurational methods (e.g. complete active space self-consistent crystal field; CASSCF) *via* MOLCAS software,[103,104] which have become prominent and reliable computational methods in the field. Nevertheless, the deposition of HoO^+ and DyO^+ onto MgO would take advantage of the highly axial CF imposed by the coordinated O-atom, as well as the symmetry protected position of the MgO surface combined with its reduced phonon density, eliciting a U_{eff} that would be larger than the trivalent ion itself. This work demonstrates the significance of ligands in directing and controlling the anisotropy at a given metal-center, and that this dominant interaction is often more impactful than the local symmetry in determining the performance of a molecular magnet.

1.7 Conclusions and Outlook

It is evident that lessons that are learned on the molecular scale directly impact the properties of ensuing materials. Thus, using the smallest possible units, single-ion magnets (SIMs), a fundamental understanding of the structural and electronic properties which govern the slow relaxation and long-term maintenance of the magnetic moment can be gleaned, and this is of immediate value. From the previous work completed in the field of Ln-based SMMs, it is unmistakable that a strictly axial ligand field or point group symmetry is not a necessity for obtaining large spin reversal barriers. In fact, all that is required is a dominant CF interaction along a defined direction, whether that be from a ligand that imparts an axial or equatorial LF. However, optimizing the relaxation efficiency and retention of the magnetic moment requires a deeper understanding of the molecular structure and lattice effects. Through synthetic modifications, the strength of these interactions can be modulated, and the nature of the relaxation processes can also be fined-tuned. The future use of SMMs in technology require their incorporation into solid-state materials, and this requires a thorough understanding of their quantum behaviours and spin-phonon interactions such as the vibrational coupling. To accomplish this, SIMs represent the smallest possible unit with which to study the effects that govern the relaxation dynamics, and this warrants their continued investigation.

In the subsequent chapters of this dissertation, the themes discussed here will be relevant to the molecules presented and their observed properties. In Chapter 2, slow magnetic relaxation is achieved in non-Kramers $\mathrm{Tm^{III}}$ by favouring the prolate electron density of the $m_J = 6$ state with a largely equatorial ligand field and then investigating the effects of increased local symmetry *via* ligand substitution. In Chapter 3, the themes of magnetic axiality and magnetic coupling are investigated in two dinuclear $\mathrm{Dy^{III}}$ SMMs. The different ancillary ligands result in significant variation in the observed slow relaxation dynamics, and energy barriers to spin reversal, despite both molecules possessing the same internal bridging motif. Thus, the ancillary ligands define the height of the barrier. Chapter 4 continues with the theme of magnetic coupling in dinuclear lanthanide complexes of $\mathrm{Gd^{III}}$, $\mathrm{Dy^{III}}$, and $\mathrm{Er^{III}}$; however, the internal bridging motif is substituted for an aromatic cyclomultiene. The cycloheptatrienyl trianion facilitates ferromagnetic exchange coupling, which is not commonly observed in the 4f ions. Unfortunately, the ancillary amide ligands were found to be deleterious to the slow relaxation dynamics when used in combination with this organometallic bridge. In Chapter 5, the bridging motifs are removed, focusing on a SIM framework that includes a *bis*-amide ligand that stabilizes the $m_J = 15/2$ state of $\mathrm{Dy^{III}}$ and multistep magnetic relaxation is obtained. Unfortunately, the height of the spin reversal barrier is limited by the bite angle of the *bis*-amide ligand employed and the surrounding equatorial ligands. Thus, in Chapter 6 a *bis*-anilide ligand in which the bite angle is significantly more obtuse is utilized, and the number of hard donor atoms surrounding the equatorial position of the $\mathrm{Dy^{III}}$ is reduced. This structural modification and crystal field engineering results in a highly axial and efficient $\mathrm{Dy^{III}}$ SIM. In Chapter 7, the cumulation of these efforts and lessons is brought forth to obtain a highly desirable bonding arrangement in a 4f ion; near linear ligation of $\mathrm{Yb^{II}}$ is achieved and represents a synthetic and structural blueprint for obtaining even larger spin reversal barriers and more efficient SMMs with improved retention of the magnetic moment, for which continued work is needed.

1.8 References

(1) Sessoli, R.; Gatteschi, D.; Caneschi, A.; Novak, M. A. Magnetic Bistability in a Metal-Ion Cluster. *Nature* **1993**, *365* (6442), 141–143. https://doi.org/10.1038/365141a0.

(2) Sessoli, R.; Tsai, H. L.; Schake, A. R.; Wang, S.; Vincent, J. B.; Folting, K.; Gatteschi, D.; Christou, G.; Hendrickson, D. N. High-Spin Molecules: $[Mn_{12}O_{12}(O_2CR)_{16}(H_2O)_4]$. *J. Am. Chem. Soc.* **1993**, *115* (5), 1804–1816. https://doi.org/10.1021/ja00058a027.

(3) Gatteschi, D.; Sessoli, R.; Villain, J. *Molecular Nanomagnets*; Oxford University Press, 2006.

(4) Eliseeva, S. V.; Bünzli, J.-C. G. Rare Earths: Jewels for Functional Materials of the Future. *New J. Chem.* **2011**, *35* (6), 1165. https://doi.org/10.1039/c0nj00969e.

(5) Leuenberger, M. N.; Loss, D. Quantum Computing in Molecular Magnets. *Nature* **2001**, *410* (6830), 789–793. https://doi.org/10.1038/35071024.

(6) Ardavan, A.; Rival, O.; Morton, J. J. L.; Blundell, S. J.; Tyryshkin, A. M.; Timco, G. A.; Winpenny, R. E. P. Will Spin-Relaxation Times in Molecular Magnets Permit Quantum Information Processing? *Phys. Rev. Lett.* **2007**, *98* (5), 057201. https://doi.org/10.1103/PhysRevLett.98.057201.

(7) Feltham, H. L. C.; Brooker, S. Review of Purely 4f and Mixed-Metal Nd-4f Single-Molecule Magnets Containing Only One Lanthanide Ion. *Coord. Chem. Rev.* **2014**, *276*, 1–33. https://doi.org/10.1016/j.ccr.2014.05.011.

(8) Benelli, C.; Gatteschi, D. *Introduction to Molecular Magnetism: From Transition Metals to Lanthanides*, 1st ed.; John Wiley & Sons, Ltd, 2015.

(9) Guo, F.-S.; Day, B. M.; Chen, Y.-C.; Tong, M.-L.; Mansikkamäki, A.; Layfield, R. A. Magnetic Hysteresis up to 80 Kelvin in a Dysprosium Metallocene Single-Molecule Magnet. *Science* **2018**, *362* (6421), 1400–1403. https://doi.org/10.1126/science.aav0652.

(10) Escalera-Moreno, L.; Baldoví, J. J.; Gaita-Ariño, A.; Coronado, E. Design of High-Temperature f-Block Molecular Nanomagnets through the Control of Vibration-Induced Spin Relaxation. *Chem. Sci.* **2020**, *11* (6), 1593–1598. https://doi.org/10.1039/C9SC03133B.

(11) Escalera-Moreno, L.; Baldoví, J. J.; Gaita-Ariño, A.; Coronado, E. Spin States, Vibrations and Spin Relaxation in Molecular Nanomagnets and Spin Qubits: A Critical Perspective. *Chem. Sci.* **2018**, *9* (13), 3265–3275. https://doi.org/10.1039/C7SC05464E.

(12) Kahn, M. L.; Sutter, J.-P.; Golhen, S.; Guionneau, P.; Ouahab, L.; Kahn, O.; Chasseau, D. Systematic Investigation of the Nature of The Coupling between a Ln(III) Ion (Ln = Ce(III) to Dy(III)) and Its Aminoxyl Radical Ligands. Structural and Magnetic Characteristics of a Series of {Ln(Organic Radical)$_2$} Compounds and the Related {Ln(Nitrone)$_2$} Derivatives. *J. Am. Chem. Soc.* **2000**, *122* (14), 3413–3421. https://doi.org/10.1021/ja994175o.

(13) Benelli, C.; Gatteschi, D. Magnetism of Lanthanides in Molecular Materials with Transition-Metal Ions and Organic Radicals. *Chem. Rev.* **2002**, *102* (6), 2369–2388. https://doi.org/10.1021/cr010303r.

(14) Rinehart, J. D.; Long, J. R. Exploiting Single-Ion Anisotropy in the Design of f-Element Single-Molecule Magnets. *Chem. Sci.* **2011**, *2* (11), 2078. https://doi.org/10.1039/c1sc00513h.

(15) Baldoví, J. J.; Cardona-Serra, S.; Clemente-Juan, J. M.; Coronado, E.; Gaita-Ariño, A.; Palii, A. Rational Design of Single-Ion Magnets and Spin Qubits Based on Mononuclear Lanthanoid Complexes. *Inorg. Chem.* **2012**, *51* (22), 12565–12574. https://doi.org/10.1021/ic302068c.

(16) Orbach, R. Spin-Lattice Relaxation in Rare-Earth Salts. *Proc. R. Soc. Lond. Ser. Math. Phys. Sci.* **1961**, *264* (1319), 458–484. https://doi.org/10.1098/rspa.1961.0211.

(17) Shrivastava, K. N. Theory of Spin–Lattice Relaxation. *Phys. Status Solidi B* **1983**, *117* (2), 437–458. https://doi.org/10.1002/pssb.2221170202.

(18) Prokof'ev, N. V.; Stamp, P. C. E. Quantum Relaxation of Magnetisation in Magnetic Particles. *J. Low Temp. Phys.* **1996**, *104* (3), 143–209. https://doi.org/10.1007/BF00754094.

(19) Thomas, L.; Lionti, F.; Ballou, R.; Gatteschi, D.; Sessoli, R.; Barbara, B. Macroscopic Quantum Tunnelling of Magnetization in a Single Crystal of Nanomagnets. *Nature* **1996**, *383* (6596), 145–147. https://doi.org/10.1038/383145a0.

(20) Atanasov, M.; Zadrozny, J. M.; Long, J. R.; Neese, F. A Theoretical Analysis of Chemical Bonding, Vibronic Coupling, and Magnetic Anisotropy in Linear Iron(II) Complexes with Single-Molecule Magnet Behavior. *Chem Sci* **2013**, *4* (1), 139–156. https://doi.org/10.1039/C2SC21394J.

(21) Klein, M. J. On a Degeneracy Theorem of Kramers. *Am. J. Phys.* **1952**, *20* (2), 65–71. https://doi.org/10.1119/1.1933118.

(22) Pedersen, K. S.; Bendix, J.; Clérac, R. Single-Molecule Magnet Engineering: Building-Block Approaches. *Chem Commun* **2014**, *50* (34), 4396–4415. https://doi.org/10.1039/C4CC00339J.

(23) Giansiracusa, M. J.; Kostopoulos, A. K.; Collison, D.; Winpenny, R. E. P.; Chilton, N. F. Correlating Blocking Temperatures with Relaxation Mechanisms in Monometallic Single-Molecule Magnets with High Energy Barriers (U_{eff} > 600 K). *Chem. Commun.* **2019**, 10.1039.C9CC02421B. https://doi.org/10.1039/C9CC02421B.

(24) Liddle, S. T.; van Slageren, J. Improving f-Element Single Molecule Magnets. *Chem. Soc. Rev.* **2015**, *44* (19), 6655–6669. https://doi.org/10.1039/C5CS00222B.

(25) Abragam, A.; Bleaney, B. *Electron Paramagnetic Resonance of Transition Ions*; Clarendon P.: Oxford, 1970.

(26) Clarke, J. SQUIDs. *Sci. Am.* **1994**, *271* (2), 46–53.

(27) Layfield, R. A.; Murugesu, M. *Lanthanides and Actinides in Molecular Magnetism*, 1st ed.; John Wiley & Sons, Ltd, 2015.

(28) Liu, J.-L.; Chen, Y.-C.; Tong, M.-L. Symmetry Strategies for High Performance Lanthanide-Based Single-Molecule Magnets. *Chem. Soc. Rev.* **2018**, *47* (7), 2431–2453. https://doi.org/10.1039/C7CS00266A.

(29) Chibotaru, L. F.; Iwahara, N. Ising Exchange Interaction in Lanthanides and Actinides. *New J. Phys.* **2015**, *17* (10), 103028. https://doi.org/10.1088/1367-2630/17/10/103028.

(30) Wang, C.; Sun, R.; Chen, Y.; Wang, B.-W.; Wang, Z.-M.; Gao, S. Assembling High-Temperature Single-Molecule Magnets with Low-Coordinate Bis(Amido) Dysprosium Unit $[DyN_2]^+$ via Cl–K–Cl Linkage. *CCS Chem.* **2020**, 362–368. https://doi.org/10.31635/ccschem.020.202000138.

(31) Rinehart, J. D.; Fang, M.; Evans, W. J.; Long, J. R. A N_2^{3-} Radical-Bridged Terbium Complex Exhibiting Magnetic Hysteresis at 14 K. *J. Am. Chem. Soc.* **2011**, *133* (36), 14236–14239. https://doi.org/10.1021/ja206286h.

(32) Long, J. R. Molecular Cluster Magnets. In *Chemistry of Nanostructured Materials*; World Scientific Publishing: Hong Kong, 2003; pp 291–315.

(33) Perlepe, P. S.; Maniaki, D.; Pilichos, E.; Katsoulakou, E.; Perlepes, S. P. Smart Ligands for Efficient 3d-, 4d- and 5d-Metal Single-Molecule Magnets and Single-Ion Magnets. *Inorganics* **2020**, *8* (6), 39. https://doi.org/10.3390/inorganics8060039.

(34) Beltran, L. M. C.; Long, J. R. Directed Assembly of Metal−Cyanide Cluster Magnets. *Acc. Chem. Res.* **2005**, *38* (4), 325–334. https://doi.org/10.1021/ar040158e.

(35) Aromí, G.; Brechin, E. K. Synthesis of 3d Metallic Single-Molecule Magnets. In *Single-Molecule Magnets and Related Phenomena*; Winpenny, R., Ed.; Structure and Bonding; Springer: Berlin, Heidelberg, 2006; pp 1–67. https://doi.org/10.1007/430_022.

(36) Ishikawa, N.; Sugita, M.; Ishikawa, T.; Koshihara, S.; Kaizu, Y. Lanthanide Double-Decker Complexes Functioning as Magnets at the Single-Molecular Level. *J. Am. Chem. Soc.* **2003**, *125* (29), 8694–8695. https://doi.org/10.1021/ja029629n.

(37) Gorller-Walrand, C.; Binnemans, K. Rationalization of Crystal-Field Parametrization. In *Handbook on the physics and chemistry of rare earths*; Elsevier, 1996; pp 121–283.

(38) Chakov, N. E.; Lee, S.-C.; Harter, A. G.; Kuhns, P. L.; Reyes, A. P.; Hill, S. O.; Dalal, N. S.; Wernsdorfer, W.; Abboud, K. A.; Christou, G. The Properties of the $[Mn_{12}O_{12}(O_2CR)_{16}(H_2O)_4]$ Single-Molecule Magnets in Truly Axial Symmetry: $[Mn_{12}O_{12}(O_2CCH_2Br)_{16}(H_2O)_4]\cdot 4CH_2Cl_2$. *J. Am. Chem. Soc.* **2006**, *128* (21), 6975–6989. https://doi.org/10.1021/ja060796n.

(39) Milios, C. J.; Vinslava, A.; Wernsdorfer, W.; Moggach, S.; Parsons, S.; Perlepes, S. P.; Christou, G.; Brechin, E. K. A Record Anisotropy Barrier for a Single-Molecule Magnet. *J. Am. Chem. Soc.* **2007**, *129* (10), 2754–2755. https://doi.org/10.1021/ja068961m.

(40) Ishikawa, N.; Sugita, M.; Okubo, T.; Tanaka, N.; Iino, T.; Kaizu, Y. Determination of Ligand-Field Parameters and f-Electronic Structures of Double-Decker Bis(Phthalocyaninato)Lanthanide Complexes. *Inorg. Chem.* **2003**, *42* (7), 2440–2446. https://doi.org/10.1021/ic026295u.

(41) Yamabayashi, T.; Katoh, K.; Breedlove, B. K.; Yamashita, M. Molecular Orientation of a Terbium(III)-Phthalocyaninato Double-Decker Complex for Effective Suppression of Quantum Tunneling of the Magnetization. *Molecules* **2017**, *22* (6), 999. https://doi.org/10.3390/molecules22060999.

(42) Ishikawa, N.; Sugita, M.; Wernsdorfer, W. Quantum Tunneling of Magnetization in Lanthanide Single-Molecule Magnets: Bis(Phthalocyaninato)Terbium and Bis(Phthalocyaninato)Dysprosium Anions. *Angew. Chem. Int. Ed.* **2005**, *44* (19), 2931–2935. https://doi.org/10.1002/anie.200462638.

(43) AlDamen, M. A.; Cardona-Serra, S.; Clemente-Juan, J. M.; Coronado, E.; Gaita-Ariño, A.; Martí-Gastaldo, C.; Luis, F.; Montero, O. Mononuclear Lanthanide Single Molecule Magnets Based on the Polyoxometalates $[Ln(W_5O_{18})_2]^{9-}$ and $[Ln(\beta_2\text{-}SiW_{11}O_{39})_2]^{13-}$ (Ln^{III} = Tb, Dy, Ho, Er, Tm, and Yb). *Inorg. Chem.* **2009**, *48* (8), 3467–3479. https://doi.org/10.1021/ic801630z.

(44) Zhou, G.-J.; Han, T.; Ding, Y.-S.; Chilton, N. F.; Zheng, Y.-Z. Metallacrowns as Templates for Diabolo-like $LnCu_8$ Complexes with Nearly Perfect Square Antiprismatic Geometry. *Chem. – Eur. J.* **2017**, *23* (62), 15617–15622. https://doi.org/10.1002/chem.201703830.

(45) Layfield, R. A.; McDouall, J. J. W.; Sulway, S. A.; Tuna, F.; Collison, D.; Winpenny, R. E. P. Influence of the N-Bridging Ligand on Magnetic Relaxation in an Organometallic Dysprosium Single-Molecule Magnet. *Chem.-Eur. J.* **2010**, *16* (15), 4442–4446. https://doi.org/10.1002/chem.201000158.

(46) Layfield, R. A. Organometallic Single-Molecule Magnets. *Organometallics* **2014**, *33* (5), 1084–1099. https://doi.org/10.1021/om401107f.

(47) Jiang, S.-D.; Wang, B.-W.; Sun, H.-L.; Wang, Z.-M.; Gao, S. An Organometallic Single-Ion Magnet. *J. Am. Chem. Soc.* **2011**, *133* (13), 4730–4733. https://doi.org/10.1021/ja200198v.

(48) Poremba, P.; Reißmann, U.; Noltemeyer, M.; Schmidt, H.-G.; Brüser, W.; Edelmann, F. T. Cyclooctatetraenyl Complexes of the Early Transition Metals and Lanthanides VIII. Anionic Sandwich Complexes of the Lanthanides Containing Silylated Cyclooctatraenyl Ligands. *J. Organomet. Chem.* **1997**, *544* (1), 1–6. https://doi.org/10.1016/S0022-328X(97)00281-7.

(49) Lorenz, V.; Edelmann, A.; Blaurock, S.; Freise, F.; Edelmann, F. T. A Surprising Solvent Effect on the Crystal Structure of an Anionic Lanthanide Sandwich Complex. *Organometallics* **2007**, *26* (26), 6681–6683. https://doi.org/10.1021/om7006776.

(50) Jeletic, M.; Lin, P.-H.; Le Roy, J. J.; Korobkov, I.; Gorelsky, S. I.; Murugesu, M. An Organometallic Sandwich Lanthanide Single-Ion Magnet with an Unusual Multiple Relaxation Mechanism. *J. Am. Chem. Soc.* **2011**, *133* (48), 19286–19289. https://doi.org/10.1021/ja207891y.

(51) Le Roy, J. J.; Jeletic, M.; Gorelsky, S. I.; Korobkov, I.; Ungur, L.; Chibotaru, L. F.; Murugesu, M. An Organometallic Building Block Approach to Produce a Multidecker 4f Single-Molecule Magnet. *J. Am. Chem. Soc.* **2013**, *135* (9), 3502–3510. https://doi.org/10.1021/ja310642h.

(52) Le Roy, J. J.; Korobkov, I.; Murugesu, M. A Sandwich Complex with Axial Symmetry for Harnessing the Anisotropy in a Prolate Erbium(III) Ion. *Chem Commun* **2014**, *50* (13), 1602–1604. https://doi.org/10.1039/C3CC48557A.

(53) Ungur, L.; Le Roy, J. J.; Korobkov, I.; Murugesu, M.; Chibotaru, L. F. Fine-Tuning the Local Symmetry to Attain Record Blocking Temperature and Magnetic Remanence in a Single-Ion Magnet. *Angew. Chem. Int. Ed.* **2014**, *53* (17), 4413–4417. https://doi.org/10.1002/anie.201310451.

(54) Münzfeld, L.; Schoo, C.; Bestgen, S.; Moreno-Pineda, E.; Köppe, R.; Ruben, M.; Roesky, P. W. Synthesis, Structures and Magnetic Properties of $[(\eta^9\text{-}C_9H_9)Ln(\eta^8\text{-}C_8H_8)]$ Super Sandwich Complexes. *Nat. Commun.* **2019**, *10* (1), 3135. https://doi.org/10.1038/s41467-019-10976-6.

(55) Xémard, M.; Zimmer, S.; Cordier, M.; Goudy, V.; Ricard, L.; Clavaguéra, C.; Nocton, G. Lanthanidocenes: Synthesis, Structure, and Bonding of Linear Sandwich Complexes of Lanthanides. *J. Am. Chem. Soc.* **2018**, *140* (43), 14433–14439. https://doi.org/10.1021/jacs.8b09081.

(56) Ungur, L.; Chibotaru, L. F. Magnetic Anisotropy in the Excited States of Low Symmetry Lanthanide Complexes. *Phys. Chem. Chem. Phys.* **2011**, *13* (45), 20086. https://doi.org/10.1039/c1cp22689d.

(57) Ungur, L.; Chibotaru, L. F. Strategies Toward High-Temperature Lanthanide-Based Single-Molecule Magnets. *Inorg. Chem.* **2016**, *55* (20), 10043–10056. https://doi.org/10.1021/acs.inorgchem.6b01353.

(58) Willson, S. P.; Andrews, L. Characterization of the Reaction Products of Laser-Ablated Late Lanthanide Metal Atoms with Molecular Oxygen: Infrared Spectra of LnO, LnO^+, LnO^-, LnO_2, LnO_2^-, LnO_3^-, and $(LnO)_2$ in Solid Argon. *J. Phys. Chem. A* **1999**, *103* (35), 6972–6983. https://doi.org/10.1021/jp991338m.

(59) Gregson, M.; Chilton, N. F.; Ariciu, A.-M.; Tuna, F.; Crowe, I. F.; Lewis, W.; Blake, A. J.; Collison, D.; McInnes, E. J. L.; Winpenny, R. E. P.; Liddle, S. T. A Monometallic Lanthanide Bis(Methanediide) Single Molecule Magnet with a Large Energy Barrier and Complex Spin Relaxation Behaviour. *Chem. Sci.* **2016**, *7* (1), 155–165. https://doi.org/10.1039/C5SC03111G.

(60) Ding, Y.-S.; Chilton, N. F.; Winpenny, R. E. P.; Zheng, Y.-Z. On Approaching the Limit of Molecular Magnetic Anisotropy: A Near-Perfect Pentagonal Bipyramidal Dysprosium(III) Single-Molecule Magnet. *Angew. Chem. Int. Ed.* **2016**, *55* (52), 16071–16074. https://doi.org/10.1002/anie.201609685.

(61) Krylov, D. S.; Liu, F.; Avdoshenko, S. M.; Spree, L.; Weise, B.; Waske, A.; Wolter, A. U. B.; Büchner, B.; Popov, A. A. Record-High Thermal Barrier of the Relaxation of Magnetization in the Nitride Clusterfullerene $Dy_2ScN@C_{80}$-I_h. *Chem. Commun.* **2017**, *53* (56), 7901–7904. https://doi.org/10.1039/C7CC03580B.

(62) Kazin, P. E.; Zykin, M. A.; Utochnikova, V. V.; Magdysyuk, O. V.; Vasiliev, A. V.; Zubavichus, Y. V.; Schnelle, W.; Felser, C.; Jansen, M. "Isolated" DyO^+ Embedded in a Ceramic Apatite Matrix Featuring Single-Molecule Magnet Behavior with a High Energy Barrier for Magnetization Relaxation. *Angew. Chem. Int. Ed.* **2017**, *56* (43), 13416–13420. https://doi.org/10.1002/anie.201706391.

(63) Blagg, R. J.; Ungur, L.; Tuna, F.; Speak, J.; Comar, P.; Collison, D.; Wernsdorfer, W.; McInnes, E. J. L.; Chibotaru, L. F.; Winpenny, R. E. P. Magnetic Relaxation Pathways in Lanthanide Single-Molecule Magnets. *Nat. Chem.* **2013**, *5* (8), 673–678. https://doi.org/10.1038/nchem.1707.

(64) Guo, Y.-N.; Ungur, L.; Granroth, G. E.; Powell, A. K.; Wu, C.; Nagler, S. E.; Tang, J.; Chibotaru, L. F.; Cui, D. An NCN-Pincer Ligand Dysprosium Single-Ion Magnet Showing Magnetic Relaxation via the Second Excited State. *Sci. Rep.* **2014**, *4* (1), 5471. https://doi.org/10.1038/srep05471.

(65) Singh, S. K.; Gupta, T.; Shanmugam, M.; Rajaraman, G. Unprecedented Magnetic Relaxation via the Fourth Excited State in Low-Coordinate Lanthanide Single-Ion Magnets: A Theoretical Perspective. *Chem Commun* **2014**, *50* (98), 15513–15516. https://doi.org/10.1039/C4CC05522E.

(66) Liu, J.; Chen, Y.-C.; Liu, J.-L.; Vieru, V.; Ungur, L.; Jia, J.-H.; Chibotaru, L. F.; Lan, Y.; Wernsdorfer, W.; Gao, S.; Chen, X.-M.; Tong, M.-L. A Stable Pentagonal Bipyramidal Dy(III) Single-Ion Magnet with a Record Magnetization Reversal Barrier over 1000 K. *J. Am. Chem. Soc.* **2016**, *138* (16), 5441–5450. https://doi.org/10.1021/jacs.6b02638.

(67) Chen, Y.-C.; Liu, J.-L.; Ungur, L.; Liu, J.; Li, Q.-W.; Wang, L.-F.; Ni, Z.-P.; Chibotaru, L. F.; Chen, X.-M.; Tong, M.-L. Symmetry-Supported Magnetic Blocking at 20 K in Pentagonal Bipyramidal Dy(III) Single-Ion Magnets. *J. Am. Chem. Soc.* **2016**, *138* (8), 2829–2837. https://doi.org/10.1021/jacs.5b13584.

(68) Ding, Y.; Han, T.; Zhai, Y.; Reta, D.; Chilton, N. F.; Winpenny, R. E. P.; Zheng, Y. A Study of Magnetic Relaxation in Dysprosium(III) Single-Molecule Magnets. *Chem. – Eur. J.* **2020**, *26* (26), 5893–5902. https://doi.org/10.1002/chem.202000646.

(69) Goodwin, C. A. P.; Ortu, F.; Reta, D.; Chilton, N. F.; Mills, D. P. Molecular Magnetic Hysteresis at 60 Kelvin in Dysprosocenium. *Nature* **2017**, *548* (7668), 439–442. https://doi.org/10.1038/nature23447.

(70) Guo, F.-S.; Day, B. M.; Chen, Y.-C.; Tong, M.-L.; Mansikkamäki, A.; Layfield, R. A. A Dysprosium Metallocene Single-Molecule Magnet Functioning at the Axial Limit. *Angew. Chem. Int. Ed.* **2017**, *56* (38), 11445–11449. https://doi.org/10.1002/anie.201705426.

(71) Day, B. M.; Guo, F.-S.; Layfield, R. A. Cyclopentadienyl Ligands in Lanthanide Single-Molecule Magnets: One Ring to Rule Them All? *Acc. Chem. Res.* **2018**, *51* (8), 1880–1889. https://doi.org/10.1021/acs.accounts.8b00270.

(72) Meng, Y.-S.; Zhang, Y.-Q.; Wang, Z.-M.; Wang, B.-W.; Gao, S. Weak Ligand-Field Effect from Ancillary Ligands on Enhancing Single-Ion Magnet Performance. *Chem.–Eur. J.* **2016**, *22* (36), 12724–12731. https://doi.org/10.1002/chem.201601934.

(73) Randall McClain, K.; Gould, C. A.; Chakarawet, K.; Teat, S. J.; Groshens, T. J.; Long, J. R.; Harvey, B. G. High-Temperature Magnetic Blocking and Magneto-Structural Correlations in a Series of Dysprosium(III) Metallocenium Single-Molecule Magnets. *Chem. Sci.* **2018**, *9* (45), 8492–8503. https://doi.org/10.1039/C8SC03907K.

(74) Goodwin, C. A. P.; Reta, D.; Ortu, F.; Chilton, N. F.; Mills, D. P. Synthesis and Electronic Structures of Heavy Lanthanide Metallocenium Cations. *J. Am. Chem. Soc.* **2017**, *139* (51), 18714–18724. https://doi.org/10.1021/jacs.7b11535.

(75) Gould, C. A.; McClain, K. R.; Yu, J. M.; Groshens, T. J.; Furche, F.; Harvey, B. G.; Long, J. R. Synthesis and Magnetism of Neutral, Linear Metallocene Complexes of Terbium(II) and Dysprosium(II). *J. Am. Chem. Soc.* **2019**, *141* (33), 12967–12973. https://doi.org/10.1021/jacs.9b05816.

(76) Dreiser, J. Molecular Lanthanide Single-Ion Magnets: From Bulk to Submonolayers. *J. Phys. Condens. Matter* **2015**, *27* (18), 183203. https://doi.org/10.1088/0953-8984/27/18/183203.

(77) Urdampilleta, M.; Klyatskaya, S.; Cleuziou, J.-P.; Ruben, M.; Wernsdorfer, W. Supramolecular Spin Valves. *Nat. Mater.* **2011**, *10* (7), 502–506. https://doi.org/10.1038/nmat3050.

(78) Kyatskaya, S.; Galán Mascarós, J. R.; Bogani, L.; Hennrich, F.; Kappes, M.; Wernsdorfer, W.; Ruben, M. Anchoring of Rare-Earth-Based Single-Molecule Magnets on Single-Walled Carbon Nanotubes. *J. Am. Chem. Soc.* **2009**, *131* (42), 15143–15151. https://doi.org/10.1021/ja906165e.

(79) Candini, A.; Klyatskaya, S.; Ruben, M.; Wernsdorfer, W.; Affronte, M. Graphene Spintronic Devices with Molecular Nanomagnets. *Nano Lett.* **2011**, *11* (7), 2634–2639. https://doi.org/10.1021/nl2006142.

(80) Aulakh, D.; Pyser, J. B.; Zhang, X.; Yakovenko, A. A.; Dunbar, K. R.; Wriedt, M. Metal–Organic Frameworks as Platforms for the Controlled Nanostructuring of Single-Molecule Magnets. *J. Am. Chem. Soc.* **2015**, *137* (29), 9254–9257. https://doi.org/10.1021/jacs.5b06002.

(81) Holmberg, R. J.; Murugesu, M. Adhering Magnetic Molecules to Surfaces. *J. Mater. Chem. C* **2015**, *3* (46), 11986–11998. https://doi.org/10.1039/C5TC03225C.

(82) Jiang, S.-D.; Wang, B.-W.; Su, G.; Wang, Z.-M.; Gao, S. A Mononuclear Dysprosium Complex Featuring Single-Molecule-Magnet Behavior. *Angew. Chem. Int. Ed.* **2010**, *49* (41), 7448–7451. https://doi.org/10.1002/anie.201004027.

(83) Nakanishi, R.; Yatoo, M. A.; Katoh, K.; Breedlove, B. K.; Yamashita, M. Dysprosium Acetylacetonato Single-Molecule Magnet Encapsulated in Carbon Nanotubes. *Materials* **2017**, *10* (1), 7. https://doi.org/10.3390/ma10010007.

(84) Singh, M. K.; Yadav, N.; Rajaraman, G. Record High Magnetic Exchange and Magnetization Blockade in $Ln_2@C_{79}N$ (Ln = Gd(III) and Dy(III)) Molecules: A Theoretical Perspective. *Chem. Commun.* **2015**, *51* (100), 17732–17735. https://doi.org/10.1039/C5CC06642E.

(85) Popov, A. A.; Yang, S.; Dunsch, L. Endohedral Fullerenes. *Chem. Rev.* **2013**, *113* (8), 5989–6113. https://doi.org/10.1021/cr300297r.

(86) Wolf, M.; Müller, K.-H.; Skourski, Y.; Eckert, D.; Georgi, P.; Krause, M.; Dunsch, L. Magnetic Moments of the Endohedral Cluster Fullerenes $Ho_3N@C_{80}$ and $Tb_3N@C_{80}$: The Role of Ligand Fields. *Angew. Chem. Int. Ed.* **2005**, *44* (21), 3306–3309. https://doi.org/10.1002/anie.200461500.

(87) Náfrádi, B.; Antal, Á.; Pásztor, Á.; Forró, L.; Kiss, L. F.; Fehér, T.; Kováts, É.; Pekker, S.; Jánossy, A. Molecular and Spin Dynamics in the Paramagnetic Endohedral Fullerene $Gd_3N@C_{80}$. *J. Phys. Chem. Lett.* **2012**, *3* (22), 3291–3296. https://doi.org/10.1021/jz301250j.

(88) Westerström, R.; Dreiser, J.; Piamonteze, C.; Muntwiler, M.; Weyeneth, S.; Brune, H.; Rusponi, S.; Nolting, F.; Popov, A.; Yang, S.; Dunsch, L.; Greber, T. An Endohedral Single-Molecule Magnet with Long Relaxation Times: $DySc_2N@C_{80}$. *J. Am. Chem. Soc.* **2012**, *134* (24), 9840–9843. https://doi.org/10.1021/ja301044p.

(89) Krylov, D. S.; Liu, F.; Brandenburg, A.; Spree, L.; Bon, V.; Kaskel, S.; Wolter, A. U. B.; Büchner, B.; Avdoshenko, S. M.; Popov, A. A. Magnetization Relaxation in the Single-Ion Magnet $DySc_2N@C_{80}$: Quantum Tunneling, Magnetic Dilution, and Unconventional Temperature Dependence. *Phys. Chem. Chem. Phys.* **2018**, *20* (17), 11656–11672. https://doi.org/10.1039/C8CP01608A.

(90) Westerström, R.; Dreiser, J.; Piamonteze, C.; Muntwiler, M.; Weyeneth, S.; Krämer, K.; Liu, S.-X.; Decurtins, S.; Popov, A.; Yang, S.; Dunsch, L.; Greber, T. Tunneling, Remanence, and Frustration in Dysprosium-Based Endohedral Single-Molecule Magnets. *Phys. Rev. B* **2014**, *89* (6), 060406. https://doi.org/10.1103/PhysRevB.89.060406.

(91) Demir, S.; Jeon, I.-R.; Long, J. R.; Harris, T. D. Radical Ligand-Containing Single-Molecule Magnets. *Coord. Chem. Rev.* **2015**, *289–290*, 149–176. https://doi.org/10.1016/j.ccr.2014.10.012.

(92) Hu, Z.; Dong, B.-W.; Liu, Z.; Liu, J.-J.; Su, J.; Yu, C.; Xiong, J.; Shi, D.-E.; Wang, Y.; Wang, B.-W.; Ardavan, A.; Shi, Z.; Jiang, S.-D.; Gao, S. Endohedral Metallofullerene as Molecular High Spin Qubit: Diverse Rabi Cycles in $Gd_2@C_{79}N$. *J. Am. Chem. Soc.* **2018**, *140* (3), 1123-1130. https://doi.org/10.1021/jacs.7b12170.

(93) Rinehart, J. D.; Fang, M.; Evans, W. J.; Long, J. R. Strong Exchange and Magnetic Blocking in N_2^{3-}-Radical-Bridged Lanthanide Complexes. *Nat. Chem.* **2011**, *3* (7), 538–542. https://doi.org/10.1038/nchem.1063.

(94) Liu, F.; Krylov, D. S.; Spree, L.; Avdoshenko, S. M.; Samoylova, N. A.; Rosenkranz, M.; Kostanyan, A.; Greber, T.; Wolter, A. U. B.; Büchner, B.; Popov, A. A. Single Molecule Magnet with an Unpaired Electron Trapped between Two Lanthanide Ions inside a Fullerene. *Nat. Commun.* **2017**, *8* (1), 16098. https://doi.org/10.1038/ncomms16098.

(95) Steinbrecher, M.; Sonntag, A.; Dias, M. dos S.; Bouhassoune, M.; Lounis, S.; Wiebe, J.; Wiesendanger, R.; Khajetoorians, A. A. Absence of a Spin-Signature from a Single Ho Adatom as Probed by Spin-Sensitive Tunneling. *Nat. Commun.* **2016**, *7* (1), 10454. https://doi.org/10.1038/ncomms10454.

(96) Miyamachi, T.; Schuh, T.; Märkl, T.; Bresch, C.; Balashov, T.; Stöhr, A.; Karlewski, C.; André, S.; Marthaler, M.; Hoffmann, M.; Geilhufe, M.; Ostanin, S.; Hergert, W.; Mertig, I.; Schön, G.; Ernst, A.; Wulfhekel, W. Stabilizing the Magnetic Moment of Single Holmium Atoms by Symmetry. *Nature* **2013**, *503* (7475), 242–246. https://doi.org/10.1038/nature12759.

(97) Donati, F.; Rusponi, S.; Stepanow, S.; Wäckerlin, C.; Singha, A.; Persichetti, L.; Baltic, R.; Diller, K.; Patthey, F.; Fernandes, E.; Dreiser, J.; Šljivančanin, Ž.; Kummer, K.; Nistor, C.; Gambardella, P.; Brune, H. Magnetic Remanence in Single Atoms. *Science* **2016**, *352* (6283), 318–321. https://doi.org/10.1126/science.aad9898.

(98) Hirjibehedin, C. F.; Lin, C.-Y.; Otte, A. F.; Ternes, M.; Lutz, C. P.; Jones, B. A.; Heinrich, A. J. Large Magnetic Anisotropy of a Single Atomic Spin Embedded in a Surface Molecular Network. *Science* **2007**, *317* (5842), 1199–1203. https://doi.org/10.1126/science.1146110.

(99) Balashov, T.; Schuh, T.; Takács, A. F.; Ernst, A.; Ostanin, S.; Henk, J.; Mertig, I.; Bruno, P.; Miyamachi, T.; Suga, S.; Wulfhekel, W. Magnetic Anisotropy and Magnetization Dynamics of Individual Atoms and Clusters of Fe and Co on Pt(111). *Phys. Rev. Lett.* **2009**, *102* (25), 257203. https://doi.org/10.1103/PhysRevLett.102.257203.

(100) Loth, S.; Etzkorn, M.; Lutz, C. P.; Eigler, D. M.; Heinrich, A. J. Measurement of Fast Electron Spin Relaxation Times with Atomic Resolution. *Science* **2010**, *329* (5999), 1628–1630. https://doi.org/10.1126/science.1191688.

(101) Khajetoorians, A. A.; Lounis, S.; Chilian, B.; Costa, A. T.; Zhou, L.; Mills, D. L.; Wiebe, J.; Wiesendanger, R. Itinerant Nature of Atom-Magnetization Excitation by Tunneling Electrons. *Phys. Rev. Lett.* **2011**, *106* (3), 037205. https://doi.org/10.1103/PhysRevLett.106.037205.

(102) Donati, F.; Singha, A.; Stepanow, S.; Wäckerlin, C.; Dreiser, J.; Gambardella, P.; Rusponi, S.; Brune, H. Magnetism of Ho and Er Atoms on Close-Packed Metal Surfaces. *Phys. Rev. Lett.* **2014**, *113* (23), 237201. https://doi.org/10.1103/PhysRevLett.113.237201.

(103) Aquilante, F.; Autschbach, J.; Baiardi, A.; Battaglia, S.; Borin, V. A.; Chibotaru, L. F.; Conti, I.; De Vico, L.; Delcey, M.; Fdez. Galván, I.; Ferré, N.; Freitag, L.; Garavelli, M.; Gong, X.; Knecht, S.; Larsson, E. D.; Lindh, R.; Lundberg, M.; Malmqvist, P. Å.; Nenov, A.; Norell, J.; Odelius, M.; Olivucci, M.; Pedersen, T. B.; Pedraza-González, L.; Phung, Q. M.; Pierloot, K.; Reiher, M.; Schapiro, I.; Segarra-Martí, J.; Segatta, F.; Seijo, L.; Sen, S.; Sergentu, D.-C.; Stein, C. J.; Ungur, L.; Vacher, M.; Valentini, A.; Veryazov, V. Modern Quantum Chemistry with [Open]Molcas. *J. Chem. Phys.* **2020**, *152* (21), 214117. https://doi.org/10.1063/5.0004835.

(104) Aquilante, F.; Autschbach, J.; Carlson, R. K.; Chibotaru, L. F.; Delcey, M. G.; Vico, L. D.; Galván, I. F.; Ferré, N.; Frutos, L. M.; Gagliardi, L.; Garavelli, M.; Giussani, A.; Hoyer, C. E.; Manni, G. L.; Lischka, H.; Ma, D.; Malmqvist, P. Å.; Müller, T.; Nenov, A.; Olivucci, M.; Pedersen, T. B.; Peng, D.; Plasser, F.; Pritchard, B.; Reiher, M.; Rivalta, I.; Schapiro, I.; Segarra-Martí, J.; Stenrup, M.; Truhlar, D. G.; Ungur, L.; Valentini, A.; Vancoillie, S.; Veryazov, V.; Vysotskiy, V. P.; Weingart, O.; Zapata, F.; Lindh, R. Molcas 8: New Capabilities for Multiconfigurational Quantum Chemical Calculations across the Periodic Table. *J. Comput. Chem.* **2016**, *37* (5), 506–541. https://doi.org/10.1002/jcc.24221.

(105) Goodwin, C. A. Blocking Like it’s Hot: A Synthetic Chemists’ Path to High-Temperature Lanthanide Single Molecule Magnets. *Dalton Trans*. **2020**, *49*, 14320-14337. https://doi.org/10.1039/d0dt01904f.

(106) Bartolomé, E.; Arauzo, A.; Luzón, J.; Bartolomé, J.; Bartolomé, F. Magnetic Relaxation of Lanthanide-Based Molecular Magnets. In Handbook of magnetic materials; Elsevier, 2017; pp 1-289. https://doi.org/10.1016/bs.hmm.2017.09.002.

Chapter 2

Relaxation Dynamics in Single-Molecule Magnets of Non-Kramers Tm^{III}

2.1 Introduction

Mononuclear lanthanide complexes have become prolific in the design of new molecular magnetic materials, specifically, single-molecule magnets (SMMs).[1,2] These complexes are ideal candidates for the goal of developing high performance SMMs, as the presence of a single metal center allows for fine tuning of the electronic structure based on crystal field contributions. Of late, research efforts have been directed towards the study of low coordinate, high symmetry, mononuclear lanthanide complexes.[3–7] They have the potential to possess staggering energy barriers to magnetization reversal (U_{eff}) due to the extremely well separated nature of the crystal field (CF) microstates, which have been theorized to span energies as large as *ca.* 1800 cm^{-1} for specific geometries.[1] Thus, in recent years, molecular geometry and crystal field considerations have largely dictated the design of SMMs based off the highly anisotropic lanthanide ions, for which organometallic ligands have become fashionable.[8] Perhaps most notable, was the successful application of crystal field engineering in the development of $[Dy^{III}(Cp^{ttt})_2]^+$ (Cp^{ttt} = 1,2,4-tri(*tert*-butyl)cyclopentadienide), a molecule which possess a U_{eff} of 1837 K and blocking temperature of 60 K.[9] Much less studied, are SMMs based on non-Kramers ions, Tb^{III}, Ho^{III}, and Tm^{III}.[10] Since the seminal lanthanide example, $[Tb^{III}(Pc)_2]^-$ (Pc = phthalocyanine), a non-Kramers system,[11] very few examples of non-Kramers SMMs have been reported, especially if that ion is Tm^{III}.[12–14] This is due in part to their integer angular momenta (J), which results in intrinsic tunneling gaps, promoting magnetic relaxation through the ground state CF multiplet.[15] This facile and efficient relaxation process, known as quantum tunneling of the magnetization (QTM), drastically reduces U_{eff}, and tends to preclude hysteresis with coercivity. Indeed, the approach of designing highly symmetric ligand environments to promote multistep relaxation pathways may also be applied to the development of SMMs of non-Kramers ions.

Previously, the Murugesu group reported that areneides, such as the cyclooctatetraenide (COT^{2-}) are very effective in producing significant magnetic axiality in the ground state of $[Er^{III}(COT)_2]^-$, subsequently favoring magnetic relaxation through higher CF states.[16] These contributions have demonstrated that the π-electron cloud of COT provides a dominant ligand field, which enhances uniaxial magnetic anisotropy in prolate Er^{III} ions.[17] While Er^{III} is a Kramers ion with $J = 15/2$, theoretically, the ligand field generated by COT may also yield the same desirable effects in other prolate ions, even those with integer angular momentum projections, such as Tm^{III}. This may allow for stabilization of the largest magnetic moment in the ground CF multiplet as well as enhanced purity of the m_J states, leading to the observation of slow magnetic relaxation in non-Kramers ions like Tm^{III}. While others have sought to elicit SMM behavior from this ion,[12,18] there remains a fundamental interest in determining the factors which contribute to its performance. Given the vital roles of the ligand environment and the molecular symmetry on the performance of non-Kramers SMMs, this study aims to elucidate the improvement in SMM properties when Tm^{III} is subjected to an ideal environment.

In this study, a non-traditional synthetic route towards lanthanide bis-COT complexes is utilized to systematically install COT rings on to the Tm^{III} ion. In a stepwise fashion, a piano stool complex, [Tm^{III}(η^8-COT)I(THF)$_2$] (**1-Tm**) is first isolated, and subsequently a metallocene sandwich complex [K(18-crown-6)(THF)$_2$][Tm^{III}(η^8-COT)$_2$] (**2-Tm**). Herein, the synthesis, structure, and magnetic characterization of the hetero- and homoleptic complexes are reported. The importance of local symmetry for the slow relaxation in non-Kramers Tm^{III} is discussed as it pertains to the relaxation dynamics observed under an applied static field.

2.2 Results and Discussion

2.2.1 Synthesis and Structure

Previously, the reducing power of TmI$_2$ had been utilized to perform successive reductions of COT and other arenes.[19] This methodology was utilized to generate a piano stool complex with a single COT dianion bound to the Tm^{III} ion. Thus, **1-Tm** was prepared through two subsequent one electron reductions of COT by TmI$_2$, generating TmI$_3$ as a by-product (Figure 2.1). Treatment of **1-Tm** with one equivalent of K$_2$COT results in the formation of [Tm^{III}(η^8-COT)$_2$]$^-$, which upon addition of one equivalent of 18-crown-6 and storage at room temperature for 48 h resulted in X-ray quality crystals of **2-Tm**. The synthetic route employed towards the synthesis of **2-Tm** uniquely allows for the isolation of a mono-COT complex, whereas the traditional route subjects the respective LnCl$_3$ salt to a solution of K$_2$COT to obtain the homoleptic compound in one step.[16,20] To the best of our knowledge, this is the first structural account of the ion-separated sandwich complex of the [Tm^{III}(η^8-COT)$_2$]$^-$ anion, however analogous structures of the other 4f congeners have been reported,[16,20] as well as [Li(THF)$_3$][Tm^{III}(η^8-COT)$_2$] which exhibits the metallocene structure with an inner sphere lithium ion, making this molecule unsymmetrical.[21]

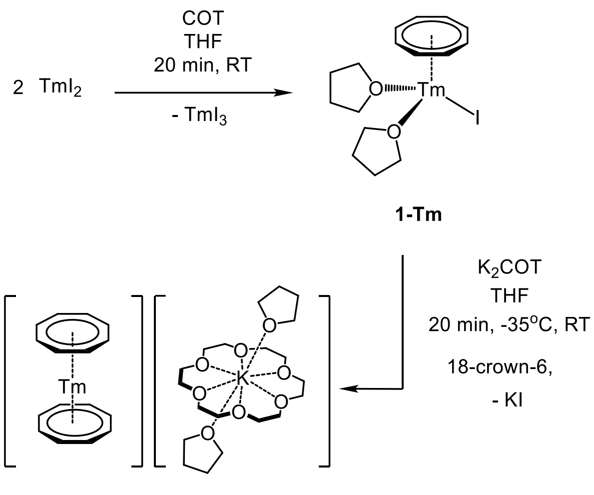

2-Tm

Figure 2.1 Synthesis of [Tm^{III}(η^8-COT)I(THF)$_2$] (**1-Tm**) and [K(18-crown-6)(THF)$_2$][Tm^{III}(η^8-COT)$_2$] (**2-Tm**); COT = cyclooctatetraene.

The structure of **1-Tm** was previously reported by Fedushkin et al.,[19] but to aid in the comparison of the two complexes and their magnetic properties, the structure collected during our study will be discussed. **1-Tm** crystallizes in the monoclinic space group $P2_1$/n, where each asymmetric unit contains one Tm^{III} ion bound to one η^8-COT dianion (Figure 2.2). A Tm^{III}-COT$_{centroid}$ distance of 1.75 Å is achieved, which is comparable to 1.76 Å, as observed in [(Tp)Tm^{III}(COT)] (Tp = hydrotris(3,5-dimethyl-1-pyrazolyl)borate).[12] The immediate coordination sphere is completed by an iodide ligand and two THF molecules. Interestingly, there is a slight elongation of the Tm-C$_{COT}$ bond distances for those C-atoms which lie above the THF molecules, demonstrating a slight asymmetry in the Tm^{III}-COT bonding (Table 2.1). This is likely caused by the steric requirements of the THF molecules compared to that of iodide. Within the lattice, the molecules are oriented such that there is a Tm^{III}---Tm^{III} intermolecular distance of 6.84 Å (Figure 2.3a), Conversely, **2-Tm** crystallizes in the triclininc space group P-1. The Tm^{III} ion is bound to two COT rings in an η^8-mode, with average Tm-C$_{COT}$ bond distances of 2.61 Å (Figure 2.2 and Table 2.1). The two COT rings exhibit an eclipsed conformation; however, this is not surprising as the Tm^{III} ion sits on a crystallographic inversion center, making the COT rings symmetry related. This in turn results in equivalent Tm^{III}---COT$_{centroid}$ distances of 1.85 Å, which are approximately 0.1 Å larger than the Tm^{III}---COT$_{centroid}$ distance in **1-Tm** and analogous to the previously reported [Tm^{III}(η^8-COT")$_2$], COT" = 1,4-bis(trimethylsilyl)cyclooctatetraenyl, (1.85 Å).[22] Nevertheless, short contacts exist between the complex anion-cation pair; however, no contacts exists between paramagnetic species, with the shortest intermolecular Tm^{III}---Tm^{III} distance of 7.74 Å (Figure 2.3b). The C---H short contacts result in distances of 2.87 and 2.79 Å between H14 and C2/C3, respectively. As well as C---H distances of 2.81 and 2.80 Å between H9 and C7/C8. As evidenced from the crystallographic parameters, **2-Tm** exhibits greater local symmetry and this is expected to decrease the intrinsic tunneling gap in this non-Kramers ion and afford improved slow magnetic relaxation properties over its parent compound, **1-Tm**.

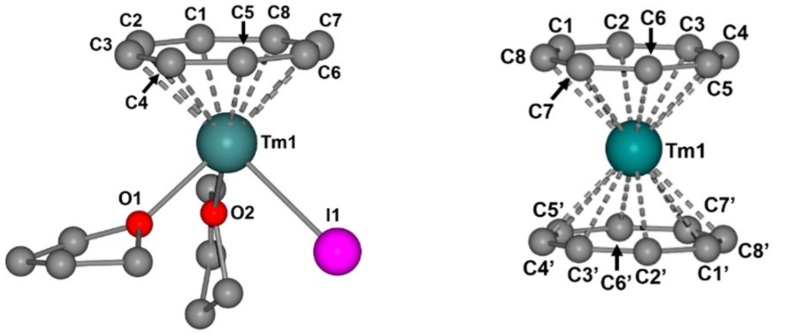

1-Tm **2-Tm**

Figure 2.2 Molecular structure of $[\mathrm{Tm^{III}}(\eta^8\text{-COT})\mathrm{I(THF)_2}]$ **1-Tm** (left) and $[\mathrm{Tm^{III}}(\eta^8\text{-COT})_2]^{-1}$ **2-Tm** (right). Colour code: Teal ($\mathrm{Tm^{III}}$), purple (K), pink (I), red (O), grey (C). Hydrogen atoms, disorder, and the cation $[\mathrm{K(18\text{-}crown\text{-}6)(THF)_2}]$ have been omitted for clarity.

Table 2.1 Tm-$\mathrm{C_{COT}}$ bond distances obtained from single crystal X-ray diffraction studies

Bond	**1-Tm**	**2-Tm**
Tm1-C1 (Å)	2.534(6)	2.615(2)
Tm1-C2 (Å)	2.555(7)	2.598(2)
Tm1-C3 (Å)	2.533(7)	2.598(2)
Tm1-C4 (Å)	2.525(7)	2.617(2)
Tm1-C5 (Å)	2.515(7)	2.620(2)
Tm1-C6 (Å)	2.524(6)	2.600(2)
Tm1-C7 (Å)	2.515(5)	2.598(2)
Tm1-C8 (Å)	2.516(5)	2.604(2)

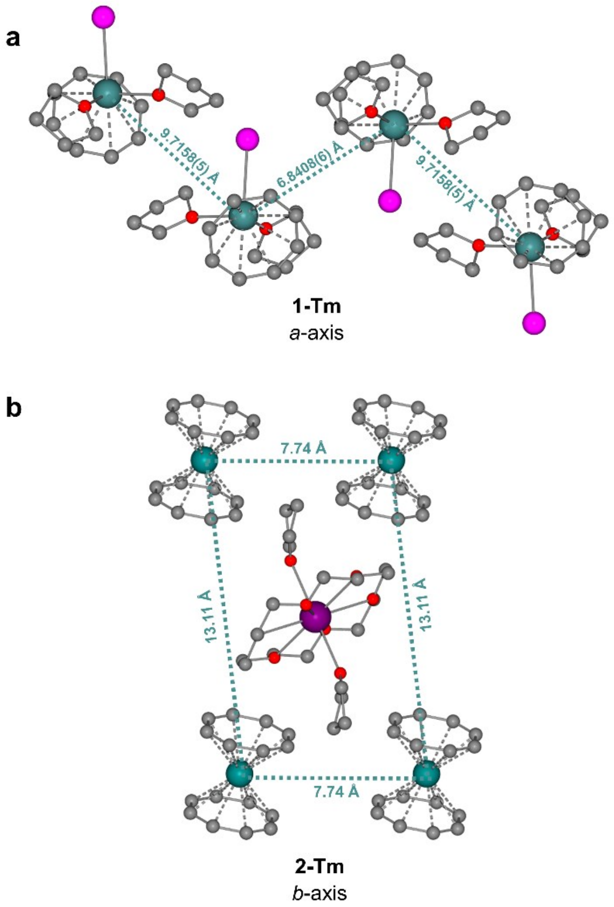

Figure 2.3 Solid state intermolecular Tm^{III}---Tm^{III} distances. (a) View along the *a*-axis of the unit cell in **1-Tm**. (b) View along the *b*-axis of the unit cell in **2-Tm**. Colour code: Teal (Tm^{III}), purple (K), pink (I), red (O), grey (C). Hydrogen atoms and disorder have been omitted for clarity.

2.2.2 Direct Current Magnetic Susceptibility

The magnetic properties of **1-Tm** and **2-Tm** were investigated with the use of a SQUID magnetometer. The variable temperature susceptibility plot (χT *vs*. T) for **1-Tm** and **2-Tm** depicts similar behavior; where upon decreasing temperature, the χT product experiences minimal deviation from linearity (i.e., Curie Law behaviour) until significantly low temperatures. The ability of the complexes to match closely with the Curie Law demonstrated that intermolecular interactions are negligible and may also suggest the presence of a well separated ground state. The room temperature χT values of 6.96 and 7.23 cm^3 K mol^{-1} for **1-Tm** and **2-Tm** respectively, are close to the expected value of 7.15 cm^3 K mol^{-1} for a Tm^{III} ($4f^{12}$, $^3H_6$, $S = 1$, $L = 5$, $g = 7/6$) ion (Figure 2.4a). Both complexes experience a rapid decrease in their χT products below 4 K, to reach final values of 4.08 and 5.48 cm^{3}Kmol^{-1} at 1.8 K. The swift drop of the χT product at low temperature may be indicative of magnetic blocking arising from the significant magnetic anisotropy inherent to the Tm^{III} ion. Close analysis of the isothermal magnetization curves revealed magnetization values of 3.05 and 2.54 μ_B at 1.9 K and 7 T for **1-Tm** and **2-Tm** (Figure 2.4b-e). While these deviate significantly from the expected value of 7 μ_B, similar results have been reported for [(η^5-Cp*)Tm^{III}(η^8-COT)] (Cp* = pentamethylcyclopentadienide).[13,23] Collectively, the data strongly suggests that the low-lying energy spectrum of the CF doublets are well separated, and this bodes well for the slow magnetic relaxation properties, as it ensures that magnetic relaxation will at least occur through the first excited state CF doublet.

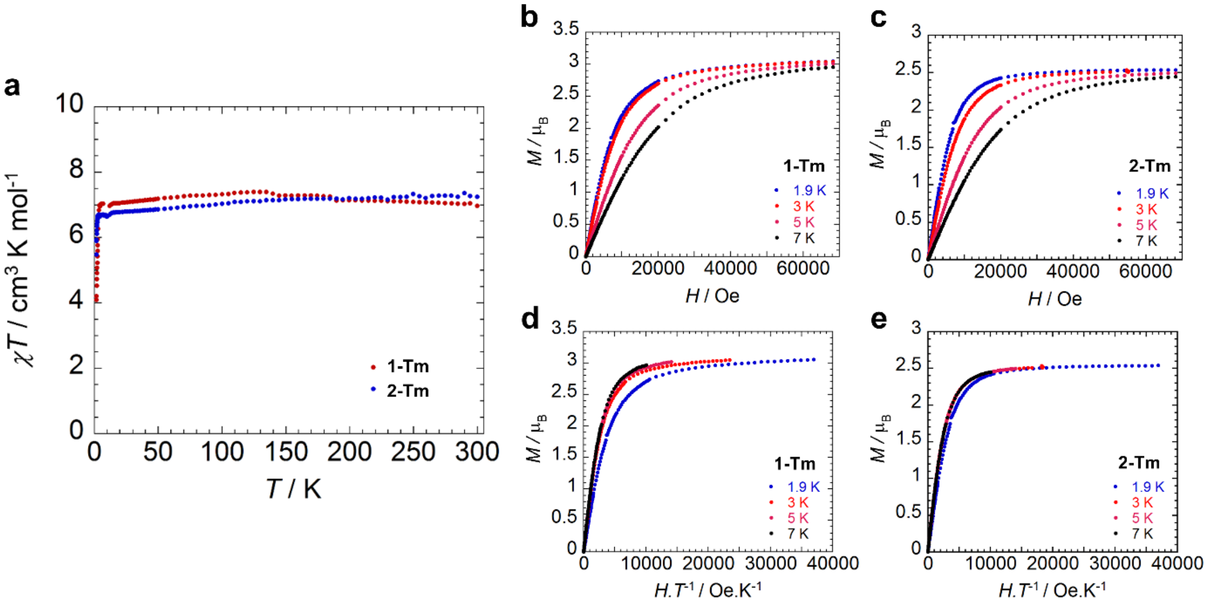

Figure 2.4 (a) Temperature dependence of the χT product at 1000 Oe for **1-Tm** (red) and **2-Tm** (blue). Solid state field dependence of the magnetization for (b) **1-Tm** and (c) **2-Tm**, and the reduced magnetization for (d) **1-Tm** and (e) **2-Tm** at the indicated temperatures.

2.2.3 Alternating Current Magnetic Susceptibility

To elucidate the presence of slow magnetic relaxation, alternating current (ac) magnetic susceptibility measurements were completed. With respect to **1-Tm**, an absence of an out-of-phase (χ") signal was observed under zero applied dc field. This behaviour was not unexpected owing to the presence of inequivalent ligand donors, minimal symmetry, and the electronic configuration of the Tm^{III} ion. As previously discussed, the non-Kramers nature of the Tm^{III} ion does not ensure that a doubly degenerate ground state will be obtained, nor does it preclude QTM. As such, to facilitate the observation of the slow relaxation in **1-Tm**, frequency dependent measurements as a function of applied dc field were completed with fields of 200 Oe – 1600 Oe (Figure 2.5). Under these conditions, a signal was obtained in the χ' and χ" susceptibilities. At high frequency, a signal in the χ" susceptibility is observed, and the signal is augmented by increasing static fields until 800 Oe, at which point there is a decrease in the observed intensity. As a result, the optimal field to observed field-induced magnetic relaxation is 800 Oe. Comparatively, when **2-Tm** was subjected to the same field dependent measurements (0 Oe – 1600 Oe) two tails were obtained in the high frequency and low frequency regions of the χ" susceptibility. At 0 Oe, the signal is exclusively in the high frequency regime, however at 200 Oe, the signal is dominant in the low frequency regime, and exhibits the greatest intensity despite the peak maxima not being observable under the frequency conditions of the magnetometer.

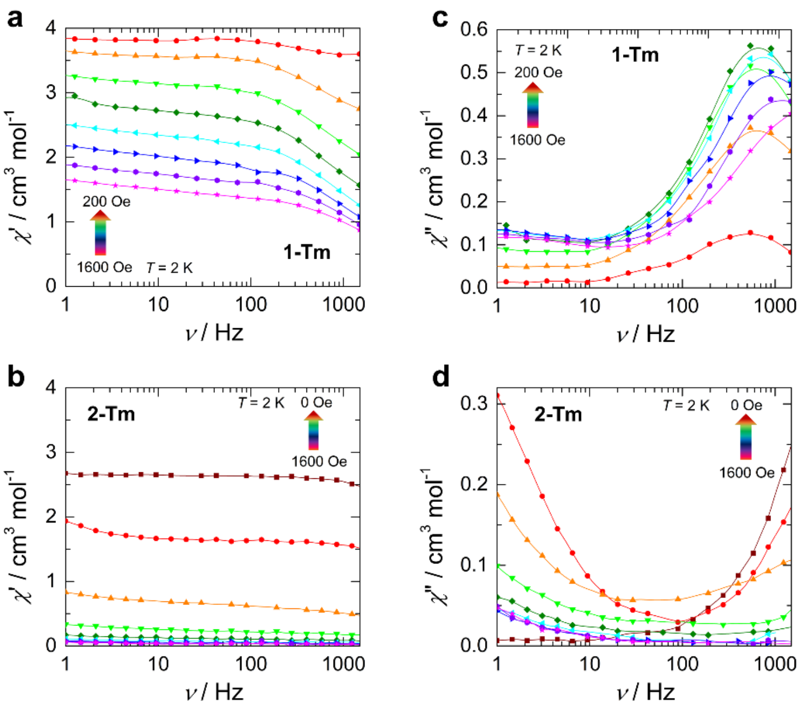

Figure 2.5 Frequency dependence of the (a-b) in-phase (χ') and (c-d) out-of-phase (χ") components of the ac magnetic susceptibility as a function of applied static field at 2 K for **1-Tm** (*top*) and **2-Tm** (*bottom*). Lines are a guide for the eye.

At the optimal dc field of H_{dc} = 800 Oe, a frequency dependent signal was observed for **1-Tm** in the χ' and χ" susceptibilities within the temperature range 1.9-10 K (Figure 2.6). Unfortunately, minimal shifting of the χ" peak maxima is observed below 1500 Hz; this is likely attributed to significant QTM. To elucidate the source of this signal, the relaxation times of the individual isothermal curves were extracted with the generalized Debye model.[24] Perhaps unsurprisingly, given the high frequency peaks, very small τ-values are achieved ($1.20 \times 10^{-4} – 2.66 \times 10^{-4}$ s) throughout the entirety of the temperature range studied.

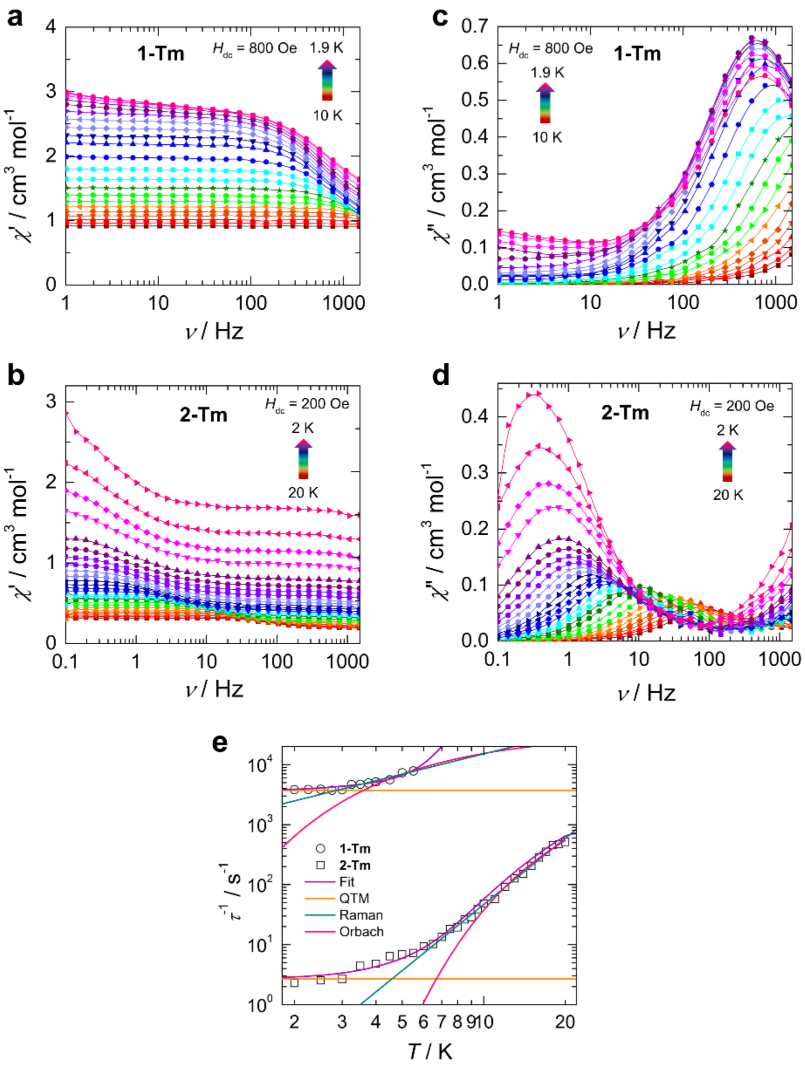

Figure 2.6 Frequency dependence of the (a-b) in-phase (χ') and (c-d) out-of-phase (χ'') components of the ac magnetic susceptibility for **1-Tm** at H_{dc} = 800 Oe (*top*), and for **2-Tm** at H_{dc} = 200 Oe (*middle*). Lines are a guide for the eye. (e) Temperature dependence of the magnetization relaxation times (τ) for **1-Tm** (hallow circles) and **2-Tm** (hollow squares). The solid purple lines represent best-fits to Equation 2.1. The orange, teal, and pink lines are the individual components of the magnetization relaxation for QTM, Raman, and Orbach processes, respectively.

Such small values suggest that the magnetic relaxation in **1-Tm** may be largely dictated by QTM, a process which is enhanced in non-Kramers systems. Further insight into the relaxation dynamics of **1-Tm** were obtained through the fit of the τ^{-1} *vs. T* plot to Equation 2.1 (Figure 2.6e). Wherein the various components are representative of the common relaxation mechanisms in Ln-based SMMs, Orbach, Raman, and QTM. The first term represents magnetic relaxation that occurs *via* the Orbach process with parameters τ_0^{-1} and U_{eff}, the second contains Raman terms C and n, and lastly, τ^{-1}_{QTM} which represents the rate of QTM.

$$\tau^{-1} = \tau_0^{-1}\exp\left(-\frac{U_{\mathrm{eff}}}{k_{\mathrm{B}}T}\right) + CT^n + \tau_{QTM}^{-1} \tag{2.1}$$

The best fit parameters for **1-Tm** to Equation 2.1 are recorded in Table 2.2. A minimal energy barrier to magnetization reversal of 7.93 K is achieved, however this is not surprising given the obtained Raman exponent (n = 6.20), which is close to expected value for a non-Kramers system (n = ca. 7).[1] Combined with a QTM rate on the order of milliseconds, magnetic relaxation through excited CF states is improbable for this system. Thus, even with the application of a static field to lift the degeneracy of the CF states, rapid relaxation through the ground state remains. The presence of coordinated solvent is likely to drastically influence the orientation of the main magnetic axis in the ground state,[6] further facilitating this type of relaxation. In non-Kramers systems such as **1-Tm**, asymmetric components such as these in the molecular structure drastically influence the intrinsic tunneling gap, resulting in diminished SMM properties.[15,25]

Table 2.2 Summary of best-fit parameters to Equation 2.1

Compound	**1-Tm**	**2-Tm**
H_{dc} / Oe	800	200
U_{eff} / K	7.93	53.3
τ_0 / s	1.18 x 10^{-4}	1.28 x 10^{-4}
C / $s^{-1}K^{-n}$	0.059	0.010
n	6.20	3.66
τ_{QTM} / s^{-1}	373.1	2.695

In stark contrast to the data obtained for **1-Tm**, **2-Tm** displays a signal in its χ' and χ" susceptibilities in the absence of an applied static field (H_{dc} = 0 Oe), yielding only high frequency tails (Figure 2.7). The presence of these tails precludes the determination of zero field slow relaxation dynamics.

Although, with the application of a small dc field, H_{dc} = 200 Oe, as determined from the field dependent measurements, frequency dependent behavior is obtained (Figure 2.6). The application of such a small dc field in order to observe relaxation is rare in $\mathrm{Tm}^{\mathrm{III}}$ complexes, as much larger fields have been employed previously (1 - 2 kOe).[12,18] At this magnitude of field (~200 Oe for **2-Tm**), the potential for inducing intermolecular interactions and long-range magnetic ordering is significantly reduced unlike the previous examples.

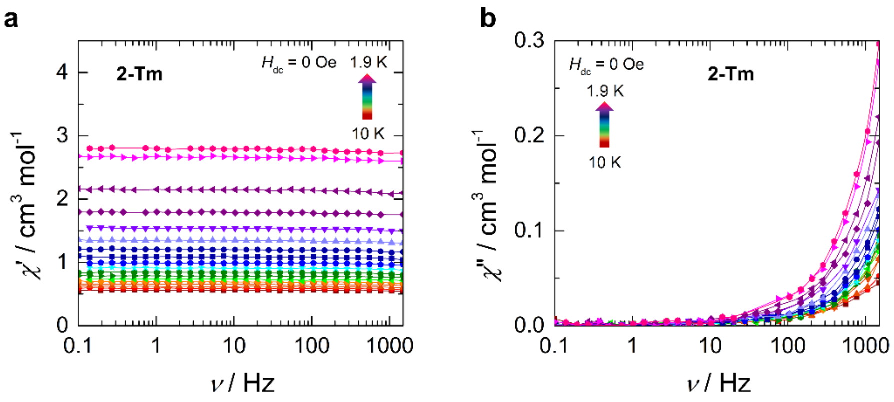

Figure 2.7 Frequency dependence of the in-phase, χ', (a) and out-of-phase, χ'', (b) components of the ac magnetic susceptibility for **2-Tm** in the absence of an applied static field (H_{dc} = 0 Oe).

Within the temperature range 9-20 K, a single peak is observed in the χ'' susceptibility, and when below 8 K, a bimodal isothermal susceptibility is observed, such that there is an onset of high frequency tails in addition to the main relaxation process. Each isothermal susceptibility curve was fit to the generalized Debye model, assuming a single process, to extract the relaxation times. Not only do the χ' and χ'' signals of **2-Tm** occur over a greater temperature range than **1-Tm**, but the relaxation times that are achieved (1.82 x 10^{-3} - 0.538 s) for **2-Tm** are orders of magnitude larger than those measured for **1-Tm**. Indeed, this is correlated with the obtained best fit parameters from the fit of the τ^{-1} *vs.* T plot to Equation 2.1, which are recorded in Table 2.2. The results of which reveal a Raman exponent of 3.66, this is lower than what is expected for a non-Kramers system (n = ca. 7),[2] which may suggest that there are not enough lattice phonons of appropriate frequency to efficiently promote this type of relaxation.[2] In comparison to **1-Tm**, the rate of QTM occurs on a much slower time scale (2.68 x 10^{-3} s *vs.* 0.371 s), providing evidence that magnetic relaxation through this process is less efficient than it is in **1-Tm**. Collectively, the decrease in efficiency of the Raman and QTM processes allows **2-Tm** to relax through a slower pathway which is likely through thermally accessible CF states, producing a U_{eff} of 53.3 K. The energy barrier to magnetization reversal of **2-Tm** results in an 85% increase over **1-Tm,** illustrating that QTM in the ground state is minimized in **2-**

Tm compared to **1-Tm**. As a consequence of the reduced tunneling in **2-Tm**, a small opening in the magnetic hysteresis measurements at 1.8 K and zero-field is afforded (Figure 2.8). Comparatively, the same measurement on **1-Tm** produced only a butterfly-shaped curve, with openings at higher fields. The absence of coercivity in **1-Tm** at the lowest measurable temperature of 1.8 K demonstrates the dominance of QTM in this system. Notably, at higher temperatures, **2-Tm** does not exhibit the same zero-field openings in its magnetization hysteresis measurements, and the openings in the high-field region quickly dissipate for **1-Tm** at elevated temperatures.

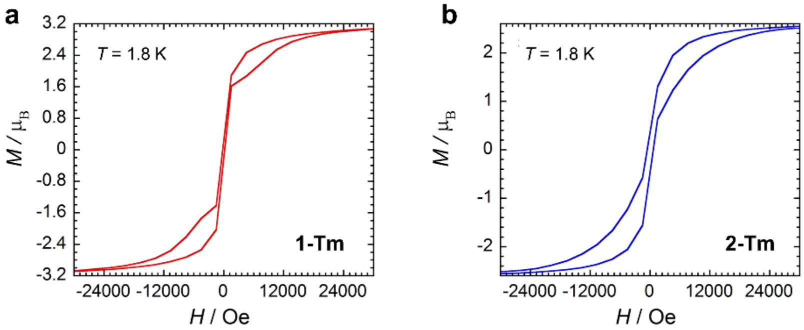

Figure 2.8 Magnetic hysteresis data for (a) **1-Tm** and (b) **2-Tm** collected at 1.8 K and an average sweep rate of 23 Oe s^{-1}. In all measurements, data were collected starting at $H = 0$ Oe, sweeping to $H = 50$ kOe and then cycling to $H = -50$ kOe and back to $H = 50$ kOe.

2.3 Summary and Conclusion

This chapter has presented a successful stepwise addition of cyclooctatetraenyl to [Tm^{III}(η^8-COT)I(THF)$_2$] (1-**Tm**) to obtain [K(18-crown-6)(THF)$_2$][Tm^{III}(η^8-COT)$_2$] (**2-Tm**). This resulted in increased local symmetry at the Tm^{III} ion by removal of the coordinated solvent molecules and iodide ligands. Through the characterization of the static and dynamic magnetic properties of these hetero- and homoleptic species, field-induced SMM behaviour was elucidated for both compounds.

Overall, **2-Tm** showed greater improvements in the magnetic relaxation dynamics over **1-Tm**. A larger energy barrier to spin reversal was achieved, $U_{\mathrm{eff}} = 53.3$ K, under a smaller applied field of 200 Oe for **2-Tm**; whereas a static field of 800 Oe was needed to observe an out-of-phase signal for **1-Tm**. Moreover, the rate of QTM was two orders of magnitude faster for the heteroleptic **1-Tm**. Collectively, this demonstrated the significance of increased local symmetry at the metal center, for decreasing the contributions of fast through-barrier relaxation mechanisms such as QTM. This illustrates that small perturbations in the crystal field of non-Kramers SMMs can cause drastic reductions from their ideal performance. Thus, if we wish to take advantage of the immense angular momenta afforded by Tm^{III}, then careful synthetic design and isolation of highly symmetric ligand environments are necessary.

2.4 Experimental Details

2.4.1 General Procedures

All reactions and subsequent manipulations were performed under anaerobic and anhydrous conditions using a standard Schlenk-line or nitrogen-atmosphere glovebox. Tetrahydrofuran (THF) and dimethoxyethane (DME), were dried on columns of activated alumina using a J.C. Meyer solvent purification system, degassed with successive freeze-pump-thaw cycles, and stored over activated 3 Å molecular sieves. Anhydrous TmI_2 and potassium metal were purchased from Sigma Aldrich; these chemicals were used as received. 18-crown-6 (18-c-6) was purchased from Sigma Aldrich and purified *via* vacuum sublimation at 0.019 Torr. 1,3,5,7-cyclooctatetraene was purchased from TCI and bubble degassed with argon prior to use. **K_2COT** was prepared as previously reported,[20] with the only modification occurring for the solvent, where THF was replaced with DME. The preparation of $[Tm^{III}(\eta^8\text{-COT})I(THF)_2]$,[19] was modified from previously published report as described below. Infrared spectra were recorded on a Nicolet Nexus 550 FT-IR spectrometer using transmission mode in the 4000-600 cm^{-1} range; solid samples were prepared under an inert atmosphere and sandwiched between transparent NaCl plates. NMR spectra were acquired on a Bruker Avance-II 300 MHz spectrometer at 298 K. Elemental analysis were conducted by Canadian Microanalytical, Delta, BC.

2.4.2 Experimental Procedures

Synthesis of $[Tm^{III}(\eta^8\text{-COT})I(THF)_2]$ (1-Tm). Under an inert atmosphere, a solution of 1,3,5,7-cyclooctatetraene (0.1 mL, 0.888 mmol) in THF was added slowly to a slurry of TmI_2 (368 mg, 0.870 mmol) in THF. The green slurry became red upon immediate addition of 1,3,5,7-cyclooctatetraene. The solution was stirred for 30 min at room temperature and then filtered over a fine frit to remove any remaining TmI_2 and TmI_3. The filtrate was collected and concentrated, additional TmI_3 was precipitated. TmI_3 was removed *via* filtration over Celite, red block X-ray quality single crystals were grown from the filtrate at room temperature overnight. Isolated crystals are air and moisture sensitive. Yield = 72-74%. IR (neat, cm^{-1}): 2972 (br), 2892 (m), 1866 (m), 1754 (m), 1621 (m), 1563 (w), 1482 (w), 1470 (w), 1445 (w), 1366 (w), 1344 (m), 1311 (m), 1245 (m), 1182 (m), 1068 (m), 1018 (m), 853 (m), 799 (m), 750 (m), 717 (m), 671 (m), 627 (m). ^{1}H NMR (THF-d^8, 298 K, δ/ppm): 2.54 (s, 8 H, *THF*, FWHM: 92 Hz), 1.15 (s, 8 H, *THF*, FWHM: 138 Hz), -182.32 (br, s, 8 H, C_8H_8, FWHM: 4044 Hz). CHN analysis (found, calc.) for $C_{16}H_{24}IO_2Tm$: C (34.40, 35.31); H (4.60, 4.45); N (<0.3, 0.00).

Synthesis of [K(18-c-6)(THF)$_2$][Tm^{III}(η^8-COT)$_2$] (2-Tm). Under an inert atmosphere, a solution of **K$_2$COT** (27 mg, 0.07 mmol) in THF is added dropwise to a solution of **1-Tm** (33 mg, 0.06 mmol) in THF at -35°C. The solution is stirred at room temperature for 20 min and the reaction mixture filtered over Celite and subsequently washed three times with THF. The filtrate was collected and concentrated. 1 equivalent of 18-crown-6 (16mg, 0.06 mmol) was added in 1 mL of THF. Single-crystal X-ray quality red needles were obtained after 48 h at room temperature. Isolated crystals are air and moisture sensitive. Yield = 66%. IR (neat, cm^{-1}): 2852 (w), 1599 (w), 1469 (m), 1349 (m), 1282 (m), 1246 (m), 1234 (m), 1104 (m), 964 (s), 897 (s), 838 (s), 800 (m), 760 (m), 743 (s), 681 (s), 628 (w). ^{1}H NMR (THF-d^8, 298 K, δ/ppm): 78.22 (br, s, 24 H, *18C6*, FWHM: 1075 Hz), 5.40 (br, s, 8 H, *THF*, FWHM: 388 Hz), 0.07 (br, s, 8 H, *THF*, FWHM: 308 Hz), -177.72 (br, s, 16 H, C_8H_8, FWHM: 9554 Hz). CHN analysis (found, calc.) for $C_{36}H_{56}KO_8Tm$: C (52.09, 52.42); H (6.17, 6.84); N (<0.3, 0.00).

2.4.3 Crystallography

Structural information has been previously reported for **1-Tm**. However, for the purposes of completeness our parameters are included below. Data collection results for compounds **1-Tm** and **2-Tm** represent the best data sets obtained in several trials for each sample. The crystals were mounted on thin glass fibers using paraffin oil. Prior to data collection crystals were cooled to 200 K. Data were collected on a Bruker AXS KAPPA or SMART single crystal diffractometer equipped with a sealed Mo tube source (λ = 0.71073 Å) APEX II CCD detector. Raw data collection and processing were performed with APEX II software package from BRUKER AXS.[26] Initial unit cell parameters were determined from 60 data frames with 0.3° *ω* scan each, collected at the different sections of the Ewald sphere. Semi-empirical absorption corrections based on equivalent reflections were applied.[27] Systematic absences in the diffraction data set and unit-cell parameters were consistent with monoclinic **P***2$_1$/n* (№14) for compound **1-Tm** and triclinic **P**-*1* (№2) for compound **2-Tm**. Solutions in the centrosymmetric space groups for both samples yielded chemically reasonable and computationally stable results of refinement. Structures were solved by direct methods, completed with difference Fourier synthesis, and refined with full-matrix least-squares procedures based on F^2.

For all the compounds all hydrogen atoms positions were calculated based on the geometry of related non-hydrogen atoms. All hydrogen atoms were treated as idealized contributions during the refinement. All scattering factors are contained in several versions of the SHELXTL program library, with version v.7.14 being used.[28]

Table 2.3 Crystallographic data for **1-Tm** and **2-Tm**

Compound	**1-Tm**	**2-Tm**
Empirical formula	$C_{16}H_{24}IO_2Tm$	$C_{36}H_{56}KO_8Tm$
Formula weight	544.18	824.83
Crystal size, mm	0.130x0.080x0.060	0.300x0.100x0.070
Crystal system	Monoclinic	Triclinic
Space group	**P***2₁/n*	**P**-*1*
Z	4	1
a, Å	8.4178(2)	7.7365(2)
b, Å	9.3602(3)	9.3103(2)
c, Å	22.0805(6)	13.1135(3)
α, °	90	85.0171(12)
β, °	97.3536(14)	83.5823(11)
γ, °	90	89.4078(13)
Volume, $Å^3$	1725.46(8)	935.09(4)
Calculated density, Mg/m^3	2.095	1.465
Absorption coefficient, mm^{-1}	3.930	2.530
T (K)	200(2)	200(2)
F(000)	1032	424
Θ range for data collection, °	2.366 to 28.317	2.196 to 28.320
Limiting indices	h = ±11, k = ±112, l = ±29	h = ±10, k = ±12, l = ±17
Reflections collected / unique	14763	8104
R(int)	0.0219	0.0130
Completeness to Θ = 28.32, %	98.7	97.7
Max. and min. transmission	0.7457 and 0.4954	0.7457 and 0.5254
Data / restraints / parameters	4228 / 96 / 199	4519 / 6 / 220
Goodness-of-fit on F^2	1.046	1.033
Final R indices $[I>2\sigma(I)]^a$	R1 = 0.0341, wR2 = 0.0743	R1 = 0.0198, wR2 = 0.0525
R indices (all data)	R1 = 0.0420, wR2 = 0.0780	R1 = 0.0199, wR2 = 0.0525
Largest diff. peak/hole, $e\cdot Å^{-3}$	2.897 and -2.889	0.792 and -0.519

$^a R = R_1 = \sum||F_0| - |F_c||/\sum|F_0|$; $wR_2 = \{\sum[w(F_0^2 - F_c^2)^2/\sum[w(F_0)^2]]^{1/2}$; $w = 1/[\delta^2(F_o^2) + (ap)^2 + bp]$, where $p = [\max(F_0^2, 0) + 2F_c^2]/3$

2.4.4 Magnetometry

The magnetic susceptibility measurements were obtained using a Quantum Design SQUID magnetometer MPMS-XL7 operating between 1.8 and 300 K. DC measurements were performed on polycrystalline samples of 12 mg for **1-Tm** and **2-Tm**. The samples were wrapped in a polyethylene bag under an inert atmosphere, and subjected to a field of 0 to 7 T. The magnetization data were collected at 100 K to check for ferromagnetic impurities that were absent in both samples. Diamagnetic corrections were applied for the sample holder and the inherent diamagnetism of the sample was estimated with the use of Pascals constants.

2.5 References

(1) Ungur, L.; Chibotaru, L. F. Strategies toward High-Temperature Lanthanide-Based Single-Molecule Magnets. *Inorg. Chem.* **2016**, *55* (20), 10043–10056. https://doi.org/10.1021/acs.inorgchem.6b01353.

(2) Liddle, S. T.; van Slageren, J. Improving f-Element Single Molecule Magnets. *Chem. Soc. Rev.* **2015**, *44* (19), 6655–6669. https://doi.org/10.1039/C5CS00222B.

(3) Zhang, P.; Zhang, L.; Wang, C.; Xue, S.; Lin, S.-Y.; Tang, J. Equatorially Coordinated Lanthanide Single Ion Magnets. *J. Am. Chem. Soc.* **2014**, *136* (12), 4484–4487. https://doi.org/10.1021/ja500793x.

(4) Gregson, M.; Chilton, N. F.; Ariciu, A.-M.; Tuna, F.; Crowe, I. F.; Lewis, W.; Blake, A. J.; Collison, D.; McInnes, E. J. L.; Winpenny, R. E. P.; Liddle, S. T. A Monometallic Lanthanide Bis(Methanediide) Single Molecule Magnet with a Large Energy Barrier and Complex Spin Relaxation Behaviour. *Chem. Sci.* **2016**, *7* (1), 155–165. https://doi.org/10.1039/C5SC03111G.

(5) Chen, Y.-C.; Liu, J.-L.; Ungur, L.; Liu, J.; Li, Q.-W.; Wang, L.-F.; Ni, Z.-P.; Chibotaru, L. F.; Chen, X.-M.; Tong, M.-L. Symmetry-Supported Magnetic Blocking at 20 K in Pentagonal Bipyramidal Dy(III) Single-Ion Magnets. *J. Am. Chem. Soc.* **2016**, *138* (8), 2829–2837. https://doi.org/10.1021/jacs.5b13584.

(6) Harriman, K. L. M.; Brosmer, J. L.; Ungur, L.; Diaconescu, P. L.; Murugesu, M. Pursuit of Record Breaking Energy Barriers: A Study of Magnetic Axiality in Diamide Ligated Dy ^{III} Single-Molecule Magnets. *J. Am. Chem. Soc.* **2017**, *139* (4), 1420–1423. https://doi.org/10.1021/jacs.6b12374.

(7) Ding, Y.-S.; Chilton, N. F.; Winpenny, R. E. P.; Zheng, Y.-Z. On Approaching the Limit of Molecular Magnetic Anisotropy: A Near-Perfect Pentagonal Bipyramidal Dysprosium(III) Single-Molecule Magnet. *Angew. Chem. Int. Ed.* **2016**, *55* (52), 16071–16074. https://doi.org/10.1002/anie.201609685.

(8) Layfield, R. A. Organometallic Single-Molecule Magnets. *Organometallics* **2014**, *33* (5), 1084–1099. https://doi.org/10.1021/om401107f.

(9) Guo, F.-S.; Day, B. M.; Chen, Y.-C.; Tong, M.-L.; Mansikkamäki, A.; Layfield, R. A. A Dysprosium Metallocene Single-Molecule Magnet Functioning at the Axial Limit. *Angew. Chem. Int. Ed.* **2017**, *56* (38), 11445–11449. https://doi.org/10.1002/anie.201705426.

(10) Pointillart, F.; Cador, O.; Le Guennic, B.; Ouahab, L. Uncommon Lanthanide Ions in Purely 4 f Single Molecule Magnets. *Coord. Chem. Rev.* **2017**, *346*, 150–175. https://doi.org/10.1016/j.ccr.2016.12.017.

(11) Ishikawa, N.; Sugita, M.; Ishikawa, T.; Koshihara, S.; Kaizu, Y. Lanthanide Double-Decker Complexes Functioning as Magnets at the Single-Molecular Level. *J. Am. Chem. Soc.* **2003**, *125* (29), 8694–8695. https://doi.org/10.1021/ja029629n.

(12) Meng, Y.-S.; Qiao, Y.-S.; Zhang, Y.-Q.; Jiang, S.-D.; Meng, Z.-S.; Wang, B.-W.; Wang, Z.-M.; Gao, S. Can Non-Kramers Tm ^{III} Mononuclear Molecules Be Single-Molecule Magnets (SMMs)? *Chem. - Eur. J.* **2016**, *22* (14), 4704–4708. https://doi.org/10.1002/chem.201600023.

(13) Jiang, S.-D.; Liu, S.-S.; Zhou, L.-N.; Wang, B.-W.; Wang, Z.-M.; Gao, S. Series of Lanthanide Organometallic Single-Ion Magnets. *Inorg. Chem.* **2012**, *51* (5), 3079–3087. https://doi.org/10.1021/ic202511n.

(14) Cardona-Serra, S.; Clemente-Juan, J. M.; Coronado, E.; Gaita-Ariño, A.; Camón, A.; Evangelisti, M.; Luis, F.; Martínez-Pérez, M. J.; Sesé, J. Lanthanoid Single-Ion Magnets Based on Polyoxometalates with a 5-Fold Symmetry: The Series $[LnP_5W_{30}O_{110}]^{12-}$ (Ln^{3+} = Tb, Dy, Ho, Er, Tm, and Yb). *J. Am. Chem. Soc.* **2012**, *134* (36), 14982–14990. https://doi.org/10.1021/ja305163t.

(15) Tang, J.; Zhang, P. *Lanthanide Single Molecule Magnets*; Springer, 2015.

(16) Ungur, L.; Le Roy, J. J.; Korobkov, I.; Murugesu, M.; Chibotaru, L. F. Fine-Tuning the Local Symmetry to Attain Record Blocking Temperature and Magnetic Remanence in a Single-Ion Magnet. *Angew. Chem. Int. Ed.* **2014**, *53* (17), 4413–4417. https://doi.org/10.1002/anie.201310451.

(17) Le Roy, J. J.; Korobkov, I.; Murugesu, M. A Sandwich Complex with Axial Symmetry for Harnessing the Anisotropy in a Prolate Erbium(III) Ion. *Chem Commun* **2014**, *50* (13), 1602–1604. https://doi.org/10.1039/C3CC48557A.

(18) Amjad, A.; Figuerola, A.; Sorace, L. Tm(III) Complexes Undergoing Slow Relaxation of Magnetization: Exchange Coupling and Aging Effects. *Dalton Trans.* **2017**, *46* (12), 3848–3856. https://doi.org/10.1039/C6DT04691F.

(19) Fedushkin, I. L.; Bochkarev, M. N.; Dechert, S.; Schumann, H. A Chemical Definition of the Effective Reducing Power of Thulium(II) Diiodide by Its Reactions with Cyclic Unsaturated Hydrocarbons. *Chem.–Eur. J.* **2001**, *7* (16), 3558–3563. https://doi.org/10.1002/1521-3765(20010817)7:16<3558::AID-CHEM3558>3.0.CO;2-H.

(20) Meihaus, K. R.; Long, J. R. Magnetic Blocking at 10 K and a Dipolar-Mediated Avalanche in Salts of the Bis(η^8-Cyclooctatetraenide) Complex $[Er(COT)_2]^-$. *J. Am. Chem. Soc.* **2013**, *135* (47), 17952–17957. https://doi.org/10.1021/ja4094814.

(21) Rabe, G. W.; Zhang-Preße, M.; Golen, J. A.; Rheingold, A. L. Bis(Cyclooctatetraenyl)Thulium Lithium Tris(Tetrahydrofuran). *Acta Crystallogr. Sect. E Struct. Rep. Online* **2003**, *59* (5), m255–m256. https://doi.org/10.1107/S1600536803007591.

(22) Rausch, J.; Apostolidis, C.; Walter, O.; Lorenz, V.; Hrib, C. G.; Hilfert, L.; Kühling, M.; Busse, S.; Edelmann, F. T. One Ligand Fits All: Lanthanide and Actinide Sandwich Complexes Comprising the 1,4-Bis(Trimethylsilyl)Cyclooctatetraenyl (=COT″) Ligand. *New J. Chem.* **2015**, *39* (10), 7656–7666. https://doi.org/10.1039/C5NJ00991J.

(23) Jiang, S.-D.; Wang, B.-W.; Sun, H.-L.; Wang, Z.-M.; Gao, S. An Organometallic Single-Ion Magnet. *J. Am. Chem. Soc.* **2011**, *133* (13), 4730–4733. https://doi.org/10.1021/ja200198v.

(24) Gatteschi, D.; Sessoli, R.; Villain, J. *Molecular Nanomagnets*; Oxford University Press, 2006.

(25) Ungur, L.; Chibotaru, L. F. Magnetic Anisotropy in the Excited States of Low Symmetry Lanthanide Complexes. *Phys. Chem. Chem. Phys.* **2011**, *13* (45), 20086. https://doi.org/10.1039/c1cp22689d.

(26) *V.2012 Bruker AXS*; Bruker: Madison, Wisconsin, 2005.

(27) Blessing, R. H. An Empirical Correction for Absorption Anisotropy. *Acta Crystallogr. A* **1995**, *51* (1), 33–38. https://doi.org/10.1107/S0108767394005726.

(28) Sheldrick, G. M. A Short History of *SHELX*. *Acta Crystallogr. A* **2008**, *64* (1), 112–122. https://doi.org/10.1107/S0108767307043930.

Chapter 3

Modulating the Relaxation Dynamics in Dinuclear Single-Molecule Magnets *via* Ancillary Ligands

3.1 Introduction

Single-molecule magnets (SMMs) are discrete molecules which display a bistable ground state separated by an energy barrier which a spin must overcome in order to reverse the orientation of its magnetic moment.[1,2] Energy is required in order to accomplish this flip and is acquired through an energy transfer between the paramagnetic system and the lattice, effectively known as spin-lattice relaxation.[3] Unfortunately, quantum tunnelling of the magnetization (QTM) is prevalent in lanthanide (Ln) ions, facilitating the transition of the magnetic moment through the ground state without surmounting an energy barrier. This is due in part to the classically dense energy spectra for Ln ions combined with saturated coordination environments that typically result in tunnel splittings.[4] Overall, this fast process limits the potential energy barrier to spin inversion and prohibits SMMs from becoming technologically relevant. Previously, weak exchange interactions in the SMM $[Mn_4O_3Cl_4(O_2CEt)_3(py)_3]_2$ (O_2CEt = propionate; py = pyridine), were reported to shift the tunnel resonances away from zero-field,[5] demonstrating that exchange coupling is an effective means for moderating QTM and promoting slow relaxation of the magnetization. Indeed, this has already been demonstrated in a number of Dy^{III}-based SMMs.[6–10] This requires that the strength of magnetic coupling between spin carriers be larger than the temperature domain of QTM.[11,12] However, this is not trivial; a substantial drawback is that polynuclear lanthanide complexes often exhibit weak magnetic coupling (exchange and dipolar) owing to their shielded 4f valence orbitals. This means that their magnetic properties are often dictated by the single-ion properties of the isolated metal ions and their respective single-ion magnetic anisotropies.[13,14] Therefore, a combination of both strong single-ion anisotropy and suitable exchange coupling should be used as design elements to obtain even better and more efficient SMMs. Several strategies are now widely accepted and employed for increasing the magnetic axiality of a 4f SMM. These include increasing the local symmetry at the metal ion,[15,16] approximating specific symmetry point groups which are absent of transverse crystal field operators,[17,18] and creating strong metal-ligand interactions along a defined axis or plane.[19–21]

In this study the static and dynamic magnetic properties of two structurally related dinuclear Dy^{III} compounds, $[Dy^{III}\{N(SiMe_3)_2\}_2(\mu\text{-Cl})(THF)]_2$ (**3-Dy**) and $[Dy^{III}(\eta^8\text{-COT})(\mu\text{-Cl})(THF)]_2$ (**4-Dy**), are presented and analyzed. While a number of previous studies have investigated the identity, orientation, and number of bridging atoms on the magnetic coupling of 4f ions,[22] few consider the effects of the remaining coordination sphere on the overall magnetic properties. The structurally similar $\{Dy_2(\mu\text{-}Cl)_2\}$ core of the presented molecules allowed for the comparison of the ancillary ligand effects on the relaxation dynamics, the magnetic anisotropy and axiality, as well as the extent of coupling between the 4f ions. The trimethylsilyl amido and cyclooctatetraenyl (COT) ancillary ligands were chosen for their respective and differing ligand fields and stabilization effects on the $J = 15/2$ manifold of the Dy^{III} ion. The large diffuse π-electron cloud of the COT ligand produces a largely equatorial ligand field resulting in the destabilization of the Ising states with the largest magnetic moment (i.e., crystal field mcirostates).[15,23] Whereas, the amido-based ligands provide direct coordination of a mostly localized negative charge, which when strategically placed about the Dy^{III} ion, can elicit significant stabilization of the Ising states.[24] *Ab initio* calculations on compounds **3-Dy** and **4-Dy** are presented to facilitate the comparison and understanding of the role of differing ancillary ligands on the relaxation dynamics and magnetic properties of dinuclear Dy^{III} SMMs.

3.2 Results and Discussion

3.2.1 Synthesis and Structure

With the rigorous exclusion of oxygen and moisture **3-Dy** and **4-Dy** were synthesized with modifications to the previously reported preparations of $[Dy^{III}\{N(SiMe_3)_2\}_2(\mu\text{-}Cl)(THF)]_2$,[25] and $[Er^{III}(\eta^8\text{-}COT)(\mu\text{-}Cl)(THF)]_2$.[26] Compound **3-Dy** was prepared from the direct reaction of $DyCl_3$ and $NaN(SiMe_3)_2$ in THF (Figure 3.1). To prevent the formation of the *tris*-amido compound, $[Dy^{III}\{N(SiMe_3)_2\}_3]$, the addition of $NaN(SiMe_3)_2$ is performed at reduced temperatures (-35°C) over a period of 20 minutes, after which the reaction mixture is gradually warmed to room temperature. To ensure the removal of NaCl, the THF was removed *in vacuo* and the product extracted into toluene. Following centrifugation, and the resuspension of the solid in pentanes, the product was obtained as colourless needless in 62% yield, that were of X-ray quality.

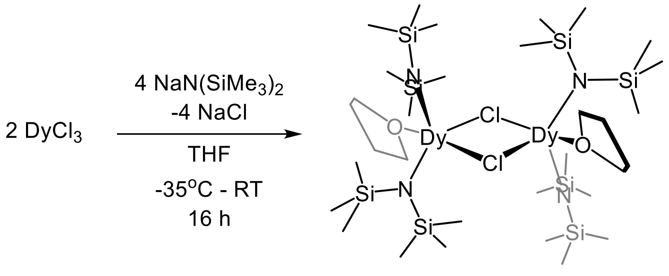

3-Dy

Figure 3.1 Synthesis of $[Dy^{III}\{N(SiMe_3)_2\}_2(\mu\text{-}Cl)(THF)]_2$ (**3-Dy**).

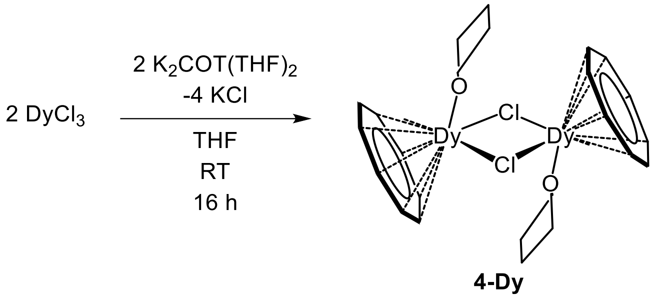

4-Dy

Figure 3.2 Synthesis of $[Dy^{III}(\eta^8\text{-COT})(\mu\text{-Cl})(THF)]_2$ (**4-Dy**).

Preparation of **4-Dy** was completed by the slow addition of $K_2COT(THF)_2$ to a slurry of $DyCl_3$ (Figure 3.2); $K_2COT(THF)_2$ was prepared from the direct alkali metal reduction of cyclooctatetraene with two equivalents of K^0. The addition of $K_2COT(THF)_2$ to $DyCl_3$ must be slow as to prevent the formation of the *bis*-COT compound, $[Dy^{III}(\eta^8\text{-COT})_2]^-$, and loss of the chloride ligands. The salt by-products were removed by centrifugation following the completion of the reaction, and the solvent was removed from the supernatant. Extraction into hot THF, followed by hot filtration and diffusion of n-hexanes afforded X-ray quality yellow crystals of **4-Dy** in 40% yield.

Single crystal X-ray diffraction (SCXRD) data collected on **3-Dy**, matches the previously reported metrics (*vide infra*).[25] Additionally, while the Er^{III} congener of **4-Dy** has been reported,[26] the present study includes the isotypic structure for Dy^{III} (Figure 3.3). Both complexes possess a planar $\{Dy_2(\mu\text{-Cl})_2\}$ core, with internal Cl1-Dy1-Cl1' angles of 74.57° (**3-Dy**) and 81.62° (**4-Dy**), and internal Dy1-Cl1-Dy1' angles of 105.43° and 98.38°, for **3-Dy** and **4-Dy** respectively (Table 3.1). These angles give rise to different intramolecular $Dy^{III}\cdots Dy^{III}$ distances effectively resulting in a longer distance for **3-Dy** (4.3419(5) Å) compared to **4-Dy** (4.135(1) Å). Moreover, the primary coordination sphere of both complexes includes one molecule of THF per Dy^{III} ion. The Dy-O_{THF} bond distances are nearly a tenth of an angstrom longer in **3-Dy** (2.412(3) Å) than **4-Dy** (2.368(2) Å), and their relative orientations about the $\{Dy_2(\mu\text{-Cl})_2\}$ core differ significantly due to the ancillary ligands employed. The Dy-O_{THF} bond of **3-Dy** is nearly coplanar with the $\{Dy_2(\mu\text{-Cl})_2\}$ core (O1-Dy1-Cl1$\angle$ = 149.04(7)°), while the Dy-O_{THF} bond of **4-Dy** is perpendicular to the $\{Dy_2(\mu\text{-Cl})_2\}$ core($\angle$ = 81.30(5)°). Given the oxophilic nature of the 4f ions, this relative orientation of the O-atom about the metal center is expected to have significant effects on the magnetic axiality of each compound.

More specifically, the coordination environment of **3-Dy** is completed by two trimethylsilyl amide ancillary ligands per Dy^{III} ion. This results in a pentacoordinate geometry which closely resembles that of (NN^{TBS})DyI(THF)$_2$, (NN^{TBS} = fc(NHSi^{t}BuMe$_2$)$_2$, fc = 1,1′ ferrocenediyl; **7-Dy**; *presented in Chapter 5, vide infra*), a diamide-based SMM with a large multistep relaxation pathway (U_{eff} = 770 K).[27] The structure of **3-Dy** contains short Dy-N bond distances of 2.215(3) Å and 2.236(3) Å with a N1-Dy1-N2 angle of 117.8(1)°, which is expected to be a strong director for the orientation of the main magnetic axis in the ground state. In the case of **4-Dy**, a single cyclooctatetraenyl (COT^{2-}) ancillary ligand coordinates to each Dy^{III} ion in a η^8-fashion (Dy1-C$_{\text{avg}}$ = 2.55 Å). The COT^{2-} ligands slightly tilt away from the intramolecular Dy$^{III}\cdots$Dy^{III} axis, resulting in a COTcentroid-Dy1-Dy1' angle of 153.41(1)°. A Dy-COT$_{\text{centroid}}$ distance of 1.7891(4) Å is comparatively shorter than the homoleptic [Dy^{III}(η^8-COT)$_2$]$^-$ complex (1.89(3) Å and 1.91(8) Å),[15] suggesting that greater electrostatic interactions are present in this compound, which may have an influence over the resulting magnetic properties.[28,29]

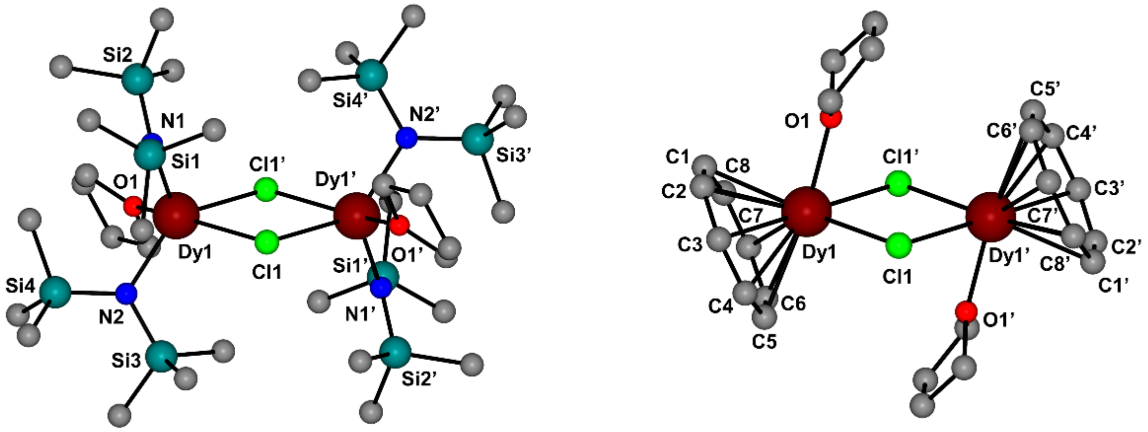

3-Dy **4-Dy**

Figure 3.3 Molecular structure of [Dy^{III}{N(SiMe$_3$)$_2$}$_2$(μ-Cl)(THF)]$_2$ **3-Dy** (left) and [Dy^{III}(η^8-COT)(μ-Cl)(THF)]$_2$ **4-Dy** (right). Colour code: Dark red (Dy^{III}), teal (Si), green (Cl), blue (N), red (O), grey (C). Hydrogen atoms omitted for clarity.

Table 3.1 Selected bond lengths and angles from single crystal X-ray diffraction studies for **3-Dy** and **4-Dy**

Metric	**3-Dy**	**4-Dy**
Dy1-Cl1 (Å)	2.737(1)	2.7350(9)
Dy1-Cl1' (Å)	2.720(1)	2.728(1)
Dy1-O1 (Å)	2.412(3)	2.368(2)
Dy1-L (Å)[a]	2.214(3) 2.236(3)	1.789
Dy1---Dy1' (Å)	4.3419(5)	4.135(1)
Dy1-Cl1-Dy1' (°)	105.43(3)	98.38(2)
Cl1-Dy1-Cl1' (°)	74.57(3)	81.62(2)
O1-Dy1-Cl1 (°)	149.04(7)	81.30(5)
N1-Dy1-N2 (°)	117.8(1)	-

[a] The Dy1-L distance for compound **4-Dy** corresponds to the Dy-COT$_{centroid}$ distance

3.2.2 Direct Current Magnetic Susceptibility

The direct current (dc) magnetic susceptibility measurements revealed a characteristic temperature dependence for both compounds. The near identical behaviour for **3-Dy** and **4-Dy** results in a gradual decrease of the susceptibility in the plot of χT *vs.* T from 27.51 cm^{3}Kmol^{-1} and 28.45 cm^{3}Kmol^{-1} at 300 K, for **3-Dy** and **4-Dy** respectively (Figure 3.4a). These values are in good agreement with the expected value of 28.34 cm^{3}Kmol^{-1} for two non-interacting Dy^{III} ions ($^6H_{15/2}$, $S = 5/2$, $L = 5$, $g = 4/3$). This means that any interactions between metal centers are negligible at 300 K, which is anticipated for the 4f ions owing to their shielded valence orbitals. The variable temperature susceptibility of both **3-Dy** and **4-Dy** revealed similar profiles, where upon cooling from 300 K there is a slight decrease in the χT products until 20 K. This gradual decrease is most likely a result of thermal depopulation of the microstates of the $J = 15/2$ manifold. Below 20 K, a substantial decrease in the χT products results in final values of 14.22 cm^{3}Kmol^{-1} (**3-Dy**) and 5.33 cm^{3}Kmol^{-1} (**4-Dy**) at 1.8 K. This marked decrease in the susceptibility is not surprising given the expected contribution from magnetic interactions such as dipole-dipole interactions between spin carriers within these molecules.[30] This is further supported by the close intramolecular Dy$^{III}\cdots$Dy^{III} distances of 4.3419(5) Å (**3-Dy**) and 4.134(1) Å (**4-Dy**). While exchange interactions may also be operable in these systems via μ-Cl ions, the classically weak nature of such interactions suggests that dipole-dipole interactions are dominant. Further to this, we suspect that these interactions would be stronger in **4-Dy** due to the shorter intramolecular Dy$^{III}\cdots$Dy^{III} distance, as well as closer intermolecular Dy$^{III}\cdots$Dy^{III} distances

(10.30 Å vs. 7.10 Å), leading to an overall smaller χT value at 1.8 K. Nevertheless, in both systems contributions from unquenched orbital angular momentum, leading to magnetic blocking on the time scale of the experiment, may also be influencing the low temperature behaviour of the χT products. Isothermal magnetization measurements were completed in the temperature range of 1.8-7 K under applied static fields up to 7 T (Figure 3.4b-c). Under these conditions, the magnetic moments of 10.84 μ_B (**3-Dy**) and 10.41 μ_B (**4-Dy**) are obtained at 1.9 K and largest possible field of 7 T. While the magnetization values are in the expected range for dinuclear Dy^{III} complexes, the shape of the curves do not exhibit a clear plateau in the high field region; this may be indicative of low-lying excited states. Moreover, the reduced magnetization exhibits non-superimposable isothermal curves (Figure 3.4d-e), which may be attributed to the inherent magnetic anisotropy of the Dy^{III} ions or low-lying excited states.

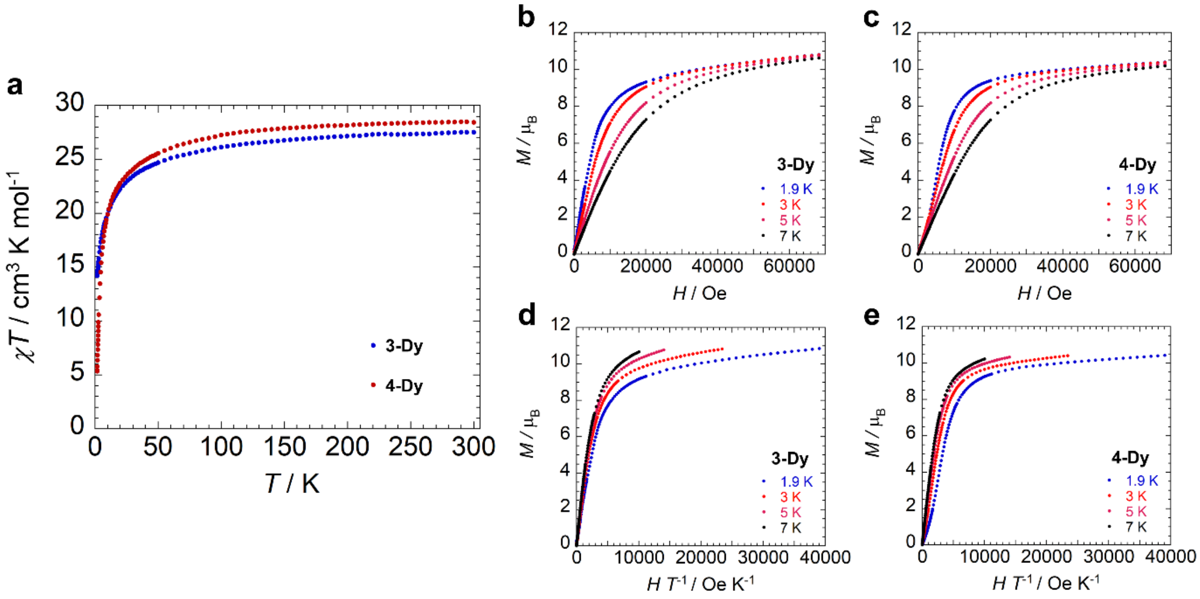

Figure 3.4 (a) Temperature dependence of the χT product at 1000 Oe for **3-Dy** (blue) and **4-Dy** (red). Solid state field dependence of the magnetization for (b) **3-Dy** and (c) **4-Dy**, and the reduced magnetization for (d) **3-Dy** and (e) **4-Dy** at the indicated temperatures.

3.2.3 Alternating Current Susceptibility

To probe the presence of magnetic anisotropy in these systems, alternating current (ac) magnetic susceptibility measurements were performed on **3-Dy** and **4-Dy** with a 3.78 Oe driving field (H_{ac} = 3.78 Oe) and zero applied static field (H_{dc} = 0 Oe). The in-phase (χ') and out-of-phase (χ") components of the ac susceptibility as a function of ac frequency (v) display prominent SMM behaviour for both **3-Dy** and **4-**

Dy (Figure 3.5). Frequency dependent behaviour was observed below 40 K for **3-Dy**. Below 8 K, peak maxima in the χ" component of the ac susceptibility were not observable. In the case of **4-Dy**, frequency dependent behaviour was observable at much lower temperatures, beginning at 9 K, a single peak shifted towards lower frequencies with decreasing temperature until 5 K. Below this temperature, the frequency dependent behaivour was arrested, coinciding with a marked decrease in the ac susceptibility values from 5-1.8 K. This behaviour contrasts what is often observed in frequency independent relaxation (i.e., quantum tunneling of the magnetization (QTM)), which typically exhibits increased ac susceptibility at the low temperature limit.[31] For both compounds, the χ' and χ" data were satisfactory fit to the generalized Debye model,[32,33] assuming a single relaxation time (τ). A narrow distribution of the relaxation times was achieved with average α-parameters of 0.029 (**3-Dy**) and 0.036 (**4-Dy**). This supports the use of a single relaxation time model for describing the dynamics in these systems.

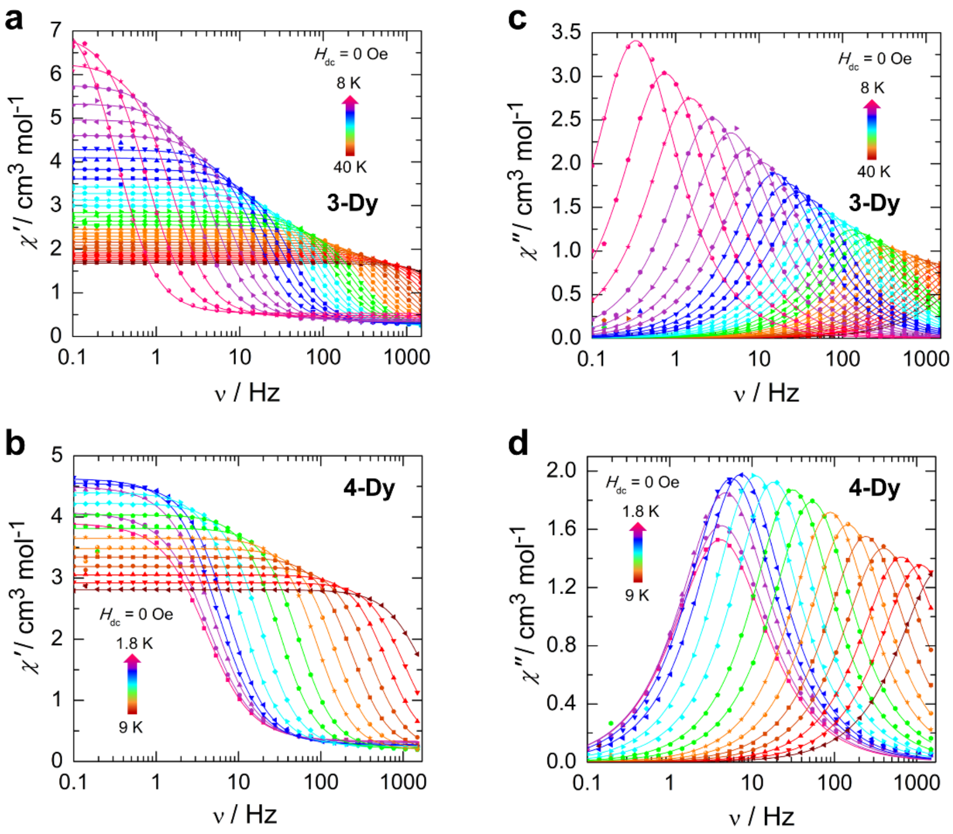

Figure 3.5 Frequency dependence of the (a-b) in-phase (χ') and (c-d) out-of-phase (χ") components of the ac magnetic susceptibility for **3-Dy** (*top*) and **4-Dy** (*bottom*) collected in the absence of an applied external field (H_{dc} = 0 Oe). Solid lines represent the best-fits to the generalized Debye model.

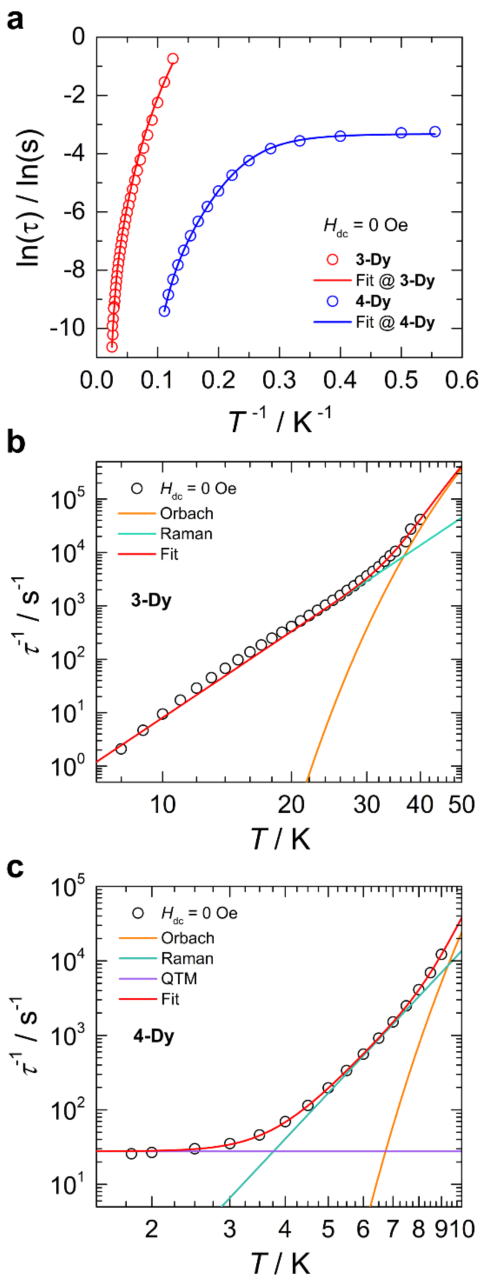

Figure 3.6 (a) Arrhenius plot of the relaxation times (τ) obtained from the generalized Debye model for **3-Dy** (red) and **4-Dy** (blue) for data under a zero-applied dc field (H_{dc} = 0 Oe). Solid lines represent best-fits to Equation 3.1. Temperature dependence of the magnetic relaxation times when H_{dc} = 0 Oe for (b) **3-Dy** and (c) **4-Dy**. The red solid lines represent the sum of the relaxation processes as per Equation 3.1. The orange, teal, and purple lines are the individual components of the magnetization relaxation for Orbach, Raman, and QTM processes, respectively.

To gain insight into the relaxation dynamics which govern the slow magnetic relaxation in **3-Dy** and **4-Dy**, the temperature dependent relaxation times were fit using Equation 3.1, accounting for contributions from QTM, Orbach and Raman relaxation mechanisms (Figure 3.6). The best-fit parameters are summarized in Table 3.2.

$$\tau^{-1} = \tau_{QTM}^{-1} + \tau_0^{-1}\exp\left(-\frac{U_{\text{eff}}}{k_{\text{B}}T}\right) + CT^n \tag{3.1}$$

With respect, to **3-Dy**, at the high temperature limit of the slow relaxation, the dominant process is the thermally activated Orbach pathway, eliciting an energy barrier to spin reversal of U_{eff} = 517.8 K (359.9 cm^{-1}) with a pre-exponential factor of τ_0 = 8.47 x 10^{-11} s. The obtained U_{eff} is in excellent agreement with the computed energy of the second excited stated, 357.1 cm^{-1}; this means that thermal relaxation likely occurs through this state. While the Orbach process dominates the high temperature limit, the *log-log* plot (τ^{-1} *vs.* T) of the relaxation rates is characterized by a strongly linear relationship with temperature, this suggests that the overall dominant pathway is Raman (Figure. 3.6b). Notably, these relaxation times for **3-Dy** do not follow the typical T^9 dependence for Kramers systems, as expected for Dy$^{\text{III}}$ ions.[3] Attempts to restrain the exponent to n = 9 or n = 7, in the case of a strongly coupled system or one with field induced mixing of excited states,[34] did not reproduce the data successfully. However, deviations from the expected T^9 dependence have been previously observed in other SMMs of highly anisotropic ions (i.e., Dy$^{\text{III}}$, Co$^{\text{II}}$).[21,35–37] Across the entirety of the temperature range studied, no other contributions from additional relaxation processes were needed to reproduce the data; meaning that a QTM regime was not observed for **3-Dy**.

Table 3.2 Magnetic relaxation parameters obtained from the fit of the temperature dependent relaxation times for **3-Dy** and **4-Dy** to Equation 3.1. Best fits were obtained with QTM (**4-Dy**), Orbach and Raman contributions.

	3-Dy H_{dc} **= 0 Oe**	**4-Dy** H_{dc} **= 0 Oe**
U_{eff}	517.8 K / 359.9 cm^{-1}	139.6 K / 97.0 cm^{-1}
τ_0	8.47 x 10^{-11} s	3.54 x 10^{-11} s
C	3.53 x 10^{-5} s^{-1} K^{-n}	6.22 x 10^{-3} s^{-1} K^{-n}
n	5.36	6.34
τ_{QTM}	-	27.7 s^{-1}

Comparatively, analysis of the relaxation times for **4-Dy** revealed that the relaxation dynamics incorporate components of Orbach, Raman, and QTM processes. Like **3-Dy**, the high temperature regime is best represented by the thermally activated Orbach process with an energy barrier to spin reversal of U_{eff} = 139.6 K (97.0 cm^{-1}) and a pre-exponential factor of $\tau_0 = 3.54 \times 10^{-11}$ s. It should be noted that this process is only characteristic of a minor portion of the collected data, that is both a consequence of the magnetic relaxation only being observable below 9 K, and with the Raman process being more dominant over the studied temperature range. However, the experimentally obtained U_{eff}-value matches the computed energy of 97.7 cm^{-1} corresponding to relaxation through the second excited state for **4-Dy**. This alludes to the validity of the fitted parameters despite few data points corresponding to this process. Furthermore, with decreasing temperature the Raman pathway becomes predominant, as evidenced by the linear portion of the relaxation times on the *log-log* scale (Figure 3.6c). The relaxation times for **4-Dy** deviate from the expected T^9 dependence associated for Kramers ions,[3] this was similarly observed for **3-Dy**; however, in the case of **4-Dy** this may arise from the intramolecular magnetic coupling between the Dy^{III} ions. Despite attempts to restrain this Raman exponent to n = 7, the slope of the relaxation times was not accurately reproduced; however, the obtained value of n = 6.34 is close to this anticipated value. Lastly, at the low temperature limit, below 5 K, the relaxation times begin to plateau, and are best characterized as QTM with a relaxation rate of 27.7 s^{-1}.

The presence of a non-negligible QTM regime in the relaxation dynamics of **4-Dy** prompted the investigation of the field-dependent relaxation dynamics in **4-Dy**. Magnetic relaxation will occur through the path of least resistance; with respect to QTM, degenerate microstates allow for facile relaxation without surmounting an energy barrier. To circumvent this, applied static fields may be utilized to shift the microstates out of resonance with one another, allowing for the observation of more effective and more clear magnetic relaxation. As such, ac measurements were performed on **4-Dy** at a fixed temperature of 2 K and the applied static field was varied from 0-2000 Oe in 200 Oe increments (Figure 3.7a). Frequency dependent behaviour was observed, with shifting peak maxima in the χ" component from *ca*. 4.2 Hz at 0 Oe to 0.16 Hz at 2000 Oe. Above 2000 Oe, a peak maximum was not observed as the signal shifted beyond the frequency limitations of the magnetometer, thus, preventing the full elucidation of the relaxation dynamics. To observe the full range of the relaxation behavior, the same frequency dependent measurement was completed at a slightly elevated temperature of 5 K. Under these conditions, the χ" component of the ac susceptibility did not produce a frequency dependent signal; and all *iso*-field susceptibilities appeared to perfectly trace on top of each other (Figure 3.7b). However, upon fitting the field dependent ac measurements at 5 K with the generalized Debye model, minor differences in the relaxation times were obtained that were not prominent on the *log*-frequency scale. These relaxation times, and the relaxation times from the fit of the 2 K field dependent data were further analyzed to determine the contributions from various field dependent relaxation mechanisms to the overall relaxation dynamics for compound **4-Dy**.

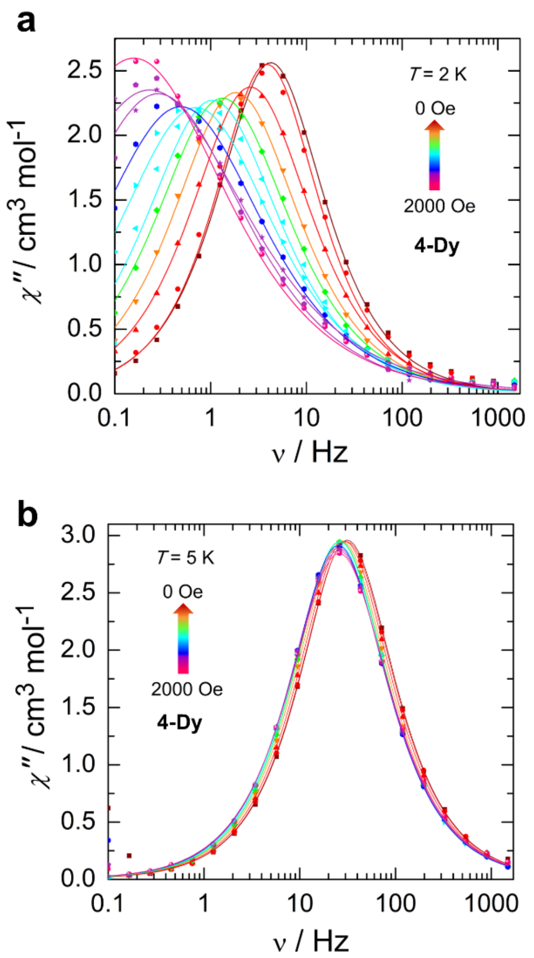

Figure 3.7 Frequency dependence of the out-of-phase (χ") component of the ac susceptibility as a function of applied static field, collected at a constant temperature of (a) T = 2 K and (b) T = 5 K for **4-Dy**. Individual curves are presented for each field in the range 0-2000 Oe in 200 Oe increments. Solid lines represent best fits to the generalized Debye model.

The field dependent relaxation times were fit using Equation 3.2, accounting for contributions from QTM and direct relaxation mechanisms (Figure 3.8). The best-fit parameters are summarized in Table 3.3. In this function, a constant (D) was included to account for any thermally accessible relaxation pathways. While this is expected to be negligible at the experiment's temperature of 2 K, due to low-lying excited states and the lack of saturation observed in the magnetization, *M vs. H* plots, it may be necessary to invoke for the fit of the 5 K data. The inclusion of this constant is commonly employed when the field dependent measurement cannot be completed at the lowest measurable temperatures.[38–40]

$$\tau^{-1} = AH^4 + \frac{B_1}{1 + B_2H^2} + D \tag{3.2}$$

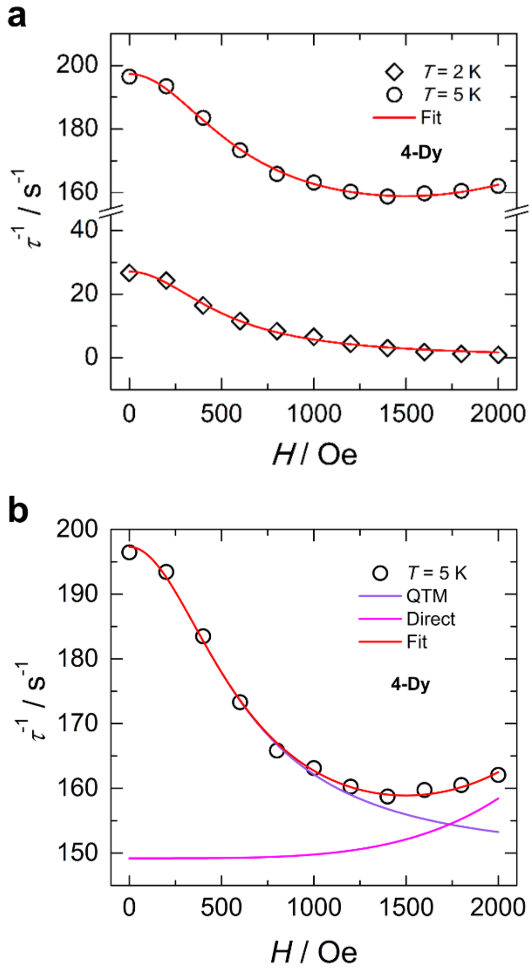

Figure 3.8 (a) Field dependence of the magnetic relaxation times (τ) for **4-Dy** collected at 2 K (hollow diamonds) and 5 K (hollow circles). Solid red lines represent best fits to the Equation 3.2. (b) Individual components of the magnetic relaxation represented by their individual functions; QTM (purple) and direct (pink).

At 2 K, the fit of the field-dependent relaxation times is characterized solely by QTM ($B_1/(1+B_2H^2)$). Within this term, the B_1 parameter is approximated to the rate of QTM from the temperature dependent data. Here, the tunneling rate is in perfect agreement with the rate determined from the fit of the temperature dependent data; the QTM rate from the field dependent fit at 2 K was 27.1 s^{-1} and the rate from the temperature dependent fit was 27.7 s^{-1}. Comparatively, the fit of the relaxation times at 5 K required terms for QTM, direct and thermally activated processes. The best fit parameters produced a larger B_1 term of 48.10 s^{-1}, which fundamentally implies that QTM is more efficient at 5 K *vs.* 2 K. While the origin of this behaviour is not clear or easily understood, a number of factors may contribute, such as temperature and field dependent QTM,[41] coupling between the Dy^{III} ions (as evidenced by the decrease in susceptibility),[11] and enhanced direct processes.[42]

Table 3.3 Summary of best-fit parameters of the field dependent relaxation times to Equation 3.2 for **4-Dy**

Temperature	**2 K**	**5 K**
A / $s^{-1}Oe^{-4}K^{-1}$	-	1.16 x 10^{-16}
$B1$ / s^{-1}	27.08	48.10
$B2$ / Oe^{-2}	3.72 x 10^{-6}	2.71 x 10^{-6}
D	-	149.19

3.2.4 Theoretical Analysis

Ab initio calculations on the full molecular structures of **3-Dy** and **4-Dy** were performed using MOLCAS-8.2 package.[43] X-ray atomic positions were employed without further computational refinement. All *ab initio* calculations were of the CASSCF / RASSI / SINGLE_ANISO kind[44] using only the $4f^n$ shell of one lanthanide ion as the active space. The neighbouring Dy^{III} ion in **3-Dy** and **4-Dy** were described by a diamagnetic Lu^{III} ion, which has a fully occupied 4f shell. This computational change is considered to have only a minor effect on the extracted crystal field splitting on the individual metal sites. All atoms were described by ANO-RCC basis sets,[45] which include relativistic corrections as of second-order Douglas-Kroll Hess theory.[46,47] All electronic states for S=5/2, 3/2 and 1/2 arising from $4f^9$ electronic configuration were computationally optimized and employed further in the spin-orbit coupling in RASSI.[48,49] This means that the spin-orbit coupling matrix built within the RASSI calculation included all 735 spin states, giving rise to 2002 spin-orbit states. All the spin-orbit eigenstates were further employed for the computation of the EPR *g*-tensor on individual metal sites (Table 3.4) and the corresponding main magnetic axes (Figure 3.9, dashed lines) and parameters of the crystal field.[29]

Table 3.4 *Ab initio* predicted low-lying energy spectra for **3-Dy** and **4-Dy** (in cm^{-1}). Bolded values correspond to the height of the experimental anisotropy barrier (U_{eff}).

3-Dy		**4-Dy**	
VDZP	VTZP	VDZP	VTZP
0.0	0.0	0.0	0.0
188.7	194.8	76.9	79.5
357.1	**368.9**	**97.7**	**96.1**
499.6	516.9	122.1	129.6
607.9	629.1	165.5	183.5
690.0	713.8	175.6	204.6
741.0	767.2	292.8	230.8
858.5	882.6	641.9	648.4
Main values of the g tensor of the ground Kramers doublet			
1.95 x 10^{-4}	2.77 x 10^{-4}	0.061	0.103
2.75 x 10^{-4}	3.89 x 10^{-4}	0.109	0.108
19.787	19.781	19.608	19.389

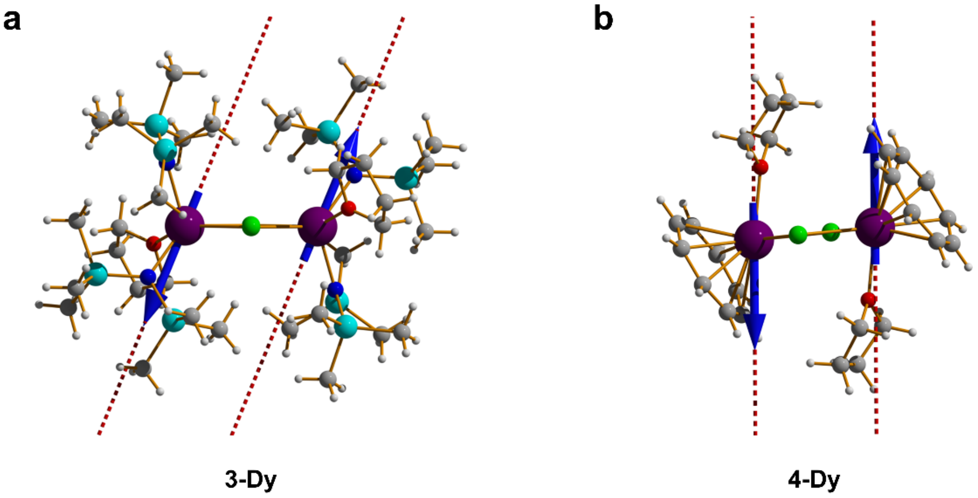

3-Dy **4-Dy**

Figure 3.9 *Ab initio* calculated main anisotropy axes (dashed lines) in the ground state for (a) **3-Dy** and (b) **4-Dy**. Blue arrows show the orientation of the local magnetic moments on the Dy$^{\mathrm{III}}$ sites in the ground exchange coupled state. Colour code: Purple (Dy$^{\mathrm{III}}$), cyan (Si), green (Cl), blue (N), red (O), grey (C), white (H).

The orientation of the main magnetic axis in the ground state is shown superimposed on the molecular structures of both **3-Dy** and **4-Dy** in Figure 3.9. Notably, the magnetic axiality of the individual Dy^{III} sites in **3-Dy** is much higher compared to the magnetic axiality of the Dy^{III} sites in **4-Dy**. This fact is reflected in the larger ratio between axial/non-axial crystal field parameters and in the perpendicular components of the *g*-tensor, g_X and g_Y (Table 3.4). While both molecules possess highly axial ground states, the perpendicular *g*-tensors for **3-Dy** ($g_X = 2.77 \times 10^{-4}$, $g_Y = 3.89 \times 10^{-4}$) are three orders of magnitude smaller than **4-Dy** ($g_X = 0.103$, $g_Y = 0.108$). The main anisotropy axes in **3-Dy** lie in the plane formed by N1-Dy1-N2, revealing the dominant role of the trimethylsilyl amide ligands for stabilizing this particular arrangement of the magnetic axiality in the ground state. The same anisotropy motif was previously found in several Ln-based molecular magnets.[50–52] One possible route to further improve the single-ion axiality would be in separating one of the $Dy\{N(SiMe_3)_2\}_2$ units in **3-Dy** as far as possible from the other N-Dy-N site and also from chloride ions. This would allow for significant lowering of the equatorial ligand field in the perpendicular direction to the main anisotropy axis, which would make the axial field even stronger. The dominant role of the trimethylsilyl amide ligands is due to a cumulative effect of covalent and electrostatic interactions. The calculated LoProp atomic charges[53] on the bonded nitrogen ligand atoms are -1.3, twice as large as compared to chlorine ligand atoms. In addition to this negative charge, the Dy-N bonds are significantly shorter than other Dy-L bonds, showing strong covalence and electrostatic effects. Overall, this results in greater crystal field splitting, with the microstates spanning 882.6 cm^{-1}, representing the theoretical height for which magnetic relaxation could occur, albeit assuming no/limited transverse effects.

In **4-Dy**, the orientation of the main magnetic axis is the result of the cumulative effects of the COT^{2-} and THF ligands. The COT^{2-} taken alone exerts an equatorial ligand field, stabilizing the states with $m_J = \pm 1/2$ components in the ground state; with respect to the axis connecting the Dy and the center of the COT^{2-} ring. Whereas the THF ligand, taken alone, brings an axial contribution along the Dy-O chemical bond. Since the Dy-O bond is almost perpendicular to the Dy-COT axis, the two effects are cumulative, and therefore set the anisotropy axis as depicted in Figure 3.9b. In both cases, **3-Dy** and **4-Dy**, the effect of the bridging chlorine ligands seems to induce neutral and/or destructive effects on the magnetic axiality; these ions contribute towards increasing the non-axial ligand field, i.e., ligand field contributions that are perpendicular to the main magnetic axis. Moreover, if the magnetic coupling between Ln^{III} ions is not sufficiently strong to warrant the presence of these bridging moieties it is best for the overall performance of the SMM to minimize metal-ligand interactions in this equatorial position.

To obtain an estimate of the extent of the exchange interaction between metals sites in the presented compounds, the broken-symmetry density-functional theory (BS-DFT) approach was used.[54–56] In this context, the BS-DFT calculation was performed using ORCA-3.0[57] code on the X-ray molecular structures of **3-Dy** and **4-Dy** using def2-SVP basis sets, B3LYP density functional, tight integration grids, and convergence thresholds. These BS-DFT calculations predicted that weak antiferromagnetic coupling exists between the Dy^{III} ions in **3-Dy** which is approximately ≈ -1.0 cm^{-1} in strength, and stronger antiferromagnetic coupling is predicted for **4-Dy**, that is approximately ≈ -10 cm^{-1}. This order of magnitude difference between the two complexes suggests that the decrease observed in the χ" susceptibility (Figure 3.5c) is a result of the stronger antiferromagnetic coupling in **4-Dy**.[51] The intramolecular Dy1---Dy1' distance is marginally smaller in **4-Dy** (4.135(1) Å) than the intramolecular distance in **3-Dy** (4.3419(5) Å), which may account for this difference in coupling strength. Nevertheless, the magnetic exchange interactions in both compounds are antiferromagnetic, and are not sufficiently strong compared to other previously investigated systems,[22] which further supports the focus on the ancillary ligands to achieve more efficient SMMs.

3.3 Summary and Conclusion

Overall, the analysis of the field and temperature dependent relaxation times for **3-Dy** and **4-Dy** effectively demonstrate that increased axial anisotropy leads to slower relaxation rates,[58] This is a highly attractive feature in the design of more efficient SMMs which magnetically relax through over barrier mechanisms. The analysis presented herein elicited effective energy barriers to magnetization reversal of U_{eff} = 517.8 K (359.9 cm^{-1}) for **3-Dy** and U_{eff} = 139.6 K (97.0 cm^{-1}) for **4-Dy**, corresponding to relaxation through the second excited state for both compounds. The absence of a tunnelling component in **3-Dy** is thus attributed to the presence of the amide ancillary ligands, and these findings support that amide ancillary ligands are more effective in harnessing uniaxial magnetic anisotropy in Ln-based SMMs over arene style ligands, especially in the Dy^{III} context. Moreover, the trimethylsilyl amide ligands produce a dominant ligand field, acting on the crystal field of the Dy^{III} ion more strongly than COT. This resulted in the splitting of the microstates to occur over 882.6 cm^{-1}, representing a 1.4x increase over the splitting for **4-Dy** (648.1 cm^{-1}).

It is interesting to note that while **4-Dy** is by no means a high-performing SMM, it is the most effective COT-containing Dy^{III}-based SMM (U_{eff} = 139.6 K) that has been characterized thus far on the basis of measured U_{eff} values (U_{eff} = 9-43 K).[15,16,59–62] **4-Dy** is the only Dy^{III}-based COT SMM where the Dy^{III} centre is also strongly influenced by a hard σ-donor through direct coordination (i.e., the THF ligands) in addition to aromatic π-ligands. These THF ligands are the main directors for magnetic anisotropy, and the COT plays a secondary role. Moreover, the predicted coupling between the Dy^{III} ions in **4-Dy** is an order of magnitude larger than **3-Dy**, albeit the coupling is antiferromagnetic in nature. This combined with the axiality of the molecule provides ample evidence for the reconsideration of COT and other bulky aromatic ligands in the design of Dy^{III}-based SMMs and warrants their continued investigation. Although, if the overall goal is to produce high-energy barrier magnets with promise of technological relevance, amido-based ligands may also prove useful owing to their strong electrostatic (and potentially covalent) interactions which yield greater magnetic axiality and crystal field splitting, and as a consequence more efficient relaxation dynamics.

3.4 Experimental Details

3.4.1 General Procedures

All operations were performed in a M. Braun glovebox under an atmosphere of purified dinitrogen or using high vacuum standard Schlenk techniques. Solvents were dried using a J.C. Meyer solvent system, degassed with successive freeze-pump-thaw cycles, and stored over activated 3Å molecular sieves for 48 h prior to use. Anhydrous $DyCl_3$ was purchased from Strem Chemicals and used as received, 1,3,5,7-cyclooctatetraene was purchased from Alfa Aesar and bubble degassed with argon prior to use. Tetrahydrofuran-*d*$_8$ and $CDCl_3$ were purchased from either Cambridge Isotope Laboratories or C/D/N Isotopes, degassed with successive freeze-pump-thaw cycles and dried over activated 3Å molecular sieves. Celite used for filtration was dried under vacuum while heating to 180 °C for 5 days. K_2COT was prepared according to literature procedure.[61] $[Dy^{III}\{N(SiMe_3)_2\}_2(\mu\text{-Cl})(THF)]_2$ (**3-Dy**) was previously reported,[25] however, modifications to the procedure are detailed below. $[Dy^{III}(\eta^8\text{-COT})(\mu\text{-Cl})(THF)]_2$ (**4-Dy**) was prepared with modifications to the synthesis of the reported Er^{III} analogue, $[Er^{III}(\eta^8\text{-COT})(\mu\text{-Cl})(THF)]_2$.[26] All NMR data reported were measured using a Bruker AVANCE II 300 MHz spectrometer at 298 K, and the ^1H NMR spectra were referenced to the residual solvent signal. Infrared spectra were recorded on a Nicolet Nexus 550 FT-IR spectrometer using transmission mode in the 4000-600 cm^{-1} range; solid samples were prepared under an inert atmosphere and sandwiched between transparent NaCl plates. Elemental analyses were conducted by Canadian Microanalytical, Delta, BC.

3.4.2 Experimental Procedures

Synthesis of $[Dy^{III}\{N(SiMe_3)_2\}_2(\mu\text{-Cl})(THF)]_2$ (3-Dy). The synthesis of **3-Dy** was adapted from the literature substituting $DyCl_3$ for $LnCl_3$ (Ln = Gd, Yb).[63] To a 20 mL scintillation vial, $DyCl_3$ (300 mg, 1.116 mmol) was added along with 5 mL of THF to form a slurry. $NaN(Si(CH_3)_3)_2$ (409 mg, 2.232 mmol) was added to a second vial and dissolved in 15 mL of THF. Both vials were cooled to -35 °C. At -35 °C, the $NaN(Si(CH_3)_3)_2$ solution was pipetted into the $DyCl_3$ slurry while stirring and the mixture was left to stir overnight gradually warming to room temperature. The THF was removed *in vacuo* and the solids were extracted into 15 mL toluene. After stirring for 1 h, the white precipitates were removed by centrifugation (30 min, 3360 rpm) and the toluene was removed from the supernatant *in vacuo*. 15 mL of pentanes was added to the solids, left to stir for 1 h, then the undissolved solids removed by centrifugation. From the supernatant, crystals were obtained at -35 °C as colourless, translucent needles. Yield = 62 %. IR (neat, cm^{-1}): 3775 (w), 3718 (w), 3633 (w), 3578 (m), 2272 (m), 3327 (w), 2947 (s, br), 2895 (s, br), 2702 (w), 2496 (w), 2468 (m), 2387(w), 2349 (m), 2280 (w), 2257 (w), 2219 (w), 2081 (m), 1996 (w), 1952 (w), 1908 (m), 1855 (m), 1722 (w), 1640 (m), 1565 (w), 1451 (s), 1370 (m), 1346 (m), 1334 (m), 1284 (s), 1239 (s), 1187 (m), 978 (s), 934 (s), 861 (m), 828 (s), 808 (s), 769 (m), 729 (w), 693 (w), 671 (m), 611 (s), 517 (w), 491 (m), 465 (m), 441 (m), 415 (m). ^{1}H NMR ($CDCl_3$, 298 K, δ/ppm): 3.20 (br, d, 16 H, *THF*-coordinated), 0.55 (d, 130 H, *THF*-free solvent), -102.90 (s, 72 H, N(Si(C*H3*)3)2). CHN analysis (found, calc.) for $C_{32}H_{88}N_4O_2Si_8Cl_2Dy_2$: C (31.25, 32.53); H (7.74, 7.51); N (4.95, 4.74).

Synthesis of [Dy^{III}(η^8-COT)(μ-Cl)(THF)]$_2$·(THF)$_x$ (4-Dy). Synthesis of **4-Dy** was modified from the previously reported procedure for the Er^{III} analog [Er^{III}(η^8-COT)(μ-Cl)(THF)]$_2$;[26] the only modification was the replacement of $ErCl_3$ with $DyCl_3$. A slurry of $DyCl_3$ (470 mg, 1.748 mmol) was prepared in a 50 mL round bottom flask with 10 mL of THF. To this, a solution of K_2COT (571 mg, 1.748 mmol) in 20 mL of THF was added dropwise over a 20 min period. Following complete addition, the reaction mixture stirred for 12 h at room temperature, followed by centrifugation (30 min, 3360 rpm). The supernatant was collected and the THF removed *via* reduced pressure. The solids were extracted into minimal THF with heat (100 ^{o}C) in a sealed 20 mL scintillation vial. Any remaining solids were removed by filtration over Celite. Yellow crystals were obtained by hexanes diffusion into the THF solution. Yield = 40 %. IR (neat, cm^{-1}): 2954 (m), 2921 (m), 2848 (m), 2726 (w), 2348(w), 2044 (w), 1888 (w), 1855 (w), 1743 (m), 1603 (m), 1555 (w), 1537 (w), 1463 (s), 1378 (s), 1365 (m), 1341 (w), 1312 (w), 1295 (w), 1261 (m), 1215 (m), 1185 (w), 1160 (w), 1130 (w), 1074 (s), 1021 (s), 973 (w), 884 (s), 808 (w), 762 (w), 749 (s), 702 (s), 435 (s, br). ^{1}H NMR (THF-d_8, 298 K, δ/ppm): 63.44 (br, s, 8 H, C8*H*8), 6.76 (d, 8 H, *THF*). CHN analysis (found, calc.) for $C_{24}H_{32}O_2Cl_2Dy_2{\cdot}OC_4H_8$: C (41.25, 40.99); H (5.89, 4.91); N (<0.3, 0.00); 1 eq. of THF was added in calculations to account for experimental results.

3.4.3 Crystallography

Data collection results for **4-Dy** represent the best data sets obtained in several trials. The crystals were mounted on thin glass fibers using paraffin oil and were cooled to 200 K prior to data collection. Data were collected on a Bruker AXS Smart single crystal diffractometer equipped with a sealed Mo tube source (λ = 0.71073 Å) and APEX II CCD detector. Raw data collection and processing were performed with APEX II software package from Bruker AXS. Data was collected using φ and ω scan collection strategies. Semi-empirical absorption corrections based on equivalent reflections were applied. Systematic absences in the diffraction data set and unit cell parameters were consistent with monoclinic **P**2_1/c (№14). Solutions in the centrosymmetric space group yielded chemically reasonable and computationally stable results of refinement. The structure was solved by direct methods, completed with difference Fourier synthesis, and refined with full matrix least-squares procedures based on F^2. All hydrogen atom positions were calculated based on the geometry of related non-hydrogen atoms. All hydrogen atoms were treated as idealized contributions during the refinement. All scattering factors are contained in several versions of the SHELXTL program library, with version v.7.14 being used.

Structural information has been previously reported for **3-Dy**,[25] as such unit cell measurements of single-crystals were obtained and found to match the previously reported sample. Details regarding the unit cell measurements obtained in this study are summarized in Table 3.6.

Table 3.5 Crystallographic data for **4-Dy**

Compound	**4-Dy**
Empirical formula	$C_{24}H_{32}Cl_2Dy_2O_2$
Formula weight	748.39
Crystal size, mm	0.463 x 0.240 x 0.170
Crystal system	Monoclinic
Space group	$\boldsymbol{P}\ 2_1/c$
Z	2
a, Å	9.4808(3)
b, Å	11.070(3)
c, Å	12.574(3)
α, °	90
β, °	110.647(5)
γ, °	90
Volume, Å^3	1225.3(6)
Calculated density, Mg/m^3	2.028
Absorption coefficient, mm^{-1}	6.287
T (K)	200(2)
F(000)	716
Θ range for data collection, °	2.313-31.371
Limiting indices	h=±13, k=±15, $-18 \leq l \leq 17$
Reflections collected / unique	28915/3823
R(int)	0.0323
Completeness to Θ = 28.32, %	99.9
Max. and min. transmission	0.7462 and 0.3458
Data / restraints / parameters	3823/0/136
Goodness-of-fit on F^2	1.102
Final R indices $[I>2\sigma(I)]$[a]	$R_1 = 0.0201$, $wR_2 = 0.0467$
R indices (all data)	$R_1 = 0.0218$, $wR_2 = 0.0473$
Largest diff. peak/hole, e·Å^{-3}	1.166 and -1.153

[a] $R = R_1 = \Sigma||F_0| - |F_c||/ \Sigma|F_0|$; $wR_2 = \{\Sigma[w (F_0^2 - F_c^2)^2/\Sigma[w(F_0)^2]]^{1/2}$; $w = 1/[\delta^2(F_o^2) + (ap)^2 + bp]$, where $p = [\max (F_0^2, 0) + 2F_c^2]/3$

Table 3.6 Comparison of crystallographic data for compound **3-Dy**

Compound	3-Dy (previous)	3-Dy (this work)
Empirical formula	$C_{32}H_{88}Dy_2N_4O_2Si_8Cl_2$	$C_{32}H_{88}Dy_2N_4O_2Si_8Cl_2$
Formula weight	1181.66	1181.66
Crystal system	Monoclinic	Monoclinic
Space group	$\boldsymbol{P}\,2_1/n$	$\boldsymbol{P}\,2_1/n$
a, Å	14.2365(15)	14.33
b, Å	12.9802(13)	13.03
c, Å	16.4682(19)	16.46
α, °	90	90
β, °	113.943(3)	113.77
γ, °	90	90
Volume, $Å^3$	2781	2817
T (K)	223	200

3.4.4 Magnetometry

The magnetic susceptibility measurements were obtained using a Quantum Design SQUID magnetometer MPMS-XL7 operating between 1.8 and 300 K. DC measurements were performed on polycrystalline samples of 20.0 mg for **3-Dy** and 9.2 mg **4-Dy**. The samples were restrained with silicon grease and wrapped in a polyethylene bag under an inert atmosphere, and subjected to a field of 0 to 7 T. The magnetization data were collected at 100 K to check for ferromagnetic impurities that were absent in both samples. Diamagnetic corrections were applied for the sample holder and the inherent diamagnetism of the sample was estimated with the use of Pascals constants.

3.4.5 Computational Details

All calculations were performed using MOLCAS-8.2 package[43] and employed SCXRD structural data. All calculations were of the CASSCF/RASSI/SINGLE_ANISO kind.[44] Active space for the CASSCF method included the $4f^n$ configuration only. The neighbouring paramagnetic Dy^{III} ion was replaced with a diamagnetic Lu^{III} ion, for which the 4f shell is fully occupied. All atoms were described with ANO-RCC basis sets VDZP and VTZP.[45] These include relativistic corrections of second-order Douglas-Kroll Hess theory.[46,47] All electronic states for $S = 5/2$, $3/2$, and $1/2$ arising from the $4f^9$ electronic configuration were computationally optimized and employed further in the spin-orbit coupling in RASSI.[48,49] The spin-orbit coupling matrix built within the RASSI calculation included all 735 spin states, giving rise to 2002 spin-orbit states. All the spin-orbit eigenstates were then used to compute the g-tensors on individual Dy^{III} sites.

3.5 References

(1) Gatteschi, D.; Sessoli, R.; Villain, J. *Molecular Nanomagnets*; Oxford University Press, 2006.

(2) Layfield, R. A.; Murugesu, M. *Lanthanides and Actinides in Molecular Magnetism*, 1st ed.; John Wiley & Sons, Ltd, 2015.

(3) Shrivastava, K. N. Theory of Spin–Lattice Relaxation. *Phys. Status Solidi B* **1983**, *117* (2), 437–458. https://doi.org/10.1002/pssb.2221170202.

(4) Ungur, L.; Chibotaru, L. F. Strategies Toward High-Temperature Lanthanide-Based Single-Molecule Magnets. *Inorg. Chem.* **2016**, *55* (20), 10043–10056. https://doi.org/10.1021/acs.inorgchem.6b01353.

(5) Wernsdorfer, W.; Aliaga-Alcalde, N.; Hendrickson, D. N.; Christou, G. Exchange-Biased Quantum Tunnelling in a Supramolecular Dimer of Single-Molecule Magnets. *Nature* **2002**, *416* (6879), 406–409. https://doi.org/10.1038/416406a.

(6) Han, T.; Ding, Y.-S.; Li, Z.-H.; Yu, K.-X.; Zhai, Y.-Q.; Chilton, N. F.; Zheng, Y.-Z. A Dichlorido-Bridged Dinuclear Dy(III) Single-Molecule Magnet with an Effective Energy Barrier Larger than 600 K. *Chem. Commun.* **2019**, *55* (55), 7930–7933. https://doi.org/10.1039/C9CC02436K.

(7) Han, T.; Giansiracusa, M. J.; Li, Z.; Ding, Y.; Chilton, N. F.; Winpenny, R. E. P.; Zheng, Y. Exchange-Biasing in a Dinuclear Dysprosium(III) Single-Molecule Magnet with a Large Energy Barrier for Magnetisation Reversal. *Chem. – Eur. J.* **2020**, *26* (30), 6773–6777. https://doi.org/10.1002/chem.202000719.

(8) Pineda, E. M.; Lan, Y.; Fuhr, O.; Wernsdorfer, W.; Ruben, M. Exchange-Bias Quantum Tunnelling in a CO_2-Based Dy_4-Single Molecule Magnet. *Chem. Sci.* **2017**, *8* (2), 1178–1185. https://doi.org/10.1039/C6SC03184F.

(9) Meng, Y.-S.; Xiong, J.; Yang, M.-W.; Qiao, Y.-S.; Zhong, Z.-Q.; Sun, H.-L.; Han, J.-B.; Liu, T.; Wang, B.-W.; Gao, S. Experimental Determination of Magnetic Anisotropy in Exchange-Bias Dysprosium Metallocene Single-Molecule Magnets. *Angew. Chem. Int. Ed.* **2020**, *59* (31), 13037–13043. https://doi.org/10.1002/anie.202004537.

(10) Pugh, T.; Tuna, F.; Ungur, L.; Collison, D.; McInnes, E. J. L.; Chibotaru, L. F.; Layfield, R. A. Influencing the Properties of Dysprosium Single-Molecule Magnets with Phosphorus Donor Ligands. *Nat. Commun.* **2015**, *6* (1), 7492. https://doi.org/10.1038/ncomms8492.

(11) Guo, Y.-N.; Xu, G.-F.; Wernsdorfer, W.; Ungur, L.; Guo, Y.; Tang, J.; Zhang, H.-J.; Chibotaru, L. F.; Powell, A. K. Strong Axiality and Ising Exchange Interaction Suppress Zero-Field Tunneling of Magnetization of an Asymmetric Dy_2 Single-Molecule Magnet. *J. Am. Chem. Soc.* **2011**, *133* (31), 11948–11951. https://doi.org/10.1021/ja205035g.

(12) Bhunia, A.; Gamer, M. T.; Ungur, L.; Chibotaru, L. F.; Powell, A. K.; Lan, Y.; Roesky, P. W.; Menges, F.; Riehn, C.; Niedner-Schatteburg, G. From a Dy(III) Single Molecule Magnet (SMM) to a

Ferromagnetic [Mn(II)Dy(III)Mn(II)] Trinuclear Complex. *Inorg. Chem.* **2012**, *51* (18), 9589–9597. https://doi.org/10.1021/ic300065x.

(13) Woodruff, D. N.; Winpenny, R. E. P.; Layfield, R. A. Lanthanide Single-Molecule Magnets. *Chem. Rev.* **2013**, *113* (7), 5110–5148. https://doi.org/10.1021/cr400018q.

(14) Mironov, V. S. Superexchange Interaction between Lanthanide Ions. Spin-Hamiltonian Calculations for the and Superexchange. *J. Phys. Condens. Matter* **1996**, *8* (49), 10551–10580. https://doi.org/10.1088/0953-8984/8/49/042.

(15) Ungur, L.; Le Roy, J. J.; Korobkov, I.; Murugesu, M.; Chibotaru, L. F. Fine-Tuning the Local Symmetry to Attain Record Blocking Temperature and Magnetic Remanence in a Single-Ion Magnet. *Angew. Chem. Int. Ed.* **2014**, *53* (17), 4413–4417. https://doi.org/10.1002/anie.201310451.

(16) Le Roy, J. J.; Jeletic, M.; Gorelsky, S. I.; Korobkov, I.; Ungur, L.; Chibotaru, L. F.; Murugesu, M. An Organometallic Building Block Approach to Produce a Multidecker 4f Single-Molecule Magnet. *J. Am. Chem. Soc.* **2013**, *135* (9), 3502–3510. https://doi.org/10.1021/ja310642h.

(17) Liu, J.-L.; Chen, Y.-C.; Tong, M.-L. Symmetry Strategies for High Performance Lanthanide-Based Single-Molecule Magnets. *Chem. Soc. Rev.* **2018**, *47* (7), 2431–2453. https://doi.org/10.1039/C7CS00266A.

(18) Ungur, L.; Chibotaru, L. F. Magnetic Anisotropy in the Excited States of Low Symmetry Lanthanide Complexes. *Phys. Chem. Chem. Phys.* **2011**, *13* (45), 20086. https://doi.org/10.1039/c1cp22689d.

(19) Zhang, P.; Jung, J.; Zhang, L.; Tang, J.; Le Guennic, B. Elucidating the Magnetic Anisotropy and Relaxation Dynamics of Low-Coordinate Lanthanide Compounds. *Inorg. Chem.* **2016**, *55* (4), 1905–1911. https://doi.org/10.1021/acs.inorgchem.5b02792.

(20) Hilgar, J. D.; Bernbeck, M. G.; Flores, B. S.; Rinehart, J. D. Metal–Ligand Pair Anisotropy in a Series of Mononuclear Er–COT Complexes. *Chem. Sci.* **2018**, *9* (36), 7204–7209. https://doi.org/10.1039/C8SC01361F.

(21) Norel, L.; Darago, L. E.; Le Guennic, B.; Chakarawet, K.; Gonzalez, M. I.; Olshansky, J. H.; Rigaut, S.; Long, J. R. A Terminal Fluoride Ligand Generates Axial Magnetic Anisotropy in Dysprosium Complexes. *Angew. Chem. Int. Ed.* **2018**, *57* (7), 1933–1938. https://doi.org/10.1002/anie.201712139.

(22) Habib, F.; Murugesu, M. Lessons Learned from Dinuclear Lanthanide Nano-Magnets. *Chem. Soc. Rev.* **2013**, *42* (8), 3278. https://doi.org/10.1039/c2cs35361j.

(23) Rinehart, J. D.; Long, J. R. Exploiting Single-Ion Anisotropy in the Design of f-Element Single-Molecule Magnets. *Chem. Sci.* **2011**, *2* (11), 2078. https://doi.org/10.1039/c1sc00513h.

(24) Chilton, N. F. Design Criteria for High-Temperature Single-Molecule Magnets. *Inorg. Chem.* **2015**, *54* (5), 2097–2099. https://doi.org/10.1021/acs.inorgchem.5b00089.

(25) Zhou, F.; Zhang, S.; Zhao, Y.; Zhang, C.; Cheng, X.; Zheng, L.; Zhang, Y.; Li, Y. Dinuclear Dysprosium and Ytterbium Complexes Incorporating N,N-Bis(Pyrrolyl-α-Methyl)-N-Methylamine Ligand: Syntheses and Structures. *Z. Für Anorg. Allg. Chem.* **2009**, *635* (15), 2636–2641. https://doi.org/10.1002/zaac.200900256.

(26) Hilgar, J. D.; Flores, B. S.; Rinehart, J. D. Ferromagnetic Coupling in a Chloride-Bridged Erbium Single-Molecule Magnet. *Chem. Commun.* **2017**, *53* (53), 7322–7324. https://doi.org/10.1039/C7CC02356A.

(27) Harriman, K. L. M.; Brosmer, J. L.; Ungur, L.; Diaconescu, P. L.; Murugesu, M. Pursuit of Record Breaking Energy Barriers: A Study of Magnetic Axiality in Diamide Ligated Dy^{III} Single-Molecule Magnets. *J. Am. Chem. Soc.* **2017**, *139* (4), 1420–1423. https://doi.org/10.1021/jacs.6b12374.

(28) Briganti, M.; Garcia, G. F.; Jung, J.; Sessoli, R.; Le Guennic, B.; Totti, F. Covalency and Magnetic Anisotropy in Lanthanide Single Molecule Magnets: The DyDOTA Archetype. *Chem. Sci.* **2019**, *10* (30), 7233–7245. https://doi.org/10.1039/C9SC01743G.

(29) Ungur, L.; Chibotaru, L. F. Ab Initio Crystal Field for Lanthanides. *Chem.-Eur. J.* **2017**, *23* (15), 3708–3718. https://doi.org/10.1002/chem.201605102.

(30) Wernsdorfer, W.; Bhaduri, S.; Boskovic, C.; Christou, G.; Hendrickson, D. N. Spin-Parity Dependent Tunneling of Magnetization in Single-Molecule Magnets. *Phys. Rev. B* **2002**, *65* (18), 180403. https://doi.org/10.1103/PhysRevB.65.180403.

(31) Sørensen, M. A.; Hansen, U. B.; Perfetti, M.; Pedersen, K. S.; Bartolomé, E.; Simeoni, G. G.; Mutka, H.; Rols, S.; Jeong, M.; Zivkovic, I.; Retuerto, M.; Arauzo, A.; Bartolomé, J.; Piligkos, S.; Weihe, H.; Doerrer, L. H.; van Slageren, J.; Rønnow, H. M.; Lefmann, K.; Bendix, J. Chemical Tunnel-Splitting-Engineering in a Dysprosium-Based Molecular Nanomagnet. *Nat. Commun.* **2018**, *9* (1), 1292. https://doi.org/10.1038/s41467-018-03706-x.

(32) Pinkowicz, D.; Southerland, H. I.; Avendaño, C.; Prosvirin, A.; Sanders, C.; Wernsdorfer, W.; Pedersen, K. S.; Dreiser, J.; Clérac, R.; Nehrkorn, J.; Simeoni, G. G.; Schnegg, A.; Holldack, K.; Dunbar, K. R. Cyanide Single-Molecule Magnets Exhibiting Solvent Dependent Reversible "On" and "Off" Exchange Bias Behavior. *J. Am. Chem. Soc.* **2015**, *137* (45), 14406–14422. https://doi.org/10.1021/jacs.5b09378.

(33) Aubin, S. M. J.; Sun, Z.; Pardi, L.; Krzystek, J.; Folting, K.; Brunel, L.-C.; Rheingold, A. L.; Christou, G.; Hendrickson, D. N. Reduced Anionic Mn_{12} Molecules with Half-Integer Ground States as Single-Molecule Magnets. *Inorg. Chem.* **1999**, *38* (23), 5329–5340. https://doi.org/10.1021/ic990613g.

(34) Orbach, R. Spin-Lattice Relaxation in Rare-Earth Salts. *Proc. R. Soc. Lon. Ser-A.* **1961**, *264* (1319), 458-484.

(35) Rechkemmer, Y.; Breitgoff, F. D.; van der Meer, M.; Atanasov, M.; Hakl, M.; Orlita, M.; Neugebauer, P.; Neese, F.; Sarkar, B.; van Slageren, J. A Four-Coordinate Cobalt(II) Single-Ion Magnet with Coercivity and a Very High Energy Barrier. *Nat. Commun.* **2016**, *7* (1), 10467. https://doi.org/10.1038/ncomms10467.

(36) Chakarawet, K.; Bunting, P. C.; Long, J. R. Large Anisotropy Barrier in a Tetranuclear Single-Molecule Magnet Featuring Low-Coordinate Cobalt Centers. *J. Am. Chem. Soc.* **2018**, *140* (6), 2058–2061. https://doi.org/10.1021/jacs.7b13394.

(37) Yao, X.-N.; Du, J.-Z.; Zhang, Y.-Q.; Leng, X.-B.; Yang, M.-W.; Jiang, S.-D.; Wang, Z.-X.; Ouyang, Z.-W.; Deng, L.; Wang, B.-W.; Gao, S. Two-Coordinate Co(II) Imido Complexes as Outstanding Single-Molecule Magnets. *J. Am. Chem. Soc.* **2017**, *139* (1), 373–380. https://doi.org/10.1021/jacs.6b11043.

(38) Wada, H.; Ooka, S.; Iwasawa, D.; Hasegawa, M.; Kajiwara, T. Slow Magnetic Relaxation of Lanthanide(III) Complexes with a Helical Ligand. *Magnetochemistry* **2016**, *2* (4), 43. https://doi.org/10.3390/magnetochemistry2040043.

(39) Dickie, C. M.; Laughlin, A. L.; Wofford, J. D.; Bhuvanesh, N. S.; Nippe, M. Transition Metal Redox Switches for Reversible “on/off” and “Slow/Fast” Single-Molecule Magnet Behaviour in Dysprosium and Erbium Bis-Diamidoferrocene Complexes. *Chem. Sci.* **2017**, *8* (12), 8039–8049. https://doi.org/10.1039/C7SC03380J.

(40) Novikov, V. V.; Pavlov, A. A.; Nelyubina, Y. V.; Boulon, M.-E.; Varzatskii, O. A.; Voloshin, Y. Z.; Winpenny, R. E. P. A Trigonal Prismatic Mononuclear Cobalt(II) Complex Showing Single-Molecule Magnet Behavior. *J. Am. Chem. Soc.* **2015**, *137* (31), 9792–9795. https://doi.org/10.1021/jacs.5b05739.

(41) Ding, Y.-S.; Yu, K.-X.; Reta, D.; Ortu, F.; Winpenny, R. E. P.; Zheng, Y.-Z.; Chilton, N. F. Field- and Temperature-Dependent Quantum Tunnelling of the Magnetisation in a Large Barrier Single-Molecule Magnet. *Nat. Commun.* **2018**, *9* (1), 3134. https://doi.org/10.1038/s41467-018-05587-6.

(42) Moreno-Pineda, E.; Taran, G.; Wernsdorfer, W.; Ruben, M. Quantum Tunnelling of the Magnetisation in Single-Molecule Magnet Isotopologue Dimers. *Chem. Sci.* **2019**, *10*, 5138-5145. https://doi.org/10.1039/C9SC01062A.

(43) Aquilante, F.; Autschbach, J.; Carlson, R. K.; Chibotaru, L. F.; Delcey, M. G.; Vico, L. D.; Galván, I. F.; Ferré, N.; Frutos, L. M.; Gagliardi, L.; Garavelli, M.; Giussani, A.; Hoyer, C. E.; Manni, G. L.; Lischka, H.; Ma, D.; Malmqvist, P. Å.; Müller, T.; Nenov, A.; Olivucci, M.; Pedersen, T. B.; Peng, D.; Plasser, F.; Pritchard, B.; Reiher, M.; Rivalta, I.; Schapiro, I.; Segarra-Martí, J.; Stenrup, M.; Truhlar, D. G.; Ungur, L.; Valentini, A.; Vancoillie, S.; Veryazov, V.; Vysotskiy, V. P.; Weingart, O.; Zapata, F.; Lindh, R. Molcas 8: New Capabilities for Multiconfigurational Quantum Chemical

Calculations across the Periodic Table. *J. Comput. Chem.* **2016**, *37* (5), 506–541. https://doi.org/10.1002/jcc.24221.

(44) Chibotaru, L. F.; Ungur, L. *Ab Initio* Calculation of Anisotropic Magnetic Properties of Complexes. I. Unique Definition of Pseudospin Hamiltonians and Their Derivation. *J. Chem. Phys.* **2012**, *137* (6), 064112. https://doi.org/10.1063/1.4739763.

(45) Roos, B. O.; Lindh, R.; Malmqvist, P.-Å.; Veryazov, V.; Widmark, P.-O.; Borin, A. C. New Relativistic Atomic Natural Orbital Basis Sets for Lanthanide Atoms with Applications to the Ce Diatom and LuF $_3$. *J. Phys. Chem. A* **2008**, *112* (45), 11431–11435. https://doi.org/10.1021/jp803213j.

(46) Douglas, M.; Kroll, N. M. Quantum Electrodynamical Corrections to the Fine Structure of Helium. *Ann. Phys.* **1974**, *82* (1), 89–155. https://doi.org/10.1016/0003-4916(74)90333-9.

(47) Reiher, M. Relativistic Douglas–Kroll–Hess Theory. *WIREs Comput. Mol. Sci.* **2012**, *2* (1), 139–149. https://doi.org/10.1002/wcms.67.

(48) Malmqvist, P. Å.; Roos, B. O.; Schimmelpfennig, B. The Restricted Active Space (RAS) State Interaction Approach with Spin–Orbit Coupling. *Chem. Phys. Lett.* **2002**, *357* (3–4), 230–240. https://doi.org/10.1016/S0009-2614(02)00498-0.

(49) Malmqvist, P.-Å.; Roos, B. O. The CASSCF State Interaction Method. *Chem. Phys. Lett.* **1989**, *155* (2), 189–194. https://doi.org/10.1016/0009-2614(89)85347-3.

(50) Rinehart, J. D.; Fang, M.; Evans, W. J.; Long, J. R. A N_2^{3-} Radical-Bridged Terbium Complex Exhibiting Magnetic Hysteresis at 14 K. *J. Am. Chem. Soc.* **2011**, *133* (36), 14236–14239. https://doi.org/10.1021/ja206286h.

(51) Rinehart, J. D.; Fang, M.; Evans, W. J.; Long, J. R. Strong Exchange and Magnetic Blocking in N_2^{3-}-Radical-Bridged Lanthanide Complexes. *Nat. Chem.* **2011**, *3* (7), 538–542. https://doi.org/10.1038/nchem.1063.

(52) Huang, W.; Le Roy, J. J.; Khan, S. I.; Ungur, L.; Murugesu, M.; Diaconescu, P. L. Tetraanionic Biphenyl Lanthanide Complexes as Single-Molecule Magnets. *Inorg. Chem.* **2015**, *54* (5), 2374–2382. https://doi.org/10.1021/ic5029788.

(53) Gagliardi, L.; Lindh, R.; Karlström, G. Local Properties of Quantum Chemical Systems: The LoProp Approach. *J. Chem. Phys.* **2004**, *121* (10), 4494–4500. https://doi.org/10.1063/1.1778131.

(54) Gatteschi, D.; Yamaguchi, K. Opportunities for New Physics in Molecular Magnetism. In *Molecular Magnetism: From Molecular Assemblies to the Devices*; Coronado, E., Delhaès, P., Gatteschi, D., Miller, J. S., Eds.; Springer Netherlands: Dordrecht, 1996; pp 561–570. https://doi.org/10.1007/978-94-017-2319-0_22.

(55) Noodleman, Louis.; Case, D. A.; Aizman, Arie. Broken Symmetry Analysis of Spin Coupling in Iron-Sulfur Clusters. *J. Am. Chem. Soc.* **1988**, *110* (4), 1001–1005. https://doi.org/10.1021/ja00212a003.

(56) Shoji, M.; Koizumi, K.; Kitagawa, Y.; Kawakami, T.; Yamanaka, S.; Okumura, M.; Yamaguchi, K. A General Algorithm for Calculation of Heisenberg Exchange Integrals J in Multispin Systems. *Chem. Phys. Lett.* **2006**, *432* (1–3), 343–347. https://doi.org/10.1016/j.cplett.2006.10.023.

(57) Neese, F. The ORCA Program System. *WIREs Comput. Mol. Sci.* **2012**, *2* (1), 73–78. https://doi.org/10.1002/wcms.81.

(58) Ho, L. T. A.; Chibotaru, L. F. Spin-Lattice Relaxation of Magnetic Centers in Molecular Crystals at Low Temperature. *Phys. Rev. B* **2018**, *97* (2), 024427. https://doi.org/10.1103/PhysRevB.97.024427.

(59) Jiang, S.-D.; Liu, S.-S.; Zhou, L.-N.; Wang, B.-W.; Wang, Z.-M.; Gao, S. Series of Lanthanide Organometallic Single-Ion Magnets. *Inorg. Chem.* **2012**, *51* (5), 3079–3087. https://doi.org/10.1021/ic202511n.

(60) Jeletic, M.; Lin, P.-H.; Le Roy, J. J.; Korobkov, I.; Gorelsky, S. I.; Murugesu, M. An Organometallic Sandwich Lanthanide Single-Ion Magnet with an Unusual Multiple Relaxation Mechanism. *J. Am. Chem. Soc.* **2011**, *133* (48), 19286–19289. https://doi.org/10.1021/ja207891y.

(61) Meihaus, K. R.; Long, J. R. Magnetic Blocking at 10 K and a Dipolar-Mediated Avalanche in Salts of the Bis(η^8-Cyclooctatetraenide) Complex [Er(COT)$_2$]$^-$. *J. Am. Chem. Soc.* **2013**, *135* (47), 17952–17957. https://doi.org/10.1021/ja4094814.

(62) Meng, Y.-S.; Wang, C.-H.; Zhang, Y.-Q.; Leng, X.-B.; Wang, B.-W.; Chen, Y.-F.; Gao, S. (Boratabenzene)(Cyclooctatetraenyl) Lanthanide Complexes: A New Type of Organometallic Single-Ion Magnet. *Inorg. Chem. Front.* **2016**, *3* (6), 828–835. https://doi.org/10.1039/C6QI00028B.

(63) Aspinall, H. C.; Bradley, D. C.; Hursthouse, M. B.; Sales, K. D.; Walker, N. P. C.; Hussain, B. Preparation of the Bis(Trimethylsi1yl)Amido Lanthanide Chlorides [{Ln[N(SiMe,)$_2$]$_2$(μ-Cl)(thf)}$_2$] (thf = Tetrahydrofuran), and the Crystal and Molecular Structures of the Gadolinium and Ytterbium Complexes. *J Chem Soc Dalton Trans* **1989**, 4.

Chapter 4

Utilizing Amides to Elicit Magnetic Relaxation within Organometallic Bridged Complexes

4.1 Introduction

The use of η-cyclopentadienyl (η^5-C_5R_5), η-arene (η^6-C_6R_6) and η-cyclooctatetraenyl (η^8-C_8R_8) ligands in the synthesis of organolanthanide complexes is widespread. These complexes are extensively studied for their unique physical properties arising from their core 4f orbitals. While the cycloheptatrienyl trianion was first spectroscopically characterized by Bates *et al* in 1977;[1] only a single example of a η^7-C_7R_7 lanthanide complex is known.[2] There are only four reported examples of the isolation of f-element compounds with η-cycloheptatrienyl,[2–4] and only two of those reports describe their use in dinuclear systems.[2,4] The limited exploration of such species resides in the difficulty of synthetic preparation and isolation of the elusive 10 π-electron seven-membered ring with f-elements (Figure 4.1).

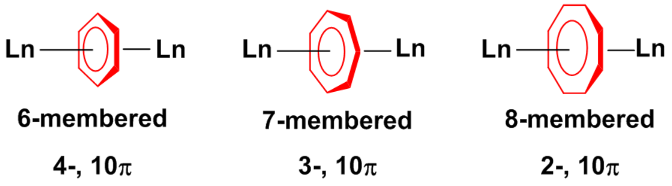

Figure 4.1 Ln^{III} ions bridged by 6-, 7- and 8-membered rings.

The amplified interest in the isolation of dinuclear lanthanide complexes with different bridging motifs arises from the ability to probe magnetic communication between metal ions, as they represent the most fundamental unit with which to study magnetic exchange interactions. Some of these reported molecules exhibit slow relaxation of the magnetization below their blocking temperature; these molecules are termed single-molecule magnets (SMMs).[5–11] Since the discovery of the first organometallic SMMs in 2010,[12] several complexes were reported to exhibit this nanomagnetic behavior.[13–17] Most of the described examples are mononuclear compounds; however, the study of dinuclear systems is of the utmost importance when we consider the technological prerequisites of the future, which, in regards to SMMs, include increasing the total spin of molecular magnets through expanding the number of paramagnetic centres. While many different bridging systems exist,[14,18,19] few examples have demonstrated the importance of planar aromatic organometallic ligands towards garnering favourable magnetic interactions.[20–22] These systems are an appealing design strategy as they may be employed as building blocks to generate higher nuclearity compounds, while they are more notably effective in harnessing the inherent magnetic anisotropy of 4f and 5f ions.[13,15–17,23,24] Previous reports from the Murugesu group with cyclooctatetraenyl-[20,21] and arene-[22] bridged systems show that a weak, yet non-negligible, interaction can be observed with coupling constants between Gd^{III} ions of -0.644 cm^{-1} and -0.488 cm^{-1}, utilizing the isotropic spin Hamiltonian ($H = -JS_a \bullet S_b$, $S_a = S_b = 7/2$) for each system respectively.

Herein, the role of the 7-membered, cycloheptatrienyl, ring in the magnetic exchange between lanthanide ions is examined and compared with its counterparts, η^6-C_6R_6 and η^8-C_8R_8. In this study we investigated how subtle structural differences in a family of rare inverse sandwich compounds influence the overall magnetic properties and clearly demonstrate the significance of η^7-C_7R_7 on the bridging interactions and magnetic axiality. The synthesis and characterization of the first structurally reported Gd^{III}, Dy^{III}, and Er^{III} compounds of the cycloheptatrienyl trianion are described. The static and dynamic magnetic properties of three isostructural dinuclear complexes, $[KLn^{III}_2(\eta^7\text{-}C_7H_7)\{N(SiMe_3)_2\}_4]$ (Ln= Gd^{III} (**5-Gd**), Dy^{III} (**5-Dy**), Er^{III} (**5-Er**)) and one structurally analogous complex, $[K(THF)_2Er^{III}_2(\eta^7\text{-}C_7H_7)\{N(SiMe_3)_2\}_4]$ (**6-Er**) are presented.

4.2 Results and Discussion

4.2.1 Synthesis and Structure

Since the first report of the synthesis of a uranium cycloheptatrienyl sandwich complex in 1995,[3] there has been limited exploration into the isolation of other f-element complexes containing cycloheptatrienyl. However, other areas of chemistry, such as organic chemistry have made use of the 6 π-electron cycloheptatrienyl cation (the tropylium ion),[25] and there have been reports of the 10 π-electron derivative in transition metal chemistry.[26] Thus, the preparation of the above mentioned complexes, was carefully designed to result in the facile formation of the trianion through employing chemistry that was previously known for lanthanide ions. In particular, this chemistry involved the polarization of C-H bonds,[27] and was further complimented by highly basic and sterically demanding ancillary ligands.

Inspired by the work of Arliguie *et al*,[4] who had utilized borohydride chemistry towards the isolation of a f-element η^7-C_7H_7 complex, in our initial synthetic attempts towards the desired late lanthanide derivatives, lanthanide borohydrides were utilized to support the inverse sandwich architecture. However, due to the highly reactive/reducing nature of the borohydrides and the non-innocent character of the cycloheptadienide ligand, isolation of such systems proved to be difficult. In order to combat the aforementioned issue, we employed *bis*(trimethylsilyl) amido ancillary ligands and have since prepared a series of dinuclear complexes of Ln = Dy^{III}, Gd^{III}, Er^{III} (Figure 4.2). Synthesis of $Ln^{III}\{N(SiMe_3)_2\}_3$ was first reported by Bradley *et al*,[28,29] and has since been revisited in order to investigate the SMM properties of the complexes, arising from their distinctive crystal field.[30] Conversely, the seven-membered bridging motif may be prepared from the commercially available 1,4-cycloheptadiene, whereupon a one-electron reduction with potassium metal in the presence of Et_3N, cycloheptadienide ($C_7H_9^-$) (Figure 4.2) is afforded. The salt, KC_7H_9, remains stable for several days under inert conditions at -35 °C.

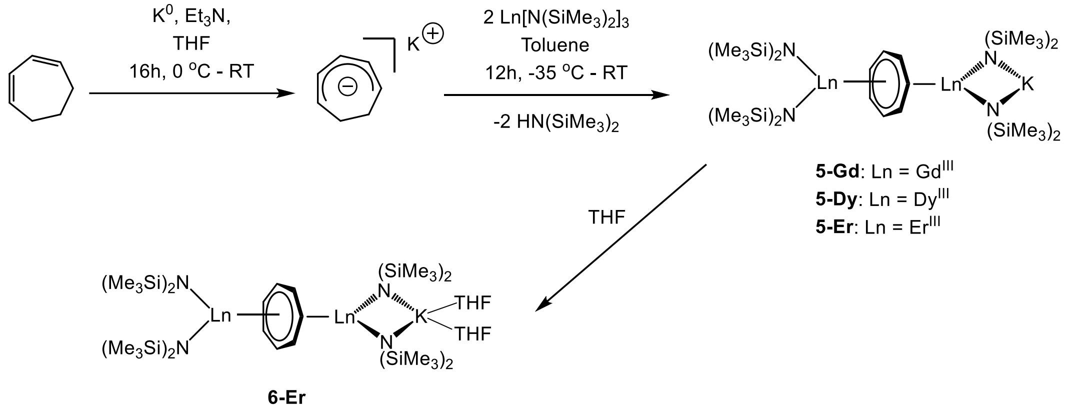

Figure 4.2 Synthesis of **5-Ln** (Ln = Gd^{III}, Dy^{III}, Er^{III}) and **6-Er**.

Solutions of lanthanide *tris*(*bis*(trimethylsilyl) amido) and potassium cycloheptadienide are combined at -35 °C in toluene and warmed to room temperature gradually. Further reduction of the cycloheptadienide to the aromatic trianion, cycloheptatrienyl, is supported by a mechanism previously reported by Miller and Dekock.[27] Initial coordination of the Ln^{III} ion results in polarization of the methylene C-H bond and subsequent proton abstraction by a strong base. Interestingly, it was first postulated that the highly basic nature of the $C_7H_9^-$ may be responsible for this abstraction, resulting in the formation of 1,4- and 1,3- isomers of cycloheptadiene. However, in this case, the loss of an amido ligand from each of the bridging Ln^{III} ions may suggest that the abstraction occurs *via* the amido, thus inducing the generation of soluble $HN(SiMe_3)_2$ species. The presence of such species was confirmed in the crude ^1H NMR of compound **5-Er** as a singlet at 0.1 ppm in toluene-d_8 at 298 K.

Nevertheless, collection of the filtrate followed by treatment with toluene and hexanes yields compounds **5-Ln**. Conversely, the solvated derivative, compound **6-Er**, can be obtained from **5-Er** *via* extraction into THF (Figure 4.3), resulting in the coordination of two molecules of THF to the bound potassium ion, and thereby limiting intermolecular interactions. X-ray quality crystals of **6-Er** were isolated from the subsequent treatment with a toluene/hexanes mixture, confirming the nature of the solvated species.

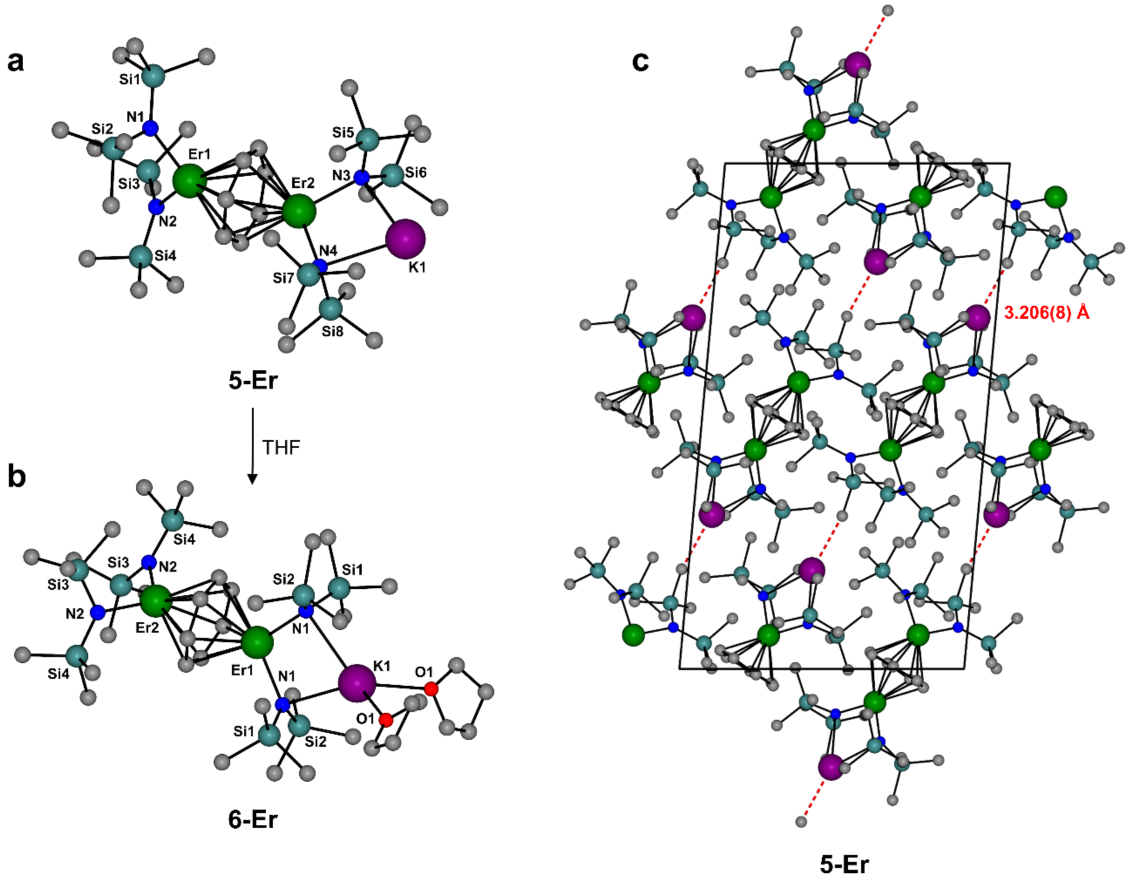

Figure 4.3 Molecular structures of (a) $[KEr^{III}_2(\eta^7\text{-}C_7H_7)\{N(SiMe_3)_2\}_4]$ **5-Er** and (b) $[K(THF)_2Er^{III}_2(\eta^7\text{-}C_7H_7)\{N(SiMe_3)_2\}_4]$ **6-Er**. (c) View along the *b*-axis of the unit cell in **5-Er**. Intermolecular K---C short contacts are shown as red dashed lines. Colour code: green (Er), purple (K), teal (Si), blue (N), red (O), grey (C). Hydrogen atoms and disorder have been omitted for clarity.

Single-crystal X-ray diffraction (SCXRD) studies revealed that compounds **5-Gd**, **5-Dy**, and **5-Er** are isostructural and crystallize in the monoclinic space group $P2_1/n$, whereas the analogous compound, **6-Er**, crystallizes in the monoclinic space group $C2/c$. The structure of the Er^{III} analogue, **5-Er**, will be the representative structure described herein (Figure 4.3a), and the structural details of **6-Er** will be discussed for comparison (Figure 4.3b). The molecular structure of **5-Er** revealed an inverse cycloheptatrienyl sandwich complex. The dinuclear compound is composed of two Er^{III} ions bridged by the 10 π-electron cycloheptatrienyl $C_7H_7^{3-}$ trianion in a η^7-bound fashion, with an Er-C bond distance range of 2.484(8)-2.629(9) Å (Table 4.1). The remaining coordination environment is occupied by two $[N(SiMe_3)_2]^-$ ligands. Interestingly, one K ion is bound to one side of the molecule *via* N atoms (N3, N4) of the $[N(SiMe_3)_2]^-$ ligands, thus making this dinuclear unit unsymmetrical. Due to this binding configuration, the N3-Er2-N4 angle of 98.6(2)° is much smaller than the N1-Er1-N2 angle of 105.7(2)°. It is noteworthy that in the case of **6-Er,** due to crystal packing effects the symmetry of the molecule is slightly higher than in **5-Er**. Other notable differences include two bound THF solvent molecules, which complete the coordination sphere of the K ion.

Table 4.1 Selected distances and angles from single crystal X-ray diffraction studies

	5-Gd	**5-Dy**	**5-Er**	**6-Er**
Ln-N (Å)	2.32 Å	2.28 Å	2.26 Å	
	2.33 Å	2.29 Å	2.27 Å	2.26 Å
	2.38 Å	2.35 Å	2.32 Å	2.32 Å
	2.39 Å	2.35 Å	2.33 Å	
Ln-C (Å)	2.54-2.68 Å	2.51-2.65 Å	2.48-2.63 Å	2.49-2.68 Å
K-N (Å)	2.93 Å	2.92 Å	2.93 Å	3.05 Å
	2.96 Å	2.95 Å	2.95 Å	
K-O_{THF} (Å)	-	-	-	2.68 Å
N-Ln-N (°)	97.8°	98.3°	98.6°	102.1°
	106.2°	106.3°	105.7°	111.0°
Ln---Ln (Å)	4.09 Å	4.02 Å	3.96 Å	3.97 Å

Close inspection of the packing arrangement of **5-Er** reveals a close contact between the K ion and a carbon atom (C14) from the $[\text{N}(\text{SiMe}_3)_2]^-$ (3.206(8) Å), which subsequently promotes a linear chain-like arrangement of the molecules (Figure 4.3c). Interestingly, in the case of compound **6-Er** a head-to-tail packing arrangement is still observed, generating a chain-like array, however, there are no close contacts that exist beyond H-H interactions.[31] In regards to compound **5-Er**, the intramolecular Er^{III}---Er^{III} distance of 3.9580(7) Å is slightly shorter than the distance observed in a COT” (1,4-*bis*(trimethylsilyl)cyclooctatetraenyl dianion) bridged Er_2 dimer (4.1109(5) Å) or arene bridged Er_2 compound (4.067(1) Å).[21,22] A similar Sm_2 inverse sandwich analogue was reported with a bridging COT and terminal $[\text{N}(\text{SiMe}_3)_2]^-$ ligands with a Sm^{III}---Sm^{III} distance of 4.308(1) Å.[32] However, the larger distance in the case of the Sm^{III} example is primarily due to the larger ionic radii of the Sm^{III} ion. Finally, it is noteworthy that the Nd^{III} analogue of the reported example exhibits a Nd^{III}---Nd^{III} distance of 4.213(3) Å, this is presumably a result of the electron rich borohydride ancillary ligands, which allow for increased electron donation to the electropositive Nd^{III} ions.[2]

The central cycloheptatrienyl ligand adopts a planar geometry, owing to its 10π-electron aromatic configuration, with the largest atom deviation being 0.06 Å out of the plane formed by the seven C atoms. The high charge (-3), planarity of the bridging ligand, along with the close proximity of Er^{III} ions, is expected to lead to non-negligible magnetic interactions *via* the delocalized π-orbitals of the cycloheptatrienyl ligand. Therefore, this molecule represents an ideal candidate to probe the exchange interactions between metal ions, while also studying the ligand field effects of the bridging unit in comparison with its COT and arene counterparts.

4.2.2 Direct Current Magnetic Susceptibility

Direct current (dc) magnetic susceptibility measurements were performed using a SQUID magnetometer on crushed crystalline samples of complexes **5-Ln** and **6-Er**, prepared under an inert atmosphere. Variable temperature magnetic susceptibility measurements under a 0.1 T applied field in the temperature range 1.9-300 K are shown in Figure 4.4. At room temperature, the χT values of complexes **5-Gd**, **5-Dy**, **5-Er**, and **6-Er** are 15.37, 28.34, 22.54 and 22.49 cm^3Kmol^{-1}, respectively. These values are in good agreement with the expected theoretical values of 15.76 (Gd^{III}: $^8S_{7/2}$, $S = 7/2$, $L = 0$, $g_J = 2$), 28.34 (Dy^{III}: $^6H_{15/2}$, $S = 5/2$, $L = 5$, $g_J = 4/3$) and 22.49 cm^3Kmol^{-1} (Er^{III}: $^4I_{15/2}$, $S = 3/2$, $L = 6$, $g_J = 6/5$) for two non-interacting lanthanide ions. For **5-Gd**, the χT product remains constant down to 50 K, followed by a gradual decrease with temperature to reach a minimum value of 5.84 cm^3Kmol^{-1} at 1.9 K. This downturn of the χT product can be attributed to the intramolecular antiferromagnetic interactions between the spin carriers (4.0869(7) Å).

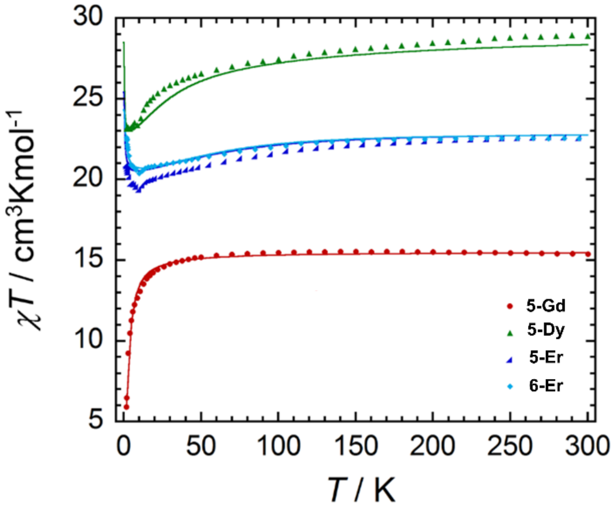

Figure 4.4 Temperature dependence of the χT product at 0.1 T for compound **5-Gd** (●), **5-Dy** (▲), **5-Er** (◢), and **6-Er** (◆), with χ being the molar magnetic susceptibility per molecule defined as *M/H*. Solid line for **5-Gd** represents the fit as determined from the application of the 2*J* formalism. Solid lines for **5-Dy**, **5-Er**, and **6-Er** correspond to *ab initio* calculated magnetic susceptibilities, using the method described in the text. The calculated susceptibility for **5-Dy** has been scaled by +2.5%.

Owing to the isotropic nature of Gd^{III} ions, the strength of interactions between the two lanthanide ions can be quantified. Application of the Van Vleck equation to the Kambe's vector coupling method was completed by using the isotropic spin Hamiltonian (Equation 4.1), with $S_a = S_b = 7/2$, which was used to fit the variation of χT *vs.* T. The best-fit yielded a J value of -0.134 cm^{-1} for compound **5-Gd**. The obtained J value is rather weak as a consequence of the shielded 4f-orbitals of Gd^{III} having minimal orbital overlap with the bridging ligand.

$$\mathcal{H} = -2J \sum_{\langle a,b \rangle} \vec{S}_a \cdot \vec{S}_b \qquad \textbf{(4.1)}$$

In comparison with the 6- and 8-membered rings, the obtained coupling constant for Gd^{III} is slightly smaller, and unfortunately did not lead to a direct trend related to ring size and charge density. When considering both the dipolar and exchange contributions to the coupling, as determined by *ab initio* methods (*vide infra*), both components for the 7-membered ring remain the smallest of any of the computed parameters. Perhaps an explanation for this lies within the ligand field contributions from the ancillary ligands. This may be considered from a formal charges perspective, such that the cycloheptatrienyl bridge adopts a formal charge of -3, which, when distributed over seven atoms, is diluted to approximately -0.43 per C atom. Conversely, the charge distribution over the amido N-atom remains highly concentrated. Thus, the interaction with the amido ligands remains dominant (*vide infra*) compared to the donating ability of the bridging C_7-moiety. This was further proven through our computational studies of the main magnetic axis and LoProp charges (*vide infra*). Lastly, the presence of the potassium ion prevents the Ln^{III} ions from receiving equal electronic donation from the amido ancillary ligands, where the electron density of N3 and N4 would be split between Er2 and K1, thereby making Er2 less electron rich in comparison to Er1.

In the case of the anisotropic compounds **5-Dy**, **5-Er**, and **6-Er**, the χT profile differs significantly from the Gd^{III} analogue. For example, the χT product of compound **5-Dy** decreases very slowly from 300 K with temperature, followed by a more rapid decrease below 20 K to reach a minimum value of 23.15 cm^3 K mol^{-1} at 1.9 K. Whereas, the χT product of compounds **5-Er** and **6-Er** exhibit a slightly different trend upon decreasing temperature. The χT products for compounds **5-Er** and **6-Er** decrease gradually from 300 K to a minimum value below 15 K of 19.64 cm^3 K mol^{-1} and 20.53 cm^3 K mol^{-1}, respectively. This decrease in the χT product is followed by a rapid increase below 10 K to reach maximum values of 20.92 cm^3 K mol^{-1} and 22.58 cm^3 K mol^{-1}, respectively. The final increase in the value of the χT product is attributed to intramolecular ferromagnetic interactions between the Er^{III} ions. This will be further confirmed through *ab initio* calculations (*vide infra*).

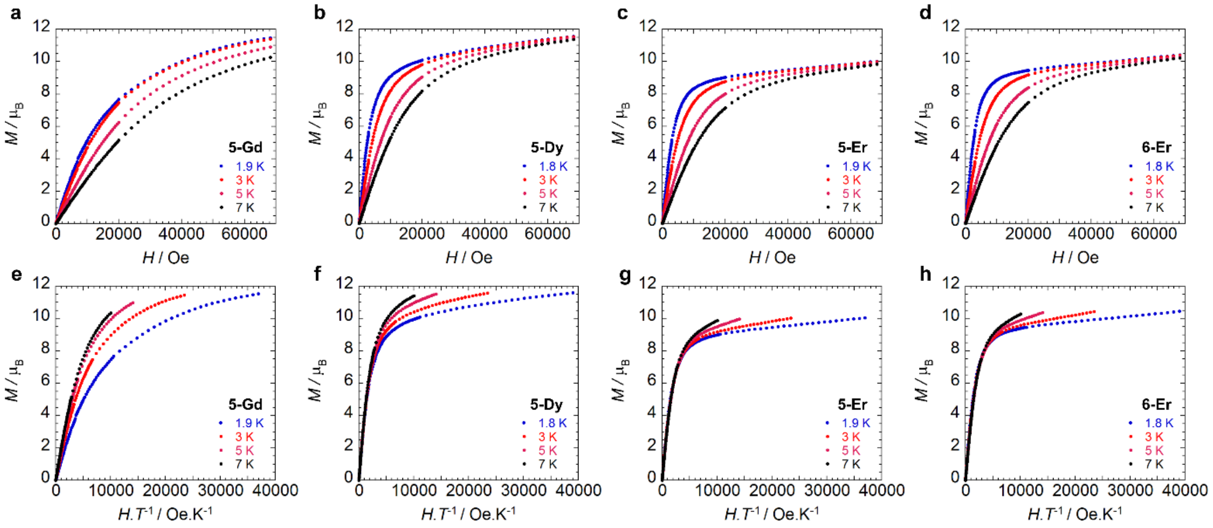

Figure 4.5 Solid state field dependence of the magnetization for **5-Gd** (a), **5-Dy** (b), **5-Er** (c), and **6-Er** (d). Field dependence of the reduced magnetization for **5-Gd** (e), **5-Dy** (f), **5-Er** (g), and **6-Er** (h).

As seen in Figure 4.5, the field dependence of the magnetization measurements performed at low temperatures exhibit non-saturation, even at 7 T and 1.9 K, for all compounds. This can be attributed to weak intramolecular antiferromagnetic interactions between the Ln^{III} ions, thereby making the low-lying excited states accessible by applying a magnetic field, even at the lowest measurable temperature of 1.8 K. This finding is further exemplified through *ab initio* calculations where the energies of the first and second excited exchange coupled states are minimally separated from the ground state (*vide infra*). In the case of compounds **5-Dy**, **5-Er**, and **6-Er** the presence of magnetic anisotropy is also likely to contribute to this lack of saturation in the magnetization. Contrary to the COT” bridged counterparts, no hysteretic behaviour was observed down to 1.8 K; therefore, alternating current (ac) magnetic susceptibility measurements were performed to investigate the potential SMM behaviour of the anisotropic compounds **5-Dy**, **5-Er**, and **6-Er**.

4.2.3 Alternating Current Magnetic Susceptibility

An ac driving field of 3.78 Oe was utilized to probe the slow relaxation dynamics of the anisotropic compounds; however, no ac signal was observed at zero applied dc field for all compounds. This is commonly observed for lanthanide systems with significant quantum tunneling of the magnetization (QTM). However, this QTM can be minimized upon application of a static dc field. As such a frequency dependent signal was observed for all three compounds (Figure 4.6) with the application of an optimized dc field. With respect to compound **5-Dy**, the application of a dc field of 2000 Oe allowed for the observation of a low frequency signal below 4 K. The out-of-phase susceptibility (χ'') of this process exhibited minimal shifting in peak maxima with regards to frequency upon decreasing temperature.

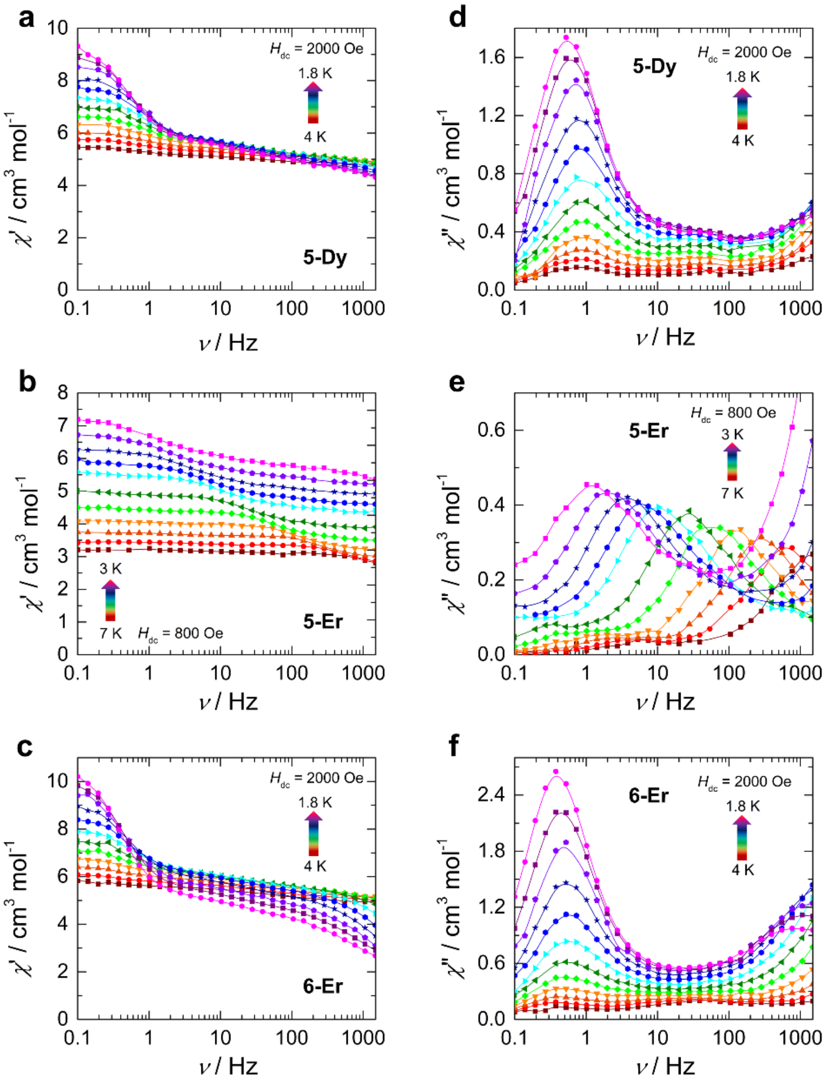

Figure 4.6 Frequency dependence of the (a-c) in-phase (χ') and (d-f) out-of-phase (χ'') components of the ac susceptibility for **5-Dy** under H_{dc} = 2000 Oe, **5-Er** under H_{dc} = 800 Oe, and **6-Er** under H_{dc} = 2000 Oe between 0.1 and 1000 Hz, at the indicated temperatures. Lines are a guide for the eye.

This type of behaviour may be indicative of a dominant QTM regime. This is not surprising due to the potential for low lying exchange coupled states, thereby enabling a shortcut in the energy barrier such that the first excited state lies only minimally above the ground state with a calculated energy of 1.9×10^{-5} cm^{-1} (*vide infra,* Table 4.3). However, we cannot rule out the possibility of intermolecular interactions, as application of large static fields has been shown to propagate spin-spin interactions.[33,34] These types of interactions may lead to the formation of magnetic domains, consequently precluding the analysis from a molecular perspective. Due to these phenomena, an effective energy barrier for this process could not be extracted from this data set. Alternatively, a frequency-dependent χ" signal was observed under a static dc field for **5-Er** (Figure 4.6e). The lack of overlapping peak maxima at low temperatures suggests that QTM is minimized with the application of an optimal static field of 800 Oe. Observation of shifting peak maxima to lower frequencies below 7 K demonstrates the presence of slow relaxation of the magnetization in **5-Er**, indicating field-induced slow relaxation. From the χ" component of the ac data measured between 7 and 3 K the Arrhenius law (Equation 4.2) was employed in order to extract an effective energy barrier of 58 K, and a pre-exponential factor of 2.9 x 10^{-8} s (Figure 4.7). More notably, the frequency dependent behaviour is most likely attributed to single-ion properties, as the observation of a second relaxation process at high frequencies becomes evident below 3.75 K. Full analysis of this process could not be completed due to frequency limitations (0.1-1500 Hz) of the magnetometer. From a structural perspective, the observed single-ion behaviour of **5-Er** is not surprising given the non-centrosymmetric nature of the molecule. Inequivalent metal ion sites have elicited dual relaxation processes at low temperatures in previous studies.[35–41] However, with respect to compound **5-Er**, this is easily visualized *via* the lack of inversion center within the molecule as a consequence of the coordinated potassium ion.

$$\tau^{-1} = \tau_0^{-1}\exp\left(-\frac{U_{\mathrm{eff}}}{k_B T}\right) \tag{4.2}$$

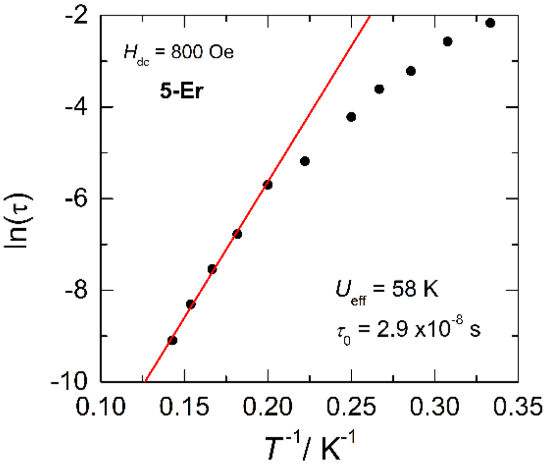

Figure 4.7 Arrhenius plot using χ" ac data for **5-Er** collected under an applied static field, H_{dc} = 800 Oe. The red line represents the fit of the linear high temperature region to Equation 4.2.

The observed magnetic behaviour of **5-Er** greatly contrasts the results obtained for the Dy^{III} analogue, **5-Dy**, suggesting that the cycloheptatrienyl trianion, along with the $[N(SiMe_3)_2]^-$ ancillary ligands, provide a more suitable ligand field for Er^{III} ions. These findings strongly correlate with previous work in the Murugesu group, including studies on COT'' bridging ligands, where the zero field energy barrier was improved upon from 25 K for the Dy^{III} analogue to 306 K for Er^{III}.[20,21] Moreover, the Murugesu group also demonstrated that the ligand field provided by the delocalized π-cloud promoted greater magnetic axiality in Er^{III} ions over Dy^{III} ions in single-ion sandwich complexes of COT.[42] While this remains true of the delocalized π-cloud and Er^{III} ions in the present study, the effects of the amido ligands proved dominant over the cycloheptatrienyl, effectively generating greater magnetic axiality in **5-Dy**, (*vide infra*). This is in accordance with previous studies, such that the axial orientation of highly charged negative donor atoms favour the oblate electron density of Dy^{III} ions.[43–48]

The out-of-phase magnetic component of the ac susceptibility for **6-Er** revealed two independent relaxation processes below 4 K, similar to compound **5-Er** (Figure 4.6). Once again this is not surprising given the unsymmetrical nature of the complex.[35–40] In order to probe each of these processes, an optimal dc field of 1000 Oe was used to elucidate the nature of the high frequency process, whereas an optimal field of 2000 Oe was employed in the study of the low frequency process. Unfortunately, the nature of the collected data precluded the extraction of an energy barrier to spin reversal, however, it did prove fruitful in gaining further understanding of the interactions occurring within this system. Interestingly, the low frequency processes exhibited similar characteristics as **5-Dy**, whereupon decreasing temperature, the resulting χ" signal increased in intensity but demonstrated little-to-no frequency dependent behaviour. Again, this is most likely a result of the low-lying exchange states, which promote QTM. Our computational studies (*vide infra*) elucidated a first excited state energy of 7.7×10^{-5} cm $^{-1}$, for compound **6-Er** further supporting the nature of this process. Once more, it is worth noting that at large magnetic fields it becomes difficult to confer whether the observed properties are solely molecular in nature, due to the potential of induced spin-spin intermolecular interactions.[33,34] Nonetheless, the presence of the secondary relaxation process at higher frequencies exhibits shifting peak maxima towards lower frequency upon decreasing temperature (Figure 4.6). Interestingly, this plot is characterized by decreasing susceptibility intensity for an *iso*-temperature curve with decreasing temperature. This type of behaviour has been similarly noted in single-chain magnets , where inter-chain spin-spin interactions give rise to decreasing susceptibility values.[49,50] Even under the optimal field of 1000 Oe, there is a decrease in intensity of the χ" component (Figure 4.8). While it is difficult to fully characterize the nature of the high frequency process, the preliminary data suggests that it relies on an intermolecularly driven process/relaxation. This finding may also

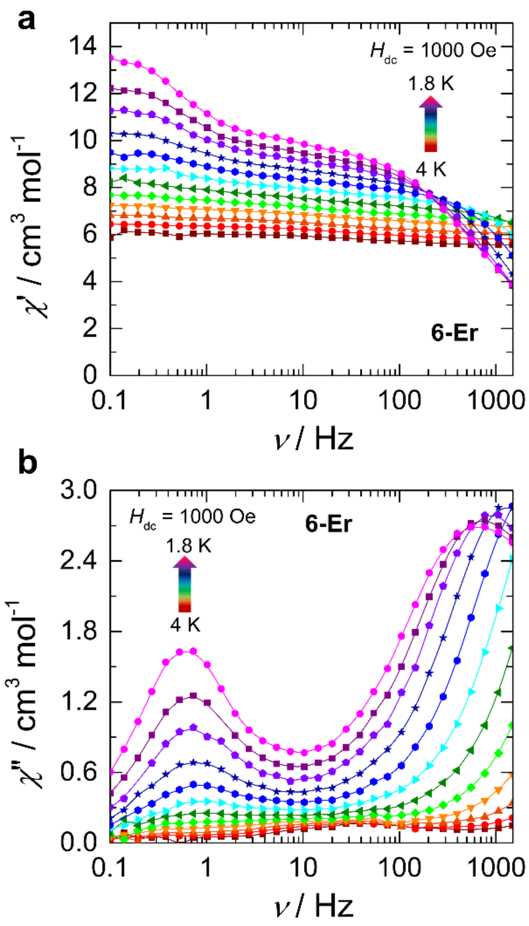

Figure 4.8 Frequency dependence of the (a) in-phase (χ') and (b) out-of-phase (χ") components of the ac susceptibility for **6-Er** under H_{dc} = 1000 Oe between 0.1 and 1000 Hz, at the indicated temperatures. Lines are a guide for the eye.

explain the tails observed in the high frequency region of the out-of-phase susceptibility for compounds **5-Dy** and **5-Er**. In fact, it is not uncommon in Ln-based systems to observe a secondary process as a result of intermolecular interactions.[34,51–53] Further investigation into the frequency dependent ac susceptibility measurements as a function of dc field for **5-Dy**, **5-Er**, and **6-Er** (Figure 4.9), revealed an unusual field dependence in the second relaxation, such that, the high frequency process appears to be augmented by weak static fields. This is likely a result of a direct relaxation process which is promoted by neighbouring spins,[40,54] thus, supporting the proposed intermolecularly driven relaxation process.

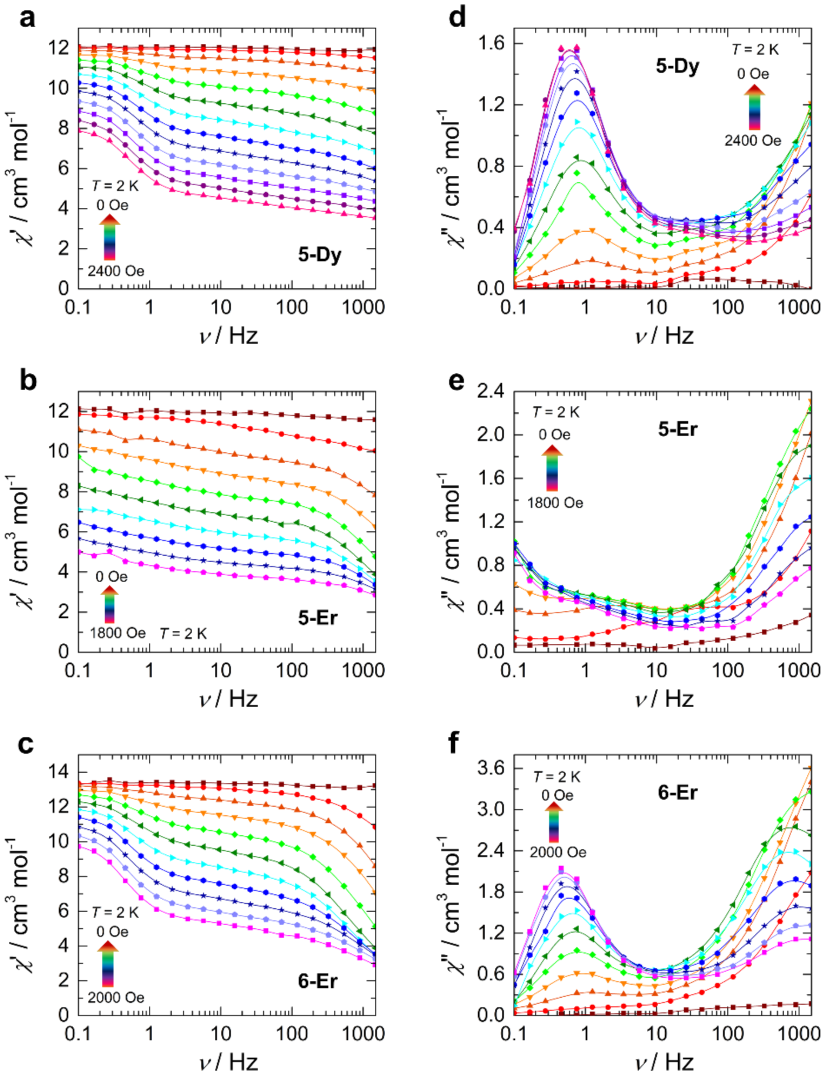

Figure 4.9 Frequency dependence of the (a-c) in-phase (χ') and (d-f) out-of-phase (χ'') components of the ac susceptibility as a function of applied static field at 2 K for **5-Dy** (top), 5-Er (middle), and **6-Er** (bottom). Lines are a guide for the eye.

4.2.4 Theoretical Analysis

Ab initio calculations for **5-Dy**, **5-Er**, and **6-Er** were performed to gain additional insight into the electronic and magnetic structures of these compounds. All calculations performed were CASSCF/RASSI/SINGE_ANISO,[55] and employed SCXRD structural data. Electronic and magnetic properties of the individual Ln^{III} sites were obtained through fragment *ab initio* calculations. Calculated structures are identical to those obtained for **5-Dy**, **5-Er**, and **6-Er**, where the neighbouring Ln sites are computationally replaced by the diamagnetic Lu^{III} ion. The CASSCF wave function included all possible electron distributions within the 4f ^{9} (for Dy^{III}) and 4f^{11} (for Er^{III}), shells only, while the remaining orbitals were kept doubly occupied. The orbitals and coefficients of the individual configurations were optimized self consistently for all electronic states arising from this definition of the active space. The spin-orbit interaction (described within the AMFI approximation) included all optimized spin states for Er^{III} (**5-Er** and **6-Er**), while for **5-Dy** only a limited number of states could be mixed, namely 21 spin sextet, 128 spin quartet and 130 spin doublet states, which resulted in 898 spin-orbit levels. The obtained low-lying states, arising from the ground J=15/2 multiplet on individual Ln sites, are provided in Table 4.2.

Table 4.2 Electronic and magnetic properties of the individual metal sites in compounds **5-Dy**, **5-Er**, and **6-Er**, obtained from ab initio calculations (in cm^{-1}).

5-Dy		**5-Er**		**6-Er**	
Dy1	**Dy2**	**Er1**	**Er2**	**Er1**	**Er2**
0	0	0	0	0	0
116	69	122	74	68	88
328	270	148	138	136	149
530	441	211	188	182	199
720	614	262	231	228	249
851	754	334	285	289	332
1010	854	525	476	476	523
1214	1021	573	501	508	589
Main values of the g tensor in the ground Kramers doublet					
0.008	0.027	0.016	0.013	0.007	0.019
0.020	0.089	0.039	0.057	0.049	0.064
18.825	18.370	17.763	17.978	17.883	17.782
Angle with the N-Ln-N plane (degrees)					
1.3	1.3	87.0	88.6	89.3	90.0

As observed in Table 4.2, the g-tensors in the ground Kramers doublet states of the individual sites in compounds **5-Dy**, **5-Er**, and **6-Er** are relatively axial in nature ($g_{X,Y} << g_Z$). Where the axiality of the ground doublet states are also related to the axiality of the crystal field acting on the Ln sites. For the Dy^{III} sites, the main anisotropy axis is oriented in plane of the N-Dy-N atoms, almost parallel to the N-N direction (Figure 4.10). This orientation is related to the much stronger crystal field effect arising from the N-atoms. In particular, the calculated LoProp charges[56] on the N-atoms (-1.28) are the largest among all neighbouring atoms of the Ln^{III} sites. The covalent ligand field effect arising from the N-atoms is also dominant among all neighbouring atoms. This is revealed by the Dy-N bonds, which are the shortest formed by the lanthanide sites in this environment. In this respect, the role of the central ring in the local axiality of the Dy^{III} sites is diminished and is in fact rather destructive as compared to the ligand field imposed by amido groups. In a case where the central ring and the neighbouring Ln^{III} site were absent, the magnetic axiality on one Dy^{III} site would be significantly stronger. These findings were not surprising given that recent reports have demonstrated the significant impact of highly anionic donor ligands in linear-like coordination geometries, with which such compounds should theoretically yield staggering energy barrier values.[44–46]

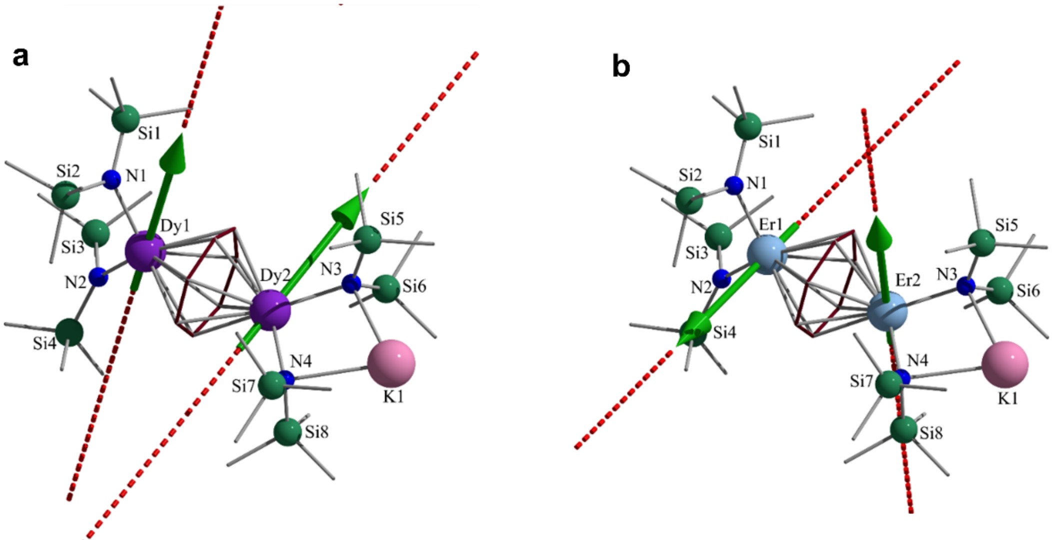

5-Dy **5-Er**

Figure 4.10 *Ab initio* calculated main anisotropy axes (dashed lines) on the Ln^{III} sites in the ground state for (a) **5-Dy** and (b) **5-Er**. Green arrows show the orientation of the local magnetic moments on the Ln^{III} sites in the ground exchange coupled state. Colour code: Purple (Dy^{III}), light blue (Er^{III}), teal (Si), pink (K), blue (N), grey (C). Hydrogen atoms omitted for clarity.

In stark contrast to these Dy-based findings, significantly different orientations for the ground state magnetic anisotropies were obtained for the Er sites in compounds **5-Er** and **6-Er** (Table 4.2, Figure 4.10b). For these compounds, the main magnetic axes are oriented almost perpendicular to the N-Er-N planes. This drastic change in the orientations of the main magnetic axes between Dy^{III} and Er^{III} atoms in a very similar axial ligand field is due to the opposite signs of the Stevens parameters, α and β, which are related to the second and fourth rank operators of the ground ionic J=15/2 multiplet for Dy^{III} and Er^{III}.[57] This is seen from the fact that the anisotropy of the highest (8th) Kramers doublet of the Dy sites (which are greatly destabilized due to the crystal field) is in fact almost parallel to the anisotropy of the ground doublet for the Er^{III} ion in the same crystal field, thus demonstrating the complementary nature of Dy^{III} and Er^{III} ions. This effect was previously observed in the case of $[\mathrm{Er}^{III}(\eta^8\text{-COT})_2]^-$ and $[\mathrm{Dy}^{III}(\eta^8\text{-COT})_2]^-$ anions.[42] Similar arrangements of the local magnetic axes were revealed with the previously studied $Er^{III}_2C_6$ (η^6-C_6R_6) compounds.[22]

The above reported *ab initio* results for separate Ln^{III} sites in **5-Dy**, **5-Er**, and **6-Er** were further employed in the computation of the exchange spectrum and magnetic properties of the dinuclear complexes using the POLY_ANISO program.[58,59] In this approach, the exchange interaction between magnetic sites is considered within the Lines model,[60] describing the exchange interaction between the localized spins in the absence of the spin-orbit interaction on sites by one parameter for the interacting metal pair. By explicitly considering the spin-orbit interaction on metal sites, the Lines model leads to an exchange matrix, which effectively describes the anisotropic exchange interaction between sites. In particular, the contribution of the intramolecular dipole−dipole magnetic coupling is accounted for exactly, because all the necessary data are made available through the *ab initio* calculations. On the basis of the resulting exchange spectrum of the entire system, all macroscopic magnetic properties were computed. The total magnetic interaction (exchange + dipolar) between the lowest Kramers doublets on lanthanide sites can be cast in a good approximation by the non-collinear Ising Hamiltonian (Equation 4.3), where J_{exch} and J_{dip} are parameters of the exchange and dipolar couplings respectively, while the $s_{1z} = ½$ is the pseudospin of the ground states of the metal sites. Best-fit exchange parameters, J_{exch}, and the calculated parameters of the dipolar magnetic coupling, J_{dip}, for the investigated compounds, alongside the resulting exchange spectrum are given in Table 4.3.

$$\mathcal{H}_{\text{exch}} = -(J_{\text{exch}} + J_{\text{dip}}) s_{1z} \cdot s_{2z} \quad \textbf{(4.3)}$$

An alternative approach for the estimation of the exchange coupling parameters in di- and poly-nuclear compounds is given by the broken-symmetry density functional theory approach (BS-DFT).[62] Unfortunately, the BS-DFT approach is not directly applicable for most of the lanthanides given the multiconfigurational nature of their ground states and their near-degenerate status as a result of weak crystal field effects. However, an estimation of the exchange in lanthanide-containing compounds is still achievable from the BS-DFT calculations. To this end, the isotropic closest metals computationally replace the anisotropic metal sites of the investigated compounds, while the ligand framework is kept intact. BS-DFT calculations are performed straightforwardly for the isotropic equivalent of the investigated compound. The extracted J_{iso} parameter has to be later rescaled to reflect the exchange Hamiltonian between the true spins of the original anisotropic metal sites. This method was employed with reasonable success in several previous studies.[63] For the present compounds, the estimated exchange parameters from the BS-DFT studies are *ferromagnetic* 1.14 cm^{-1} for **5-Dy**, 2.45 cm^{-1} for **5-Er** and 3.16 cm^{-1} for **6-Er**, correlating reasonably with the ferromagnetic exchange values obtained within the Lines model (Table 4.3). A comparison between the calculated and measured magnetic susceptibilities is depicted in Figure 4.4. A clear reduction in the dipolar magnetic coupling values for **5-Dy**, **5-Er**, and **6-Er** is obtained with respect to the previously investigated dinuclear compounds containing the 6-membered bridging moiety.[22] The reduction of J_{dip} is attributed to the different relative orientations of the local magnetic axes of the two Ln$^{\text{III}}$ sites, imposed by the different dihedral angles between the N-Ln-N planes. Thus, by controlling this angle through synthetic means we could, in principle, modify the magnetic dipolar interaction (and possibly the exchange) in such compounds. Through this study, we attempted to computationally assess the role of the dihedral angle between N-Ln-N planes in the dinuclear model systems **5-Dy**, and **5-Er**, and **6-Er**, as well as the role of the bridging ligand, in the magnetic behaviour as compared to those with 6- and 8- membered bridging rings. The results show that the dihedral angle in all three cases is very similar, while the Ln$^{\text{III}}$---Ln$^{\text{III}}$ distance decreases with increasing bridging ring size. We conclude, therefore, that the bulky ancillary ligands (i.e., $[N(SiMe_3)_2]^-$ ligands), and the resulting crystalline packing, are the factors responsible for defining the relative orientations of the local anisotropy axes in this series of compounds.

Table 4.3 Exchange coupled states and their magnetic anisotropy in compounds **5-Dy**, **5-Er**, and **6-Er**, employing the reported coupling parameters. Exchange and dipolar coupling parameters are given with respect to Equation 4.3

5-Dy	**5-Er**	**6-Er**
J_{dip} = -0.603	J_{dip} = -0.601	J_{dip} = -0.475
J_{exch} = +1.384	J_{exch} = +1.789	J_{exch} = +3.149
Low-lying exchange coupled states (cm^{-1})		
0.000000	0.000000	0.000000
0.000019	0.000032	0.000077
0.391064	0.598359	1.337034
0.391092	0.598405	1.337149
69.220130	74.152765	68.455939
69.220149	74.152981	68.461815
69.503274	74.260012	68.544184
69.503276	74.260236	65.550104
g_Z values[a] in the ground and first excited exchange doublet state		
29.8	28.5	27.9
22.3	21.6	22.4

[a] gX=gY=0 for Ising doublets, according to the Griffith's theorem;[61] (i.e., for systems with even number of electrons).

4.3 Summary and Conclusion

Compounds **5-Ln** and **6-Er** represent the first examples of SMMs based on the cycloheptatrienyl trianion ligand. The synthetic route to achieve the aforementioned compounds has been carefully designed to yield the facile formation of the trianion, taking advantage of sterically demanding and highly basic ancillary ligands. When combined with lanthanide ions, this type of bridging motif generated a weak, yet non-negligible, magnetic coupling constant of $J = -0.134\ \text{cm}^{-1}$ for the isotropic analogue. Through our computational modelling of the anisotropic compounds, we elucidated that the exchange coupling is more significant than the dipolar coupling, with the largest J_{exch} being $+3.149\ \text{cm}^{-1}$ for compound **6-Er**, thereby demonstrating the desirable effects of the seven-membered bridging moiety in generating exchange-coupled dinuclear lanthanide systems. This is an area of significant modern interest in quantum physics, where mediating the interaction of two metal centres *via* tuning the redox properties of the bridging motif is a method to induce significant quantum communication.[64,65] Moreover, the incorporation and measurement of these materials in molecular spintronics devices are often limited to the millikelvin regime,[66] where the surface effects on such materials are only beginning to be better understood.[61] Hence, increasing the energy barrier to spin reversal of SMMs will relax the rigorous experimental requirements to study these systems. Thus, the current high-energy barriers associated with 4f ions, attributed to single-ion behaviour, will not be sufficient. It is vital that we look to more creative ways to induce significant interactions between lanthanide ions.

4.4 Experimental Details

4.4.1 General Procedures

All reactions and subsequent manipulations were performed under anaerobic and anhydrous conditions using a standard Schlenk-line or nitrogen-atmosphere glovebox. Tetrahydrofuran (THF), toluene, and n-hexanes were dried on columns of activated alumina using a J.C. Meyer solvent purification system. Pentanes were dried via distillation over calcium hydride and subsequent passage over activated alumina. All solvents were at least reagent grade and were stored over activated 3Å molecular sieves. Anhydrous toluene-d_8 and anhydrous chloroform-d were purchased from CDN Isotopes and Sigma Aldrich respectfully, and used without further purification. Anhydrous $LnCl_3$ was purchased from Strem Chemicals, sodium bis(trimethylsilyl)amide, potassium, and 1,3-cycloheptadiene were purchased from Sigma Aldrich; these chemicals were used as received. Triethylamine was purchased from Alfa Aesar and dried by refluxing over calcium hydride, distillation, and storage over activated 3Å sieves. Potassium cycloheptadienide[67] and lanthanide tris(bis(trimethylsilylamido))[29,68] were prepared from previously reported procedures with modifications as described below. Infrared spectra were recorded on a Nicolet Nexus 550 FT-IR spectrometer using transmission mode in the 4000-600 cm^{-1} range; solid samples were prepared under an inert atmosphere and sandwiched between transparent NaCl plates. Elemental analyses were carried out with a Costech EOS 4010 CHNSO analyzer. NMR spectra were acquired on a Bruker Avance-II 300 MHz spectrometer at 298 K

4.4.2 Experimental Procedures

Synthesis of K(C_7H_9). Under an inert atmosphere, K^0 (360 mg, 9.22 mmol) was added to a reaction vessel containing 6 mL of THF and 0.96 mL of Et_3N (6.91 mmol). With vigorous stirring 1,3-cycloheptadiene (2 mL, 18.4 mmol) was added slowly to the vessel at 0 °C. Following the addition of the diene, the vessel was allowed to gradually warm to room temperature for 16 h. Addition of n-hexanes and subsequent exposure to -35 °C yielded yellow needle-like crystals. Collection of the crystals over a fine frit and subsequent washings with n-hexanes provided the product in 70% yield. IR (neat, cm^{-1}): 2826 (w), 1557 (m), 1529 (m), 1444 (m), 1363 (m), 1318 (m), 1274 (w), 1235 (w), 1215 (w), 1155 (m), 1125 (m), 1041 (m), 1006 (w), 948 (w), 889 (s), 867 (s), 771 (w), 710 (s), 634 (w), 541 (s). ^{1}H NMR ($CDCl_3$, 298 K, δ/ppm): 5.79 (m, 5H, C_{sp3}-*H*), 2.13 (m, 4H, C_{sp2}-*H*).

Synthesis of [$Ln^{III}\{N(SiMe_3)_2\}_3$], Ln = Gd, Dy, Er. Under an inert atmosphere, a slurry of $LnCl_3$ (1.86 mmol) in THF was combined with a THF solution of $NaN(SiMe_3)_2$ (5.57 mmol) at -35 °C. The reaction mixture was gradually warmed to room temperature over 16 h. Solvent was removed under reduced pressure and the subsequent solid treated with n-pentanes. The solution was filtered over Celite, the collection of the filtrate and storage at -35 °C, resulted in the formation of needle-like crystals of [$Ln\{N(SiMe_3)_2\}_3$]. Unit cell determinations matched previously reported structures for Ln = Dy and Er, however; no previous report of Ln = Gd exists.

Select characterizations for [$Gd^{III}\{N(SiMe_3)_2\}_3$]. Yield = 52 % IR (neat, cm^{-1}): 2934 (br), 1436 (m), 1235 (s), 1186 (w), 1094 (w), 1045 (w), 978 (s), 807 (w), 765 (w), 655 (m), 601 (s). ^{1}H NMR ($CDCl_3$, 298 K, δ/ppm): -11.67 (br, s, Si(C*H*$_3$)$_3$, FWHM: 5233.11 Hz).

Select characterizations for [$Dy^{III}\{N(SiMe_3)_2\}_3$]. Yield = 49 % IR (neat, cm^{-1}): 2944 (br), 1424 (m), 1236 (s), 1090 (w), 1048 (w), 974 (s), 827 (m), 768 (m), 656 (s), 604 (s). ^{1}H NMR ($CDCl_3$, 298 K, δ/ppm): -102.37 (br, s, Si(C*H*$_3$)$_3$, FWHM: 846.39 Hz).

Select characterizations for [$Er^{III}\{N(SiMe_3)_2\}_3$]. Yield = 51 % IR (neat, cm^{-1}): 2945 (br), 1423 (m), 1235 (s), 1090 (w), 1050 (w), 972 (s), 827 (m), 769 (m) 654 (m), 603 (m). ^{1}H NMR ($CDCl_3$, 298 K, δ/ppm): 62.86 (br, s, Si(C*H*$_3$)$_3$, FWHM: 2670.44 Hz).

Synthesis of [$KGd^{III}_2(\eta^7\text{-}C_7H_7)\{N(SiMe_3)_2\}_4$] (5-Gd). Under an inert atmosphere, $Gd^{III}\{N(SiMe_3)_2\}_3$ (58%, 0.350 mmol) was added to a cold solution of K(C_7H_9) (80 mg, 0.605 mmol) at -35 °C in 10 mL of toluene. The reaction mixture was stirred for 12 h, gradually warming to room temperature. The filtrate was then collected and solvent was removed under reduced pressure to achieve an orange-brown oil. Subsequent treatment with toluene and n-hexanes yielded X-ray quality crystals of **5-Gd**, (yield = 22 - 26 %). Isolated X-ray diffraction quality crystals are air and moisture sensitive. Bulk purity of compound **5-Gd** was determined by X-ray powder diffraction, *vide infra*. IR (neat, cm^{-1}): 2940 (w), 2892 (w), 1587 (br), 1494 (w), 1433 (br), 1240 (s), 1180 (w), 1066 (w), 992 (m), 931 (w), 872 (m), 815 (s), 740 (m), 693 (w), 655 (m). ^{1}H NMR (toluene-d_8, 298 K, δ/ppm): -196.04 (br, s, 17.8H, $Si(CH_3)_3$, FWHM: 24.52 Hz), -196.93 (br, s, 7H, C_7H_7, FWHM: 34.76 Hz), -197.28 (br, s, 16.9H, $Si(CH_3)_3$, FWHM: 34.46 Hz), -198.09 (br, s, 35.8H, $Si(CH_3)_3$, FWHM: 26.38 Hz). ^{1}H NMR integrations have been calibrated to seven protons on C_7H_7. Anal. Calcd. for $C_{31}H_{79}Gd_2KN_4Si_8$: C, 34.28; H, 7.33; N, 5.16. Found: C, 34.60; H, 7.12; N, 4.93.

Synthesis of [$KDy^{III}_2(\eta^7-C_7H_7)\{N(SiMe_3)_2\}_4$] (5-Dy). Compound **5-Dy** was prepared in an analogous manner to **5-Gd.** X-ray quality crystals of **5-Dy**, (yield = 22 - 26 %). Isolated X-ray diffraction quality crystals are air and moisture sensitive. Bulk purity of compound **2** was determined by X-ray powder diffraction, *vide infra*. IR (neat, cm^{-1}): 2939 (w), 2891 (w), 1595 (br), 1494 (w), 1421 (br), 1241 (s), 1180 (w), 1083 (w), 999 (m), 932 (w), 879 (m), 820 (s), 729 (m), 694 (w), 662 (m). ^{1}H NMR (toluene-d_8, 298 K, δ/ppm): 95.43 (br, s, 17.5H, $Si(CH_3)_3$, FWHM: 3604.57 Hz), -34.12 (br, s, 17.9H, $Si(CH_3)_3$, FWHM: 3739.31 Hz), -76.68 (br, s, 36.9H, $Si(CH_3)_3$, FWHM: 305.09 Hz), -100.81 (br, s, 7H, C_7H_7, FWHM: 256.67 Hz). ^{1}H NMR integrations have been calibrated to seven protons on C_7H_7. Anal. Calcd. for $C_{31}H_{79}Dy_2KN_4Si_8$: C, 33.95; H, 7.26; N, 5.11. Found: C, 33.71; H, 6.97; N, 5.43.

Synthesis of [$KEr^{III}_2(\eta^7-C_7H_7)\{N(SiMe_3)_2\}_4$] (5-Er). Compound **5-Er** was prepared in an analogous manner to **5-Gd**. X-ray quality crystals of **5-Er**, (yield = 22 - 26 %). Isolated X-ray diffraction quality crystals are air and moisture sensitive. Bulk purity of compound 3 was determined by X-ray powder diffraction, *vide infra*. IR (neat, cm^{-1}): 2949 (w), 2892 (w) 1662 (w), 1603 (w), 1495 (w), 1435 (br), 1249 (s), 1180 (m), 1079 (w), 988 (m), 931 (m), 882 (w), 822 (s), 728 (m), 693 (w), 661 (m). ^{1}H NMR (toluene-d_8, 298 K, δ/ppm): 45.98 (br, s, 17.6H, $Si(CH_3)_3$, FWHM: 723.42 Hz), 40.81 (br, s, 37.2H, $Si(CH_3)_3$, FWHM: 758.32 Hz), 15.85 (br, s, 7H, C_7H_7, FWHM: 1807.98 Hz), -98.44 (br, s, 17.8H, $Si(CH_3)_3$, FWHM: 963.65 Hz). ^{1}H NMR integrations have been calibrated to seven protons on C_7H_7. Anal. Calcd. for $C_{31}H_{79}Er_2KN_4Si_8$: C, 33.65; H, 7.20; N, 5.06. Found: C, 33.26; H, 7.09; N, 4.86.

Synthesis of [$K(THF)_2Er^{III}_2(\eta^7-C_7H_7)\{N(SiMe_3)_2\}_4$] (6-Er). Under an inert atmosphere, $Er^{III}\{N(SiMe_3)_2\}_3$ (223 mg, 0.350 mmol) was added to a cold solution of $K(C_7H_9)$ (80 mg, 0.605 mmol) at -35 °C in 10 mL of toluene. The reaction mixture was stirred for 12 h, gradually warming to room temperature. The filtrate was collected, extracted into THF, and the subsequent filtrate was evaporated to dryness with reduced pressure to achieve an orange-brown oil. Treatment with toluene and n-hexanes yielded x-ray quality crystals of **6-Er**, (yield = 32 %). Isolated X-ray diffraction quality crystals are air and moisture sensitive. IR (neat, cm^{-1}): 2941 (s), 2884 (s), 1461 (w), 1425 (m), 1369 (w), 1243 (s), 1181 (w), 1085 (s), 1052 (m), 989 (m), 869 (m), 818 (m), 753 (m), 711 (w), 691 (w), 662 (m), 603 (m). ^{1}H NMR (toluene-d_8, 298 K, δ/ppm): 45.15 (br, s, 17.9H, Si(CH_3)$_3$, FWHM: 914.35 Hz), 40.86 (br, s, 35.7H, Si(CH_3)$_3$, FWHM: 883.96 Hz), 35.62 (br, s, 7.9H, THF, FWHM: 570.66 Hz), 21.36 (br, s, 7.9H, THF, FWHM: 594.09 Hz), 15.60 (br, s, 7H, C_7H_7, FWHM: 110.97 Hz), -99.35 (br, s, 17.7H, Si(CH_3)$_3$, FWHM: 184.19 Hz). ^{1}H NMR integrations have been calibrated to seven protons on C_7H_7. Anal. Calcd. for $C_{39}H_{95}Er_2KN_4O_2Si_8$: C, 37.46; H, 7.66; N, 4.48. Found: C, 37.91; H, 7.29; N, 4.51.

4.4.3 X-Ray Powder Diffraction

XRPD experiments were performed using a RIGAKU Ultima IV diffractometer, equipped with a Cu-Kα radiation source (λ = 1.541836 Å), and a graphite monochromator. Scanning of the 2θ range was performed from 5-35°. XRPD pattern was consistent in 2θ values with the generated pattern from XRD, with slight discrepancies in some intensities of peaks attributed to preferred orientation and some broad amorphous character present.

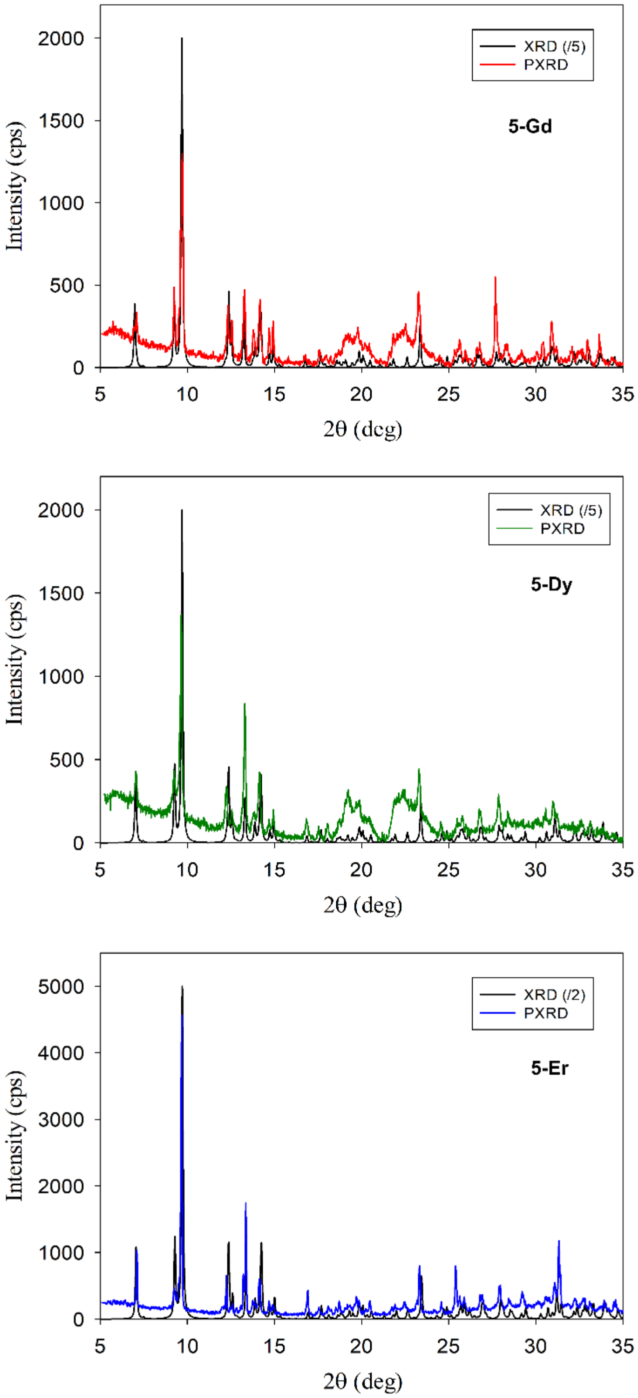

Figure 4.11 X-ray powder diffraction of **5-Gd** (red), **5-Dy** (green), and **5-Er** (blue), in the 5-35° 2θ region, as compared with the theoretical pattern generated from single crystal X-ray data (black).

4.4.4 Crystallography

Data collection results for compounds represent the best data sets obtained in several trials for each sample. The crystals were mounted on thin glass fibers using paraffin oil. Prior to data collection crystals were cooled to 200.15 K. Data were collected on a Bruker AXS KAPPA single crystal diffractometer equipped with a sealed Mo tube source ($\lambda = 0.71073$ Å) APEX II CCD detector. Raw data collection and processing were performed with APEX II software package from BRUKER AXS.[69] Diffraction data was collected with a sequence of 0.30° ω scans at 0.00, 120.0, and 240.0° in φ. Initial unit cell parameters were determined from 60 data frames with 0.3° ω scan each, collected at the different sections of the Ewald sphere. Semi-empirical absorption corrections based on equivalent reflections were applied.[70] Systematic absences in the diffraction data set and unit-cell parameters were consistent with monoclinic $\mathbf{P}2_1/n$ (№11) for compounds **5-Ln**, and monoclinic $\mathbf{C}2/c$ (№15) for compound **6-Er**. Solutions in the centrosymmetric space groups for all samples yielded chemically reasonable and computationally stable results of refinement. Structures were solved by direct methods, completed with difference Fourier synthesis, and refined with full-matrix least-squares procedures based on F^2.

For all the compounds all hydrogen atoms positions were calculated based on the geometry of related non-hydrogen atoms. All hydrogen atoms were treated as idealized contributions during the refinement. All scattering factors are contained in several versions of the SHELXTL program library, with version v.6.12 being used.[71]

Table 4.4 Crystallographic data for **5-Ln** (Ln = Gd^{III}, Dy^{III}, Er^{III}).

Compound	**5-Gd**	**5-Dy**	**5-Er**
Empirical formula	$C_{31}H_{79}Gd_2KN_4Si_8$	$C_{31}H_{79}Dy_2KN_4Si_8$	$C_{31}H_{79}Er_2KN_4Si_8$
Formula weight	1086.30	1096.80	1106.32
Crystal size, mm	0.290x0.203x0.139	0.210x0.140x0.120	0.800x0.543x0.430
Crystal system	Monoclinic	Monoclinic	Monoclinic
Space group	$\mathbf{P}2_1/n$	$\mathbf{P}2_1/n$	$\mathbf{P}2_1/n$
Z	4	4	4
a, Å	14.1700(7)	14.1259(4)	14.09464(7)
b, Å	14.2848(7)	14.2954(4)	14.2965(8)
c, Å	25.4039(12)	25.2343(6)	25.1055(13)
α, °	90	90	90
β, °	95.518(2)	95.2741(13)	95.170(3)
γ, °	90	90	90
Volume, $Å^3$	5118.3(4)	5074.1(2)	5038.3(5)
Calculated density, Mg/m^3	1.410	1.436	1.459
Absorption coefficient, mm^{-1}	2.861	3.217	3.606
T (K)	200(2)	200(2)	200(2)
F(000)	2208	2224	2240
Θ range for data collection, °	1.584 to 30.595	1.723 to 28.424	1.598 to 30.659
Limiting indices	h = ±19, k = ±20, l = ±36	h = ±18, k = ±18, l = ±33	h = ±20, k = ±20, l = ±35
Reflections collected / unique	25502	58488	26202
R(int)	-	0.0334	-
Completeness to Θ = 28.32, %	99.6	99.3	99.5
Max. and min. transmission	0.746071 and 0.531793	0.7457 and 0.5770	0.746065 and 0.304526
Data / restraints / parameters	15195 / 0 / 416	12645 / 0 / 415	15164 / 0 / 416
Goodness-of-fit on F^2	1.055	1.019	1.063
Final R indices [I>2σ(I)]	R1 = 0.0330, wR2 = 0.0626	R1 = 0.0299, wR2 = 0.0642	R1 = 0.0443 wR2 = 0.1120
R indices (all data)	R1 = 0.0544 wR2 = 0.0725	R1 = 0.0424 wR2 = 0.0693	R1 = 0.0648 wR2 = 0.1336
Largest diff. peak/hole, e·$Å^{-3}$	2.022 and -0.913	1.430 and -1.064	3.653 and -2.021

[a] $R = R_1 = \sum||F_0| - |F_c||/\sum|F_0|$; $wR_2 = \{\sum[w(F_0^2 - F_c^2)^2/\sum[w(F_0)^2]]^{1/2}$; $w = 1/[\delta^2(F_o^2) + (ap)^2 + bp]$, where $p = [\max(F_0^2, 0) + 2F_c^2]/3$

Table 4.5 Crystallographic data for **6-Er**.

Compound	**6-Er**
Empirical formula	$C_{39}H_{95}Er_2KN_4O_2Si_8$
Formula weight	1250.52
Crystal size, mm	0.677x0.530x0.200
Crystal system	Monoclinic
Space group	**C**$2/c$
Z	4
a, Å	20.1042(7)
b, Å	18.7574(6)
c, Å	16.5696(6)
α, °	90
β, °	107.8505(17)
γ, °	90
Volume, $Å^3$	5947.6(4)
Calculated density, Mg/m^3	1.397
Absorption coefficient, mm^{-1}	3.066
T (K)	200(2)
F(000)	2560
Θ range for data collection, °	1.520 to 28.381
Limiting indices	h = ±26, k = ±25, l = ±22
Reflections collected / unique	23004
R(int)	0.0258
Completeness to Θ = 28.32, %	98.1
Max. and min. transmission	0.7457 and 0.4771
Data / restraints / parameters	7321 / 657 / 286
Goodness-of-fit on F^2	1.071
Final R indices [I>2σ(I)]	R1 = 0.0384, wR2 = 0.1251
R indices (all data)	R1 = 0.0438, wR2 = 0.1325
Largest diff. peak/hole, $e{\cdot}Å^{-3}$	1.380 and -2.107

$^{a}R = R_1 = \sum||F_0| - |F_c||/ \sum|F_0|$; $wR_2 = \{\sum[w (F_0^2 - F_c^2)^2/\sum[w(F_0)^2]]\}^{1/2}$; $w = 1/[\delta^2(F_o^2) + (ap)^2 + bp]$, where $p = [\max (F_0^2, 0) + 2F_c^2]/3$

4.4.5 Magnetometry

The magnetic susceptibility measurements were obtained using a Quantum Design SQUID magnetometer MPMS-XL7 operating between 1.8 and 300 K. DC measurements were performed on polycrystalline samples of 12 mg, 15 mg, 11 mg, and 21 mg of **5-Gd**, **5-Dy**, **5-Er**, and **6-Er** respectively. Samples were wrapped in a polyethylene bag, and subjected to a field of 0 to 7 T. The magnetization data were collected at 100 K to check for ferromagnetic impurities that were absent in all of the samples. Diamagnetic corrections were applied for the sample holder and the inherent diamagnetism of the sample was estimated with the use of Pascals constants.

4.4.6 Computational Details

All calculations performed were CASSCF/RASSI/SINGLE_ANISO,[55] and employed SCXRD structural data. All atoms were described with ANO-RCC basis sets: MB-basis (minimal); VDZP-basis (medium); VTZP-basis (large). Active space for the CASSCF method included the $4f^n$ configuration only. Active orbitals have a weight of ~95% on the atomic 4f basis of the lanthanide. For Dy^{III} sites in **5-Dy**, 21 spin sextet, 128 spin quartet and 130 spin doublet states were mixed by the spin-orbit coupling within RASSI method. All states correspond to the 4f-4f transitions, i.e., are of ligand field type. No charge transfer states were considered. For the modeling of the exchange interaction between Ln^{III} sites the VTZP results were employed. Analysis of the multiplet-specific crystal-field for the Ln^{III} sites were completed using the SINGLE_ANISO program in MOLCAS. The results of which, use the *ab inito* CASSCF/RASSI wave function and energies to compute the parameters of the crystal-field of the ground *J* multiplet, which are summarized in Table 4.6.

Table 4.6 Parameters of the *ab initio* crystal field for the individual Ln^{III} sites in **5-Dy**, **5-Er**, and **6-Er** (TZP basis).

k	q	5-Dy		5-Er		6-Er	
		Dy1	Dy2	Er1	Er2	Er1	Er2
2	-2	-0.535140E-01	-0.140417E+00	-0.546539E+00	0.194653E-01	-0.189670E+00	-0.202116E-03
	-1	0.201439E+01	-0.837609E+00	-0.371786E+00	0.126786E+00	0.401697E+00	-0.248221E+00
	0	-0.551468E+01	-0.471389E+01	-0.244231E+01	-0.204053E+01	-0.205323E+01	-0.236264E+01
	1	0.231254E+00	-0.468048E+00	-0.269014E+00	-0.417252E-01	0.228275E-01	-0.964296E-01
	2	0.649035E+01	0.518941E+01	0.231406E+01	0.218899E+01	0.244990E+01	0.311724E+01
4	-4	-0.467820E-02	-0.841583E-02	0.126499E-01	0.268865E-02	0.860376E-02	-0.257562E-02
	-3	-0.709719E-01	0.278916E-01	-0.580828E-02	0.190522E-02	-0.101570E-02	0.307589E-02
	-2	-0.117192E-02	-0.427150E-02	0.288370E-02	0.513570E-03	0.160784E-02	-0.615698E-03
	-1	-0.287663E-01	0.141000E-01	0.269479E-02	-0.596242E-03	-0.167835E-02	0.944818E-03
	0	0.292096E-02	0.518216E-02	0.269434E-03	-0.144163E-03	-0.940719E-04	0.911350E-04
	1	0.407627E-02	0.109271E-02	0.355323E-03	-0.126146E-03	0.122872E-02	0.430922E-03
	2	0.423533E-01	0.483016E-01	-0.192298E-01	-0.178598E-01	-0.178150E-01	-0.201671E-01
	3	0.757695E-02	0.744148E-02	0.101029E-01	-0.784807E-03	-0.240173E-02	0.157817E-01
	4	0.302131E-01	0.338922E-01	-0.415297E-01	-0.471105E-01	-0.442765E-01	-0.407549E-01
6	-6	0.262912E-05	-0.173971E-07	0.811522E-04	0.136673E-04	0.386364E-04	-0.397995E-05
	-5	-0.352270E-03	0.114006E-03	-0.124379E-03	0.171786E-05	-0.160369E-03	0.983794E-04
	-4	-0.252467E-05	-0.158880E-04	-0.842563E-04	-0.156848E-04	-0.350193E-04	0.157681E-04
	-3	0.598729E-04	-0.857549E-05	0.971150E-04	-0.426555E-04	-0.484972E-04	-0.510964E-05
	-2	0.299320E-05	0.767148E-05	0.151308E-04	0.248996E-05	-0.132274E-05	0.469280E-05
	-1	0.662807E-04	-0.420457E-04	-0.158505E-04	0.191147E-04	0.384596E-05	0.967831E-05
	0	-0.178829E-05	-0.595496E-05	-0.207138E-04	-0.197021E-04	-0.194103E-04	-0.210516E-04
	1	-0.688711E-04	0.240167E-04	0.292318E-04	0.166737E-04	-0.304174E-04	0.371577E-06
	2	-0.115581E-03	-0.104506E-03	0.518185E-04	0.982957E-05	0.196359E-04	0.665648E-04
	3	-0.700622E-05	-0.463034E-04	-0.750018E-04	-0.797069E-04	0.456875E-04	-0.163746E-03
	4	0.120817E-03	0.114721E-03	0.187624E-03	0.188058E-03	0.170024E-03	0.162188E-03
	5	0.672395E-04	-0.540420E-04	0.122807E-03	-0.122831E-03	0.106352E-03	0.310352E-03
	6	0.135509E-04	0.856097E-06	-0.556321E-04	-0.985607E-04	-0.124296E-03	-0.171449E-03

4.5 References

(1) Bahl, J. J.; Bates, R. B.; Beavers, W. A.; Launer, C. R. Cycloheptatrienyl and Heptatrienyl Trianions. *J. Am. Chem. Soc.* **1977**, *99* (18), 6126–6127. https://doi.org/10.1021/ja00460a060.

(2) Arliguie, T.; Lance, M.; Nierlich, M.; Ephritikhine, M. Inverse Cycloheptatrienyl Sandwich Complexes of Uranium and Neodymium. *J. Chem. Soc. Dalton Trans.* **1997**, 14, 2501–2504. https://doi.org/10.1039/a701352c.

(3) Arliguie, T.; Lance, M.; Nierlich, M.; Vigner, J.; Ephritikhine, M. Synthesis and Crystal Structure of $[K(C_{12}H_{24}O_6][U(\eta\text{-}C_7H_7)_2]$, the First Cycloheptatrienyl Sandwich Compound. *J. Chem. Soc. Chem. Commun.* **1995**, 2, 183–184. https://doi.org/10.1039/C39950000183.

(4) Arliguie, T.; Lance, M.; Nierlich, M.; Vigner, J.; Ephritikhine, M. Inverse Cycloheptatrienyl Sandwich Complexes. Crystal Structure of $[U(BH_4)_2(OC_4H_8)_5][(BH_4)_3U(\mu\text{-}\eta^7,\eta^7\text{-}C_7H_7)U(BH_4)_3]$. *J. Chem. Soc. Chem. Commun.* **1994**, 7, 847–848. https://doi.org/10.1039/C39940000847.

(5) Sessoli, R.; Gatteschi, D.; Caneschi, A.; Novak, M. A. Magnetic Bistability in a Metal-Ion Cluster. *Nature* **1993**, *365* (6442), 141–143. https://doi.org/10.1038/365141a0.

(6) Blagg, R. J.; Muryn, C. A.; McInnes, E. J. L.; Tuna, F.; Winpenny, R. E. P. Single Pyramid Magnets: Dy5 Pyramids with Slow Magnetic Relaxation to 40 K. *Angew. Chem. Int. Ed.* **2011**, *50* (29), 6530–6533. https://doi.org/10.1002/anie.201101932.

(7) Ako, A. M.; Hewitt, I. J.; Mereacre, V.; Clérac, R.; Wernsdorfer, W.; Anson, C. E.; Powell, A. K. A Ferromagnetically Coupled Mn_{19} Aggregate with a Record S = 83/2 Ground Spin State. *Angew. Chem. Int. Ed.* **2006**, *45* (30), 4926–4929. https://doi.org/10.1002/anie.200601467.

(8) Williams, U. J.; Mahoney, B. D.; DeGregorio, P. T.; Carroll, P. J.; Nakamaru-Ogiso, E.; Kikkawa, J. M.; Schelter, E. J. A Comparison of the Effects of Symmetry and Magnetoanisotropy on Paramagnetic Relaxation in Related Dysprosium Single Ion Magnets. *Chem. Commun.* **2012**, *48* (45), 5593. https://doi.org/10.1039/c2cc31227a.

(9) Brown, A. J.; Pinkowicz, D.; Saber, M. R.; Dunbar, K. R. A Trigonal-Pyramidal Erbium(III) Single-Molecule Magnet. *Angew. Chem. Int. Ed.* **2015**, *54* (20), 5864–5868. https://doi.org/10.1002/anie.201411190.

(10) Li, Q.-W.; Liu, J.-L.; Jia, J.-H.; Chen, Y.-C.; Liu, J.; Wang, L.-F.; Tong, M.-L. "Half-Sandwich" Yb^{III} Single-Ion Magnets with Metallacrowns. *Chem. Commun.* **2015**, *51* (51), 10291–10294. https://doi.org/10.1039/C5CC03389F.

(11) Craig, G. A.; Marbey, J. J.; Hill, S.; Roubeau, O.; Parsons, S.; Murrie, M. Field-Induced Slow Relaxation in a Monometallic Manganese(III) Single-Molecule Magnet. *Inorg. Chem.* **2015**, *54* (1), 13–15. https://doi.org/10.1021/ic5024136.

(12) Layfield, R. A.; McDouall, J. J. W.; Sulway, S. A.; Tuna, F.; Collison, D.; Winpenny, R. E. P. Influence of the N-Bridging Ligand on Magnetic Relaxation in an Organometallic Dysprosium Single-Molecule Magnet. *Chem.-Eur. J.* **2010**, *16* (15), 4442–4446. https://doi.org/10.1002/chem.201000158.

(13) Layfield, R. A. Organometallic Single-Molecule Magnets. *Organometallics* **2014**, *33* (5), 1084–1099. https://doi.org/10.1021/om401107f.

(14) Pugh, T.; Tuna, F.; Ungur, L.; Collison, D.; McInnes, E. J. L.; Chibotaru, L. F.; Layfield, R. A. Influencing the Properties of Dysprosium Single-Molecule Magnets with Phosphorus Donor Ligands. *Nat. Commun.* **2015**, *6* (1), 7492. https://doi.org/10.1038/ncomms8492.

(15) Jiang, S.-D.; Wang, B.-W.; Sun, H.-L.; Wang, Z.-M.; Gao, S. An Organometallic Single-Ion Magnet. *J. Am. Chem. Soc.* **2011**, *133* (13), 4730–4733. https://doi.org/10.1021/ja200198v.

(16) Trifonov, A. A.; Shestakov, B.; Long, J.; Lyssenko, K.; Guari, Y.; Larionova, J. An Organoytterbium(III) Complex Exhibiting Field-Induced Single-Ion-Magnet Behavior. *Inorg. Chem.* **2015**, *54* (16), 7667–7669. https://doi.org/10.1021/acs.inorgchem.5b01318.

(17) Meihaus, K. R.; Long, J. R. Magnetic Blocking at 10 K and a Dipolar-Mediated Avalanche in Salts of the Bis(η^8-Cyclooctatetraenide) Complex $[Er(COT)_2]^-$. *J. Am. Chem. Soc.* **2013**, *135* (47), 17952–17957. https://doi.org/10.1021/ja4094814.

(18) Pugh, T.; Vieru, V.; Chibotaru, L. F.; Layfield, R. A. Magneto-Structural Correlations in Arsenic- and Selenium-Ligated Dysprosium Single-Molecule Magnets. *Chem. Sci.* **2016**, *7* (3), 2128–2137. https://doi.org/10.1039/C5SC03755G.

(19) Habib, F.; Murugesu, M. Lessons Learned from Dinuclear Lanthanide Nano-Magnets. *Chem. Soc. Rev.* **2013**, *42* (8), 3278. https://doi.org/10.1039/c2cs35361j.

(20) Le Roy, J. J.; Jeletic, M.; Gorelsky, S. I.; Korobkov, I.; Ungur, L.; Chibotaru, L. F.; Murugesu, M. An Organometallic Building Block Approach to Produce a Multidecker 4f Single-Molecule Magnet. *J. Am. Chem. Soc.* **2013**, *135* (9), 3502–3510. https://doi.org/10.1021/ja310642h.

(21) Le Roy, J. J.; Ungur, L.; Korobkov, I.; Chibotaru, L. F.; Murugesu, M. Coupling Strategies to Enhance Single-Molecule Magnet Properties of Erbium–Cyclooctatetraenyl Complexes. *J. Am. Chem. Soc.* **2014**, *136* (22), 8003–8010. https://doi.org/10.1021/ja5022552.

(22) Huang, W.; Le Roy, J. J.; Khan, S. I.; Ungur, L.; Murugesu, M.; Diaconescu, P. L. Tetraanionic Biphenyl Lanthanide Complexes as Single-Molecule Magnets. *Inorg. Chem.* **2015**, *54* (5), 2374–2382. https://doi.org/10.1021/ic5029788.

(23) Magnani, N.; Apostolidis, C.; Morgenstern, A.; Colineau, E.; Griveau, J.-C.; Bolvin, H.; Walter, O.; Caciuffo, R. Magnetic Memory Effect in a Transuranic Mononuclear Complex. *Angew. Chem. Int. Ed.* **2011**, *50* (7), 1696–1698. https://doi.org/10.1002/anie.201006619.

(24) Liu, S.-S.; Ziller, J. W.; Zhang, Y.-Q.; Wang, B.-W.; Evans, W. J.; Gao, S. A Half-Sandwich Organometallic Single-Ion Magnet with Hexamethylbenzene Coordinated to the Dy(III) Ion. *Chem. Commun.* **2014**, *50* (77), 11418–11420. https://doi.org/10.1039/C4CC04262J.

(25) Huang, W.; Diaconescu, P. L. Rare-Earth Metal π-Complexes of Reduced Arenes, Alkenes, and Alkynes: Bonding, Electronic Structure, and Comparison with Actinides and Other Electropositive Metals. *Dalton Trans.* **2015**, *44* (35), 15360–15371. https://doi.org/10.1039/C5DT02198G.

(26) Green, M. L. H.; Ng, D. K. P. Cycloheptatriene and -Enyl Complexes of the Early Transition Metals. *Chem. Rev.* **1995**, *95* (2), 439–473. https://doi.org/10.1021/cr00034a006.

(27) Miller, J. T.; Dekock, C. W. Facile Formation of the Cycloheptatrienyl Trianion by Lanthanide and Actinide Ions. *J. Organomet. Chem.* **1981**, *216* (1), 39–48. https://doi.org/10.1016/S0022-328X(00)83998-4.

(28) Bradley, D. C.; Ghotra, J. S.; Hart, F. A. Three-Co-Ordination in Lanthanide Chemistry: Tris[Bis(Trimethylsilyl)Amido]Lanthanide(III) Compounds. *J. Chem. Soc. Chem. Commun.* **1972**, No. 6, 349. https://doi.org/10.1039/c39720000349.

(29) Bradley, D. C.; Ghotra, J. S.; Hart, F. A. Low Co-Ordination Numbers in Lanthanide and Actinide Compounds. Part I. The Preparation and Characterization of Tris{bis(Trimethylsilyl)-Amido}lanthanides. *J. Chem. Soc. Dalton Trans.* **1973**, No. 10, 1021. https://doi.org/10.1039/dt9730001021.

(30) Zhang, P.; Zhang, L.; Wang, C.; Xue, S.; Lin, S.-Y.; Tang, J. Equatorially Coordinated Lanthanide Single Ion Magnets. *J. Am. Chem. Soc.* **2014**, *136* (12), 4484–4487. https://doi.org/10.1021/ja500793x.

(31) Wolstenholme, D. J.; Cameron, T. S. Comparative Study of Weak Interactions in Molecular Crystals: H−H Bonds vs Hydrogen Bonds. *J. Phys. Chem. A* **2006**, *110* (28), 8970–8978. https://doi.org/10.1021/jp061205i.

(32) Schumann, H.; Winterfeld, J.; Esser, L.; Kociok-Köhn, G. $[\{(Me_3Si)_2N\}_2Sm\{\mu(\eta^8{:}\eta^8\text{-}C_8H_8)\}\text{-}Sm\{N(SiMe_3)_2\}_2]$: An Inverse Organolanthanoid Sandwich Complex. *Angew. Chem. Int. Ed. Engl.* **1993**, *32* (8), 1208–1210. https://doi.org/10.1002/anie.199312081.

(33) Habib, F.; Korobkov, I.; Murugesu, M. Exposing the Intermolecular Nature of the Second Relaxation Pathway in a Mononuclear Cobalt(II) Single-Molecule Magnet with Positive Anisotropy. *Dalton Trans.* **2015**, *44* (14), 6368–6373. https://doi.org/10.1039/C5DT00258C.

(34) Meihaus, K. R.; Rinehart, J. D.; Long, J. R. Dilution-Induced Slow Magnetic Relaxation and Anomalous Hysteresis in Trigonal Prismatic Dysprosium(III) and Uranium(III) Complexes. *Inorg. Chem.* **2011**, *50* (17), 8484–8489. https://doi.org/10.1021/ic201078r.

(35) Liu, C.-M.; Zhang, D.-Q.; Zhu, D.-B. Field-Induced Single-Ion Magnets Based on Enantiopure Chiral β-Diketonate Ligands. *Inorg. Chem.* **2013**, *52* (15), 8933–8940. https://doi.org/10.1021/ic4011218.

(36) Guo, Y.-N.; Xu, G.-F.; Gamez, P.; Zhao, L.; Lin, S.-Y.; Deng, R.; Tang, J.; Zhang, H.-J. Two-Step Relaxation in a Linear Tetranuclear Dysprosium(III) Aggregate Showing Single-Molecule Magnet Behavior. *J. Am. Chem. Soc.* **2010**, *132* (25), 8538–8539. https://doi.org/10.1021/ja103018m.

(37) Fatila, E. M.; Rouzières, M.; Jennings, M. C.; Lough, A. J.; Clérac, R.; Preuss, K. E. Fine-Tuning the Single-Molecule Magnet Properties of a $[Dy(III)\text{-}Radical]_2$ Pair. *J. Am. Chem. Soc.* **2013**, *135* (26), 9596–9599. https://doi.org/10.1021/ja403794d.

(38) Das, S.; Dey, A.; Biswas, S.; Colacio, E.; Chandrasekhar, V. Hydroxide-Free Cubane-Shaped Tetranuclear [Ln_4] Complexes. *Inorg. Chem.* **2014**, *53* (7), 3417–3426. https://doi.org/10.1021/ic402827b.

(39) Feng, M.; Pointillart, F.; Lefeuvre, B.; Dorcet, V.; Golhen, S.; Cador, O.; Ouahab, L. Multiple Single-Molecule Magnet Behaviors in Dysprosium Dinuclear Complexes Involving a Multiple Functionalized Tetrathiafulvalene-Based Ligand. *Inorg. Chem.* **2015**, *54* (8), 4021–4028. https://doi.org/10.1021/acs.inorgchem.5b00272.

(40) Ren, M.; Xu, Z.-L.; Wang, T.-T.; Bao, S.-S.; Zheng, Z.-H.; Zhang, Z.-C.; Zheng, L.-M. Homochiral Mononuclear Dy-Schiff Base Complexes Showing Field-Induced Double Magnetic Relaxation Processes. *Dalton Trans.* **2016**, *45* (2), 690–695. https://doi.org/10.1039/C5DT03800F.

(41) Venugopal, A.; Tuna, F.; Spaniol, T. P.; Ungur, L.; Chibotaru, L. F.; Okuda, J.; Layfield, R. A. A Hydride-Ligated Dysprosium Single-Molecule Magnet. *Chem Commun* **2013**, *49* (9), 901–903. https://doi.org/10.1039/C2CC38036F.

(42) Ungur, L.; Le Roy, J. J.; Korobkov, I.; Murugesu, M.; Chibotaru, L. F. Fine-Tuning the Local Symmetry to Attain Record Blocking Temperature and Magnetic Remanence in a Single-Ion Magnet. *Angew. Chem. Int. Ed.* **2014**, *53* (17), 4413–4417. https://doi.org/10.1002/anie.201310451.

(43) Rinehart, J. D.; Long, J. R. Exploiting Single-Ion Anisotropy in the Design of f-Element Single-Molecule Magnets. *Chem. Sci.* **2011**, *2* (11), 2078. https://doi.org/10.1039/c1sc00513h.

(44) Gregson, M.; Chilton, N. F.; Ariciu, A.-M.; Tuna, F.; Crowe, I. F.; Lewis, W.; Blake, A. J.; Collison, D.; McInnes, E. J. L.; Winpenny, R. E. P.; Liddle, S. T. A Monometallic Lanthanide Bis(Methanediide) Single Molecule Magnet with a Large Energy Barrier and Complex Spin Relaxation Behaviour. *Chem. Sci.* **2016**, *7* (1), 155–165. https://doi.org/10.1039/C5SC03111G.

(45) Chilton, N. F. Design Criteria for High-Temperature Single-Molecule Magnets. *Inorg. Chem.* **2015**, *54* (5), 2097–2099. https://doi.org/10.1021/acs.inorgchem.5b00089.

(46) Chilton, N. F.; Goodwin, C. A. P.; Mills, D. P.; Winpenny, R. E. P. The First Near-Linear Bis(Amide) f-Block Complex: A Blueprint for a High Temperature Single Molecule Magnet. *Chem. Commun.* **2015**, *51* (1), 101–103. https://doi.org/10.1039/C4CC08312A.

(47) Ungur, L.; Chibotaru, L. F. Magnetic Anisotropy in the Excited States of Low Symmetry Lanthanide Complexes. *Phys. Chem. Chem. Phys.* **2011**, *13* (45), 20086. https://doi.org/10.1039/c1cp22689d.

(48) Chen, Y.-C.; Liu, J.-L.; Ungur, L.; Liu, J.; Li, Q.-W.; Wang, L.-F.; Ni, Z.-P.; Chibotaru, L. F.; Chen, X.-M.; Tong, M.-L. Symmetry-Supported Magnetic Blocking at 20 K in Pentagonal Bipyramidal Dy(III) Single-Ion Magnets. *J. Am. Chem. Soc.* **2016**, *138* (8), 2829–2837. https://doi.org/10.1021/jacs.5b13584.

(49) Cassaro, R. A. A.; Reis, S. G.; Araujo, T. S.; Lahti, P. M.; Novak, M. A.; Vaz, M. G. F. A Single-Chain Magnet with a Very High Blocking Temperature and a Strong Coercive Field. *Inorg. Chem.* **2015**, *54* (19), 9381–9383. https://doi.org/10.1021/acs.inorgchem.5b01431.

(50) Tangoulis, V.; Lalia-Kantouri, M.; Gdaniec, M.; Papadopoulos, Ch.; Miletic, V.; Czapik, A. New Type of Single Chain Magnet: Pseudo-One-Dimensional Chain of High-Spin Co(II) Exhibiting Ferromagnetic Intrachain Interactions. *Inorg. Chem.* **2013**, *52* (11), 6559–6569. https://doi.org/10.1021/ic400557f.

(51) Rinehart, J. D.; Meihaus, K. R.; Long, J. R. Observation of a Secondary Slow Relaxation Process for the Field-Induced Single-Molecule Magnet $U(H_2BPz_2)_3$. *J. Am. Chem. Soc.* **2010**, *132* (22), 7572–7573. https://doi.org/10.1021/ja1009019.

(52) Cosquer, G.; Pointillart, F.; Golhen, S.; Cador, O.; Ouahab, L. Slow Magnetic Relaxation in Condensed versus Dispersed Dysprosium(III) Mononuclear Complexes. *Chem.-Eur. J.* **2013**, *19* (24), 7895–7903. https://doi.org/10.1002/chem.201300397.

(53) Ren, M.; Bao, S.-S.; Ferreira, R. A. S.; Zheng, L.-M.; Carlos, L. D. A Layered Erbium Phosphonate in Pseudo-D5h Symmetry Exhibiting Field-Tunable Magnetic Relaxation and Optical Correlation. *Chem. Commun.* **2014**, *50* (57), 7621. https://doi.org/10.1039/c4cc02085e.

(54) Car, P.-E.; Perfetti, M.; Mannini, M.; Favre, A.; Caneschi, A.; Sessoli, R. Giant Field Dependence of the Low Temperature Relaxation of the Magnetization in a Dysprosium(Iii)–DOTA Complex. *Chem. Commun.* **2011**, *47* (13), 3751. https://doi.org/10.1039/c0cc05850e.

(55) Aquilante, F.; Vico, L. D.; Ferré, N.; Ghigo, G.; Malmqvist, P.-åke; Neogrády, P.; Pedersen, T. B.; Pitoňák, M.; Reiher, M.; Roos, B. O.; Serrano-Andrés, L.; Urban, M.; Veryazov, V.; Lindh, R. MOLCAS 7: The Next Generation. *J. Comput. Chem.* **2010**, *31* (1), 224–247. https://doi.org/10.1002/jcc.21318.

(56) Gagliardi, L.; Lindh, R.; Karlström, G. Local Properties of Quantum Chemical Systems: The LoProp Approach. *J. Chem. Phys.* **2004**, *121* (10), 4494–4500. https://doi.org/10.1063/1.1778131.

(57) Abragam, A.; Bleaney, B. *Electron Paramagnetic Resonance of Transition Ions,*; Clarendon P.: Oxford, 1970.

(58) Chibotaru, L. F.; Ungur, L. *Ab Initio* Calculation of Anisotropic Magnetic Properties of Complexes. I. Unique Definition of Pseudospin Hamiltonians and Their Derivation. *J. Chem. Phys.* **2012**, *137* (6), 064112. https://doi.org/10.1063/1.4739763.

(59) Ungur, L.; Thewissen, M.; Costes, J.-P.; Wernsdorfer, W.; Chibotaru, L. F. Interplay of Strongly Anisotropic Metal Ions in Magnetic Blocking of Complexes. *Inorg. Chem.* **2013**, *52* (11), 6328–6337. https://doi.org/10.1021/ic302568x.

(60) Lines, M. E. Orbital Angular Momentum in the Theory of Paramagnetic Clusters. *J. Chem. Phys.* **1971**, *55* (6), 2977–2984. https://doi.org/10.1063/1.1676524.

(61) Griffith, J. S. Spin Hamiltonian for Even-Electron Systems Having Even Multiplicity. *Phys. Rev.* **1963**, *132* (1), 316–319. https://doi.org/10.1103/PhysRev.132.316.

(62) Ruiz, E.; Cano, J.; Alvarez, S.; Alemany, P. Broken Symmetry Approach to Calculation of Exchange Coupling Constants for Homobinuclear and Heterobinuclear Transition Metal Complexes. *J. Comput. Chem.* **1999**, *20* (13), 1391–1400. https://doi.org/10.1002/(SICI)1096-987X(199910)20:13<1391:AID-JCC6>3.0.CO;2-J.

(63) Langley, S. K.; Wielechowski, D. P.; Vieru, V.; Chilton, N. F.; Moubaraki, B.; Abrahams, B. F.; Chibotaru, L. F.; Murray, K. S. A CrIII2DyIII2 Single-Molecule Magnet: Enhancing the Blocking Temperature through 3d Magnetic Exchange. *Angew. Chem. Int. Ed.* **2013**, *52* (46), 12014–12019. https://doi.org/10.1002/anie.201306329.

(64) Lehmann, J.; Gaita-Ariño, A.; Coronado, E.; Loss, D. Spin Qubits with Electrically Gated Polyoxometalate Molecules. *Nat. Nanotechnol.* **2007**, *2* (5), 312–317. https://doi.org/10.1038/nnano.2007.110.

(65) Wagner, S.; Kisslinger, F.; Ballmann, S.; Schramm, F.; Chandrasekar, R.; Bodenstein, T.; Fuhr, O.; Secker, D.; Fink, K.; Ruben, M.; Weber, H. B. Switching of a Coupled Spin Pair in a Single-Molecule Junction. *Nat. Nanotechnol.* **2013**, *8* (8), 575–579. https://doi.org/10.1038/nnano.2013.133.

(66) Vincent, R.; Klyatskaya, S.; Ruben, M.; Wernsdorfer, W.; Balestro, F. Electronic Read-out of a Single Nuclear Spin Using a Molecular Spin Transistor. *Nature* **2012**, *488* (7411), 357–360. https://doi.org/10.1038/nature11341.

(67) Yasuda, H.; Ohnuma, Y.; Yamauchi, M.; Tani, H.; Nakamura, A. Chemistry of Dienyl Anions. I. Crystalline Dienyl Anions by Direct Reaction of Conjugated and Non-Conjugated Dienes with Alkali Metals in the Presence of Et_3N. *Bull. Chem. Soc. Jpn.* **1979**, *52* (7), 2036–2045. https://doi.org/10.1246/bcsj.52.2036.

(68) Schuetz, S. A.; Day, V. W.; Sommer, R. D.; Rheingold, A. L.; Belot, J. A. Anhydrous Lanthanide Schiff Base Complexes and Their Preparation Using Lanthanide Triflate Derived Amides. *Inorg. Chem.* **2001**, *40* (20), 5292–5295. https://doi.org/10.1021/ic010060l.

(69) *V.2012 Bruker AXS*; Bruker: Madison, Wisconsin, 2005.

(70) Blessing, R. H. An Empirical Correction for Absorption Anisotropy. *Acta Crystallogr. A* **1995**, *51* (1), 33–38. https://doi.org/10.1107/S0108767394005726.

(71) Sheldrick, G. M. A Short History of *SHELX*. *Acta Crystallogr. A* **2008**, *64* (1), 112–122. https://doi.org/10.1107/S0108767307043930.

Chapter 5

Influence of Equatorial Ligands in a Highly Axial Bis-Amide Single-Molecule Magnet

5.1 Introduction

Magnetic anisotropy is arguably the most influential parameter that determines the performance of a lanthanide single-molecule magnet (SMM). The ability to design molecular species with defined magnetic axiality has allowed chemists to produce molecules with large energy barriers to spin reversal (U_{eff}) and, in some cases, magnetic blocking, reaching blocking temperatures (T_{B}) as high as 80 K.[1] Those SMMs containing only a single metal center, single-ion magnets (SIMs), have recently garnered significant interest in the field of molecular magnetism, as the observed magnetic properties exist in the absence of magnetic exchange interactions, meaning that the experimentally determined performance of SIMs must arise from the combination of unquenched orbital angular momentum and crystal field contributions. This allows for a tailored synthetic approach, which, in recent years, has evolved to include high symmetry crystal fields,[2–5] the introduction of main group ligands,[6] and the implementation of bulky ligands to obtain low coordination numbers.[7] The common theme among all of these approaches is to harness the maximum magnetic anisotropy from the lanthanide (Ln) ion. The inherent magnetic anisotropy of the 4f ions results from the combination of large magnetic moments and spin-orbit coupling, in which contributions from the crystal field can significantly enhance the magnetic anisotropy of a lanthanide SIM. In this respect, recent reports focused on generating design criteria for eliciting strictly axial anisotropy.[8,9]

The motivation for the study presented herein resulted from the work presented in Chapter 4, along with the findings from a previous study in the Murugesu group. These independent reports investigated the magnetic coupling and SMM behaviour in a series of dinuclear lanthanide SMMs bridged through aromatic carbocycles.[10,11] Both studies confirmed that despite magnetic coupling occurring through the 7- and 6-membered rings, their presence ultimately hindered the SMM properties. More specifically, the work on the 6-membered tetranionic biphenyl systems utilized a rigid ferrocene diamide framework to support the inverse sandwich architecture, that possessed unprecedented uniaxial anisotropy, along the shortest Dy-N bond.[10] Thus, by removing the central bridging moiety, the crystal field imposed by the amide groups would, in theory, lead to enhanced SMM properties, since linearly coordinated negatively charged donor atoms may harness the maximum angular momentum of the Dy^{III} ion. This unique class of diamide ligands parallels the structural features of the diketiminates that have been popular in the fields of molecular magnetism, catalysis, and bioinorganic chemistry.[12,13] However, the ferrocene diamides are dianionic as opposed to the monoanionic nature of diketiminates and have the ability to produce a wider bite angle, while still maintaining a rigid backbone. The latter is an attractive feature for increasing the linearity and mimicking two-coordinate Dy^{III} compounds, which remain a synthetic challenge. Thus, these designer ligands represent a promising alternative to generating pseudo-axiality in Dy^{III} compounds. To this end, the static and dynamic magnetic properties of $(NN^{TBS})Dy^{III}(I)(THF)_2$, **7-Dy** ($NN^{TBS}$ = $fc(NHSi^{t}BuMe_2)_2$, fc = 1,1′ ferrocenediyl, Figure 5.1) are presented herein, along with fragment *ab initio* calculations which together elucidate a unique approach toward Dy^{III} molecules with defined magnetic axiality.

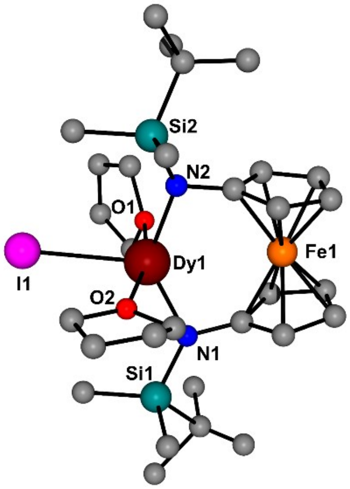

7-Dy

Figure 5.1 Molecular structure of $(NN^{TBS})Dy^{III}(I)(THF)_2$, **7-Dy** ($NN^{TBS}$ = $fc(NHSi^{t}BuMe_2)_2$, fc = 1,1′ ferrocenediyl). Colour code: dark red (Dy^{III}), orange (Fe^{II}), pink (I), teal (Si), blue (N), red (O), grey (C). Hydrogen atoms and disorder have been omitted for clarity.

5.2 Results and Discussion

5.2.1 Structural Description

The synthesis and structure of **7-Dy** were previously reported along with the tetranionic biphenyl complexes;[10] however, for the purpose of establishing a connection between the molecule and its magnetic properties, the structure will be discussed herein. Complex **7-Dy** crystallizes in the triclinic space group *P*-1. Each asymmetric unit contains one Dy^{III} ion coordinated to one NN^{TBS} ligand through two anionic nitrogen atoms, producing a bite angle of 134.7(2)°. The coordination sphere is completed by two molecules of THF and an iodide. The exact geometry of this five-coordinated Dy^{III} was confirmed *via* SHAPE analysis, producing results consistent with a trigonal bipyramidal geometry of D_{3h} symmetry (Table 5.1).[14]

Table 5.1 SHAPE analysis of **7-Dy** relative to an ideal 5-vertex polyhedron shown.[14] The best match is displayed in bold.

SHAPE Code	Point Group	Description	1-Dy
PP-5	D_{5h}	Pentagon	34.648
vOC-5	C_{4v}	Vacant octahedron	7.187
TBPY-5	D_{3h}	Trigonal bipyramid	**1.004**
SPY-5	C_{4v}	Square pyramid	5.330
JTBPY-5	D_{3h}	Johnson trigonal bipyramid	4.762

Short Dy-N distances of 2.21(2) and 2.20(6) Å are observed, with less than fifteen reported examples with Dy-N distances shorter or equal to 2.20 Å;[15–23] a significant number of these examples are endohedral metallofullerenes (*ca.* 2.06 Å) in which the N-atom does not bear any substituents.[24–26] The Dy-N distances of **7-Dy** are smaller than the sum of the ionic radii (2.62 Å),[27] suggesting that a dominant electrostatic interaction exists between the N-atoms of the NN^{TBS} ligand and the Dy^{III} ion. The presence of such strong interactions in the axial positions of this Kramers ion has the ability to harness significant magnetic anisotropy, through taking advantage of its oblate electron density.[28] Theoretically, large T_B and U_{eff} values may be expected to arise from such a bonding interaction. Moreover, the remaining ligands are expected to play a less dominate role for the orientation of the anisotropy axis. The Dy-I distance of 3.090(2) Å is marginally longer than that found in [Dy^{III}(η^5-Cp")$_2$(I)] (Cp" = 1,2,4-tris(trimethylsilyl)cyclopentadienyl; 2.901 Å),[29] [Dy^{III}(Cp*)$_2$(I)(THF)] (2.982 Å),[30] and [Dy^{III}(η^8-COT)(I)(THF)$_2$] (3.053 Å);[31] whereas the Dy-O distances of 2.367(3) Å and 2.389(6) Å are commonly observed for molecules with coordinated THF. Within the lattice, a minimum Dy^{III}–Dy^{III} distance of 9.776(5) Å is achieved. While direct and superexchange pathways have been considered negligible at this distance, intermolecular dipolar interactions remain a possibility. At such a scale, slower relaxation processes have been attributed to dipolar mediated relaxations in 5f SIMs.[32] Collectively, the presence of strong metal-ligand interactions along a defined orientation and the well separated nature of the paramagnetic centers are expected to yield strong slow relaxation dynamics originating from the Dy^{III} ion.

5.2.2 Direct Current Magnetic Susceptibility

The magnetic properties of **7-Dy** were measured using a SQUID magnetometer. Under an applied static field of 1000 Oe, a room temperature χT value of 13.99 cm^{3}Kmol^{-1} is achieved, that is in good agreement with the theoretical value of 14.17 cm^{3}Kmol^{-1} for a Dy^{III} ($^6H_{15/2}$, $S = 5/2$, $L = 5$, $g = 4/3$) ion (Figure 5.2). The obtained value is slightly smaller than the theoretical value, presumably due to the splitting of the $^6H_{15/2}$ ground state.[2] Upon cooling, the χT product remains relatively constant until 8 K, revealing a well separated low-lying energy spectrum (*vide infra*). Below this temperature, the χT product rapidly drops, to a minimum value of 9.67 cm^{3}Kmol^{-1} 1.8 K. The abrupt decrease in the χT profile is indicative of magnetic blocking, where the system cannot reach an equilibrated population distribution. This phenomenon has been observed in other highly anisotropic SMMs.[2,7,33,34] To complement this, the *iso*-temperature magnetization curve at 1.9 K saturates at 5.28 μ_B mol^{-1}, further suggesting the well separated nature of the ground state (Figure 5.3). Large separations between the ground state and excited states are highly sought after as they typically lead to large spin reversal barriers. This finding is also in accordance with the *ab initio* determined energy of the second Kramers doublet (KD), possessing an energy of 414.6 cm^{-1} (*vide infra*). This is one of the largest separations observed between the ground and excited states in any Dy^{III} SMMs.[2,7,33,34] This large separation ensures that thermal relaxation will at least occur *via* this energy, yielding an impressive barrier to the slow relaxation of the magnetization.

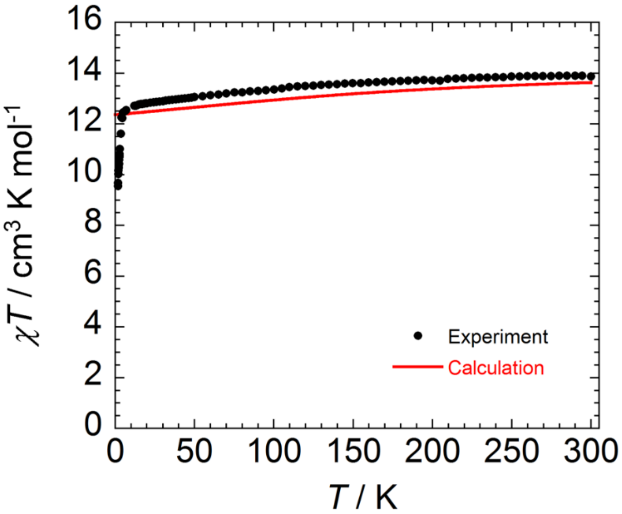

Figure 5.2 Temperature dependence of the χT product at 0.1 T for **7-Dy**. Experimental data is represented by black circles and *ab initio* calculated magnetic susceptibility depicted by the solid red line.

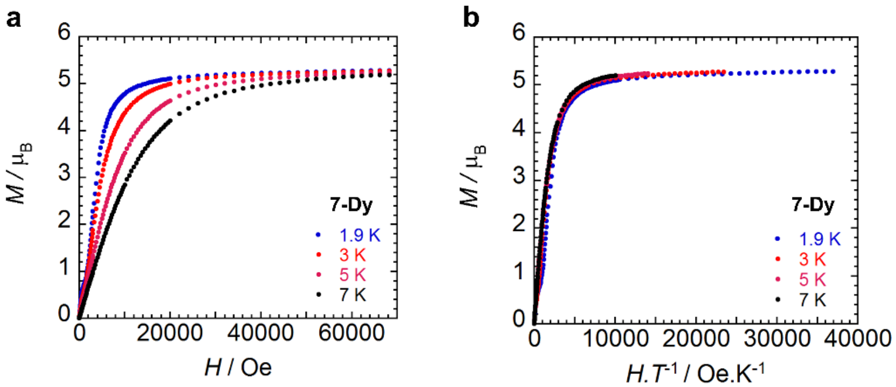

Figure 5.3 (a) Field dependence of the magnetization and (b) the reduced magnetization for **7-Dy** at the indicated temperatures

As the variable temperature susceptibility and variable field magnetization measurements have indicated desirable properties in terms of magnetic anisotropy, the presence of magnetic blocking was then probed with magnetic hysteresis measurements. Using an average field sweep rate of 23 Oes^{-1}, the dc field was sweeped in the range of 50 to -50 kOe eliciting clear magnetic hysteresis at 1.9 K for **7-Dy** (Figure 5.4).

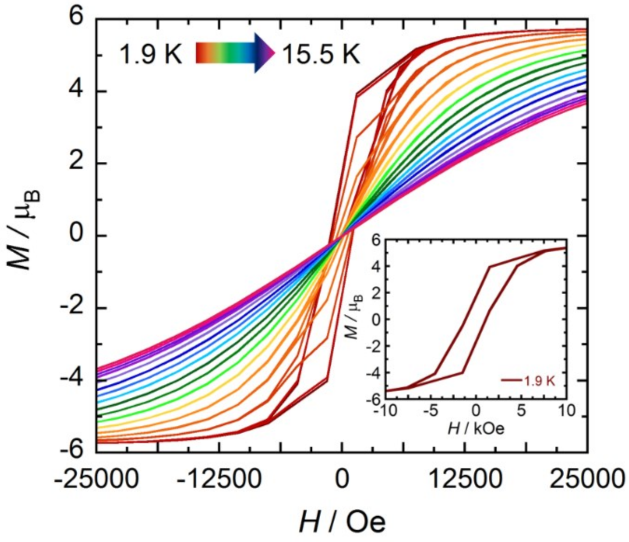

Figure 5.4 Magnetic hysteresis data for **7-Dy** between 1.9 and 15.5 K. Data were collected at an average sweep rate of 23 Oe s^{-1}. In all measurements, data were collected starting at $H = 0$ Oe, sweeping to $H = 50$ kOe, and then cycling to $H = -50$ kOe and back to $H = 50$ kOe. *Inset*: magnetic hysteresis data depicting coercivity at 1.9 K.

With successive cycling, the temperature was increased to 2.0 K and up to a maximum of 15.5 K in increments of 0.5 K. Distinct openings at zero field were observed up to a maximum temperature of 5 K, after which only minor openings can be observed up to 14 K at higher magnetic fields. Comparatively, the abrupt drop in the χT product at 8 K also serves as a reference in terms of magnetic blocking. However, the discrepancy between these observed values may result as a consequence of mixed relaxation processes, specifically Raman and direct relaxation mechanisms that can occur at low temperatures.[7] The possibility of mixed relaxation mechanisms cannot be discarded given the low temperature data of the alternating current (ac) susceptibility, as well as the obtained distribution of relaxation times (*vide infra*).

5.2.3 Alternating Current Magnetic Susceptibility

Ac susceptibility measurements were completed in the absence of an applied static field (H_{dc} = 0 Oe), within the range 0.1-1500 Hz. Under these conditions, a signal was observed in the in-phase (χ') and out-of-phase (χ") components of the ac susceptibility between 1.9 and 60 K (Figure 5.5).

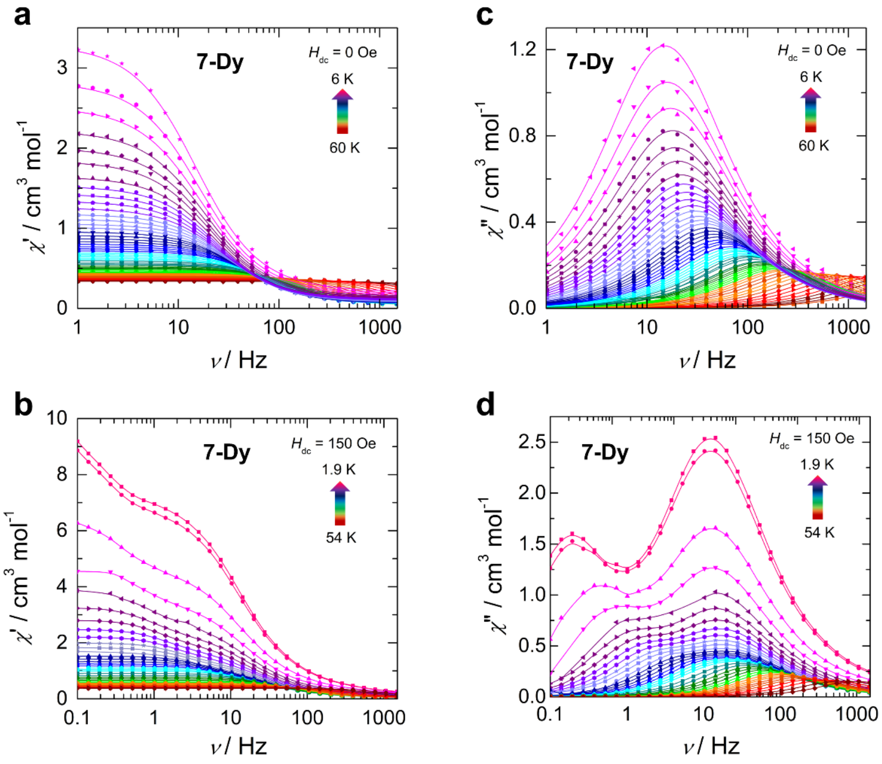

Figure 5.5 Frequency dependence of the (a-b) in-phase (χ') and (c-d) out-of-phase (χ") components of the ac susceptibility for **7-Dy** in the absence of an applied static field, H_{dc} = 0 Oe (*top*), and under an applied field, H_{dc} =150 Oe (*bottom*), at the indicated temperatures. Solid lines represent best fits to the generalized Debye model.

Frequency dependent behaviour was obtained with shifting peak maxima toward lower frequency, indicating slow relaxation of the magnetization. The relaxation times (τ) were extracted for each isotemperature curve of the χ' and χ" susceptibilities *via* the generalized Debye model.[35] A narrow distribution of relaxation times was found, yielding α-values ≤ 0.17 over the entire data set. Comparatively, fitting the Argand plots to the generalized Debye model produced similar results (α ≤ 0.22), with only a single deviation occurring for the 6 K curve (α = 0.50), therefore indicating that a reasonable and reproducible fit of the relaxation times was achieved.

The zero-field relaxation times extracted from the χ" data were then plotted on *ln*(τ) *vs.* T^{-1} axes and fit to the Arrhenius law (i.e., linear fit) to determine the extent of magnetic relaxation *via* thermally activated processes, namely Orbach relaxation (Equation 5.1). The best-fit parameters yielded an effective energy barrier to spin reversal of U_{eff} = 770.8 K (535.7 cm^{-1}) and a pre-exponential factor of τ_0 = 8.20 x 10^{-11} s (Figure 5.6a). While there are now examples of energy barriers that exceed this, a U_{eff} of this magnitude is rare in lanthanide-based systems as they often exhibit significant ground state tunneling arising from their classically dense energy spectra.[36] Indeed, there are only a few compounds which belong to this family of high U_{eff} (>700 K) SIMs.[1,5,7,33,37]

$$\tau^{-1} = \tau_0^{-1}\exp\left(-\frac{U_{\mathrm{eff}}}{k_B T}\right) \tag{5.1}$$

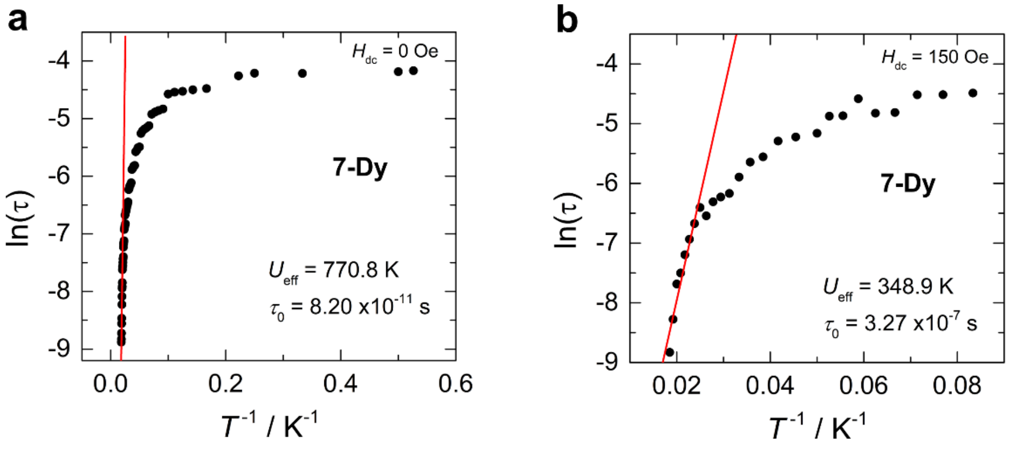

Figure 5.6 Arrhenius plot using χ" ac data for **7-Dy** collected (a) in the absence of an applied static field, H_{dc} = 0 Oe, and (b) under an applied field, H_{dc} = 150 Oe. The solid line represents the fit of the linear high temperature region to Equation 5.1.

With respect to **7-Dy**, the obtained U_{eff} of 770.8 K is in good agreement with the calculated thermally activated relaxation through the third and fourth KDs (Figure 5.8). The plot of $ln(\tau)$ *vs.* T^{-1} remains linear in the high temperature regime (Figure 5.6a), strongly correlating to a dominant thermally activated Orbach relaxation regime.[38] The plot remains linear until 26 K, when it experiences a deviation from linearity and the Arrhenius law. The observed behavior may arise from mixed relaxation mechanisms (e.g., Orbach and Raman, Raman and QTM, etc.), although it is likely dominated by QTM, which was abundantly present in the magnetization hysteresis measurements.

To probe any contribution of QTM to the obtained U_{eff} at zero-field, ac measurements were completed at a fixed temperature $T = 2$ K, and the applied static field was varied from 0-1200 Oe (Figure 5.7). The plot of χ" *vs.* ac frequency yielded a bimodal profile. At 100 Oe, a shoulder at low frequencies becomes evident, and is augmented by increased static fields until 400 Oe, where no signal was observed. This has similarly been observed at small fields in other Dy^{III} SIMs.[39] The Argand plots were fit *via* the generalized Debye model, providing a distribution of field dependent relaxation times with $0.89 \geq \alpha \geq 0.25$. To determine the origin of the secondary process, ac measurements were completed under an optimal dc field of 150 Oe. Within the temperature range 1.9-54 K a frequency dependent signal in the χ' and χ" components of the ac susceptibility was observed (Figure 5.5). Below 16 K, there is minimal shifting of the χ" peak maxima, as well as the introduction of the second, low frequency, process. Fitting the data to the Arrhenius laws yields $U_{\text{eff}} = 348.9$ K (242.5 cm^{-1}) and $\tau_0 = 3.27 \times 10^{-7}$ s (Figure 5.6b). Fitting this process revealed a distribution of relaxation times to give $0.011 \leq \alpha \leq 0.404$. From these observations, the application of static fields diminishes the SMM behavior of **7-Dy**.

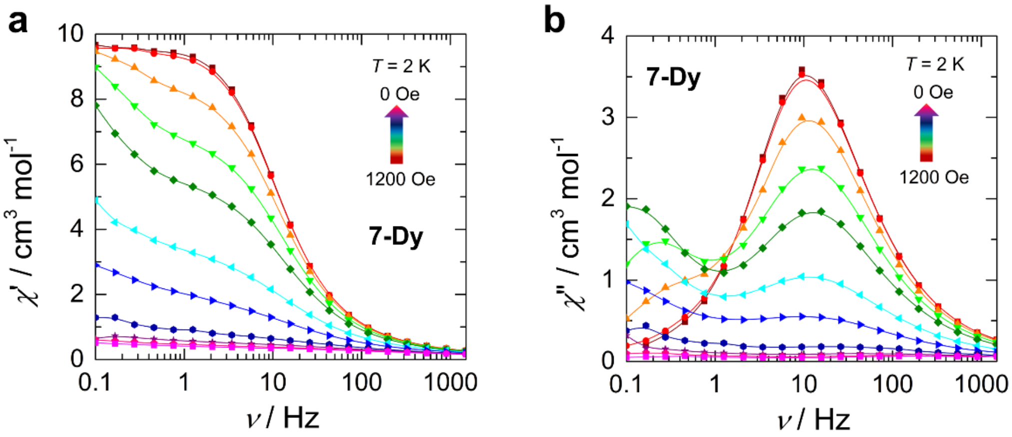

Figure 5.7 Frequency dependence of the (a) in-phase (χ') and (b) out-of-phase (χ") components of the ac susceptibility as a function of applied static field at 2 K for **7-Dy**. Lines are a guide for the eye.

5.2.4 Theoretical Analysis

Ab initio calculations were performed in order to gain additional insight into the magnetic properties and to analyze the factors that govern the magnetization blocking barrier. The magnetization blocking barrier for **7-Dy** was calculated using a previously established methodology (Figure 5.8).[40,41] The presence of zero-field SMM behaviour is rationalized on the basis of a small transverse magnetic moment of $1.5\text{x}10^{-4}$ μ_B in the ground state, that limits QTM. Similarly, tunneling through thermally activated $m_j = \pm13/2$ states (KD2; assuming purity of the low lying KDs is maintained) is also minimized, this is due to the co-linearity of the anisotropic axes of the first and second KDs (Figure 5.9). These findings correlate with the obtained *g*-tensors (Table 5.2), demonstrating significant magnetic axiality even at the $m_j = \pm11/2$ states (KD3). Given the transverse magnetic moments (indicated above the arrows in Figure 5.8), the most probable pathway for magnetic relaxation encompasses the third and fourth KDs, while the U_{eff} lies only marginally below the third KD. Thus, the presence of mixed relaxation mechanisms may contribute to the lowering of U_{eff} from the anticipated energy of the third KD. Notably, the magnetic moment of an Orbach relaxation from $m_j = -13/2$ (KD2-) to $m_j = +9/2$ (KD4+) is only narrowly smaller than the tunneling between $m_j = \pm11/2$ states (KD3), $4.2 \text{ x } 10^{-1}$ μ_B *vs*. $4.5 \text{ x } 10^{-1}$ μ_B, that would suggest that a competition between these two pathways may also contribute to the lowering of the experimental barrier.

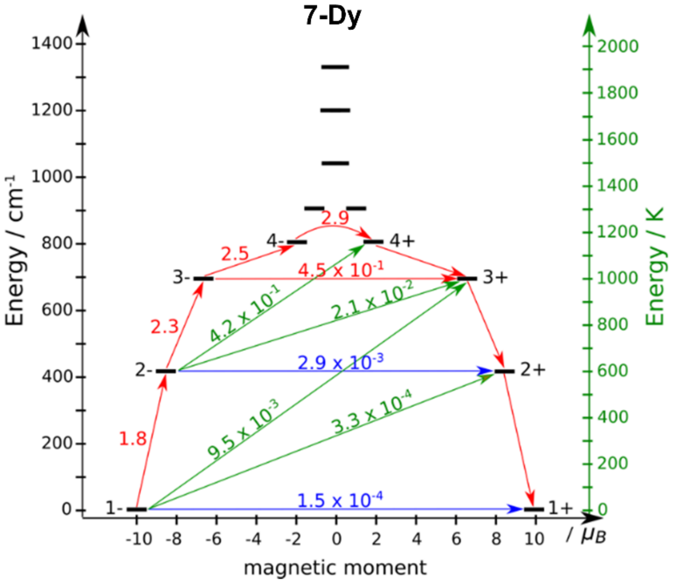

Figure 5.8 Magnetization blocking barrier of **7-Dy**. Arrows depict the most probable path for magnetic relaxation (red), QTM (blue), and Orbach relaxation (green). At temperatures where $ln(\tau) = f\left(\frac{1}{T}\right)$ dependence is linear, the temperature assisted relaxation *via* KD4 is dominant.

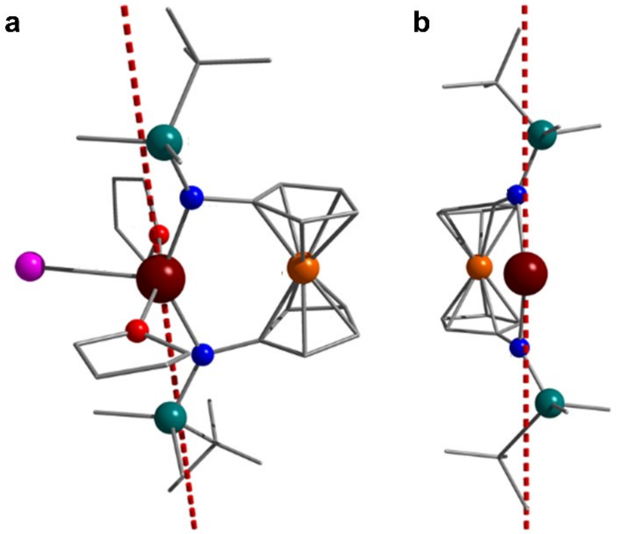

Figure 5.9 Calculated orientation of the main axis of **7-Dy** superimposed on the (a) molecular structure and (b) the fragment of the molecule depicting the metal-ligand bonding. Red dashed lines represent the magnetic axis in the ground, first excited, and second excited KD states (KD1-KD3). Colour code: dark red (Dy), orange (Fe), pink (I), teal (Si), blue (N), red (O), grey (C). Hydrogen atoms and disorder have been omitted for clarity.

Moreover, at a first glance, the matrix element connecting the opposite components of KD3 is sufficiently large (0.45 μ_B) to suggest that this doublet is the top of the barrier. However, this transition matrix moment is much larger (2.9 μ_B) for KD4, so that tunneling through the barrier can take place at this doublet when the temperature is sufficiently high. The rate of the thermally assisted tunneling transition is the product of the Boltzmann population of a given doublet and the rate of the incoherent tunneling transition between the components with opposite magnetization (i.e., KD3+ and KD3-).[42] The latter is roughly proportional to the square of the magnetic moment, μ, of the corresponding doublet state,[41] the rate of the thermally assisted tunneling is proportional to $\sim\mu^2 e^{-\frac{E}{kT}}$, where E is the energy of the doublet and k is the Boltzmann constant. Using the data from Table 5.2 and Figure 5.8, the temperature dependence of this function is plotted below (Figure 5.10). At $T = 52$ K, the ratio between relaxation *via* KD4 and KD3 ≈ 2, while this ratio doubles its value already at $T = 70$ K; this ratio exhibits a near linear increase with temperature, implying that the activated relaxation *via* the KD4 becomes dominant in the temperature domain where a linear $ln(\tau) = f\left(\frac{1}{T}\right)$ dependence is observed.

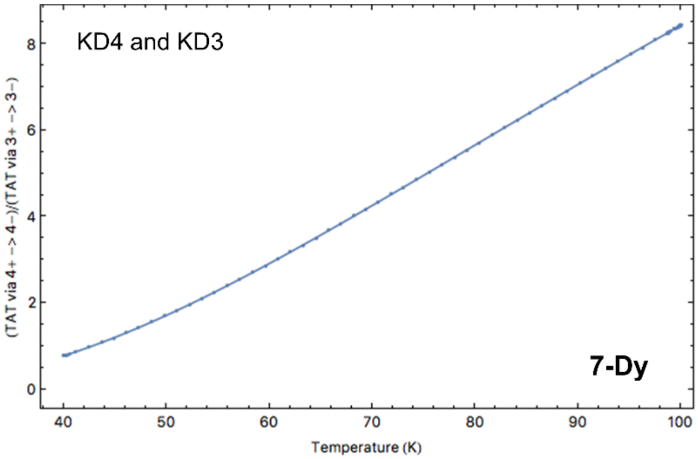

Figure 5.10 Temperature dependence of the ratio between the thermally assisted tunneling transition rates in KD4 and KD3 of **7-Dy**.

It is important to mention that *ab initio* results are not based on direct fitting of the experimental data (compared to various phenomenological models).[43] The methods may also be applied for the investigation of molecules prior to their synthesis for the evaluation of molecular properties. In this respect, three different models have been developed and analyzed in addition to **7-Dy**, in order to study the effects of the THF and iodide ligands on the magnetic properties of the title molecule. The three models have been prepared from the sequential removal of the ancillary ligands (I or THF) and their respective formal charges, producing three chemically sensible models: **7-noTHF** – containing no THF ligands, **7-noI** – containing no iodide ligand and **7-noTHFnoI**– where THF and iodide ligands were removed from the molecular structure (Figure 5.11). These models allow for a direct study of the ligand field effects that originate in **7-Dy**. In understanding the factors that contribute to lowering the U_{eff}, improved methods for augmenting the local magnetic axiality in other low coordinate $\mathrm{Dy^{III}}$ systems may be developed. The energy splitting of the ground free ion $J = 15/2$ was obtained for all models and the title compound (Figure 5.12 and Table 5.2). Analysis of the low-lying energy spectra reveals a strong increase in the splitting of the ground free ion in **7-noTHF**, as well as in **7-noI**. With respect to the second KD, there is a 15.8 % and 15.1 % increase in the energy splitting for **7-noTHF** and **7-noI**, respectively. While the difference between **7-noTHF** and **7-noI** is minimal, in the third KD, the effect of the THF compound is greater. Removal of such moieties produces a 22.2 % increase over **7-Dy**, whereas removal of the iodide ligand only produces a 13.7 % increase.

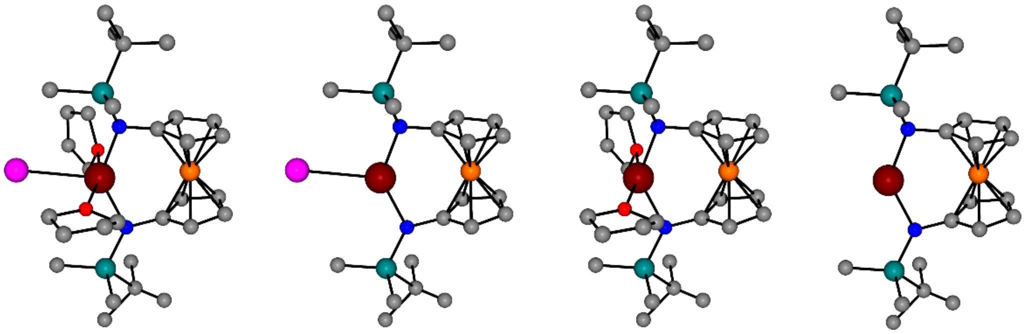

7-Dy **7-noTHF** **7-noI** **7-noTHFnoI**

Figure 5.11 Structural representations of the title compound (**7-Dy**) and the computational models based on the sequential removal of the equatorial ligands and their respective formal charges. Hydrogen atoms and disorder have been omitted for clarity. Colour code: dark red (Dy), orange (Fe), pink (I), teal (Si), blue (N), red (O), grey (C).

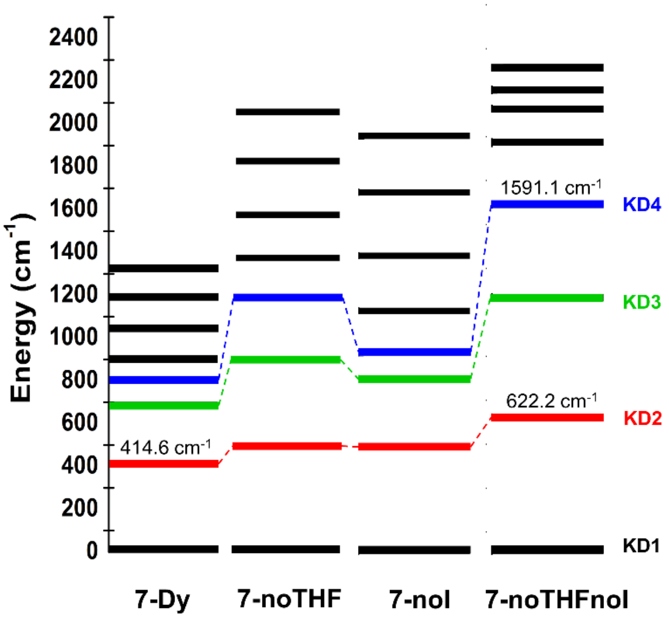

Figure 5.12 Comparison of the energy splitting of the ground free ion $J = 15/2$ multiplet for **7-Dy** and the three computational models.

This is conceivable as Dy-I bonds are characteristically weak, meaning that their contribution to the total ligand field of **1-Dy** is less relative to the oxophilic interaction of Dy^{III} with THF. It is suspected that the

THF molecules are producing a competitive ligand field, perpendicular to that generated by the N-atoms of NN^{TBS}, which likely contributes to the diminished U_{eff}.

Table 5.2 Energy splitting of the ground free ion J=15/2 multiplet in various computational models (cm^{-1}) and magnetic anisotropy in the lowest four Kramers doublet states.

KD		**7-Dy**	**7-noTHF**	**7-noI**	**7-noTHFnoI**
1		**0.0**	**0.0**	**0.0**	**0.0**
2		**414.6**	**492.5**	**488.8**	**622.2**
3		**692.2**	**890.3**	**802.0**	**1166.5**
4		803.0	1176.9	921.4	**1591.1**
5		903.3	1359.1	1111.5	1874.0
6		1038.8	1557.3	1364.1	2025.3
7		1197.7	1804.6	1653.0	2112.5
8		1327.8	2030.6	1911.8	2213.4
g tensors in the low-lying Kramers doublet states					
1	g_X	4.4 x 10^{-4}	2.4 x 10^{-5}	4.3 x 10^{-4}	3.2 x 10^{-8}
	g_Y	4.9 x 10^{-4}	3.0 x 10^{-5}	5.6 x 10^{-4}	1.6 x 10^{-7}
	g_Z	19.8894	19.8986	19.9113	19.9677
2	g_X	0.0066	2.0 x 10^{-3}	0.0412	2.5 x 10^{-5}
	g_Y	0.0104	2.6 x 10^{-3}	0.0651	2.6 x 10^{-5}
	g_Z	16.9721	16.8893	16.7914	17.0067
3	g_X	0.8911	0.1210	2.2968	0.0010
	g_Y	1.7114	0.1662	6.0679	0.0011
	g_Z	13.2157	13.7224	10.5290	14.1568
4	g_X	3.8174	2.0871	7.2834	0.0328
	g_Y	5.0097	3.0000	6.0380	0.0350
	g_Z	11.4701	9.7303	1.5554	11.4146

In the absence of transverse ligands, **7-noTHFnoI** displays a 33.3 % increase in the energy splitting of the first KD, with $g_Z >> g_X$, g_Y, even in the fourth KD (Table 5.2). This produces a near three-fold improvement (535.7 cm^{-1} *vs.* 1591.1 cm^{-1}) on the U_{eff} compared to that of **7-Dy**. The obtained *g*-tensors for **7-noI** in the fourth KD are less axial in comparison to **7-Dy**, whereas **7-noTHF** and **7-Dy** display similar *g*-tensors. The inferior axiality of **7-noI** can be explained once again by the ligand field generated by the remaining THF, thus demonstrating the immediate significance of removing or replacing these moieties with weaker-field ligands. Through this systematic study of *g*-tensors combined with the low-lying energy spectra, new insights to improve the local magnetic axiality of molecular species are achieved. Therefore, suitable equatorial ligands that do not affect the crystal field splitting of the lanthanide ion are required or if possible, new molecular systems should preclude the use of equatorial ligands.[7,9]

5.3 Summary and Conclusion

The work presented herein highlights a new design approach towards mimicking the elusive two coordinate Dy^{III}, although the presence of coordinated solvent and an iodide ligand prevent the maximum U_{eff} that could theoretically be achieved for such a system (≈1600 cm^{-1}). The functionalized ferrocene backbone of the NN^{TBS} ligand offers a unique synthetic approach towards harnessing single-ion anisotropy. Through careful synthetic modifications, the contributions of the equatorial/transverse ligands may be altered by replacement with weaker crystal field ligands, effectively allowing for fine tuning of the magnetic axiality. While two coordinate Dy^{III} compounds will undoubtedly remain a synthetic challenge, the use of rigid diamide ligands represents a promising approach for imposing pseudo-axial ligand fields in the development of high temperature lanthanide-based SIMs with predictable and defined magnetic axiality.

5.4 Experimental Details

5.4.1 Magnetometry

The magnetic susceptibility measurements were obtained using a Quantum Design SQUID magnetometer MPMS-XL7 operating between 1.8 and 300 K for dc fields ranging from -7 to 7 T. Dc susceptibility measurements were performed on a polycrystalline sample (30 mg) of **1-Dy** sealed in a polyethylene membrane prepared under an inert atmosphere, and subjected to a field of 0 to 7 T. Ac susceptibility measurements were carried out under an oscillating field of 3.78 Oe and ac frequencies 0.1 to 1500 Hz and dc fields ranging from 0 to 1200 Oe. The magnetization data were collected at 100 K to check for ferromagnetic impurities that were absent in the sample. Diamagnetic corrections were applied for the sample holder and the inherent diamagnetism of the sample was estimated with the use of Pascals constants.

5.4.2 Computational Details

All calculations were of the CASSCF/RASSI/SINGLE_ANISO kind using the MOLCAS-8.0 program package.[44] All atoms were described using all electron relativistic ANO-RCC basis sets.[45] Basis set contractions are given in Table 5.3. Standard complete active space self-consistent field (CASSCF) calculations on the full molecular structure were performed.[46] In these calculations, the $4f^9$ electronic shell of the Dy^{III} is explicitly correlated, i.e., the active space, while the remaining orbitals are described in the mean field approach (as in the conventional Hartree-Fock SCF model). All possible electronic states (of various total spins) arising from the chosen active space were optimized self-consistently and a subset of them was further mixed by the spin-orbit coupling (RASSI).[47]

Table 5.3 Contractions of the employed basis sets describing each atom in the investigated molecules (**7-Dy**, **7-noTHF**, **7-noI**, and **7-noTHFnoI**).

Atom	**Basis set contraction**	
Dy	8s7p5d3f2g1h	ANO-RCC-VTZP.
I	7s6p4d2f1g	ANO-RCC-VTZP.
Fe	6s5p3d2f1g	ANO-RCC-VTZP
Si	5s4p2d1f	ANO-RCC-VTZP
O	4s3p2d1f	ANO-RCC-VTZP
N	4s3p2d1f	ANO-RCC-VTZP
C (close)	4s3p2d1f	ANO-RCC-VTZP
C (distant)	3s2p1d	ANO-RCC-VDZP
H	2s1p	ANO-RCC-VDZP

Relativistic effects were considered in two steps, both based on Douglas Kroll Hess Hamiltonian. Scalar relativistic effects are included in the basis sets describing each atom (Table 5.3). All mono and bielectronic integrals (Couloumb, Exchange, angular momentum, AMFI, etc.) in this basis are computed and used in the subsequent calculations. Complete active space self consistent-field calculations were carried out using the $4f^9$ shell of the $\mathrm{Dy^{III}}$ site as active space. All possible electronic states arising from the active space were calculated in the mean field of other electrons. 21 spin sextet, 128 spin quartet and 130 spin doublet states were admixed by the spin-orbit coupling in the RASSI method. The spin orbit coupling was accounted within Atomic Mean Field approximation (AMFI). On the basis of the resulting spin-orbit states, all magnetic properties were computed within the SINGLE_ANISO program in MOLCAS 8.0. The parameters of the effective crystal-field Hamiltonian were extracted and are displayed in Table 5.4.

Table 5.4 Parameters of the crystal field acting on the ground J = 15/2 multiplet for all investigated structures, corresponding to the *ab initio* calculations described above. Quantization axis is chosen as the main anisotropy axis in the ground Kramers doublet state (approx. N1-N2 direction).

Rank	Proj.	7-Dy	7-noTHF	7-noI	7-noTHFnoI
2	-2	**-0.400645E+01**	0.101038E+00	**-0.106631E+01**	**-0.161376E+01**
	-1	0.405941E+00	-0.466676E+00	-0.184903E-01	0.440251E-01
	0	**-0.647155E+01**	**-0.103589E+02**	**-0.862108E+01**	**-0.129657E+02**
	1	-0.258180E+00	0.129652E+00	-0.993762E-01	0.351901E-01
	2	-0.536278E+00	**0.716930E+01**	**0.891364E+01**	**0.156931E+01**
4	-4	-0.176839E-01	-0.314061E-02	0.872897E-02	-0.232835E-03
	-3	0.182484E-02	0.166613E-02	-0.553989E-03	-0.650243E-03
	-2	0.161532E-01	-0.580665E-02	0.103611E-01	-0.649060E-02
	-1	-0.218958E-02	0.321342E-02	-0.140399E-03	0.318659E-03
	0	-0.740658E-02	-0.552651E-02	-0.845928E-02	**-0.719447E-02**
	1	0.205642E-02	-0.129581E-02	0.244054E-03	-0.388185E-03
	2	0.129277E-01	0.234839E-02	-0.195618E-01	-0.138344E-02
	3	0.245634E-02	-0.238604E-02	-0.200580E-04	-0.531144E-03
	4	0.194404E-01	-0.373949E-02	-0.190455E-01	-0.196106E-02
6	-6	-0.660711E-04	-0.319114E-04	0.149223E-03	-0.196025E-05
	-5	0.769051E-04	0.530290E-04	-0.270091E-04	0.492283E-05
	-4	-0.737630E-04	-0.479799E-04	0.303649E-04	0.764432E-05
	-3	0.838110E-05	0.359969E-04	-0.581991E-05	-0.501807E-06
	-2	-0.830042E-05	0.320602E-04	-0.677317E-04	**0.105020E-03**
	-1	-0.114537E-04	0.627986E-05	0.478879E-05	0.452025E-06
	0	0.487678E-05	0.208189E-04	0.165015E-04	0.335544E-04
	1	-0.364130E-05	0.793350E-05	-0.218247E-06	0.463353E-05
	2	-0.671008E-04	-0.152339E-03	-0.408894E-04	-0.311725E-04
	3	0.394618E-04	-0.226759E-05	0.536208E-05	0.982786E-05
	4	0.151552E-03	-0.223556E-04	-0.156674E-03	-0.344556E-04
	5	-0.112542E-04	-0.501193E-04	-0.626646E-05	0.332071E-05
	6	-0.155335E-03	-0.267344E-04	-0.142060E-03	-0.113796E-04
Recovery factor of the initial ab initio CF matrix*					
		99.2%	99.0%	99.3%	99.0%

5.5 References

(1) Guo, F.-S.; Day, B. M.; Chen, Y.-C.; Tong, M.-L.; Mansikkamäki, A.; Layfield, R. A. Magnetic Hysteresis up to 80 Kelvin in a Dysprosium Metallocene Single-Molecule Magnet. *Science* **2018**, *362* (6421), 1400–1403. https://doi.org/10.1126/science.aav0652.

(2) Chen, Y.-C.; Liu, J.-L.; Ungur, L.; Liu, J.; Li, Q.-W.; Wang, L.-F.; Ni, Z.-P.; Chibotaru, L. F.; Chen, X.-M.; Tong, M.-L. Symmetry-Supported Magnetic Blocking at 20 K in Pentagonal Bipyramidal

Dy(III) Single-Ion Magnets. *J. Am. Chem. Soc.* **2016**, *138* (8), 2829–2837. https://doi.org/10.1021/jacs.5b13584.

(3) Meihaus, K. R.; Long, J. R. Magnetic Blocking at 10 K and a Dipolar-Mediated Avalanche in Salts of the Bis(η^8-Cyclooctatetraenide) Complex $[\mathrm{Er(COT)_2}]^-$. *J. Am. Chem. Soc.* **2013**, *135* (47), 17952–17957. https://doi.org/10.1021/ja4094814.

(4) Ungur, L.; Le Roy, J. J.; Korobkov, I.; Murugesu, M.; Chibotaru, L. F. Fine-Tuning the Local Symmetry to Attain Record Blocking Temperature and Magnetic Remanence in a Single-Ion Magnet. *Angew. Chem. Int. Ed.* **2014**, *53* (17), 4413–4417. https://doi.org/10.1002/anie.201310451.

(5) Ding, Y.-S.; Chilton, N. F.; Winpenny, R. E. P.; Zheng, Y.-Z. On Approaching the Limit of Molecular Magnetic Anisotropy: A Near-Perfect Pentagonal Bipyramidal Dysprosium(III) Single-Molecule Magnet. *Angew. Chem. Int. Ed.* **2016**, *55* (52), 16071–16074. https://doi.org/10.1002/anie.201609685.

(6) Pugh, T.; Tuna, F.; Ungur, L.; Collison, D.; McInnes, E. J. L.; Chibotaru, L. F.; Layfield, R. A. Influencing the Properties of Dysprosium Single-Molecule Magnets with Phosphorus Donor Ligands. *Nat. Commun.* **2015**, *6* (1), 7492. https://doi.org/10.1038/ncomms8492.

(7) Gregson, M.; Chilton, N. F.; Ariciu, A.-M.; Tuna, F.; Crowe, I. F.; Lewis, W.; Blake, A. J.; Collison, D.; McInnes, E. J. L.; Winpenny, R. E. P.; Liddle, S. T. A Monometallic Lanthanide Bis(Methanediide) Single Molecule Magnet with a Large Energy Barrier and Complex Spin Relaxation Behaviour. *Chem. Sci.* **2016**, *7* (1), 155–165. https://doi.org/10.1039/C5SC03111G.

(8) Chilton, N. F. Design Criteria for High-Temperature Single-Molecule Magnets. *Inorg. Chem.* **2015**, *54* (5), 2097–2099. https://doi.org/10.1021/acs.inorgchem.5b00089.

(9) Ungur, L.; Chibotaru, L. F. Strategies toward High-Temperature Lanthanide-Based Single-Molecule Magnets. *Inorg. Chem.* **2016**, *55* (20), 10043–10056. https://doi.org/10.1021/acs.inorgchem.6b01353.

(10) Huang, W.; Le Roy, J. J.; Khan, S. I.; Ungur, L.; Murugesu, M.; Diaconescu, P. L. Tetraanionic Biphenyl Lanthanide Complexes as Single-Molecule Magnets. *Inorg. Chem.* **2015**, *54* (5), 2374–2382. https://doi.org/10.1021/ic5029788.

(11) Harriman, K. L. M.; Le Roy, J. J.; Ungur, L.; Holmberg, R. J.; Korobkov, I.; Murugesu, M. Cycloheptatrienyl Trianion: An Elusive Bridge in the Search of Exchange Coupled Dinuclear Organolanthanide Single-Molecule Magnets. *Chem. Sci.* **2017**, *8* (1), 231–240. https://doi.org/10.1039/C6SC01224H.

(12) Fortier, S.; Le Roy, J. J.; Chen, C.-H.; Vieru, V.; Murugesu, M.; Chibotaru, L. F.; Mindiola, D. J.; Caulton, K. G. A Dinuclear Cobalt Complex Featuring Unprecedented Anodic and Cathodic Redox Switches for Single-Molecule Magnet Activity. *J. Am. Chem. Soc.* **2013**, *135* (39), 14670–14678. https://doi.org/10.1021/ja405284t.

(13) Guillet, G. L.; Sloane, F. T.; Ermert, D. M.; Calkins, M. W.; Peprah, M. K.; Knowles, E. S.; Čižmár, E.; Abboud, K. A.; Meisel, M. W.; Murray, L. J. Preorganized Assembly of Three Iron(II) or Manganese(II) β-Diketiminate Complexes Using a Cyclophane Ligand. *Chem. Commun.* **2013**, *49* (59), 6635. https://doi.org/10.1039/c3cc43395a.

(14) Alvarez, S.; Llunell, M. Continuous Symmetry Measures of Penta-Coordinate Molecules: Berry and Non-Berry Distortions of the Trigonal Bipyramid. *J. Chem. Soc. Dalton Trans.* **2000**, No. 19, 3288–3303. https://doi.org/10.1039/b004878j.

(15) Zhang, J.; Yi, W.; Chen, Z.; Zhou, X. Room Temperature C–N Bond Cleavage of Anionic Guanidinate Ligand in Rare-Earth Metal Complexes. *Dalton Trans.* **2013**, *42* (16), 5826. https://doi.org/10.1039/c3dt00014a.

(16) Anfang, S.; Harms, K.; Weller, F.; Borgmeier, O.; Lueken, H.; Schilder, H.; Dehnicke, K. Phosphaniminato-Komplexe Seltener Erden. Synthese und Kristallstrukturen von $[M_2(C_5H_5)_3(NPPh_3)_3]\cdot3C_7H_8$ mit M = Y, Dy und Er. Magnetische Eigenschaften von $[Dy_2(C_5H_5)_3(NPPh_3)_3]\cdot3C_7H_8$. *Z. Für Anorg. Allg. Chem.* **1998**, *624* (1), 159–166. https://doi.org/10.1002/(SICI)1521-3749(199801)624:1<159::AID-ZAAC159>3.0.CO;2-Z.

(17) Zhang, P.; Zhang, L.; Wang, C.; Xue, S.; Lin, S.-Y.; Tang, J. Equatorially Coordinated Lanthanide Single Ion Magnets. *J. Am. Chem. Soc.* **2014**, *136* (12), 4484–4487. https://doi.org/10.1021/ja500793x.

(18) Zhao, L.; Xue, S.; Tang, J. A Dodecanuclear Dysprosium Wheel Assembled by Six Vertex-Sharing Dy_3 Triangles Exhibiting Slow Magnetic Relaxation. *Inorg. Chem.* **2012**, *51* (11), 5994–5996. https://doi.org/10.1021/ic3005807.

(19) Wu, Y.; Wang, S.; Zhu, X.; Yang, G.; Wei, Y.; Zhang, L.; Song, H. Synthesis, Characterization, and Catalytic Activity of Rare Earth Metal Amides Supported by a Diamido Ligand with a CH_2SiMe_2 Link. *Inorg. Chem.* **2008**, *47* (12), 5503–5511. https://doi.org/10.1021/ic800496d.

(20) Han, T.; Ding, Y.-S.; Li, Z.-H.; Yu, K.-X.; Zhai, Y.-Q.; Chilton, N. F.; Zheng, Y.-Z. A Dichlorido-Bridged Dinuclear Dy(III) Single-Molecule Magnet with an Effective Energy Barrier Larger than 600 K. *Chem. Commun.* **2019**, *55* (55), 7930–7933. https://doi.org/10.1039/C9CC02436K.

(21) Long, J.; Tolpygin, A. O.; Cherkasov, A. V.; Lyssenko, K. A.; Guari, Y.; Larionova, J.; Trifonov, A. A. Single-Molecule Magnet Behavior in Dy^{3+} Half-Sandwich Complexes Based on Ene-Diamido and Cp* Ligands. *Organometallics* **2019**, *38* (4), 748–752. https://doi.org/10.1021/acs.organomet.8b00901.

(22) Zhang, G.; Deng, B.; Wang, S.; Wei, Y.; Zhou, S.; Zhu, X.; Huang, Z.; Mu, X. Di and Trinuclear Rare-Earth Metal Complexes Supported by 3-Amido Appended Indolyl Ligands: Synthesis,

Characterization and Catalytic Activity towards Isoprene 1,4-Cis Polymerization. *Dalton Trans.* **2016**, *45* (39), 15445–15456. https://doi.org/10.1039/C6DT02922A.

(23) Zhang, G.; Wei, Y.; Guo, L.; Zhu, X.; Wang, S.; Zhou, S.; Mu, X. Dinuclear Rare-Earth Metal Alkyl Complexes Supported by Indolyl Ligands in μ-η^2:η^1:η^1 Hapticities and Their High Catalytic Activity for Isoprene 1,4-Cis-Polymerization. *Chem.–Eur. J.* **2015**, *21* (6), 2519–2526. https://doi.org/10.1002/chem.201405179.

(24) Yang, S.; Troyanov, S. I.; Popov, A. A.; Krause, M.; Dunsch, L. Deviation from the Planaritya Large Dy_3N Cluster Encapsulated in an I_h-C_{80} Cage: An X-Ray Crystallographic and Vibrational Spectroscopic Study. *J. Am. Chem. Soc.* **2006**, *128* (51), 16733–16739. https://doi.org/10.1021/ja066814i.

(25) Krylov, D. S.; Liu, F.; Brandenburg, A.; Spree, L.; Bon, V.; Kaskel, S.; Wolter, A. U. B.; Büchner, B.; Avdoshenko, S. M.; Popov, A. A. Magnetization Relaxation in the Single-Ion Magnet $DySc_2N@C_{80}$: Quantum Tunneling, Magnetic Dilution, and Unconventional Temperature Dependence. *Phys. Chem. Chem. Phys.* **2018**, *20* (17), 11656–11672. https://doi.org/10.1039/C8CP01608A.

(26) Krylov, D. S.; Liu, F.; Avdoshenko, S. M.; Spree, L.; Weise, B.; Waske, A.; Wolter, A. U. B.; Büchner, B.; Popov, A. A. Record-High Thermal Barrier of the Relaxation of Magnetization in the Nitride Clusterfullerene $Dy_2ScN@C_{80}$-I_h. *Chem. Commun.* **2017**, *53* (56), 7901–7904. https://doi.org/10.1039/C7CC03580B.

(27) Shannon, R. D. Revised Effective Ionic Radii and Systematic Studies of Interatomic Distances in Halides and Chalcogenides. *Acta Crystallogr. Sect. A* **1976**, *32* (5), 751–767. https://doi.org/10.1107/S0567739476001551.

(28) Rinehart, J. D.; Long, J. R. Exploiting Single-Ion Anisotropy in the Design of f-Element Single-Molecule Magnets. *Chem. Sci.* **2011**, *2* (11), 2078. https://doi.org/10.1039/c1sc00513h.

(29) Jaroschik, F.; Nief, F.; Le Goff, X.-F. Sterically Hindered Cyclopentadienyl and Phospholyl Ligands in Dysprosium Chemistry. *Polyhedron* **2009**, *28* (13), 2744-2748. https://doi.org/10.1016/j.poly.2009.05.035.

(30) Meng, Y.-S.; Zhang, Y.-Q.; Wang, Z.-M.; Wang, B.-W.; Gao, S. Weak Ligand-Field Effect from Ancillary Ligands on Enhancing Single-Ion Magnet Performance. *Chem.–Eur. J.* **2016**, *22* (36), 12724–12731. https://doi.org/10.1002/chem.201601934.

(31) Münzfeld, L.; Schoo, C.; Bestgen, S.; Moreno-Pineda, E.; Köppe, R.; Ruben, M.; Roesky, P. W. Synthesis, Structures and Magnetic Properties of $[(\eta^9\text{-}C_9H_9)Ln(\eta^8\text{-}C_8H_8)]$ Super Sandwich Complexes. *Nat. Commun.* **2019**, *10* (1), 3135. https://doi.org/10.1038/s41467-019-10976-6.

(32) Rinehart, J. D.; Meihaus, K. R.; Long, J. R. Observation of a Secondary Slow Relaxation Process for the Field-Induced Single-Molecule Magnet $U(H_2BPz_2)_3$. *J. Am. Chem. Soc.* **2010**, *132* (22), 7572–7573. https://doi.org/10.1021/ja1009019.

(33) Liu, J.; Chen, Y.-C.; Liu, J.-L.; Vieru, V.; Ungur, L.; Jia, J.-H.; Chibotaru, L. F.; Lan, Y.; Wernsdorfer, W.; Gao, S.; Chen, X.-M.; Tong, M.-L. A Stable Pentagonal Bipyramidal Dy(III) Single-Ion Magnet with a Record Magnetization Reversal Barrier over 1000 K. *J. Am. Chem. Soc.* **2016**, *138* (16), 5441–5450. https://doi.org/10.1021/jacs.6b02638.

(34) Pugh, T.; Chilton, N. F.; Layfield, R. A. A Low-Symmetry Dysprosium Metallocene Single-Molecule Magnet with a High Anisotropy Barrier. *Angew. Chem. Int. Ed.* **2016**, *55* (37), 11082–11085. https://doi.org/10.1002/anie.201604346.

(35) Gatteschi, D.; Sessoli, R.; Villain, J. *Molecular Nanomagnets*; Oxford University Press, 2006.

(36) Liddle, S. T.; van Slageren, J. Improving f-Element Single Molecule Magnets. *Chem. Soc. Rev.* **2015**, *44* (19), 6655–6669. https://doi.org/10.1039/C5CS00222B.

(37) Gupta, S. K.; Rajeshkumar, T.; Rajaraman, G.; Murugavel, R. An Air-Stable Dy(III) Single-Ion Magnet with High Anisotropy Barrier and Blocking Temperature. *Chem. Sci.* **2016**, *7* (8), 5181–5191. https://doi.org/10.1039/C6SC00279J.

(38) Orbach, R. Spin-Lattice Relaxation in Rare-Earth Salts. *Proc. R. Soc. Lond. Ser. Math. Phys. Sci.* **1961**, *264* (1319), 458–484. https://doi.org/10.1098/rspa.1961.0211.

(39) Williams, U. J.; Mahoney, B. D.; DeGregorio, P. T.; Carroll, P. J.; Nakamaru-Ogiso, E.; Kikkawa, J. M.; Schelter, E. J. A Comparison of the Effects of Symmetry and Magnetoanisotropy on Paramagnetic Relaxation in Related Dysprosium Single Ion Magnets. *Chem. Commun.* **2012**, *48* (45), 5593. https://doi.org/10.1039/c2cc31227a.

(40) Ungur, L.; Chibotaru, L. F. Magnetic Anisotropy in the Excited States of Low Symmetry Lanthanide Complexes. *Phys. Chem. Chem. Phys.* **2011**, *13* (45), 20086. https://doi.org/10.1039/c1cp22689d.

(41) Ungur, L.; Thewissen, M.; Costes, J.-P.; Wernsdorfer, W.; Chibotaru, L. F. Interplay of Strongly Anisotropic Metal Ions in Magnetic Blocking of Complexes. *Inorg. Chem.* **2013**, *52* (11), 6328–6337. https://doi.org/10.1021/ic302568x.

(42) Garanin, D. A.; Chudnovsky, E. M. Thermally Activated Resonant Magnetization Tunneling in Molecular Magnets: $Mn_{12}Ac$ and Others. *Phys. Rev. B* **1997**, *56* (17), 11102–11118. https://doi.org/10.1103/PhysRevB.56.11102.

(43) Ungur, L.; Chibotaru, L. F. Ab Initio Crystal Field for Lanthanides. *Chem.-Eur. J.* **2017**, *23* (15), 3708–3718. https://doi.org/10.1002/chem.201605102.

(44) Aquilante, F.; Autschbach, J.; Carlson, R. K.; Chibotaru, L. F.; Delcey, M. G.; Vico, L. D.; Galván, I. F.; Ferré, N.; Frutos, L. M.; Gagliardi, L.; Garavelli, M.; Giussani, A.; Hoyer, C. E.; Manni, G. L.;

Lischka, H.; Ma, D.; Malmqvist, P. Å.; Müller, T.; Nenov, A.; Olivucci, M.; Pedersen, T. B.; Peng, D.; Plasser, F.; Pritchard, B.; Reiher, M.; Rivalta, I.; Schapiro, I.; Segarra-Martí, J.; Stenrup, M.; Truhlar, D. G.; Ungur, L.; Valentini, A.; Vancoillie, S.; Veryazov, V.; Vysotskiy, V. P.; Weingart, O.; Zapata, F.; Lindh, R. Molcas8: New Capabilities for Multiconfigurational Quantum Chemical Calculations across the Periodic Table. *J. Comput. Chem.* **2016**, *37* (5), 506–541. https://doi.org/10.1002/jcc.24221.

(45) Roos, B. O.; Lindh, R.; Malmqvist, P.-Å.; Veryazov, V.; Widmark, P.-O.; Borin, A. C. New Relativistic Atomic Natural Orbital Basis Sets for Lanthanide Atoms with Applications to the Ce Diatom and LuF_3. *J. Phys. Chem. A* **2008**, *112* (45), 11431–11435. https://doi.org/10.1021/jp803213j.

(46) Roos, B. O. The Complete Active Space Self-Consistent Field Method and Its Applications in Electronic Structure Calculations. In *Advances in Chemical Physics*; John Wiley & Sons, Ltd, 2007; pp 399–445. https://doi.org/10.1002/9780470142943.ch7.

(47) Malmqvist, P. Å.; Roos, B. O.; Schimmelpfennig, B. The Restricted Active Space (RAS) State Interaction Approach with Spin–Orbit Coupling. *Chem. Phys. Lett.* **2002**, *357* (3–4), 230–240. https://doi.org/10.1016/S0009-2614(02)00498-0.

Chapter 6

Relaxation Dynamics in See-Saw Shaped Dy^{III} Single-Molecule Magnets

6.1 Introduction

Since the discovery of domain-independent magnetism of molecular origin in 1993,[1] single-molecule magnets (SMMs) have captivated the imagination of researchers for their potential use in advanced magnetic materials and applications. In particular, these molecules exhibit a magnetic memory response, or hysteresis, where molecular magnetization persists upon removal of the external magnetic field.[2,3] This makes SMMs potentially suitable for new high-capacity, magnetic-based data storage devices or even quantum computing.[4,5] A major drawback, however, is the magnetic blocking temperature (T_B), a figure of merit for the ability to retain magnetization, that is often limited to cryogenic temperatures typically nearing the boiling point of liquid helium. While several factors can affect T_B and SMM activity, an important parameter to overall SMM performance is the effective energy barrier to magnetic spin reversal (U_{eff}). Large U_{eff} values (> 1000 K / 695 cm^{-1}) are requisite for maintaining SMM activity at elevated temperatures.[3,6]

In this regard, recent attention has been focused on the development of lanthanide based SMMs with staggering U_{eff}.[3,6] Traditionally, the core-like 4f-orbitals were described as insensitive to covalent ligand field contributions, which allows for significant orbital degeneracy and spin-orbit coupling that gives way to large magnetic moments. However, both electrostatic and covalent contributions to the crystal field affect the splitting of magnetic microstates, thus enhancing the magnetic anisotropy.[7–10] Based upon crystal field theory, the symmetry, point charge effects, and the relative shape of the 4f free-ion electron density should be considered when designing ligand frameworks to maximize magnetic anisotropy and consequently U_{eff} values.[6,11–13]

This strategy has recently proven effective with oblate-shaped Dy^{III} in near-linear or linearly dominant crystal fields.[14–22] For instance, in Chapter 5, the compound (NN^{TBS})Dy^{III}(I)(THF)$_2$ (**7-Dy**; NN^{TBS} = Fc(NHSi^{t}BuMe$_2$)$_2$), utilized a diamide ligand to produce a highly axial crystal field for the Dy^{III} ion with N-Dy-N = 134.7(2)°, affording a SMM with an appreciable U_{eff} = 770.8 K (535.7 cm^{-1}) / 910 K (632.5 cm^{-1}).[19,23] Although not mononuclear, in a related system, the two monodentate anilide ligands in [Dy^{III}(N$^{RR'}$)$_2$(μ-Cl)$_2$K]$_n$ (N$^{RR'}$ = {N(SiMe$_3$)(C$_6$H$_3$^{i}Pr$_2$-2,6)}$^-$) afforded a U_{eff} = 1578 K in zero field.[24] In [Dy^{III}(O^{t}Bu)$_2$(py)$_5$][BPh$_4$], the *trans* oriented (O-Dy-O = 178.91(9)°) alkoxide donors and, in relation, the less donating equatorially-bound pyridine ligands gave rise to a SMM with a tremendous U_{eff} = 1815 K (1261.5 cm^{-1}) and T_{B} = 14 K (ZFC-FC susceptibilities).[15] This was recently surpassed by $[(\mathrm{Cp}^{i\mathrm{Pr}5})\mathrm{Dy}^{\mathrm{III}}(\mathrm{Cp}^*)][\mathrm{B}(\mathrm{C}_6\mathrm{F}_5)_4]$ ($\mathrm{Cp}^{\mathrm{iPr}5}$ = 1,2,3,4,5-(^{i}Pr)$_5$C$_5$; Cp* = 1,2,3,4,5-(Me)C$_5$), which fully excludes equatorial ligands to give near-linear coordinated dysprosium (Cp-Dy-Cp = 162.507(1)°). In this case, the metal complex displays a record setting U_{eff} = 2217 K (1541 cm^{-1}) and a remarkable T_{B} = 80 K (25 Oe s^{-1}) that exceeds the temperature of liquid nitrogen (77 K).[13]

These results clearly demonstrate a successful design criterion for enhancing magnetic anisotropy; yet several questions remain. With respect to Dy$^{\mathrm{III}}$, the linear deviation tolerance of the axial ligation mode is not fully established. While linear two-coordinate dysprosium has been predicted as optimal for maximizing U_{eff},[6,14] five-coordinate and seven-coordinate Dy$^{\mathrm{III}}$ in $(\mathrm{NN}^{\mathrm{TBS}})\mathrm{Dy}^{\mathrm{III}}(\mathrm{I})(\mathrm{THF})_2$ (**7-Dy**) and $[\mathrm{Dy}^{\mathrm{III}}(\mathrm{O}^t\mathrm{Bu})_2(\mathrm{py})_5][\mathrm{BPh}_4]$, respectively, still exhibit notable magnetic anisotropy enhancements due to strong metal-ligand interactions along a defined axis, regardless of their molecular geometry or symmetry. This strong interaction and axiality enhancement define the barrier of magnetization spin reversal; however, as energy barriers continue to rise, the through-barrier mechanisms become increasingly more important to understand. Spin-vibrational coupling has been identified for facilitating these processes (i.e., Raman relaxation). Strategies to suppress vibrational coupling have been reported as ways to improve the performance of SMMs without necessarily increasing the U_{eff}.[25,26] Increasing the rigidity of ligand frameworks represents the most accessible and tunable approach for synthetic chemists.[27,28] Thus, the effects of coordination geometry, total coordination number, and the identity/role of the ligands in processes beyond quantum tunneling of the magnetization (QTM) have yet to be completely determined.

The synthesis and characterization of the U$^{\mathrm{III}}$ compound $\mathrm{L}^{\mathrm{Ar}}\mathrm{U}^{\mathrm{III}}(\mathrm{I})(\mathrm{DME})$ (L^{Ar} = $\{\mathrm{C}_6\mathrm{H}_4[(2,6\text{-}^i\mathrm{PrC}_6\mathrm{H}_3)\mathrm{NC}_6\mathrm{H}_4]_2\}^{2-}$) was previously reported, featuring a terphenyl bisanilide ligand with near-linear coordinated nitrogen atoms (N1−U1−N2 =162.8(1)°).[29] In $\mathrm{L}^{\mathrm{Ar}}\mathrm{U}^{\mathrm{III}}(\mathrm{I})(\mathrm{DME})$, the uranium atom is tethered above a central phenyl ring, which exhibits nominal metal-arene interactions. As such, this central ring acts to block several coordination sites on the metal. Structurally, this platform provides a number of attractive features for utilization with Dy$^{\mathrm{III}}$ in pursuit of enhanced SMM properties. It possesses a defined orientation for the magnetic anisotropy (N1-M-N2), as well as a tethered backbone for increased ligand stiffness, combined with an X-ligand which represents a tunable position for the investigation of halide effects on the overall magnetic properties.

In this chapter, the magnetic characterization of two Dy$^{\mathrm{III}}$ metal complexes, $[\mathrm{K}(\mathrm{DME})_3][\mathrm{L}^{\mathrm{Ar}}\mathrm{Dy}^{\mathrm{III}}(\mathrm{Cl})_2]$ (**8-Dy**) and $[\mathrm{K}(\mathrm{DME})_4][\mathrm{L}^{\mathrm{Ar}}\mathrm{Dy}^{\mathrm{III}}(\mathrm{I})_2]$ (**9-Dy**), which each feature a Dy$^{\mathrm{III}}$ ion with an unusual see-saw geometry and near-linear N-Dy-N arrangement are presented. The relaxation dynamics of each system are analyzed, and a fundamental link between the different structural features (i.e., the transverse ligand architecture and halide ancillary ligands) and the observed magnetic properties is investigated.

6.2 Results and Discussion

6.2.1 Synthesis and Structural Studies

Following the procedure for the synthesis of the *N*,*N*-chelated {[ArNCC(Me)]$_2$CH}Dy^{III}(Cl)$_2$(THF)$_2$,[30] a solution of DyCl$_3$ and [K(DME)$_2$]$_2$L^{Ar} in THF was heated at 60 °C for two days, giving a mixture from which **8-Dy** was isolated in low yield as a THF solvate. Notably, the formation of **8-Dy**·THF under these conditions is accompanied by unreacted DyCl$_3$ and a significant amount of protonated H$_2$L^{Ar} despite strictly anhydrous conditions. This result suggested that **8-Dy** may become unstable at elevated temperatures. To counter this, addition of DyCl$_3$ to a thawing THF solution of [K(DME)$_2$]$_2$L^{Ar} followed by warming to room temperature and stirring for 12 h gives **8-Dy** as air and moisture sensitive crystals in 47% yield after recrystallization from DME (Figure 6.1). Similarly, **9-Dy** was synthesized using identical conditions to those of **8-Dy**, giving 55% crystalline yield**.**

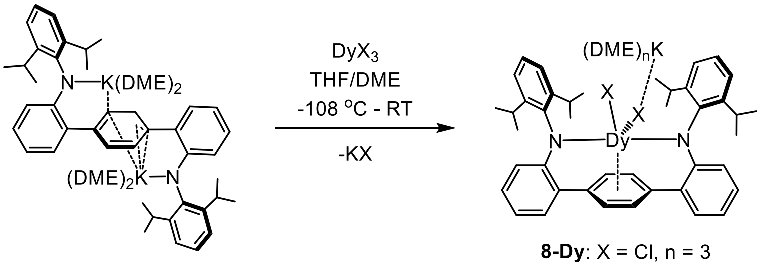

8-Dy: X = Cl, n = 3
9-Dy: X = I, n = 4

Figure 6.1 Synthesis of [K(DME)$_3$][LArDy^{III}(Cl)$_2$] (**8-Dy**) and [K(DME)$_4$][LArDy^{III}(I)$_2$] (**9-Dy**).

Compound **8-Dy** crystallizes at -25 °C in the monoclinic space group *Cc* (Table 6.3). The X-ray diffraction analysis at 100 K reveals two independent molecules in the asymmetric unit, each exhibiting severe positional and solvent disorder. However, data collection at 15 K under a He cryostream shows a crystallographic phase transition to monoclinic *Pn* with four well-resolved molecules in the asymmetric unit (**8-Dy1**, **8-Dy2**, **8-Dy3**, **8-Dy4**; Figure 6.2). Comparatively, **9-Dy** crystallises at -35 ºC in the triclinic space group $P\bar{1}$ (Figure 6.3). As compared to **7-Dy**, (NN^{TBS})Dy^{III}(I)(THF)$_2$ (Dy-N = avg. 2.21 Å), [Dy^{III}(N$^{RR'}$)$_2$(µ-Cl)$_2$K]$_n$ (Dy-N = avg. 2.25 Å), and [Li(THF)$_4$][Dy^{III}(NPh$_2$)$_4$] (Dy-N = avg. 2.29 Å),[19,24,31] the Dy-N distances in **8-Dy** (2.379(9)-2.416(8) Å) and **9-Dy** (2.402(7)-2.438(8) Å) are substantially elongated.

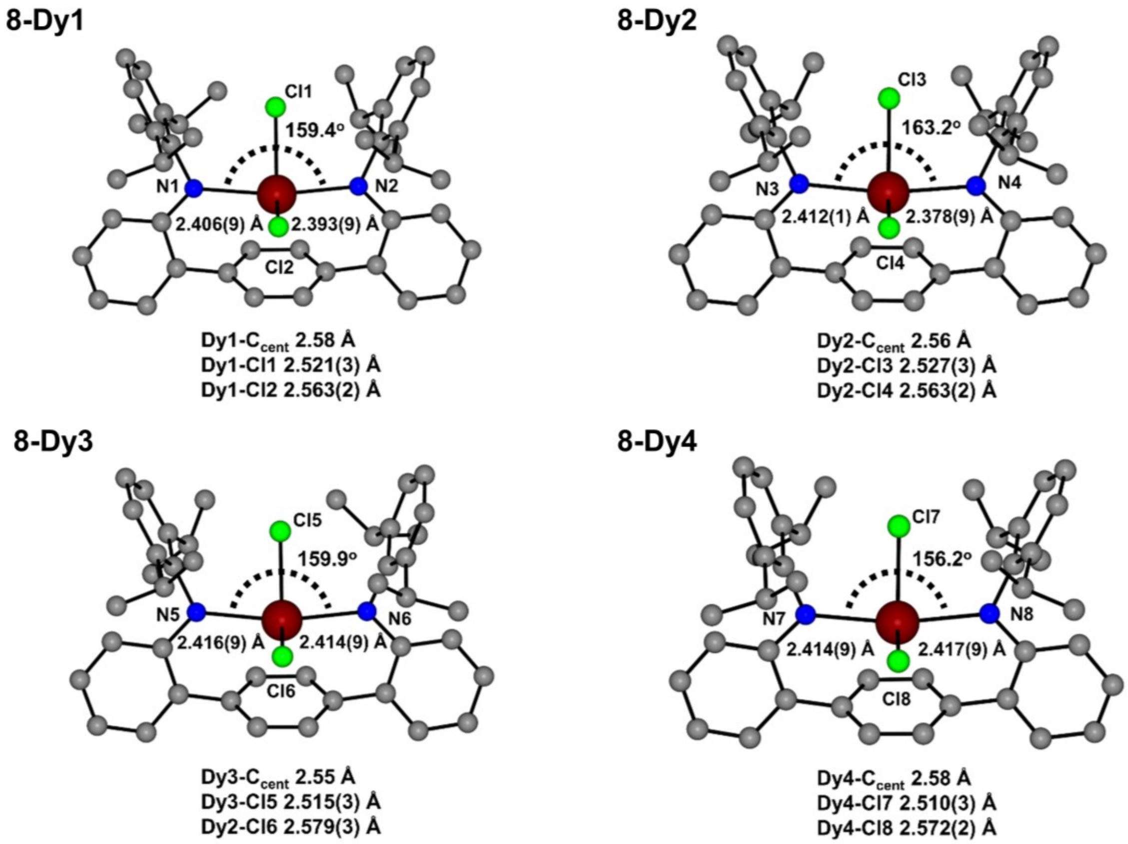

Figure 6.2 Molecular structures of the four crystallographically independent molecules in the asymmetric unit of **8-Dy** (monoclinic *Pn*) collected under a He cryostream at 15 K. Colour code: Dark red (Dy^{III}), green (Cl), blue (N), grey (C). Protons and [K(DME)$_3$] cations are removed for clarity. The dotted arch depicts the N-Dy-N angle, and the Dy-N distances are displayed below their representative bonds on the molecules. Dy-C$_{cent}$ and Dy-Cl distances are presented below the molecules.

These larger Dy-N distances may be attributed to the transverse structure of the bis-anilide ligand, constraining the N-donor atoms into positions where the Dy-N distances are relatively long. Yet, the ligand bite angle in **8-Dy** (N-Dy-N = avg. 159.9°) and **9-Dy** (N-Dy-N = 160.4(2)°) is more obtuse than that of **7-Dy**, (NN^{TBS})Dy^{III}(I)(THF)$_2$ (N-Dy-N = 134.7(2)°) and [Dy^{III}(N$^{RR'}$)$_2$(μ-Cl)$_2$K]$_n$ (N-Dy-N = avg. 131.6°). Collectively, this demonstrates the inter-complementary role of the bite angle and distances in the ligand design of such metal complexes. Although the extent of the interactions between the Dy^{III} ion and the central terphenyl ring (Dy-C$_{cent}$ = avg. 2.56 Å for **8-Dy**, and Dy-C$_{cent}$ = 2.55 Å for **9-Dy**) cannot be fully excluded from the discussion, they are assumed to be minimal due to the neutral charge of this moiety. Comparatively, the compound [((^{Ad,Me}ArO)$_3$mes)Dy^{III}] exhibits a similar tethered arene backbone (Dy-C$_{cent.}$ = 2.368 Å),[32] further supporting the weak Dy-arene interaction in **8-Dy** and **9-Dy**. Thus, any metal-π interactions present in **8-Dy** and **9-Dy** are not strong directors of the magnetic anisotropy (*vide infra*). The remaining coordination sites on the Dy^{III} ion are occupied by two halide ions, which possess distances typical for Dy-X (**8-Dy**; Dy-Cl = 2.510(3)-2.579(3) Å and **9-Dy**; Dy-I = 2.9355(7)-2.9771(5) Å).[33] Thus, the Dy^{III} ion in **8-Dy** and **9-Dy** adopts an unusual see-saw type geometry because of the coordination environment enforced by the bulky, transverse ligand architecture.

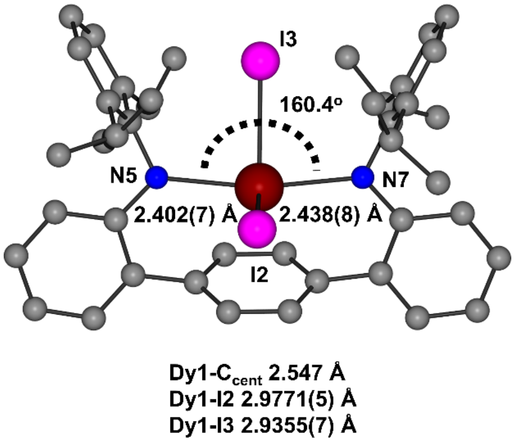

9-Dy

Figure 6.3 Molecular structure of **9-Dy**. Colour code: Dark red (Dy^{III}), pink (I), blue (N), grey (C). Protons and $[K(DME)_4]$ cation are removed for clarity. The dotted arch depicts the N-Dy-N angle, and the Dy-N distances are displayed below their representative bonds on the molecules. Dy-Ccent and Dy-Cl distances are presented below the molecule.

6.2.2 Theoretical Analysis

Ab initio calculations on two of the molecules in the asymmetric unit of **8-Dy** featuring the maximum (**8-Dy2**) and minimum (**8-Dy4**) N-Dy-N angles (162.7° and 156.2°, respectively) as well as **9-Dy** were completed with SO-CASSCF(9,7)/ANO-RCC in MOLCAS 8.0.[34] The computed eight Kramer's doublets (KDs) of $^6H_{15/2}$ span 1120 cm^{-1} (**8-Dy2**), 998 cm^{-1} (**8-Dy4**), and 1173 cm^{-1} (**9-Dy**) (Table 6.1). The ground KDs have large principal *g*-tensors; g'_z = 19.9567 (**8-Dy2**), 19.8300 (**8-Dy4**), and 19.883 (**9-Dy**), in which the magnetic axis is nearly collinear to the Dy-N bonds. Compounds **8-Dy** and **9-Dy** are isotypic and as a representative example, the main magnetic axis in the ground state of **8-Dy2** is superimposed on the molecular structure in Figure 6.4. Previously, the amido N-atoms of $(NN^{TBS})Dy^{III}(I)(THF)_2$, **7-Dy** were proven to be greater directors of magnetic anisotropy over the bound halide and solvent (THF).[19] Thus, it is not surprising that the strong electrostatic interaction of the N-atoms of the bisanilide ligand in **8-Dy** and

9-Dy dictates the orientation of the main magnetic axis of the Dy^{III} ions more strongly than the coordinated halide ions or any interactions from the central terphenyl ring.

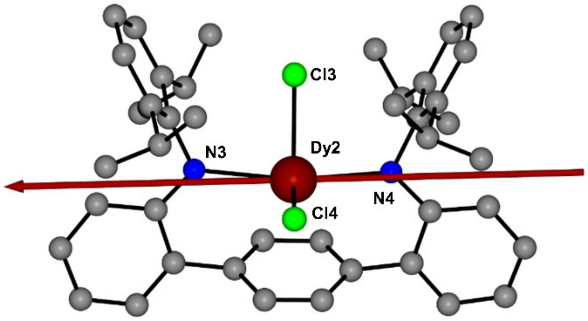

Figure 6.4 Calculated orientation of the main magnetic axis in the ground Kramers doublet of **8-Dy2** superimposed on the molecular structure. Colour code: Dark red (Dy^{III}), green (Cl), blue (N), grey (C). Protons and [K(DME)$_3$] cations are removed for clarity.

There is negligible transverse anisotropy in the ground state KDs of all the species studied, suggesting that there should be an absence of ground-state QTM. The first excited KD lies at 323 cm^{-1}, 294 cm^{-1} and 337 cm^{-1} for **8-Dy2**, **8-Dy4**, and **9-Dy** respectively. The second and third excited state KDs also have highly axial principal *g*-values, which suggests that thermally activated relaxation should occur at least through these states. Significant transverse components of the *g*-tensor are observed at the 4th KD for **8-Dy2** (g'_x = 2.7977, g'_y = 6.161, g'_z = 8.9011), **8-Dy4** (g'_x = 1.9353, g'_y = 3.4765, g'_z = 10.1002), and **9-Dy** (g'_x = 1.6501, g'_y = 1.3082, g'_z = 11.1331). Large principal *g*-tensors; g'_z = 19.0299 (**8-Dy2**), 19.0753 (**8-Dy4**), and 18.714 (**9-Dy**); are obtained once again in the 8th KD for all species. Thus, thermal relaxation is expected to occur *via* the 4th KD for both **8-Dy** and **9-Dy** with activation energies of 1088-1204 K (**8-Dy**) and 1304 K (**9-Dy**).

As a representative example, the calculated transition matrix probabilities of compound **8-Dy2** displays minimal ground state QTM, with a transition magnetic moment of 8.2 x 10^{-5} μ_B (Figure 6.5). The transition magnetic moment of the 2nd KD is two orders of magnitude larger (5.1 x 10^{-3} μ_B) than the ground state (1st KD), which coincides with an increase in the transverse components of the *g*-tensor for the 2nd KD (g'_x = 0.0138, g'_y = 0.0165). At the 3rd KD, the transition magnetic moment is an order of magnitude larger (4.2 x 10^{-2} μ_B) than the previous and correlates to a proportional increase in the transverse components of the *g*-tensor (g'_x = 0.1142, g'_y = 0.1363). The vertical transition moments connecting the states of the same magnetization in increasing energy (Figure 6.5; *blue lines*) are significantly larger than the corresponding transverse moments, promoting a multistep relaxation pathway until the 4th KD. Here, the transverse moment (1.6 μ_B) becomes sufficiently large enough to yield efficient thermally activated quantum tunnelling of the magnetization (TA-QTM). To confirm the anisotropy and relaxation dynamics predicted *via ab initio* methods for **8-Dy** and **9-Dy**, the magnetic properties were analyzed with SQUID magnetometry.

Table 6.1 Energy splitting of the ground free ion $J = 15/2$ multiplet and the effective *g*-tensors for the low lying KDs for **8-Dy2**, **8-Dy4**, and **9-Dy**.

KD		**8-Dy2**	**8-Dy4**	**9-Dy**
1		0	0	0
2		323	294	337
3		630	567	663
4		837	756	906
5		882	789	1028
6		936	841	1051
7		1000	884	1089
8		1120	998	1173
g-tensors for low lying Kramers doublet states				
1	g'1	0.0003	0.0003	0.0001
	g'2	0.0002	0.0002	0.0001
	g'3	**19.9567**	**19.8300**	**19.883**
2	g'1	0.0138	0.0132	0.0106
	g'2	0.0165	0.0156	0.0094
	g'3	**17.1339**	**17.0367**	**17.0716**
3	g'1	0.1142	0.1233	0.0365
	g'2	0.1363	0.1518	0.0279
	g'3	**14.2045**	**14.1589**	**14.2201**
4	g'1	2.7977	1.9353	1.6501
	g'2	6.161	3.4765	1.3082
	g'3	8.9011	10.1002	11.1331
5	g'1	13.0964	0.8381	2.4631
	g'2	3.9578	0.1176	3.5013
	g'3	1.275	17.9999	12.3088
6	g'1	8.1422	11.3617	10.8352
	g'2	10.693	5.5460	3.7841
	g'3	3.326	4.3763	0.9453
7	g'1	15.9639	0.1488	12.14865
	g'2	1.1859	0.9389	6.1477
	g'3	0.4726	14.7273	1.9997
8	g'1	0.0181	0.0439	0.3807
	g'2	0.0981	0.0198	0.2456
	g'3	19.0299	19.0753	18.714

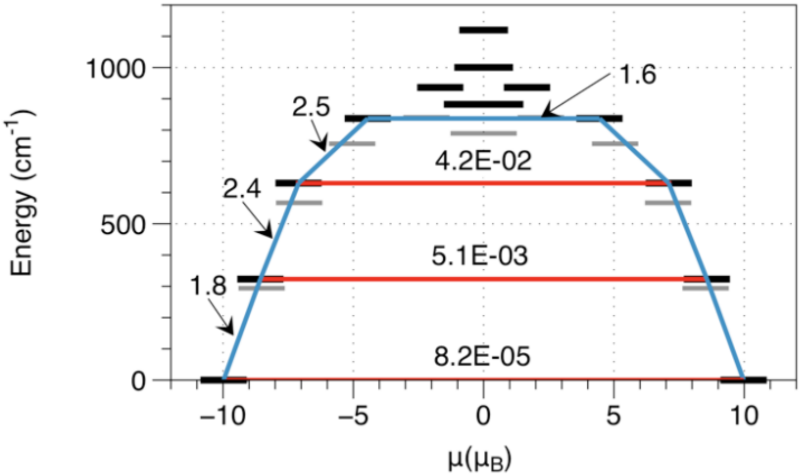

Figure 6.5 Ligand field splitting of the ground term $^6H_{15/2}$ of **8-Dy2** (black bars) and **8-Dy4** (grey bars) where each KD components are spaced according to the effective magnetic projections (*x*-axis). Blue lines depict transitions with largest transition moments calculated with SINGLE_ANISO[35] whereas red lines depict unlikely transitions. The effective barrier for relaxation of the magnetization due to thermally activated process is limited by the energy of the 4th KD.

6.2.3 Direct Current Magnetic Susceptibility Studies

The direct current (dc) magnetic susceptibility studies revealed a characteristic temperature dependence for both compounds. The near identical behaviour for **8-Dy** and **9-Dy** results in a gradual decrease in the plot of χT *vs.* T from 13.97 cm^3·K·mol^{-1} (**8-Dy**) and 13.89 cm^3·K·mol^{-1} (**9-Dy**) at 300 K down to *ca.* 7 K suggesting strong crystal field splitting (Figure 6.6). Below this temperature, a rapid decrease to final χT products of 7.92 cm^3·K·mol^{-1} (**8-Dy**) and 7.93 cm^3·K·mol^{-1} (**9-Dy**) at 1.8 K are observed. This behaviour is typical of high-performing SMMs as a result of the onset of magnetic blocking. The high temperature χT products of **8-Dy** and **9-Dy** are close to the expected value of 14.17 cm^3·K·mol^{-1} for a free Dy^{III} ion ($^6H_{15/2}$, $S = 5/2$, $L = 5$, $g = 4/3$). The general shape of the susceptibility, in addition to the values, is in good agreement with the ab initio calculated susceptibility which considers the local electrostatic environment of the Dy^{III} ion. The field dependent magnetization collected at 1.9, 3, 5, and 7 K for **1** and **2** exhibits sinusoidal character at low fields and reaches saturation values of 5.096 μ_B (**8-Dy**) and 5.122 μ_B (**9-Dy**) at 70 kOe (Figure 6.7). The low saturation values are indicative of an axial, well isolated ground state.[17,21,36–39]

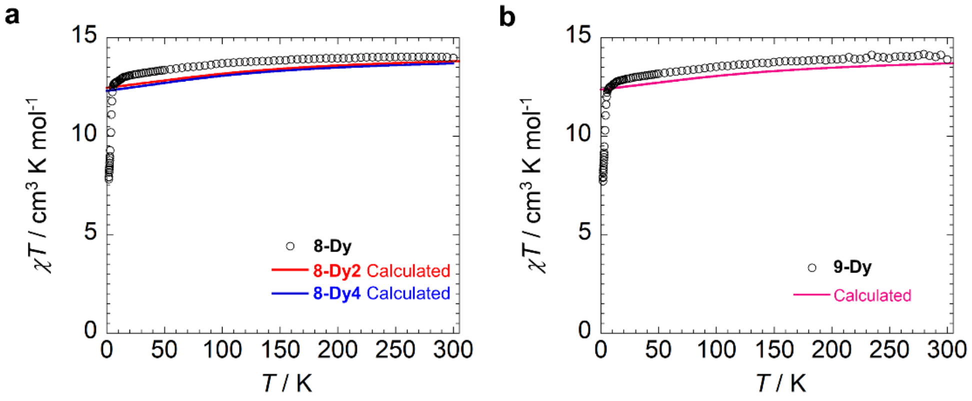

Figure 6.6 Temperature dependence of the χT product under an applied dc field of 1000 Oe for (a) **8-Dy** and (b) **9-Dy**. Experimental data is represented by black hollow circles. *Ab initio* calculated magnetic susceptibility depicted by solid lines. For **8-Dy**, two of the four crystallographically independent molecules, **8-Dy2** (red) and **8-Dy4** (blue) which possess the upper and lower limits of the metrical data; N-Dy-N angles of 162.3° (**8-Dy2**) and 156.2° (**8-Dy4**) are modeled independently.

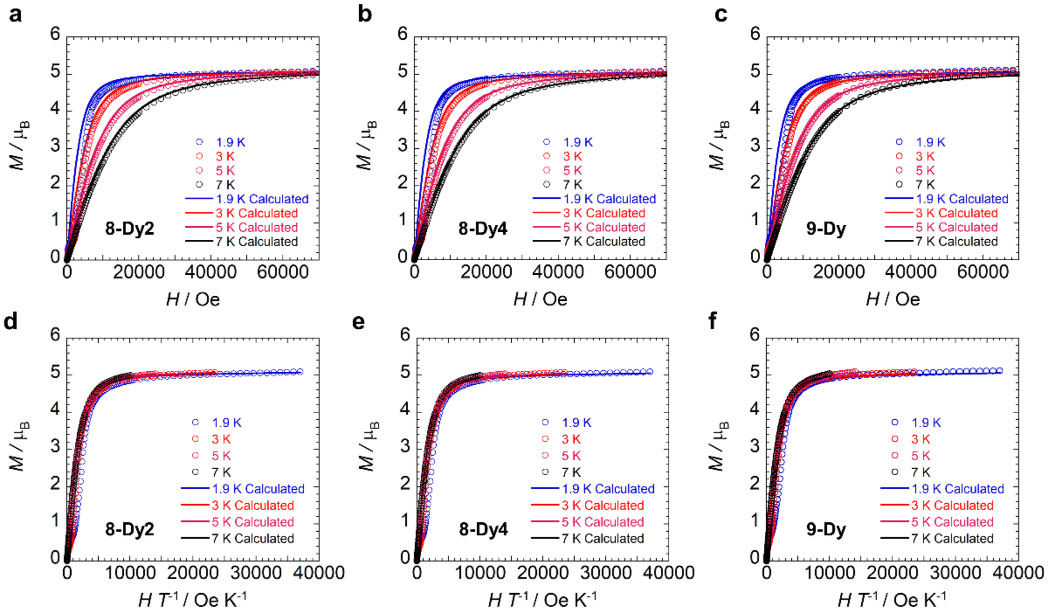

Figure 6.7 Solid state field dependence of the (a-c) magnetization and (d-f) reduced magnetization at the indicated temperatures. Experimental data is represented by hollow circles and the calculated data represented by solid lines. For **8-Dy**, the magnetization values were calculated for two of the four crystallographically independent molecules in the unit cell, **8-Dy2** and **8-Dy4**, which possess the upper and lower limits of the metrical data; N-Dy-N angles of 162.3° (**8-Dy2**) and 156.2° (**8-Dy4**).

The field-cooled (FC) and zero-field cooled (ZFC) susceptibility measurements were collected to confirm the presence of magnetic blocking as suggested by the low temperature profiles of the variable temperature susceptibility (Figure 6.8). A clear divergence of the FC and ZFC curves occurs at 4.4 K (0.21 K min^{-1}) for both compounds, although the maximum in the ZFC susceptibilities are at 4.0 K, which is often used as a mark of T_B. Given this prospect of magnetic blocking, the magnetic hysteresis properties of **8-Dy** and **9-Dy** were measured. A mean field sweep rate of 13.6 and 12.2 Oe s^{-1}, was used for **8-Dy** and **9-Dy**, respectively (Figure 6.9). Under these conditions, nearly identical waist-restricted magnetization hysteresis loops were observed from 1.8-5.8 K for **8-Dy** and **9-Dy**. At 1.8 K, the hysteresis loops are open when $H \neq 0$ Oe, with a maximum coercive field of 3687.2 Oe for **8-Dy** and 3274.5 Oe for **9-Dy**. When nearing 0 Oe, the magnetization experiences a drastic decrease with no retention of the magnetic moment, indicative of QTM. At 5.8 K, the loops remain open when $H \neq 0$ Oe with a coercive field of 448.0 Oe (**8-Dy**) and 407.3 (**9-Dy**), above this temperature openings were not observable. The identical ZFC-FC susceptibilities and magnetic hysteresis loops of **8-Dy** and **9-Dy** suggests that the presence of a light *vs*. heavy halide has little effect on the blocking properties and the compound's ability to retain magnetization. However, due to the variability of T_B with applied field and sweeping rate (of field or temperature), relaxation times were investigated for these compounds with the use of ac magnetic susceptibility.

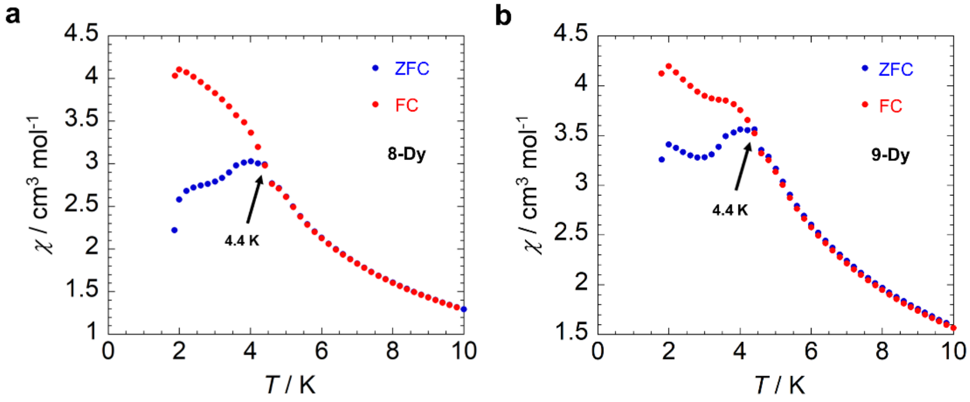

Figure 6.8 Zero-field-cooled and field-cooled (ZFC-FC) curves for (a) **8-Dy** and (b) **9-Dy** under an applied static field of 1000 Oe. Data were collected at a mean sweep rate of 0.21 K min^{-1}. ZFC-FC susceptibilities bifurcate at 4.4 K as indicated by the arrow in both samples.

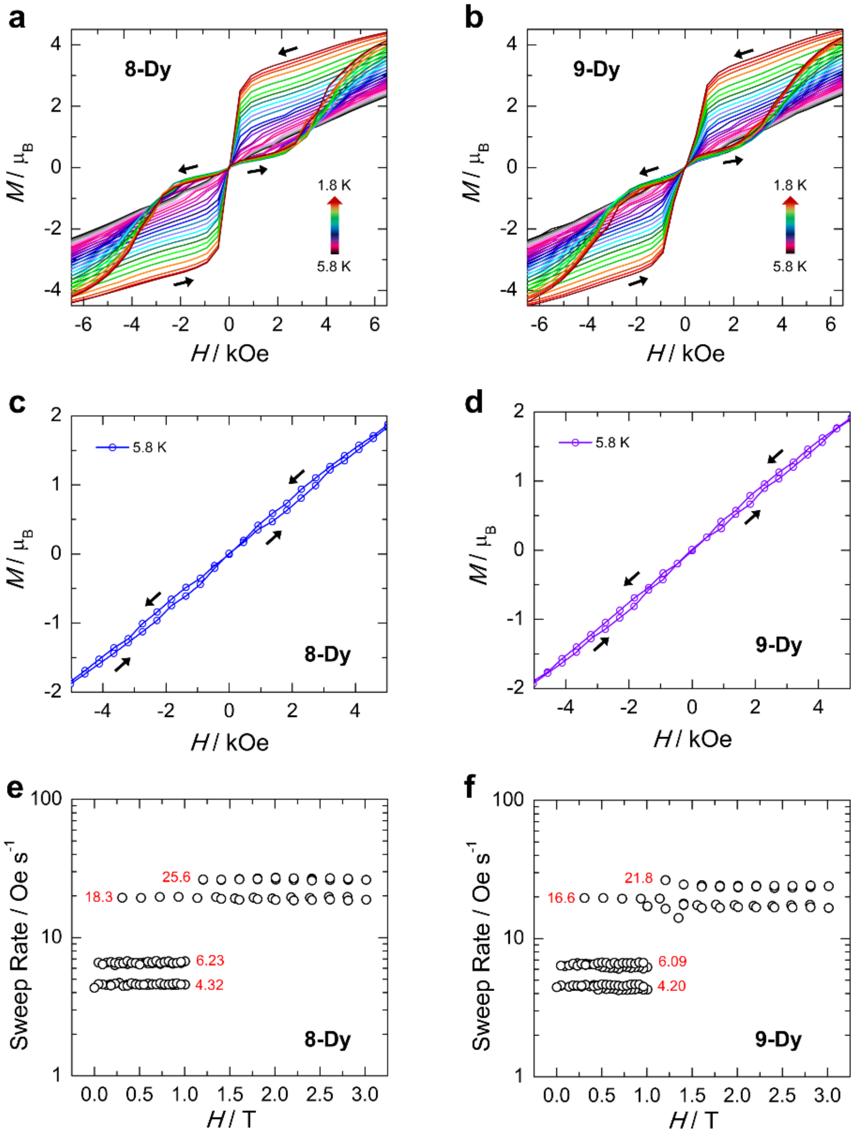

Figure 6.9 Magnetic hysteresis data for (a) **8-Dy** and (b) **9-Dy** in the temperature range 1.8-5.8 K. Magnetic hysteresis data at the lowest measured temperature *T* = 1.8 K for (c) **8-Dy** and (d) **9-Dy**. The average sweep rate was calculated at different field intervals, with a mean sweep rate of (e) 13.6 Oe s^{-1} and (f) 12.2 Oe s^{-1}, respectively.

6.2.4 Alternating Current Magnetic Susceptibility Studies

The high temperature magnetic relaxation times were probed by ac magnetic susceptibility measurements in the temperature range of 1.9-70 K for **8-Dy** and 7-62 K for **9-Dy**. using a driving field of H_{ac} = 3.78 Oe and H_{dc} = 0 Oe. The in-phase (χ') and out-of-phase (χ") components of the ac susceptibility as a function of ac frequency (v) for **8-Dy** display prominent SMM behaviour, with frequency dependent behaviour observable below 70 K (Figure 6.10). Below 15 K, there is little frequency dependence on χ''. Comparatively, in the χ' and χ'' susceptibilities for **9-Dy**, a signal was observed at a marginally smaller temperature of 62 K and persists as a frequency dependent signal until 8 K (Figure 6.10). It should be noted that the loss of frequency dependence behaviour occurs at a lower frequency for **9-Dy** than **8-Dy** (0.8 Hz *vs.* 8 Hz), suggesting that QTM effects in **8-Dy** are greater. The magnetization relaxation times (τ) were extracted by fitting the individual χ' and χ'' isothermal curves to the generalized Debye model.[40,41] Across the entirety of the temperature range studied, a minimal distribution of the relaxation times was obtained for **8-Dy**, $\alpha_{\chi'} = 0\text{-}0.256$ and $\alpha_{\chi''} = 0\text{-}0.286$, as well as for **9-Dy**, $\alpha_{\chi'} = 0.015\text{-}0.460$ and $\alpha_{\chi''} = 0.048\text{-}0.336$.

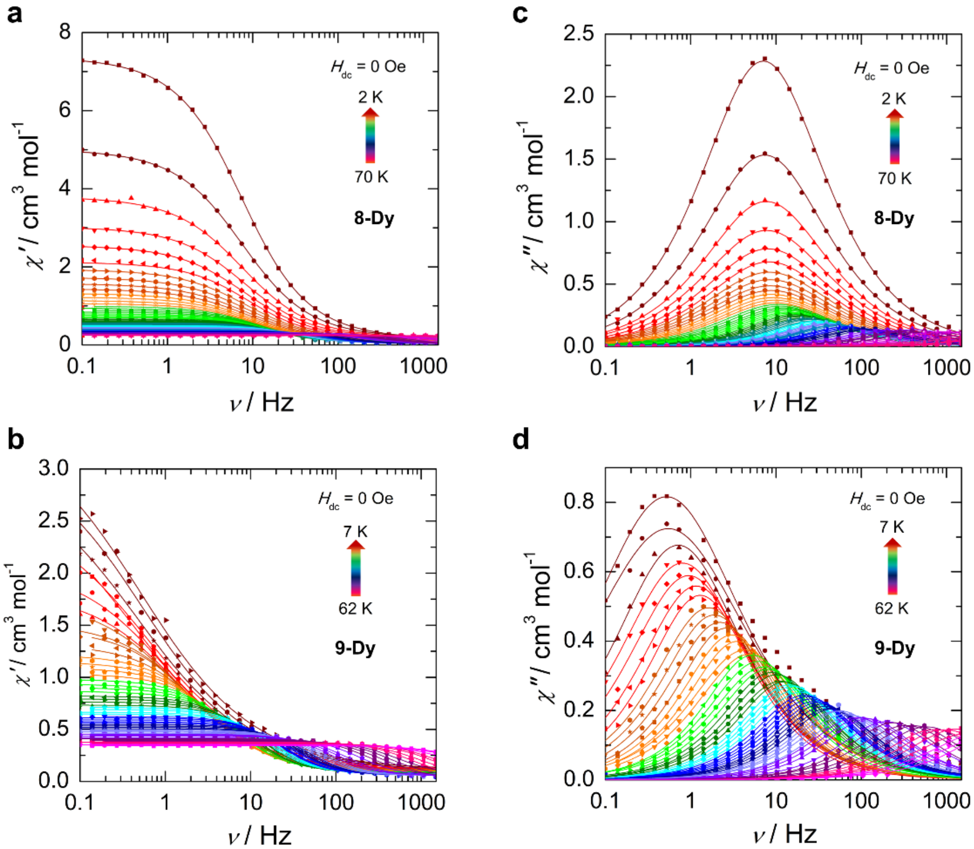

Figure 6.10 Frequency dependence of the (a-b) in-phase (χ') and (c-d) out-of-phase (χ'') components of the ac susceptibility for **8-Dy** and **9-Dy** collected in the absence of an applied static field, $H_{dc} = 0$ Oe, at the indicated temperatures. Solid lines represent best fits to the generalized Debye model.

Due to the limited frequency dependence of the χ' and χ" signals at low temperatures, ac measurements were performed at a fixed temperature of 20 K and the applied static field was varied from 0-5000 Oe (Figure 6.11). Frequency dependent behaviour was observed between 0 and 400 Oe for **8-Dy**, above which very minute changes in the characteristic frequency were observed. Similarly, **9-Dy** displayed frequency dependent behaviour between 0 and 1000 Oe; however, the deviation in peak maxima occurred over a much narrower frequency range (2-5 Hz *vs.* 2-14 Hz). A local minimum in the characteristic frequency was obtained at 600 and 1200 Oe for **8-Dy** and **9-Dy**, respectively (Figure 6.11c). At these fields, QTM effects are minimized, yielding longer relaxation times. The field dependent relaxation times were obtained *via* the generalized Debye model and reveal a 6-fold increase in the relaxation time upon application of a static field for **8-Dy**. The short relaxation time of τ = 12 ms, when H_{dc} = 0 Oe, increases to τ = 72 ms at 600 Oe; comparatively, the optimal field of 1200 Oe for **9-Dy** results in a relaxation time of 84 ms, a 2.5x increase from the zero-field time (τ = 34 ms). This relaxation time is longer than that obtained under the optimal static field for the chloro-derivative, despite the need for a larger applied static field. In fact, across the entirety of the studied field range, the iodo-derivative, **9-Dy**, exhibits longer relaxation times compared to **8-Dy**.

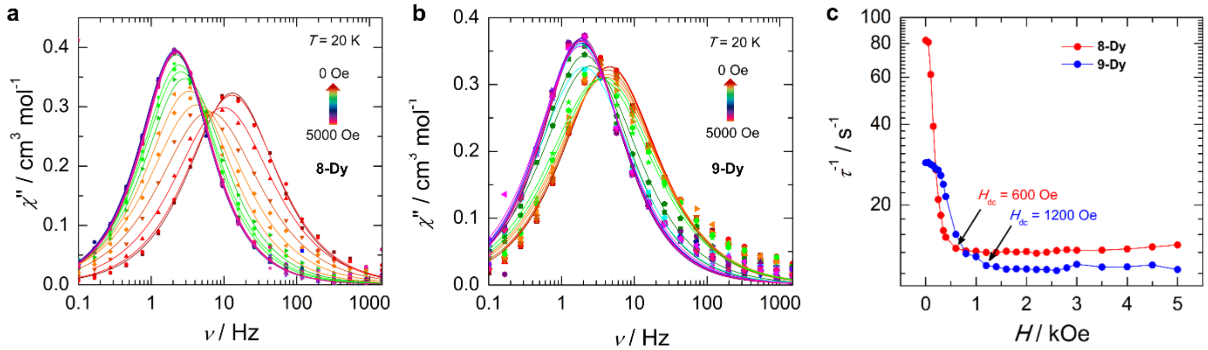

Figure 6.11 Frequency dependence of the out-of-phase (χ") component of the ac susceptibility as a function of applied static field, collected a constant temperature, T = 20 K, for (a) **8-Dy** and (b) **9-Dy**. (c) Field dependence of the relaxation times (τ) at a fixed temperature of 20 K for compound **8-Dy** (red) and compound **9-Dy** (blue). The relaxation times were obtained from the generalized Debye model. The minimum represents the optimal static field for which the relaxation time is the longest and QTM is reduced.

With the goal of increasing the SMM performance of both **8-Dy** and **9-Dy** by limiting the zero-field QTM, ac susceptibility studies were completed at their respective optimal fields, 600 Oe for **8-Dy** and 1200 Oe for **9-Dy**. The effects of intermolecular interactions should also be negligible, as a field of 400 Oe or greater was determined to be necessary for decoupling the dipolar interaction between nearest neighbours in the crystal lattice. Under these conditions, **8-Dy** exhibited frequency dependent behaviour in the χ’ and χ” components of the ac susceptibility throughout the entirety of the measured temperature range T = 10-70 K (Figure 6.12). The τ-values were obtained from the fits of the χ’ and χ” isotherms to the generalized Debye model,[14] which produced $\alpha_{\chi'}$ = 0-0.0745 and $\alpha_{\chi''}$ = 0-0.0561, indicating a very narrow distribution of the relaxation times. With respect to **9-Dy**, upon application of a static field of 1200 Oe, frequency dependent behaviour was observed from 10-62 K in the χ’ and χ” susceptibilities (Figure 6.12). Below 10 K, a maximum was not observed in the χ” *vs.* ν plot. A narrow distribution of relaxation times was also found for this data set ($\alpha_{\chi'}$ = 0-0.371 and $\alpha_{\chi''}$ = 0-0.264).

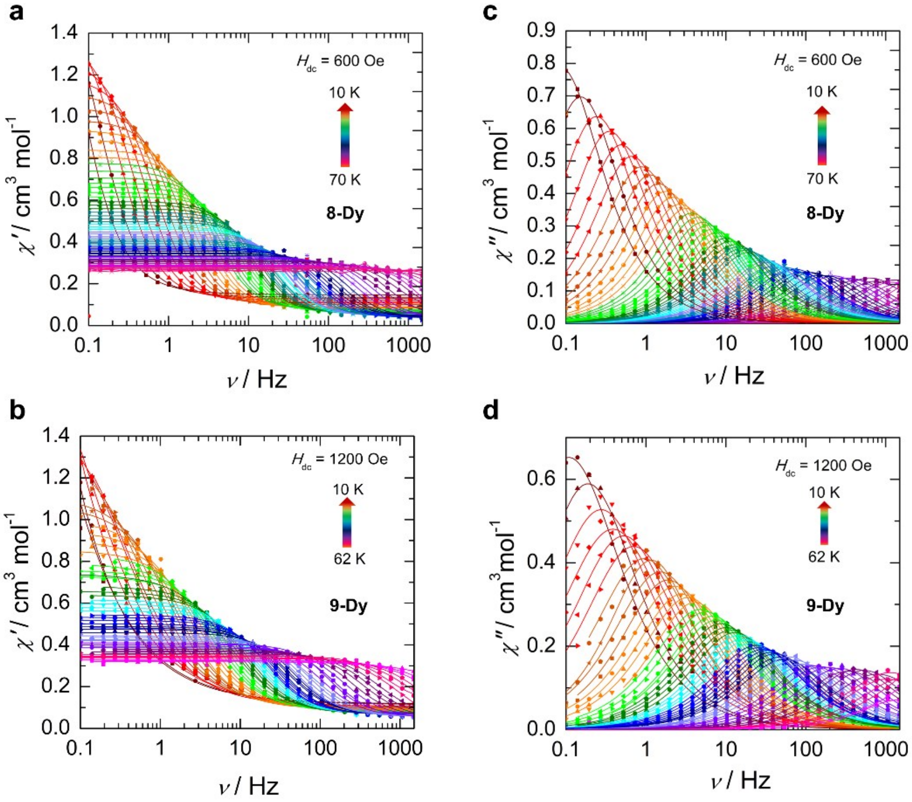

Figure 6.12 Frequency dependence of the (a-b) in-phase (χ’) and (c-d) out-of-phase (χ”) components of the ac susceptibility for **8-Dy** and **9-Dy** collected under an applied static field of optimal strength for both **8-Dy** (H_{dc} = 600 Oe) and **9-Dy** (H_{dc} = 1200 Oe). Solid lines represent best fits to the generalized Debye model.

Insight into the magnetic relaxation dynamics was obtained through the analysis and fitting of the τ^{-1} *vs.* T plots of **8-Dy** and **9-Dy** (Figure 6.13). Commonly, relaxation in SMMs is described by QTM, Orbach, and Raman mechanisms (Equation 6.1). Each of these processes possess unique temperature and field dependences which allow for the interpretation of the relaxation dynamics of each SMM. To account for these different relaxation regimes, the temperature dependent relaxation times were fit for QTM, Orbach, and Raman relaxations (Equation 6.2).

$$\tau^{-1} = \tau_{QTM}^{-1} + \tau_{Orbach}^{-1} + \tau_{Raman}^{-1} \tag{6.1}$$

$$\tau^{-1} = \tau_{QTM}^{-1} + \tau_0^{-1}\exp\left(-\frac{U_{\mathrm{eff}}}{k_{\mathrm{B}}T}\right) + CT^{n} \tag{6.2}$$

These five parameters effectively reproduce the experimental relaxation times over their respective temperature domains. For compounds **8-Dy** and **9-Dy**, the Orbach relaxation is dominate above *ca.* 48 K, the Raman is active between *ca.* 10-48 K, and only at H_{dc} = 0 Oe is QTM observed below *ca.* 10 K. The best fit parameters are summarized in Table 6.2.

Table 6.2 Magnetic relaxation parameters obtained from the fit of the temperature dependent relaxation times for **8-Dy** and **9-Dy**. Best fits were obtained with QTM, Orbach, and Raman contributions.

	8-Dy		**9-Dy**	
	H_{dc} = 0 Oe	**H_{dc} = 600 Oe**	**H_{dc} = 0 Oe**	**H_{dc} = 1200 Oe**
τ_{QTM}	0.023 s	-	0.33 s	-
τ_0	7.01 x 10^{-14} s	4.81 x 10^{-14} s	3.37 x 10^{-14} s	3.58 x 10^{-12} s
U_{eff}	1334 K / 927 cm^{-1}	1366 K / 949 cm^{-1}	1278 K / 888 cm^{-1}	1016 K / 705 cm^{-1}
C	3.01 x 10^{-3} s^{-1} K^{-n}	4.80 x 10^{-5} s^{-1} K^{-n}	9.89 x 10^{-4} s^{-1} K^{-n}	3.61 x 10^{-5} s^{-1} K^{-n}
n	3.0	4.17	3.35	4.22

The fit of the relaxation dynamics reveals large spin reversal barriers in zero field, U_{eff} = 1334 K/927 cm^{-1} (**8-Dy**) and 1278 K/888 cm^{-1} (**9-Dy**), with attempt times (τ_0) in the range 10^{-11}–10^{-15} s, as is for other high-U_{eff} SMMs (> 1000 K/ 695 cm^{-1}).[13,15,16,18,42] The lack of change in the energy barrier despite the difference in halide ion bound to the $\mathrm{Dy^{III}}$ ion is likely a consequence of the halide not being situated along the anisotropy axis; instead the transverse bisanilide ligand dictates the height of the barrier. To support this, there is little change in the energy barriers with application of the respective optimal static fields as this process is a function of the crystal field splitting manifold. For compounds **8-Dy** and **9-Dy**, the U_{eff} values are in good agreement with the prediction from the *ab initio* results, that magnetic relaxation would occur *via* the 4th KD (*ca.* 900 cm^{-1}).

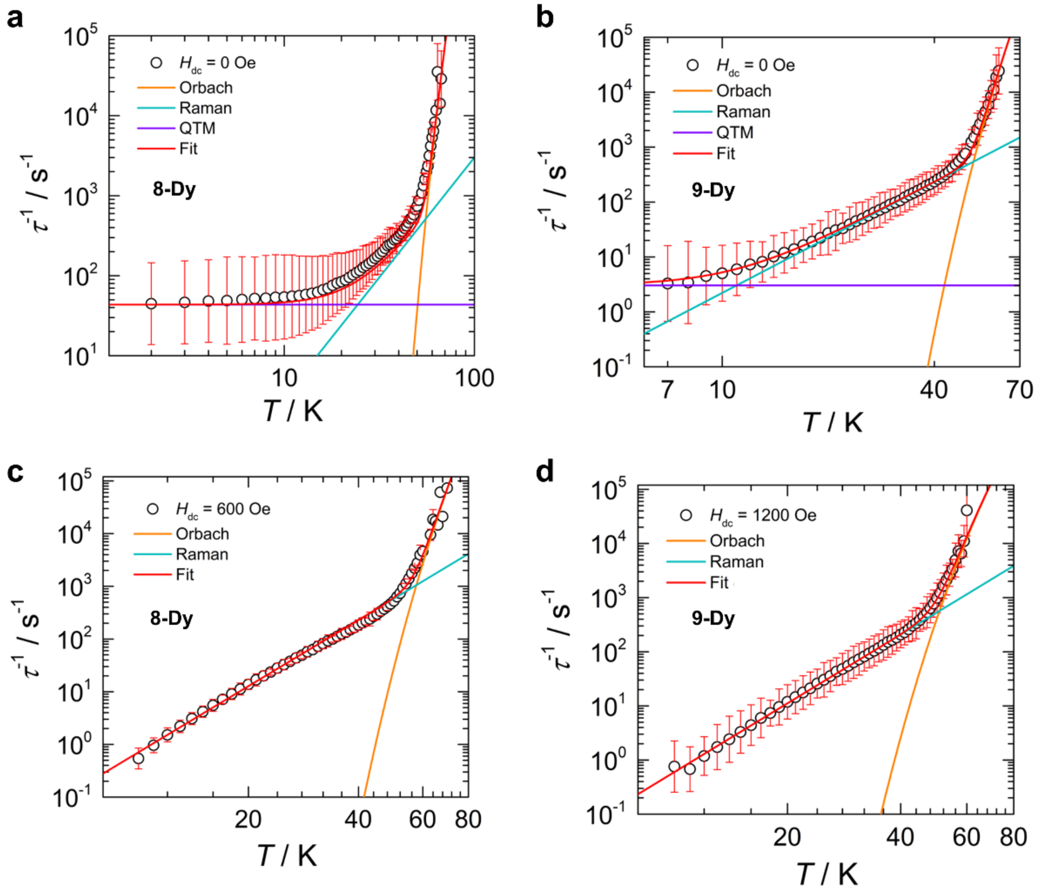

Figure 6.13 Temperature dependence of the magnetic relaxation times (τ) when H_{dc} = 0 Oe for (a) **8-Dy** and (b) **9-Dy**. The respective analysis on the field-induced relaxation times when (c) H_{dc} = 600 Oe for **8-Dy** and (d) H_{dc} = 1200 Oe for **9-Dy**. The red solid lines represent best-fits to Equation. 6.2. The orange, teal, and purple lines are the individual components of the magnetization relaxation for Orbach, Raman, and QTM processes, respectively. The estimated standard deviations of the relaxation time have been calculated from the α-parameters of the generalized Debye fits with the log-normal distribution.

With respect to Raman relaxation, the C and n parameters remain relatively constant for **8-Dy** (C = 3.01 x 10^{-3}s^{-1}K^{-n}; n = 3.0) and **9-Dy** (C = 9.89 x 10^{-4}s^{-1}K^{-n}; n = 3.35) at zero field. Despite the similar parameters, the relaxation times for this regime are longer for **9-Dy**. In fact, at zero field, and 30 K, the relaxation time is more than twice (2.62 x) as long for **9-Dy** (0.011 s) compared to **8-Dy** (0.006 s). While at their respective optimal fields, the discrepancy in the Raman relaxation times at this temperature is negligible ($\tau \approx$ 0.016 s). At the higher temperature limit of this relaxation process, there are only minor differences in the relaxation times for **8-Dy** and **9-Dy**. This may be indicative of contributions from the Orbach relaxation as the two compounds have very similar crystal field splittings (*vide supra*).

Lastly, at zero-field, the relaxation dynamics of **8-Dy** and **9-Dy** at low temperature are characterized by a QTM rate on the order of milliseconds. In the absence of an applied static field, **9-Dy** has notably less contributions from tunnelling pathways compared to **8-Dy**. The rate of tunnelling is considerably slower in the iodo-derivative compared to the rate of **8-Dy** (43.48 s^{-1} *vs.* 3.03 s^{-1}). This represents a decrease in the efficiency of the QTM process by a factor of 14 for **9-Dy**.

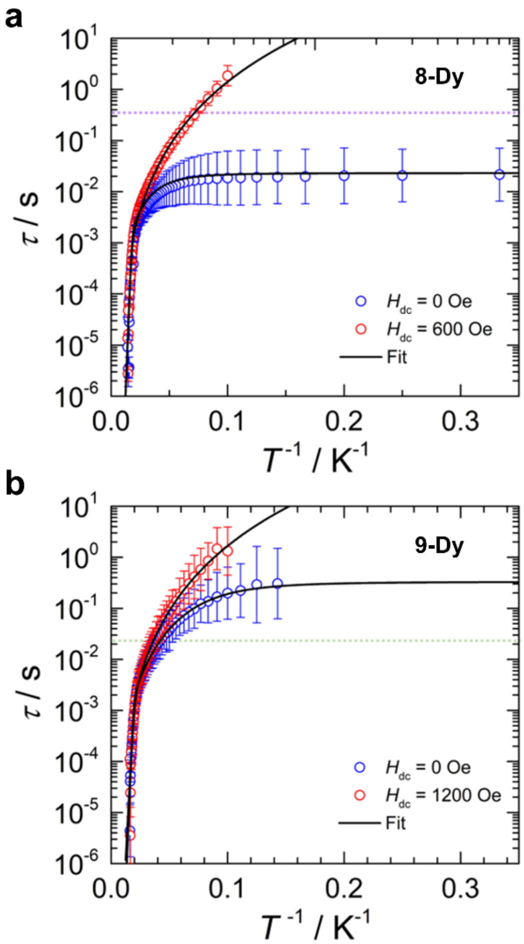

Figure 6.14 (a) Temperature dependence of the magnetic relaxation times (τ) when H_{dc} = 0 Oe (blue) and H_{dc} = 600 Oe (red) for compound **8-Dy**. Solid lines represent best-fits to Equation 6.2. The estimates standard deviations of the relaxation time have been calculated from the α-parameters of the generalized Debye fits. (b) The corresponding data for compound **9-Dy**. The dashed lines represent the QTM rates for compound **8-Dy** (green) and **9-Dy** (purple), demonstrating a faster QTM rate for **8-Dy**.

To illustrate this significant difference, the QTM rates of **8-Dy** (green) and **9-Dy** (purple) have been represented as dotted lines on the opposing τ *vs.* T^{-1} plots (Figure 6.14). This means the tunnelling mechanism is more efficient and faster in the chloro-derivative which may be a consequence of the shorter Dy-X distance of **8-Dy** (2.510(3)-2.579(3) Å) *vs.* **9-Dy** (2.9355(7)-2.9771(5) Å), resulting in marginally larger transverse components (g'_x, g'_y) of the anisotropy for **8-Dy** (*vide supra*). Nonetheless, it is evident that varying the halide ions results in notable changes in the rate of the through-barrier relaxations.

6.3 Summary and Conclusion

In conclusion, the bisanilide terphenyl ligand $[L^{Ar}]^{2-}$, when coordinated to Dy^{III}, gives rise to an unusual, see-saw shaped metal ion geometry. The transverse coordination mode of the ligand, combined with the free-ion oblate-shaped electron density of Dy^{III}, leads to two SMMs with impressive energy barriers to spin reversal U_{eff} = 1334 K (927cm^{-1}) and 1299 K (903 cm^{-1}) in zero field. The crystal field imposed by the bisanilide ligand is the most dominant influence on the crystal field regardless of the ancillary halide (Cl *vs.* I), thus it defines the height of the energy barrier. However, it is clear that the presence of a heavy halide leads to longer relaxation times on average, resulting in a 564% increase in zero field. While it has been proposed that the weaker more diffuse interaction of the iodide ligand would lead to overall greater SMM performance, the direct effects of this are not indicated by the U_{eff}, instead small changes to relaxation dynamics are observed. Most notably, a 14x increase in the efficiency of the QTM pathway is observed when chloride ions are bound to the Dy^{III} ion. When dominant, the Raman relaxation pathway is more than twice (2.62x) as fast in the chloride (**8-Dy**) analogue *vs*. the iodide (**9-Dy**) Thus, incorporating heavier atoms into high-performing Dy^{III} SMMs is an effective way to increase the relaxation times of through-barrier relaxation pathways, which would ultimately allow the Orbach process to preside over a wider temperature regime. Yet, their incorporation will not necessarily improve the U_{eff} or the blocking capabilities of a SMM, as the relative location of the heavy atoms with respect to the anisotropy axis combined with the other contributors to the crystal field are all vital to defining these features.

6.4 Experimental Details

6.4.1 General Procedures

All air and moisture-sensitive operations were performed in a M. Braun dry box under an atmosphere of purified dinitrogen or using high vacuum standard Schlenk techniques. Solvents were dried using a Pure Process Technology Solvent Purification System and subsequently stored under a dinitrogen atmosphere over activated 4 Å molecular sieves. Anhydrous $DyCl_3$ was purchased from Strem Chemicals Inc. at 99.9% purity. $DyI_3(THF)_{3.5}$ was synthesized using previously reported methods.[43] $[K(DME)_2]_2L^{Ar}$ was synthesized according to the literature procedure.[29] THF-d_8 and benzene-d_6 were purchased from Cambridge Isotope

Laboratories Inc. and dried over activated 4 Å molecular sieves for 24 h prior to use. Celite used for filtration was dried under vacuum while heating at 250 °C for 24 h, subsequently cooled under vacuum, and stored under dinitrogen. All NMR data reported were measured using a Bruker AVANCE III 400 MHz spectrometer, and the ^{1}H NMR spectra are referenced to $SiMe_4$ using the residual ^{1}H solvent peaks as internal standards. UV/vis-NIR spectra were recorded using a Cary 5000 spectrophotometer. Elemental Analyses were performed by Midwest Microlabs, LLC. UV-vis/NIR spectra were recorded on a Cary 5000 spectrophotometer using toluene as a solvent.

6.4.2 Experimental Procedures

Synthesis of $[K(DME)_3][L^{Ar}Dy^{III}(Cl)_2]$ (8-Dy) . In a 20 mL scintillation vial, $DyCl_3$ (40.7 mg, 0.15 mmol) was added to THF (2 mL) with stirring, forming a colorless suspension. In a separate vial, $[K(DME)_2]_2L^{Ar}$ (150.0 mg, 0.15mmol) was dissolved in THF (4 mL), making a dark red solution. Both vials were frozen in a liquid nitrogen cooled cold-well within a glovebox. Upon thawing, the $[K(DME)_2]_2L^{Ar}$ solution was added dropwise to the thawing, stirring $DyCl_3$ suspension. The reaction was allowed to warm to room temperature and stirred for 12 h, resulting in a brown-yellow turbid solution. The mixture was filtered through a plug of Celite supported on a glass frit, passing a clear, brown-yellow solution. The filtrate was dried under reduced pressure to give a light brown-yellow solid. The solid was dissolved in DME (1 mL) and crystals of **8-Dy** were grown from storage of the DME solution at -25 °C for 3 days. Yield: 78.8 mg, 47.4%. ^{1}H NMR (25 °C, 400 MHz, THF-d_8): δ -401.5 (br s), -300.3 (br s, fwhm = 8,211 Hz), -102.8 (br s), -0.2 (br s), 12.6 (br s), 33.2 and 35.8 (overlapping br s), 64.3 (br s), 117.4 (br s), 148.7 (br s), 156.9 (br s), 212.8 (br s, fwhm = 6,276 Hz), 294.9 (br s), 317.3 (br s). UV-vis (toluene, 0.29 mM, 25 °C, $L\cdot mol^{-1}\cdot cm^{-1}$): 297 ($\varepsilon = 11{,}808$), 406 ($\varepsilon = 1{,}992$). Anal. Calcd for $C_{54}H_{76}N_2O_6KDyCl_2$: C, 57.81; H, 6.84; N, 2.50. Found: C, 58.02; H, 7.00; N, 2.58.

Synthesis of $[K(DME)_4][L^{Ar}Dy^{III}(I)_2]$ (9-Dy) . In a 20 mL scintillation vial, $DyI_3(THF)_{3.5}$ (285.0 mg, 0.288 mmol) was added to THF (6 mL) with stirring, forming a colorless suspension. In a separate vial, $[K(DME)_2]_2L^{Ar}$ (252.7 mg, 0.25 mmol) was dissolved in THF (4 mL), making a dark red solution. Both vials were cooled down to -35 °C in a cold-well within a glovebox. Then, the $[K(DME)_2]_2L^{Ar}$ solution was added dropwise to the cold, stirring $DyI_3(THF)_{3.5}$ suspension. The reaction was allowed to warm to room temperature and stirred for 12 h, resulting in a brown-red turbid solution. The mixture was filtered through a plug of Celite supported on a glass frit, passing a clear, brown-red solution. The filtrate was dried under reduced pressure to give a red solid. The solid was dissolved in DME (2 mL) and layered with pentane (2 mL). Crystals of **9-Dy** were grown from storage of the DME/pentane solution at -35 °C for 3 days. Yield: 221.7 mg, 55.7%. ^{1}H NMR (25 °C, 400 MHz, THF-d_8): δ -348.6 (br s), -156.9 (br s, fwhm = 1,052 Hz), -34.9 (br s), 11.3 (br s), 11.7 (br s), 12.5 (br s), 12.7 (br s), 13.3 (br s), 45.6 (br s, fwhm = 2,764 Hz), 53.3

(br s), 73.1 (br s, fwhm = 1,488 Hz), 80.9 (br s), 93.2 (br s), 95.1(br s), 118.9 (br s), 123.4 (br s), 129.6 (br s, fwhm = 2,148 Hz), 136.9 (br s), 165.5 (br s, fwhm = 3,208 Hz), 183.9 (br s, fwhm = 1,800 Hz), 291.3 (br s), 328.2 (br s, fwhm = 3,252 Hz). UV-vis (toluene, 0.122 mM, 25 °C, $L\cdot mol^{-1}\cdot cm^{-1}$): 285 ($\varepsilon$ = 18,860), 438 (ε = 1,435). Despite several independent attempts, a combustion analysis of **9-Dy** gave unsatisfactory values, which may be due to impurities or poor combustion properties

6.4.3 Crystallography

Single crystal X-ray studies for **8-Dy** and **9-Dy** were initially carried out on a Bruker 3-axis platform diffractometer equipped with an APEX I CCD detector using a graphite monochromator with a Mo Kα X-ray source (λ = 0.71073 Å) at 100(2) K under a flow of nitrogen gas during data collection. Alternatively, for **8-Dy**, low temperature data (15(2) K under a flow of helium gas) was collected at ChemMatCARS located at the Advanced Photon Source (APS), Argonne National Laboratory (ANL), using synchrotron radiation (λ = 0.41328 Å) in conjunction with a Bruker D8 three-circle platform goniometer equipped with Dectris PILATUS 100 detector. Samples were coated in NVH crystallographic immersion oil and mounted on a glass fiber prior to diffraction. Data was collected using φ and ω scan collection strategies. Data collection and cell parameter determination were conducted using the SMART[44] program. Integration of the data and final cell parameter refinements were performed using SAINT[45] software with data absorption correction implemented through SADABS.[46] Structure solutions were completed using direct methods determinations in SHELXTL[47,48] or Olex2[49] crystallographic packages. All hydrogen atom positions were idealized and treated as riding on the parent atom.

Table 6.3 Crystallographic data for **8-Dy** and **9-Dy.**

Compound	**8-Dy** $[K(DME)_3][L^{Ar}Dy(Cl)_2]$ (15 K)	**8-Dy** (100 K) $[K(DME)_3][L^{Ar}Dy(Cl)_2]$ (100 K)	**9-Dy** $[K(DME)_4][L^{Ar}Dy(I)_2]$ (100 K)
Empirical formula	$DyN_2Cl_2C_{42}H_{32}\cdot K(C_4H_{10}O_2)_3$	$DyN_2Cl_2C_{42}H_{32}\cdot K(C_4H_{10}O_2)_3$	$DyN_2I_2C_{42}H_{32}\cdot K(C_4H_{10}O_2)_4$
Formula weight	1121.76	1121.76	1881.21
Crystal habit, colour	Block, red orange	Block, red orange	Block, red
Crystal size, mm	0.15 x 0.15 x 0.14	0.12 x 0.13 x 0.21	0.15 x 0.15 x 0.25
Crystal system	Monoclinic	Monoclinic	Triclinic
Space group	***Pn***	***Cc***	$\boldsymbol{P\bar{1}}$
Z	2	4	1
a, Å	21.2253(8)	21.287(2)	13.2019(4)
b, Å	15.87848(7)	15.8231(9)	13.5333(4)
c, Å	34.262(1)	34.353(2)	18.6052(5)
α, °	90	90	104.305(2)
β, °	105.304(1)	105.354(2)	94.039(2)
γ, °	90	90	108.319(2)
Volume, $Å^3$	11072.1(8)	11157.9(1)	3017.91(2)
Calculated density, Mg/m^3	1.342	1.338	1.035
Absorption coefficient, mm^{-1}	1.568	0.184	1.205
F(000)	4626.3	4400	953.0
Total no. reflections	267074	153297	180319
Unique reflections	43121	25858	19676
Final R indices [$I > 2\sigma(I)$]	$R_1 = 0.0464$ $wR_2 = 0.01259$	$R_1 = 0.0543$ $wR_2 = 0.01459$	$R_1 = 0.0730$ $wR_2 = 0.01463$
Largest diff. peak/hole, $e\cdot Å^{-3}$	-2.3 and 2.2	-2.0 and 2.9	-3.43 and 4.23
Goodness-of-fit	1.043	1.119	1.153

6.4.4 Magnetometry

The magnetic susceptibility measurements were obtained using a Quantum Design SQUID magnetometer MPMS-XL7 operating between 1.8 and 300 K. DC measurements were performed on polycrystalline samples of 17.0 mg for **8-Dy** and 23.0 mg for **9-Dy**. The samples were restrained with silicon grease and wrapped in a polyethylene membrane under an inert atmosphere. The samples were subjected to DC fields of -7 to 7 T, and a 3.78 Oe driving field was used for AC measurements. The magnetization data were collected at 100 K to check for ferromagnetic impurities that were absent in both samples. Diamagnetic corrections were applied for the sample holder and the inherent diamagnetism of the samples were estimated with the use of Pascals constants.

6.4.5 Computational Details

Electronic structure calculations were performed using MOLCAS-8.0 program[34] with the following basis set: Dy-ANO-RCC-VTZP; O and Cl, N- ANO-RCC-VDZP; C and H – ANO-RCC-VDZ.[50–52] Cholesky decomposition with the "high" accuracy threshold was used for the two electron integrals to speed up the calculation and reduce memory requirements.[53,54] Scalar relativistic effects were accounted using second order Douglas-Kroll-Hess approximation.[55] Active space for CASSCF[56] calculation of spin-free states consists of seven 4*f* orbitals with 9 electrons for $\mathrm{Dy^{III}}$. Spin-orbit coupling was computed using the mean-field approximation[57] as implemented in RASSI. Molar magnetic susceptibility and magnetization were computed using SINGLE_ANISO[35] routine together with the ligand field parameters for Stevens operator equivalence representation of the ground term with the total momentum $J = 15/2$.[10]

Table 6.4 Parameters of the crystal field acting on the ground J = 15/2 multiplet for **8-Dy2**, **8-Dy4**, and **9-Dy**.

Rank	Proj.	8-Dy2	8-Dy4	9-Dy
2	-2	0.13759277070001E+01	-0.79920811552959E-01	0.16752865084159E+00
	-1	0.60568258227511E+01	0.28599494401362E+00	0.39646482700936E+00
	0	-0.55064478748947E+01	-0.52311665514918E+01	-0.66530092985073E+01
	1	0.41850561175636E+01	0.11885846759185E+01	-0.44784204178090E+00
	2	-0.68657368182833E+00	0.13981371879997E+01	0.11089368721060E+01
4	-4	-0.91760884828230E-02	-0.79920811552959E-01	0.39880372896653E-02
	-3	-0.14086244655349E-01	0.28599494401362E+00	-0.26482342836212E-02
	-2	-0.14285025336814E-02	-0.52311665514918E+01	-0.90851456298114E-02
	-1	0.20680347114299E-01	0.11885846759185E+01	-0.13738781928699E-02
	0	-0.70841322519724E-02	0.13981371879997E+01	-0.71951245336476E-02
	1	0.20734433397404E-01	-0.79920811552959E-01	-0.31869352368885E-02
	2	0.10289683903598E-01	0.28599494401362E+00	0.38389874398895E-02
	3	-0.14943562628113E-01	-0.52311665514918E+01	-0.23892900704950E-04
	4	-0.42423524791366E-02	0.11885846759185E+01	0.34016686935758E-02
6	-6	0.86158469752200E-04	-0.79361156154741E-04	-0.79361156154741E-04
	-5	-0.10633981818438E-03	-0.27267292140858E-04	0.19242112830489E-03
	-4	0.18642583169091E-04	0.68422938523818E-04	-0.20432267401460E-04
	-3	0.24224997515557E-03	0.29869891007048E-04	-0.87061230531053E-04
	-2	-0.10245005043998E-04	-0.17417071280434E-03	0.29821568924351E-04
	-1	-0.23938258563324E-03	-0.31526907569805E-04	0.15038172178457E-03
	0	0.23586180988534E-04	0.35836414935033E-04	-0.81422340169123E-06
	1	-0.30055714833460E-03	-0.54142123313893E-04	0.41048821195452E-04
	2	-0.10163342384825E-03	-0.38183385612794E-04	0.37107631720323E-04
	3	0.21065400387940E-05	-0.60463654159698E-05	-0.11360069075366E-03
	4	-0.14861094420313E-04	-0.47082382123324E-04	-0.20689940768087E-04
	5	0.37422404611554E-03	0.26440266706367E-04	0.23766420845702E-04
	6	0.17707052063856E-03	0.18254608171442E-03	-0.74637611785098E-05

6.5 References

(1) Sessoll, R.; Gatteschi, D.; Caneschi, A.; Novak, M. A. Magnetic Bistability in a Metal-Ion Cluster. *Nature* **1993**, *365*, 141–143.

(2) Feng, M.; Tong, M.-L. Single Ion Magnets from 3d to 5f: Developments and Strategies. *Chem.-Eur. J.* **2018**, *24* (30), 7574–7594. https://doi.org/10.1002/chem.201705761.

(3) Woodruff, D. N.; Winpenny, R. E. P.; Layfield, R. A. Lanthanide Single-Molecule Magnets. *Chem. Rev.* **2013**, *113* (7), 5110–5148. https://doi.org/10.1021/cr400018q.

(4) Gatteschi, D.; Sessoli, R.; Villain, J. *Molecular Nanomagnets*; Oxford University Press, 2006.

(5) Leuenberger, M. N.; Loss, D. Quantum Computing in Molecular Magnets. *Nature* **2001**, *410* (6830), 789–793. https://doi.org/10.1038/35071024.

(6) Chilton, N. F. Design Criteria for High-Temperature Single-Molecule Magnets. *Inorg. Chem.* **2015**, *54* (5), 2097–2099. https://doi.org/10.1021/acs.inorgchem.5b00089.

(7) Rinehart, J. D.; Long, J. R. Exploiting Single-Ion Anisotropy in the Design of f-Element Single-Molecule Magnets. *Chem. Sci.* **2011**, *2* (11), 2078. https://doi.org/10.1039/c1sc00513h.

(8) Briganti, M.; Garcia, G. F.; Jung, J.; Sessoli, R.; Le Guennic, B.; Totti, F. Covalency and Magnetic Anisotropy in Lanthanide Single Molecule Magnets: The DyDOTA Archetype. *Chem. Sci.* **2019**, *10* (30), 7233–7245. https://doi.org/10.1039/C9SC01743G.

(9) Jung, J.; Islam, M. A.; Pecoraro, V. L.; Mallah, T.; Berthon, C.; Bolvin, H. Derivation of Lanthanide Series Crystal Field Parameters From First Principles. *Chem.–Eur. J.* **2019**, *25* (66), 15112–15122. https://doi.org/10.1002/chem.201903141.

(10) Ungur, L.; Chibotaru, L. F. Ab Initio Crystal Field for Lanthanides. *Chem.-Eur. J.* **2017**, *23* (15), 3708–3718. https://doi.org/10.1002/chem.201605102.

(11) Chilton, N. F.; Collison, D.; McInnes, E. J. L.; Winpenny, R. E. P.; Soncini, A. An Electrostatic Model for the Determination of Magnetic Anisotropy in Dysprosium Complexes. *Nat. Commun.* **2013**, *4* (1), 2551. https://doi.org/10.1038/ncomms3551.

(12) Chilton, N. F.; Langley, S. K.; Moubaraki, B.; Soncini, A.; Batten, S. R.; Murray, K. S. Single Molecule Magnetism in a Family of Mononuclear β-Diketonate Lanthanide(III) Complexes: Rationalization of Magnetic Anisotropy in Complexes of Low Symmetry. *Chem. Sci.* **2013**, *4* (4), 1719. https://doi.org/10.1039/c3sc22300k.

(13) Guo, F.-S.; Day, B. M.; Chen, Y.-C.; Tong, M.-L.; Mansikkamäki, A.; Layfield, R. A. Magnetic Hysteresis up to 80 Kelvin in a Dysprosium Metallocene Single-Molecule Magnet. *Science* **2018**, *362* (6421), 1400–1403. https://doi.org/10.1126/science.aav0652.

(14) Chilton, N. F.; Goodwin, C. A. P.; Mills, D. P.; Winpenny, R. E. P. The First Near-Linear Bis(Amide) f-Block Complex: A Blueprint for a High Temperature Single Molecule Magnet. *Chem. Commun.* **2015**, *51* (1), 101–103. https://doi.org/10.1039/C4CC08312A.

(15) Ding, Y.-S.; Chilton, N. F.; Winpenny, R. E. P.; Zheng, Y.-Z. On Approaching the Limit of Molecular Magnetic Anisotropy: A Near-Perfect Pentagonal Bipyramidal Dysprosium(III) Single-Molecule Magnet. *Angew. Chem. Int. Ed.* **2016**, *55* (52), 16071–16074. https://doi.org/10.1002/anie.201609685.

(16) Goodwin, C. A. P.; Ortu, F.; Reta, D.; Chilton, N. F.; Mills, D. P. Molecular Magnetic Hysteresis at 60 Kelvin in Dysprosocenium. *Nature* **2017**, *548* (7668), 439–442. https://doi.org/10.1038/nature23447.

(17) Gregson, M.; Chilton, N. F.; Ariciu, A.-M.; Tuna, F.; Crowe, I. F.; Lewis, W.; Blake, A. J.; Collison, D.; McInnes, E. J. L.; Winpenny, R. E. P.; Liddle, S. T. A Monometallic Lanthanide Bis(Methanediide) Single Molecule Magnet with a Large Energy Barrier and Complex Spin Relaxation Behaviour. *Chem. Sci.* **2016**, *7* (1), 155–165. https://doi.org/10.1039/C5SC03111G.

(18) Guo, F.-S.; Day, B. M.; Chen, Y.-C.; Tong, M.-L.; Mansikkamäki, A.; Layfield, R. A. A Dysprosium Metallocene Single-Molecule Magnet Functioning at the Axial Limit. *Angew. Chem. Int. Ed.* **2017**, *56* (38), 11445–11449. https://doi.org/10.1002/anie.201705426.

(19) Harriman, K. L. M.; Brosmer, J. L.; Ungur, L.; Diaconescu, P. L.; Murugesu, M. Pursuit of Record Breaking Energy Barriers: A Study of Magnetic Axiality in Diamide Ligated Dy ^{III} Single-Molecule Magnets. *J. Am. Chem. Soc.* **2017**, *139* (4), 1420–1423. https://doi.org/10.1021/jacs.6b12374.

(20) Kilpatrick, A. F. R.; Guo, F.-S.; Day, B. M.; Mansikkamäki, A.; Layfield, R. A.; Cloke, F. G. N. Single-Molecule Magnet Properties of a Monometallic Dysprosium Pentalene Complex. *Chem. Commun.* **2018**, *54* (51), 7085–7088. https://doi.org/10.1039/C8CC03516D.

(21) Meng, Y.-S.; Xu, L.; Xiong, J.; Yuan, Q.; Liu, T.; Wang, B.-W.; Gao, S. Low-Coordinate Single-Ion Magnets by Intercalation of Lanthanides into a Phenol Matrix. *Angew. Chem. Int. Ed.* **2018**, *57* (17), 4673–4676. https://doi.org/10.1002/anie.201801223.

(22) Norel, L.; Darago, L. E.; Le Guennic, B.; Chakarawet, K.; Gonzalez, M. I.; Olshansky, J. H.; Rigaut, S.; Long, J. R. A Terminal Fluoride Ligand Generates Axial Magnetic Anisotropy in Dysprosium Complexes. *Angew. Chem. Int. Ed.* **2018**, *57* (7), 1933–1938. https://doi.org/10.1002/anie.201712139.

(23) Giansiracusa, M. J.; Kostopoulos, A. K.; Collison, D.; Winpenny, R. E. P.; Chilton, N. F. Correlating Blocking Temperatures with Relaxation Mechanisms in Monometallic Single-Molecule Magnets with High Energy Barriers (U_{eff}>600 K). *Chem. Commun.* **2019**, 10.1039.C9CC02421B. https://doi.org/10.1039/C9CC02421B.

(24) Wang, C.; Sun, R.; Chen, Y.; Wang, B.-W.; Wang, Z.-M.; Gao, S. Assembling High-Temperature Single-Molecule Magnets with Low-Coordinate Bis(Amido) Dysprosium Unit $[DyN_2]^+$ via Cl-K-Cl Linkage. *CCS Chem.* **2020**, 362–368. https://doi.org/10.31635/ccschem.020.202000138.

(25) Craig, G. A.; Sarkar, A.; Woodall, C. H.; Hay, M. A.; Marriott, K. E. R.; Kamenev, K. V.; Moggach, S. A.; Brechin, E. K.; Parsons, S.; Rajaraman, G.; Murrie, M. Probing the Origin of the Giant Magnetic Anisotropy in Trigonal Bipyramidal Ni(II) under High Pressure. *Chem. Sci.* **2018**, *9* (6), 1551–1559. https://doi.org/10.1039/C7SC04460G.

(26) Norre, M. S.; Gao, C.; Dey, S.; Gupta, S. K.; Borah, A.; Murugavel, R.; Rajaraman, G.; Overgaard, J. High-Pressure Crystallographic and Magnetic Studies of Pseudo- D_{5h} Symmetric Dy(III) and Ho(III) Single-Molecule Magnets. *Inorg. Chem.* **2020**, *59* (1), 717–729. https://doi.org/10.1021/acs.inorgchem.9b02962.

(27) Escalera-Moreno, L.; Suaud, N.; Gaita-Ariño, A.; Coronado, E. Determining Key Local Vibrations in the Relaxation of Molecular Spin Qubits and Single-Molecule Magnets. *J. Phys. Chem. Lett.* **2017**, *8* (7), 1695–1700. https://doi.org/10.1021/acs.jpclett.7b00479.

(28) Castro-Alvarez, A.; Gil, Y.; Llanos, L.; Aravena, D. High Performance Single-Molecule Magnets, Orbach or Raman Relaxation Suppression? *Inorg. Chem. Front.* **2020**, 10.1039.D0QI00487A. https://doi.org/10.1039/D0QI00487A.

(29) Fortier, S.; Aguilar-Calderón, J. R.; Vlaisavljevich, B.; Metta-Magaña, A. J.; Goos, A. G.; Botez, C. E. An *N* -Tethered Uranium(III) Arene Complex and the Synthesis of an Unsupported U–Fe Bond. *Organometallics* **2017**, *36* (23), 4591–4599. https://doi.org/10.1021/acs.organomet.7b00429.

(30) Klementyeva, S. V.; Afonin, M. Yu.; Bogomyakov, A. S.; Gamer, M. T.; Roesky, P. W.; Konchenko, S. N. Mono- and Dinuclear Rare-Earth Chlorides Ligated by a Mesityl-Substituted β-Diketiminate: Mono- and Dinuclear Rare-Earth Chlorides Ligated by a Mesityl-Substituted β-Diketiminate. *Eur. J. Inorg. Chem.* **2016**, *2016* (22), 3666–3672. https://doi.org/10.1002/ejic.201600488.

(31) Yu, K.-X.; Ding, Y.-S.; Han, T.; Leng, J.-D.; Zheng, Y.-Z. Magnetic Relaxations in Four-Coordinate Dy(III) Complexes: Effects of Anionic Surroundings and Short Dy–O Bonds. *Inorg. Chem. Front.* **2016**, *3* (8), 1028–1034. https://doi.org/10.1039/C6QI00117C.

(32) Fieser, M. E.; Palumbo, C. T.; La Pierre, H. S.; Halter, D. P.; Voora, V. K.; Ziller, J. W.; Furche, F.; Meyer, K.; Evans, W. J. Comparisons of Lanthanide/Actinide +2 Ions in a Tris(Aryloxide)Arene Coordination Environment. *Chem. Sci.* **2017**, *8* (11), 7424–7433. https://doi.org/10.1039/C7SC02337E.

(33) Parmar, V. S.; Ortu, F.; Ma, X.; Chilton, N. F.; Clérac, R.; Mills, D. P.; Winpenny, R. E. P. Probing Relaxation Dynamics in Five-Coordinate Dysprosium Single-Molecule Magnets. *Chem.–Eur. J.* **2020**, *26* (35), 7774–7778. https://doi.org/10.1002/chem.202001235.

(34) Aquilante, F.; Autschbach, J.; Carlson, R. K.; Chibotaru, L. F.; Delcey, M. G.; Vico, L. D.; Galván, I. F.; Ferré, N.; Frutos, L. M.; Gagliardi, L.; Garavelli, M.; Giussani, A.; Hoyer, C. E.; Manni, G. L.; Lischka, H.; Ma, D.; Malmqvist, P. Å.; Müller, T.; Nenov, A.; Olivucci, M.; Pedersen, T. B.; Peng, D.; Plasser, F.; Pritchard, B.; Reiher, M.; Rivalta, I.; Schapiro, I.; Segarra-Martí, J.; Stenrup, M.; Truhlar, D. G.; Ungur, L.; Valentini, A.; Vancoillie, S.; Veryazov, V.; Vysotskiy, V. P.; Weingart, O.; Zapata, F.; Lindh, R. Molcas 8: New Capabilities for Multiconfigurational Quantum Chemical Calculations across the Periodic Table. *J. Comput. Chem.* **2016**, *37* (5), 506–541. https://doi.org/10.1002/jcc.24221.

(35) Chibotaru, L. F.; Ungur, L. *Ab Initio* Calculation of Anisotropic Magnetic Properties of Complexes. I. Unique Definition of Pseudospin Hamiltonians and Their Derivation. *J. Chem. Phys.* **2012**, *137* (6), 064112. https://doi.org/10.1063/1.4739763.

(36) Pugh, T.; Chilton, N. F.; Layfield, R. A. A Low-Symmetry Dysprosium Metallocene Single-Molecule Magnet with a High Anisotropy Barrier. *Angew. Chem. Int. Ed.* **2016**, *55* (37), 11082–11085. https://doi.org/10.1002/anie.201604346.

(37) Gupta, S. K.; Rajeshkumar, T.; Rajaraman, G.; Murugavel, R. An Air-Stable Dy(III) Single-Ion Magnet with High Anisotropy Barrier and Blocking Temperature. *Chem. Sci.* **2016**, *7* (8), 5181–5191. https://doi.org/10.1039/C6SC00279J.

(38) Liu, S.-S.; Ziller, J. W.; Zhang, Y.-Q.; Wang, B.-W.; Evans, W. J.; Gao, S. A Half-Sandwich Organometallic Single-Ion Magnet with Hexamethylbenzene Coordinated to the Dy(III) Ion. *Chem. Commun.* **2014**, *50* (77), 11418–11420. https://doi.org/10.1039/C4CC04262J.

(39) Díaz-Ortega, I. F.; Herrera, J. M.; Dey, S.; Nojiri, H.; Rajaraman, G.; Colacio, E. The Effect of the Electronic Structure and Flexibility of the Counteranions on Magnetization Relaxation in $[Dy(L)_2(H_2O)_5]^{3+}$ (L = Phosphine Oxide Derivative) Pentagonal Bipyramidal SIMs. *Inorg. Chem. Front.* **2020**, *7* (3), 689–699. https://doi.org/10.1039/C9QI01412H.

(40) Pinkowicz, D.; Southerland, H. I.; Avendaño, C.; Prosvirin, A.; Sanders, C.; Wernsdorfer, W.; Pedersen, K. S.; Dreiser, J.; Clérac, R.; Nehrkorn, J.; Simeoni, G. G.; Schnegg, A.; Holldack, K.; Dunbar, K. R. Cyanide Single-Molecule Magnets Exhibiting Solvent Dependent Reversible "On" and "Off" Exchange Bias Behavior. *J. Am. Chem. Soc.* **2015**, *137* (45), 14406–14422. https://doi.org/10.1021/jacs.5b09378.

(41) Aubin, S. M. J.; Sun, Z.; Pardi, L.; Krzystek, J.; Folting, K.; Brunel, L.-C.; Rheingold, A. L.; Christou, G.; Hendrickson, D. N. Reduced Anionic Mn_{12} Molecules with Half-Integer Ground States as Single-Molecule Magnets. *Inorg. Chem.* **1999**, *38* (23), 5329–5340. https://doi.org/10.1021/ic990613g.

(42) Liu, J.; Chen, Y.-C.; Liu, J.-L.; Vieru, V.; Ungur, L.; Jia, J.-H.; Chibotaru, L. F.; Lan, Y.; Wernsdorfer, W.; Gao, S.; Chen, X.-M.; Tong, M.-L. A Stable Pentagonal Bipyramidal Dy(III) Single-Ion Magnet with a Record Magnetization Reversal Barrier over 1000 K. *J. Am. Chem. Soc.* **2016**, *138* (16), 5441–5450. https://doi.org/10.1021/jacs.6b02638.

(43) Izod, K.; Liddle, S. T.; Clegg, W. A Convenient Route to Lanthanide Triiodide THF Solvates. Crystal Structures of $LnI_3(THF)_4$[Ln = Pr] and $LnI_3(THF)_{3.5}$ [Ln = Nd, Gd, Y]. *Inorg. Chem.* **2004**, *43* (1), 214–218. https://doi.org/10.1021/ic034851u.

(44) *SMART Apex II, Version 2.1*; Bruker AXS Inc.: Madison, Wisconsin.

(45) *SAINT Software User's Guide, Version 7.34a*; Bruker AXS Inc.: Madison, Wisconsin.

(46) Blessing, R. H. An Empirical Correction for Absorption Anisotropy. *Acta Crystallogr. A* **1995**, *51* (1), 33–38. https://doi.org/10.1107/S0108767394005726.

(47) Sheldrick, G. M. Crystal Structure Refinement with *SHELXL*. *Acta Crystallogr. Sect. C Struct. Chem.* **2015**, *71* (1), 3–8. https://doi.org/10.1107/S2053229614024218.

(48) Sheldrick, G. M. *SHELXTL, 6.12*; Bruker AXS Inc.: Madison, Wisconsin.

(49) Dolomanov, O. V.; Bourhis, L. J.; Gildea, R. J.; Howard, J. A. K.; Puschmann, H. *OLEX2* : A Complete Structure Solution, Refinement and Analysis Program. *J. Appl. Crystallogr.* **2009**, *42* (2), 339–341. https://doi.org/10.1107/S0021889808042726.

(50) Roos, B. O.; Lindh, R.; Malmqvist, P.-Å.; Veryazov, V.; Widmark, P.-O.; Borin, A. C. New Relativistic Atomic Natural Orbital Basis Sets for Lanthanide Atoms with Applications to the Ce Diatom and LuF_3. *J. Phys. Chem. A* **2008**, *112* (45), 11431–11435. https://doi.org/10.1021/jp803213j.

(51) Roos, B. O.; Lindh, R.; Malmqvist, P. Å.; Veryazov, V.; Widmark, P.-O. Main Group Atoms and Dimers Studied with a New Relativistic ANO Basis Set. *J. Phys. Chem. A* **2004**, *108* (15), 2851–2858.

(52) Roos, B. O.; Veryazov, V.; Widmark, P.-O. Relativistic Atomic Natural Orbital Type Basis Sets for the Alkaline and Alkaline-Earth Atoms Applied to the Ground-State Potentials for the Corresponding Dimers. *Theor. Chem. Acc.* **2004**, *111* (2–6), 345–351. https://doi.org/10.1007/s00214-003-0537-0.

(53) Aquilante, F.; Lindh, R.; Bondo Pedersen, T. Unbiased Auxiliary Basis Sets for Accurate Two-Electron Integral Approximations. *J. Chem. Phys.* **2007**, *127* (11), 114107. https://doi.org/10.1063/1.2777146.

(54) Aquilante, F.; Pedersen, T. B.; Lindh, R.; Roos, B. O.; Sánchez de Merás, A.; Koch, H. Accurate *Ab Initio* Density Fitting for Multiconfigurational Self-Consistent Field Methods. *J. Chem. Phys.* **2008**, *129* (2), 024113. https://doi.org/10.1063/1.2953696.

(55) Wolf, A.; Reiher, M. Exact Decoupling of the Dirac Hamiltonian. IV. Automated Evaluation of Molecular Properties within the Douglas-Kroll-Hess Theory up to Arbitrary Order. *J. Chem. Phys.* **2006**, *124* (6), 064103. https://doi.org/10.1063/1.2161180.

(56) Roos, B. O. The Complete Active Space Self-Consistent Field Method and Its Applications in Electronic Structure Calculations. In *Advances in Chemical Physics*; John Wiley & Sons, Ltd, 2007; pp 399–445. https://doi.org/10.1002/9780470142943.ch7.

(57) Heß, B. A.; Marian, C. M.; Wahlgren, U.; Gropen, O. A Mean-Field Spin-Orbit Method Applicable to Correlated Wavefunctions. *Chem. Phys. Lett.* **1996**, *251* (5–6), 365–371. https://doi.org/10.1016/0009-2614(96)00119-4.

Chapter 7

Conclusion and Future Directions

7.1 Highly Anisotropic Lanthanide SMMs

This thesis presented a series of mono- and dinuclear lanthanide SMMs and analyzed their respective magnetic properties to gain a more thorough understanding of the factors that govern the relaxation dynamics in 4f systems. Often one of the features of lanthanide SMMs that limit their performance is quantum tunneling of the magnetization (QTM), and this is even more prevalent in non-Kramers ions (i.e., those with integer angular momenta). In Chapter 2 this was investigated in two closely related Tm^{III}-COT compounds, $[Tm^{III}(\eta^8\text{-COT})I(THF)_2]$ (**1-Tm**) and $[K(18\text{-crown-6})(THF)_2][Tm^{III}(\eta^8\text{-COT})_2]$ (**2-Tm**). The findings of this work demonstrated the importance of controlling symmetry at the metal center to decrease the efficiency of QTM while also simultaneously increasing the effective barrier. One of the ways to circumvent the drastic effects of QTM is to invoke magnetic coupling between spin centers. In this context, dinuclear SMMs have become ubiquitous models for studying this over several different styles of bridging units (e.g., diamagnetic organic ligands, inorganic anions, open-shell ligands, etc.) While the identity of the bridging moiety between spin-carriers is important, arguably the ancillary ligands in dinuclear and even polynuclear SMMs are just as significant in dictating the performance of an SMM. Indeed, comparing $[Dy^{III}\{N(SiMe_3)_2\}_2(\mu\text{-Cl})(THF)]_2$ (**3-Dy**) and $[Dy^{III}(\eta^8\text{-COT})(\mu\text{-Cl})(THF)]_2$ (**4-Dy**) in Chapter 3 revealed greater magnetic axiality for **3-Dy** and relaxation dynamics free of QTM. Whereas **4-Dy** is predicted to have increased magnetic coupling, this is likely a result of the relative orientations of the anisotropic axes of the Dy^{III} ions, furthering supporting the vital role that ancillary ligands play in the magnetic properties. Moreover, it was identified that the presence of bridging chloride ions diminishes the magnetic axiality of the lanthanide, hindering the SMM potential of the compounds. This sentiment was echoed in Chapter 4 where the diffuse and electron rich π-cloud of the cycloheptatrienyl trianion was thought to enhance the magnetic coupling in dinuclear compounds $[KLn^{III}_2(\eta^7\text{-}C_7H_7)\{N(SiMe_3)_2\}_4]$ (**5-Ln**) and $[K(THF)_2Er^{III}_2(\eta^7\text{-}C_7H_7)\{N(SiMe_3)_2\}_4]$ (**6-Er**) leading to reduced QTM and greater SMM performance. While ferromagnetic coupling between the 4f ions was determined for this set of compounds, the presence of the cycloheptatrienyl trianion reduced the magnetic axiality at the individual magnetic sites. This meant that the strength of the magnetic coupling was not great enough to overcome the transverse crystal field effects and QTM was still a prevalent feature of the relaxation dynamics in these dinuclear species. Thus, to truly enhance the performance and limit ground state relaxation, the individual metal sites would need to be separated; this was achieved with the use of a ferrocene diamide ligand in $[(NN^{TBS})Dy^{III}I(THF)_2]$ (**7-Dy**). Here the diamide imposes a dominant ligand field on the Dy^{III} ion, yielding a larger energy barrier to spin reversal (U_{eff} = 771 K) with open hysteresis loops. However, the directionality on the anisotropy imposed by the ferrocene diamide was not strong enough to preclude the observation of QTM. In fact, the presence of two THF molecules and an iodide ligand in the equatorial positions of this ion introduce transverse components to the crystal field, effectively promoting QTM and limiting the over barrier relaxation. We identified that the THF ligands limit this by up to 33 % more than the iodide ligand itself. It was apparent that the THF ligands would need to be removed from the primary coordination sphere, indeed in Chapter 6 the presented compounds $[K(DME)_3][L^{Ar}Dy^{III}(Cl)_2]$ (**8-Dy**) and $[K(DME)_4][L^{Ar}Dy^{III}(I)_2]$ (**9-Dy**) were devoid of solvent in the primary coordination sphere. While the identity of the halide was found to have little effect on the overall magnetic properties of the Dy^{III} ion, the wider more obtuse bite angle of the bisanilide ligand employed combined with the lack of THF in the equatorial position, preserved the axiality in the excited states of these compounds enabling multistep magnetic relaxation. This elicited the highest energy barriers observed throughout this work, with U_{eff} = 1278-1334 K in zero field. From this work it is clear that a careful balance must be achieved between the angle of donor atoms from the amido ligands, the Ln-N bond distances, and the identity of the equatorial ligands (i.e., the transverse components to the crystal field) in order to obtain efficient SMMs. The collective results of these findings are being utilized to guide the synthetic efforts of new low-coordinate lanthanide SMMs.

7.2 Next Steps from the Lessons Learned

Viewed as a holy grail approach for harnessing the maximum magnetic anisotropy of a Dy^{III} ion is the 2-coordinate linear molecular geometry. In this arrangement, the effective crystal field of the Dy^{III} spans several hundreds of wavenumbers;[1,2] combined with the lack of equatorial ligands this geometry will theoretically produce an SMM whose U_{eff} and T_B reach far beyond what has been reported to date.[3] However, this represents a significant synthetic challenge. The large ionic radii of the trivalent lanthanide ions are often saturated by several donor atoms/ligands readily yielding coordination numbers of 8 and 9. When lanthanide ions possess large cationic charges that are not sufficiently quenched by the ligands, solvent coordination and/or intramolecular reactions will occur to afford the most stabilized compound, which can drastically reduce the performance of a SMM.[4]

The work presented herein shows the strong role and emphasis of amido-based ligands in producing high-energy barrier SMMs as the localized charges of the N-atoms are very strong directors for magnetic anisotropy. Even in the earlier chapters, the dinuclear compounds presented, namely **3-Dy**, **5-Ln**, and **6-Er** were highly axial despite the presence of equatorial bridging ligands and magnetic coupling; this testifies to the ability of the amide to direct the anisotropy. Unfortunately, the silyl amide used in compounds **3-Dy**,

5-Ln, and **6-Er** is not sufficiently bulky to prevent other equatorial ligands from approaching, and with such a small R-group ($SiMe_3$), the *tris*-compounds can be readily formed. Thus, inspired by earlier work on transition metal compounds,[5] we decided to use the ligand $KN(SiMePh_2)_2$ for its steric bulk and solubility in an attempt to isolate two-coordinate linear 4f compounds. This salt is easily prepared from the deprotonation of $HN(SiMePh_2)_2$ with potassium hydride.[6] To ensure the installment of only two amido ligands, the reaction of $KN(SiMePh_2)_2$ with divalent lanthanides was investigated. Divalent lanthanide diioides, such as YbI_2 were solvated in a solution of THF, resulting in a colour change which signifies the formation of $YbI_2(THF)_x$. Subsequent addition of a solution of $KN(SiMePh_2)_2$ afforded $Yb^{II}\{N(SiMePh_2)_2\}_2$ (**10-Yb**), a divalent two-coordinate 4f compound (Figure 7.1)

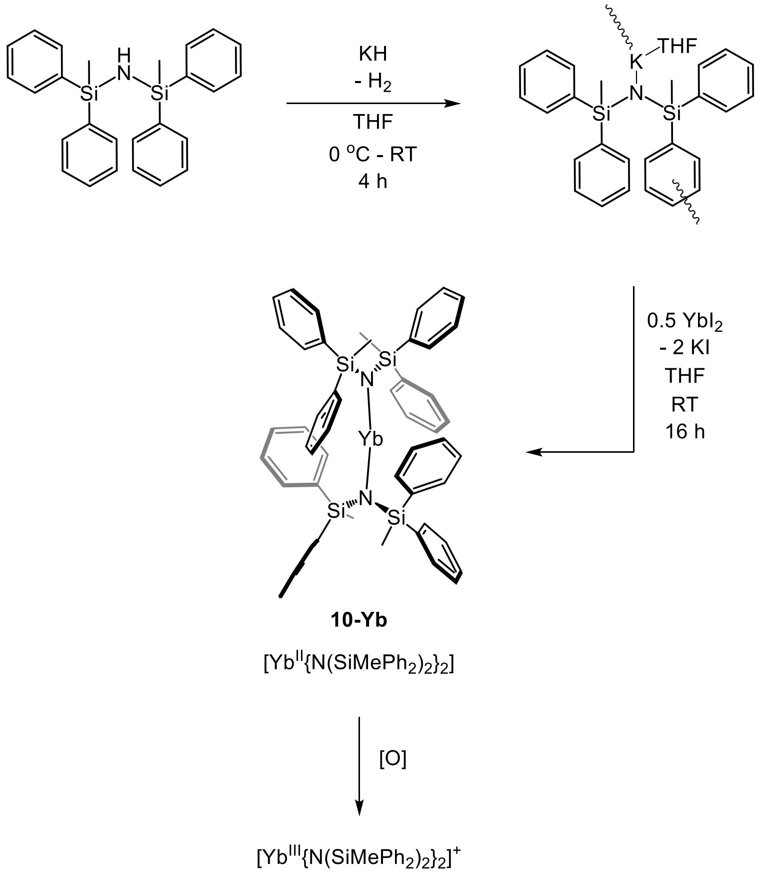

Figure 7.1 Synthetic scheme towards low coordinate 4f SMMs.

The divalent compound **10-Yb** was obtained as dark red crystals, for which we obtained a single-crystal X-ray structure (Figure 7.2). The structure revealed a two-coordinate, near linear ($N\text{-}Yb^{II}\text{-}N$ =

171.6°) yetterbium ion coordinated by two of the $[N(SiMePh_2)_2]^-$ ligands, which yield Yb^{II}-N distances of 2.34 Å and 2.36 Å (Table 7.1). These are highly desirable features in the pursuit of a Dy^{III} two-coordinate system, and we view **10-Yb** as a model in this pursuit. Notably, the predicted features for a Dy^{III} derivative require the trivalent oxidation state. A recent report has demonstrated that divalent Sm^{II}, Tm^{II} and Yb^{II} can be oxidized with either ^{t}BuCl or $[Fc][PF_6]$ to give the resulting trivalent ion with a bound halide.[7] Unfortunately, this requires an additional step to remove the bound halide, and a work-up to remove the spent oxidant. As such, we have been investigating the use of oxidants to facilitate this process from the divalent species **10-Yb** to the trivalent species directly, without the need of performing a halide abstraction. This will require the use of a compound that is bulky enough to preclude its approach to the highly activated Lewis acidic center while also being readily accessible to participate in the necessary redox chemistries.

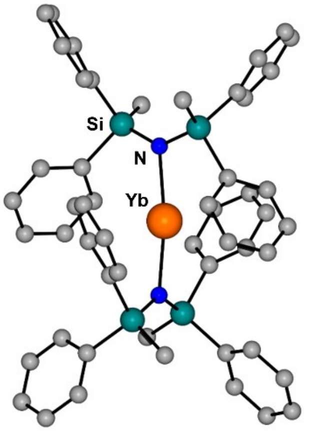

10-Yb

Figure 7.2 Solid state molecular structure of $Yb^{II}\{N(SiMePh_2)_2\}_2$ (**10-Yb**). Colour code: orange (Yb^{II}), teal (Si), blue (N), grey (C). Hydrogen atoms have been omitted for clarity.

With a fully optimized oxidation pathway, there is great promise in this route for developing new high-performing lanthanide SMMs. The work presented in this thesis has gradually shown the progression in the anisotropy barrier and relaxation dynamics from $[Dy^{III}\{N(SiMe_3)_2\}_2(\mu\text{-Cl})(THF)]_2$ (**3-Dy**) and $[KLn^{III}_2(\eta^7\text{-}C_7H_7)\{N(SiMe_3)_2\}_4]$ (**5-Ln**), whose ground states were highly axial despite the presence of significant transverse effects, to mononuclear amido-based compounds like $[(NN^{TBS})Dy^{III}(I)(THF)_2]$ (**7-Dy**), $[K(DME)_3][L^{Ar}Dy^{III}(Cl)_2]$ (**8-Dy**), and $[K(DME)_4][L^{Ar}Dy^{III}(I)_2]$ (**9-Dy**). Perhaps unsurprisingly, a trend emerges such that a wider more obtuse N-Ln-N angle is desirable for promoting axiality in each doublet state, yet a strong and short Ln-N bond distance is also required. These are often competing and differing features which need to be carefully balanced to achieve even greater amido-based lanthanide SMMs. Thus, a barrier that closely resembles that predicted for [$Dy^{III}Im^{Dipp}NCl_2(THF)_3$] (*ca.* 3700 K) may be achievable using the synthetic route that is being developed; if the structural metrics of **10-Yb** are any indication, it should exhibit a barrier much larger than even the highest reported herein (*ca.* 1300 K for **8-Dy** and **9-Dy**).

Table 7.1 Structure-property relationships at a glance.

Compound	**N-Ln-N (°)**	**Ln-N (Å)**[a]	U_{eff} **(K) /** H_{dc} **(Oe)**	τ_{QTM} **(s^{-1})**
1-Tm	-	1.75	7.93 / 800	373.1
2-Tm	-	1.85	53.3 / 200	2.70
3-Dy	117.8	2.21-2.24	518 / 0	[b]
4-Dy	-	1.79	140 / 0	27.7
5-Gd	97.8-106.2	2.32-2.39	[c]	[c]
5-Dy	98.3-106.3	2.28-2.35	[d]	[d]
5-Er	98.6-105.7	2.26-2.33	58 / 800	[e]
6-Er	102.1-111.0	2.26-2.32	[d]	[d]
7-Dy	137.7	2.20-2.21	770 / 0	[e]
8-Dy	163.2	2.38-2.41	1334 / 0	43.48
9-Dy	160.3	2.40-2.44	1278 / 0	3.03
10-Yb	171.6	2.34-2.36	[f]	[f]
$Dy(Im^{Dipp}N)_2$[g]	*ca.* 180	2.21	3761	-

[a] for COT-based compounds the distance corresponds to the $Ln\text{-}COT_{centroid}$ distance; [b] QTM not observed in experimental data; [c] isotropic compound, no ac data collected; [d] slow relaxation dynamics not observed during experiment; [e] QTM observed but not quantified; [f] diamagnetic compound, no magnetic data collected; [g] theoretical compound, calculated from [$Dy^{III}Im^{Dipp}NCl_2(THF)_3$]8

7.3 Outlook and Commentary on Lanthanide SMMs

The technological relevance of SMMs hinges on raising the blocking temperature (T_B) for the long-term maintenance of the magnetic moment. The quest for understating the fundamental link between the energy barrier to spin inversion (U_{eff}) and T_B remains an ongoing challenge in the field. New work suggests a close link between the blocking temperature and Raman relaxation in high-U_{eff} SMMs,9 yet no conclusive correlation exists for all SMMs. Experimentalists and theorists have a thorough understanding of the factors that influence the height of the anisotropic barrier; however, a similar and definitive understanding for the blocking temperature is lacking. This has resulted in SMMs with very large barriers and minimal magnetic hysteresis and has resulted in the non-linear advancement of blocking temperatures. During the course of my doctorate work, the T_B of SMMs has seen massive improvements from $T_B = 14$ K (which was the highest reported for many years),[10,11] to T_B = 20 K,[12] and then with blocking at liquid nitrogen temperatures and beyond.[3,13,14] Closely linked to these advancements in lanthanide-based SMMs are the concurrent advancements in synthetic 4f chemistry,[15–18] 4f oxidation state diversity,[19,20] and computational chemistry.[21–23] It goes without saying that many of the discoveries and synthetic work in the field of lanthanide SMMs (and in this thesis) have been made possible due to significant advances in computational modelling of 4f systems.[24–26] *Ab initio* methods now exist for accurately determining the orientation of the anisotropy axes in molecules from structural data and/or models (i.e., without experimental and/or structural data); these predictive methods have guided efforts towards the isolation of new SMMs.[1,27,28] Undoubtedly, continued advances in computational methods for 4f systems will continue to aid in the development of new SMMs and continue to guide experimentalists.

When I began, a well-established approach in the Murugesu group was employing the rigorous synthetic and design control that lanthanide organometallic chemistry afforded to isolate high-performing SMMs. Previously, the Murugesu group demonstrated the effectiveness of arenes such as cyclooctatetraene in the maximizing the anisotropy of prolate Er^{III} ions.[10,29,30] More recently, a significant focus on cyclopentadienyl complexes of oblate Dy^{III} ions continues to yield large figures of merit for SMM performance,[31] making organometallic chemistry a mainstay in the field of lanthanide SMMs. Notably, many of the top performing lanthanide based SMMs require strict anaerobic conditions owing to their lack of thermodynamic stability, and involve the use of glovebox and Schlenk techniques, the examples presented within this thesis are no different. Some believe that this represents a significant barrier for SMM-based technologies in terms of practicability and application and will need to be addressed to increase the technological readiness of SMMs.

Moreover, to exploit the properties of these molecules, in applications such as information storage, spintronics, etc., it is crucial to transfer the molecules from the crystalline state to surfaces. In this form, the molecules can be electrically addressed by STM methods such as probe microscopy with single-molecule sensors.[32–34] It is of great interest to develop systems which are sublimable for surface functionalization and ultimately device fabrication.[35] Indeed, this is an area of research itself with challenges associated to the retention of the magnetic properties once the molecules are deposited onto surfaces.[36] While much of the work in the field of lanthanide SMMs is burgeoning, there are still a lot of improvements to be made from a practical perspective. For example, for molecules to be easily sublimable on to surfaces, requires thermal stability and stability with respect to a vacuum. However, after more than two decades of research, the field of single-molecule magnets approaches the pinnacle era for the applications that they were initially proposed for circa 1993. This warrants their continued investigation and efforts by chemists, physicists, and theorists.

7.4 References

(1) Ungur, L.; Chibotaru, L. F. Strategies toward High-Temperature Lanthanide-Based Single-Molecule Magnets. *Inorg. Chem.* **2016**, *55* (20), 10043–10056. https://doi.org/10.1021/acs.inorgchem.6b01353.

(2) Chilton, N. F.; Goodwin, C. A. P.; Mills, D. P.; Winpenny, R. E. P. The First Near-Linear Bis(Amide) f-Block Complex: A Blueprint for a High Temperature Single Molecule Magnet. *Chem. Commun.* **2015**, *51* (1), 101–103. https://doi.org/10.1039/C4CC08312A.

(3) Guo, F.-S.; Day, B. M.; Chen, Y.-C.; Tong, M.-L.; Mansikkamäki, A.; Layfield, R. A. Magnetic Hysteresis up to 80 Kelvin in a Dysprosium Metallocene Single-Molecule Magnet. *Science* **2018**, *362* (6421), 1400–1403. https://doi.org/10.1126/science.aav0652.

(4) Day, B. M.; Guo, F.-S.; Giblin, S. R.; Sekiguchi, A.; Mansikkamäki, A.; Layfield, R. A. Rare-Earth Cyclobutadienyl Sandwich Complexes: Synthesis, Structure and Dynamic Magnetic Properties. *Chem. Eur. J.* **2018**, *24*, 16779-16782. https://doi.org/10.1002/chem.201804776.

(5) Chen, H.; Bartlett, R. A.; Dias, H. V. R.; Olmstead, M. M.; Power, P. P. The Use of Very Crowded Silylamide Ligands -N(SiMe$_n$Ph$_{3-n}$)$_2$(n = 0, 1, or 2) to Synthesize Crystalline, Two-Coordinate, Derivatives to Manganese(II), Iron(II), and Cobalt(II) and the Free Ion [Ph$_3$SiNSiPh$_3$]$^-$. *J. Am. Chem. Soc.* **1989**, *111* (12), 4338–4345. https://doi.org/10.1021/ja00194a028.

(6) Torvisco, A.; Decker, K.; Uhlig, F.; Ruhlandt-Senge, K. Heavy Alkali Metal Amides: Role of Secondary Interactions in Metal Stabilization. *Inorg. Chem.* **2009**, *48* (23), 11459–11465. https://doi.org/10.1021/ic901767c.

(7) Mills, D.; Nicholas, H.; Vonci, M.; Goodwin, C.; Winpenny, R.; J. L. McInnes, E.; Chilton, N.; Murphy, S.; Wei, S. L.; Cassim, D. Electronic Structures of Bent, Formally Two-Coordinate Lanthanide(III) Cations. *Chem. Sci.* **2019**, *10*, 10493-10502. https://doi.org/10.26434/10.1039/C9SC03431E.

(8) Liu, B.-C.; Ge, N.; Zhai, Y.-Q.; Zhang, T.; Ding, Y.-S.; Zheng, Y.-Z. An Imido Ligand Significantly Enhances the Effective Energy Barrier of Dysprosium(III) Single-Molecule Magnets. *Chem. Commun.* **2019**, *55* (63), 9355–9358. https://doi.org/10.1039/C9CC04687A.

(9) Giansiracusa, M. J.; Kostopoulos, A. K.; Collison, D.; Winpenny, R. E. P.; Chilton, N. F. Correlating Blocking Temperatures with Relaxation Mechanisms in Monometallic Single-Molecule Magnets with High Energy Barriers (U_{eff} > 600 K). *Chem. Commun.* **2019**, *55*, 7025-7028. https://doi.org/10.1039/C9CC02421B.

(10) Le Roy, J. J.; Ungur, L.; Korobkov, I.; Chibotaru, L. F.; Murugesu, M. Coupling Strategies to Enhance Single-Molecule Magnet Properties of Erbium–Cyclooctatetraenyl Complexes. *J. Am. Chem. Soc.* **2014**, *136* (22), 8003–8010. https://doi.org/10.1021/ja5022552.

(11) Rinehart, J. D.; Fang, M.; Evans, W. J.; Long, J. R. Strong Exchange and Magnetic Blocking in N_2^{3-}-Radical-Bridged Lanthanide Complexes. *Nat. Chem.* **2011**, *3* (7), 538–542. https://doi.org/10.1038/nchem.1063.

(12) Chen, Y.-C.; Liu, J.-L.; Ungur, L.; Liu, J.; Li, Q.-W.; Wang, L.-F.; Ni, Z.-P.; Chibotaru, L. F.; Chen, X.-M.; Tong, M.-L. Symmetry-Supported Magnetic Blocking at 20 K in Pentagonal Bipyramidal Dy(III) Single-Ion Magnets. *J. Am. Chem. Soc.* **2016**, *138* (8), 2829–2837. https://doi.org/10.1021/jacs.5b13584.

(13) Goodwin, C. A. P.; Ortu, F.; Reta, D.; Chilton, N. F.; Mills, D. P. Molecular Magnetic Hysteresis at 60 Kelvin in Dysprosocenium. *Nature* **2017**, *548* (7668), 439–442. https://doi.org/10.1038/nature23447.

(14) Guo, F.-S.; Day, B. M.; Chen, Y.-C.; Tong, M.-L.; Mansikkamäki, A.; Layfield, R. A. A Dysprosium Metallocene Single-Molecule Magnet Functioning at the Axial Limit. *Angew. Chem. Int. Ed.* **2017**, *56* (38), 11445–11449. https://doi.org/10.1002/anie.201705426.

(15) Guo, F.-S.; Bar, A. K.; Layfield, R. A. Main Group Chemistry at the Interface with Molecular Magnetism. *Chem. Rev.* **2019**, *119*, 8479-8505. https://doi.org/10.1021/acs.chemrev.9b00103.

(16) Evans, P.; Reta, D.; Whitehead, G. F. S.; Chilton, N. F.; Mills, D. P. Bis-Monophospholyl Dysprosium Cation Showing Magnetic Hysteresis at 48 K. *J. Am. Chem. Soc.* **2019**, *141* (50), 19935–19940. https://doi.org/10.1021/jacs.9b11515.

(17) Errulat, D.; Gabidullin, B.; Mansikkamäki, A.; Murugesu, M. Two Heads Are Better than One: Improving Magnetic Relaxation in the Dysprosium Metallocene upon Dimerization by Use of an Exceptionally Weakly-Coordinating Anion. *Chem. Commun.* **2020**, *56* (44), 5937–5940. https://doi.org/10.1039/D0CC01980A.

(18) Burns, C. P.; Yang, X.; Wofford, J. D.; Bhuvanesh, N. S.; Hall, M. B.; Nippe, M. Structure and Magnetization Dynamics of Dy−Fe and Dy−Ru Bonded Complexes. *Angew. Chem. Int. Ed.* **2018**, *57* (27), 8144–8148. https://doi.org/10.1002/anie.201803761.

(19) Meihaus, K. R.; Fieser, M. E.; Corbey, J. F.; Evans, W. J.; Long, J. R. Record High Single-Ion Magnetic Moments Through $4f^n5d^1$ Electron Configurations in the Divalent Lanthanide Complexes $[(C_5H_4SiMe_3)_3Ln]^-$. *J. Am. Chem. Soc.* **2015**, *137* (31), 9855–9860. https://doi.org/10.1021/jacs.5b03710.

(20) Gould, C. A.; McClain, K. R.; Yu, J. M.; Groshens, T. J.; Furche, F.; Harvey, B. G.; Long, J. R. Synthesis and Magnetism of Neutral, Linear Metallocene Complexes of Terbium(II) and Dysprosium(II). *J. Am. Chem. Soc.* **2019**, *141* (33), 12967–12973. https://doi.org/10.1021/jacs.9b05816.

(21) Baldoví, J. J.; Cardona-Serra, S.; Clemente-Juan, J. M.; Coronado, E.; Gaita-Ariño, A.; Palii, A. Rational Design of Single-Ion Magnets and Spin Qubits Based on Mononuclear Lanthanoid Complexes. *Inorg. Chem.* **2012**, *51* (22), 12565–12574. https://doi.org/10.1021/ic302068c.

(22) Blagg, R. J.; Ungur, L.; Tuna, F.; Speak, J.; Comar, P.; Collison, D.; Wernsdorfer, W.; McInnes, E. J. L.; Chibotaru, L. F.; Winpenny, R. E. P. Magnetic Relaxation Pathways in Lanthanide Single-Molecule Magnets. *Nat. Chem.* **2013**, *5* (8), 673–678. https://doi.org/10.1038/nchem.1707.

(23) Escalera-Moreno, L.; Baldoví, J. J.; Gaita-Ariño, A.; Coronado, E. Design of High-Temperature f - Block Molecular Nanomagnets through the Control of Vibration-Induced Spin Relaxation. *Chem. Sci.* **2020**, *11* (6), 1593–1598. https://doi.org/10.1039/C9SC03133B.

(24) Ungur, L.; Chibotaru, L. F. Ab Initio Crystal Field for Lanthanides. *Chem.-Eur. J.* **2017**, *23* (15), 3708–3718. https://doi.org/10.1002/chem.201605102.

(25) Jung, J.; Atanasov, M.; Neese, F. Ab Initio Ligand-Field Theory Analysis and Covalency Trends in Actinide and Lanthanide Free Ions and Octahedral Complexes. *Inorg. Chem.* **2017**, *56* (15), 8802–8816. https://doi.org/10.1021/acs.inorgchem.7b00642.

(26) Aravena, D. Ab Initio Prediction of Tunneling Relaxation Times and Effective Demagnetization Barriers in Kramers Lanthanide Single-Molecule Magnets. *J. Phys. Chem. Lett.* **2018**, *9* (18), 5327–5333. https://doi.org/10.1021/acs.jpclett.8b02359.

(27) Gupta, T.; Singh, M. K.; Rajaraman, G. Role of Ab Initio Calculations in the Design and Development of Lanthanide Based Single Molecule Magnets. In *Organometallic Magnets*; Chandrasekhar, V., Pointillart, F., Eds.; Topics in Organometallic Chemistry; Springer International Publishing: Cham, 2018; Vol. 64, pp 281–354. https://doi.org/10.1007/3418_2018_5.

(28) Swain, A.; Sarkar, A.; Rajaraman, G. Role of Ab Initio Calculations in the Design and Development of Organometallic Lanthanide-Based Single-Molecule Magnets. *Chem.–Asian J.* **2019**, *14* (23), 4056–4073. https://doi.org/10.1002/asia.201900828.

(29) Ungur, L.; Le Roy, J. J.; Korobkov, I.; Murugesu, M.; Chibotaru, L. F. Fine-Tuning the Local Symmetry to Attain Record Blocking Temperature and Magnetic Remanence in a Single-Ion Magnet. *Angew. Chem. Int. Ed.* **2014**, *53* (17), 4413–4417. https://doi.org/10.1002/anie.201310451.

(30) Harriman, K. L. M.; Murugesu, M. An Organolanthanide Building Block Approach to Single-Molecule Magnets. *Acc. Chem. Res.* **2016**, *49* (6), 1158–1167. https://doi.org/10.1021/acs.accounts.6b00100.

(31) Day, B. M.; Guo, F.-S.; Layfield, R. A. Cyclopentadienyl Ligands in Lanthanide Single-Molecule Magnets: One Ring to Rule Them All? *Acc. Chem. Res.* **2018**, *51* (8), 1880–1889. https://doi.org/10.1021/acs.accounts.8b00270.

(32) Czap, G.; Wagner, P. J.; Xue, F.; Gu, L.; Li, J.; Yao, J.; Wu, R.; Ho, W. Probing and Imaging Spin Interactions with a Magnetic Single-Molecule Sensor. *Science* **2019**, *364* (6441), 670–673. https://doi.org/10.1126/science.aaw7505.

(33) Natterer, F. D.; Yang, K.; Paul, W.; Willke, P.; Choi, T.; Greber, T.; Heinrich, A. J.; Lutz, C. P. Reading and Writing Single-Atom Magnets. *Nature* **2017**, *543* (7644), 226–228. https://doi.org/10.1038/nature21371.

(34) Cornia, A.; Mannini, M. Single-Molecule Magnets on Surfaces. In *Molecular Nanomagnets and Related Phenomena*; Gao, S., Ed.; Structure and Bonding; Springer Berlin Heidelberg: Berlin, Heidelberg, 2014; Vol. 164, pp 293–330. https://doi.org/10.1007/430_2014_150.

(35) Dreiser, J. Molecular Lanthanide Single-Ion Magnets: From Bulk to Submonolayers. *J. Phys. Condens. Matter* **2015**, *27* (18), 183203. https://doi.org/10.1088/0953-8984/27/18/183203.

(36) Holmberg, R. J.; Murugesu, M. Adhering Magnetic Molecules to Surfaces. *J. Mater. Chem. C* **2015**, *3* (46), 11986–11998. https://doi.org/10.1039/C5TC03225C.

Appendix

A.1 Permissions Granted for the Reproduction of Published Content in Thesis

A.1.1 Chapter 1

Parts of the introduction have been adapted with permission from *Trends Chem.*, **2019**, *1* (4), 425-439. Copyright 2019 Elsevier.

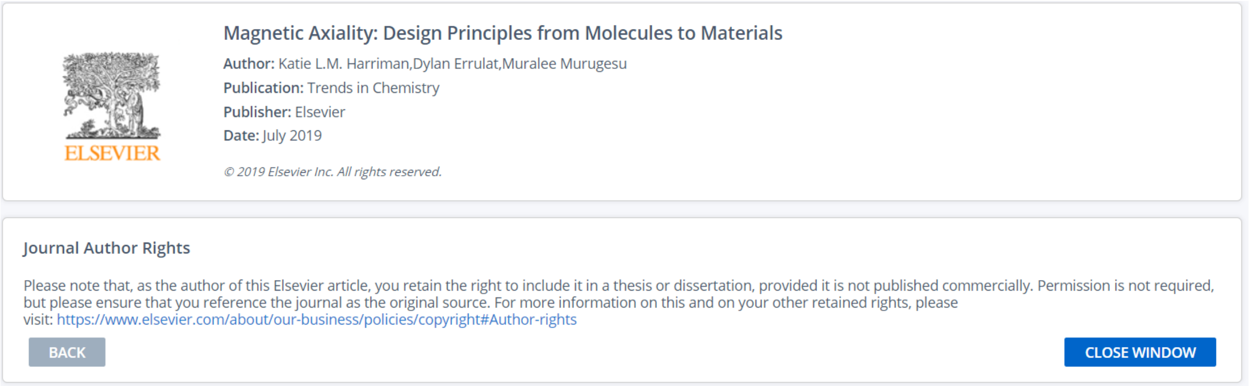

Magnetic Axiality: Design Principles from Molecules to Materials

Author: Katie L.M. Harriman,Dylan Errulat,Muralee Murugesu

Publication: Trends in Chemistry

Publisher: Elsevier

Date: July 2019

© 2019 Elsevier Inc. All rights reserved.

Journal Author Rights

Please note that, as the author of this Elsevier article, you retain the right to include it in a thesis or dissertation, provided it is not published commercially. Permission is not required, but please ensure that you reference the journal as the original source. For more information on this and on your other retained rights, please visit: https://www.elsevier.com/about/our-business/policies/copyright#Author-rights

A.1.2 Chapter 2

Adapted with permission from *Organometallics*, **2017,** *36* (23), 4515-4518. Copyright 2017 American Chemical Society.

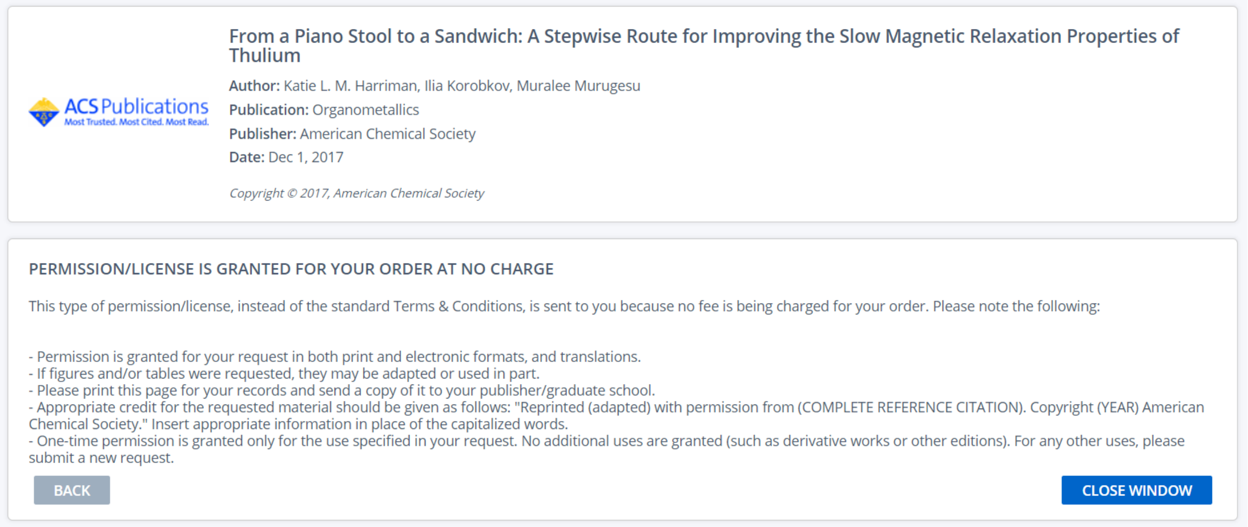

From a Piano Stool to a Sandwich: A Stepwise Route for Improving the Slow Magnetic Relaxation Properties of Thulium

Author: Katie L. M. Harriman, Ilia Korobkov, Muralee Murugesu

Publication: Organometallics

Publisher: American Chemical Society

Date: Dec 1, 2017

Copyright © 2017, American Chemical Society

PERMISSION/LICENSE IS GRANTED FOR YOUR ORDER AT NO CHARGE

This type of permission/license, instead of the standard Terms & Conditions, is sent to you because no fee is being charged for your order. Please note the following:

- Permission is granted for your request in both print and electronic formats, and translations.
- If figures and/or tables were requested, they may be adapted or used in part.
- Please print this page for your records and send a copy of it to your publisher/graduate school.
- Appropriate credit for the requested material should be given as follows: "Reprinted (adapted) with permission from (COMPLETE REFERENCE CITATION). Copyright (YEAR) American Chemical Society." Insert appropriate information in place of the capitalized words.
- One-time permission is granted only for the use specified in your request. No additional uses are granted (such as derivative works or other editions). For any other uses, please submit a new request.

A.1.3 Chapter 4

Adapted with permission from *Chem. Sci.*, **2017,** *8*, 231-240. Copyright 2017 Royal Society of Chemistry.

Cycloheptatrienyl trianion: an elusive bridge in the search of exchange coupled dinuclear organolanthanide single-molecule magnets

K. L. M. Harriman, J. J. Le Roy, L. Ungur, R. J. Holmberg, I. Korobkov and M. Murugesu, *Chem. Sci.*, 2017, **8**, 231

DOI: 10.1039/C6SC01224H

A.1.4 Chapter 5

Adapted with permission from *J. Am. Chem. Soc.*, **2017,** *139* (4), 1420-1423. Copyright 2017 American Chemical Society.

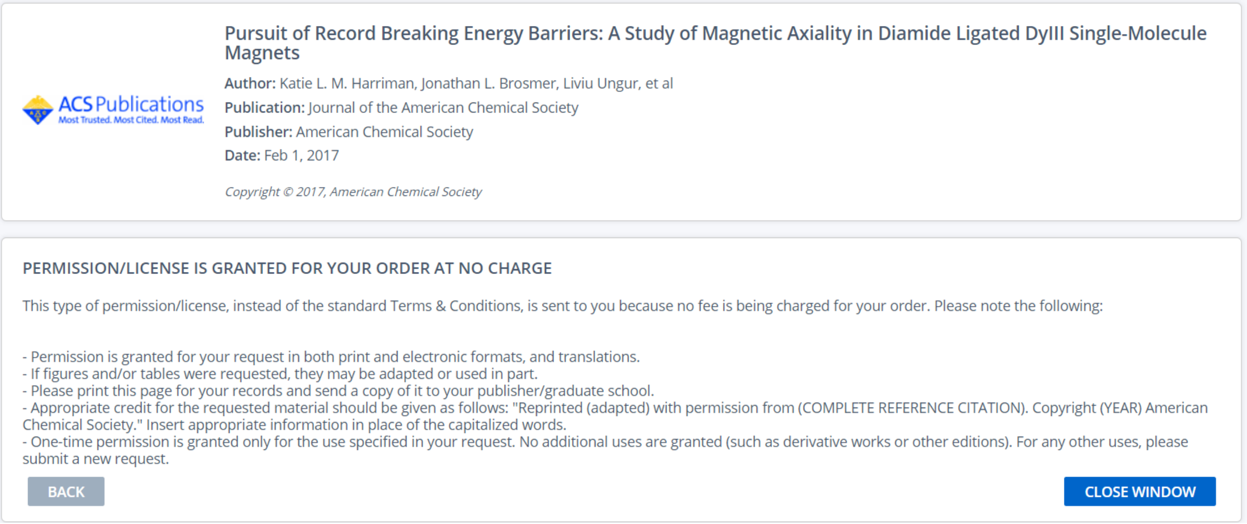

Pursuit of Record Breaking Energy Barriers: A Study of Magnetic Axiality in Diamide Ligated DyIII Single-Molecule Magnets

Author: Katie L. M. Harriman, Jonathan L. Brosmer, Liviu Ungur, et al
Publication: Journal of the American Chemical Society
Publisher: American Chemical Society
Date: Feb 1, 2017

Copyright © 2017, American Chemical Society

PERMISSION/LICENSE IS GRANTED FOR YOUR ORDER AT NO CHARGE

This type of permission/license, instead of the standard Terms & Conditions, is sent to you because no fee is being charged for your order. Please note the following:

- Permission is granted for your request in both print and electronic formats, and translations.
- If figures and/or tables were requested, they may be adapted or used in part.
- Please print this page for your records and send a copy of it to your publisher/graduate school.
- Appropriate credit for the requested material should be given as follows: "Reprinted (adapted) with permission from (COMPLETE REFERENCE CITATION). Copyright (YEAR) American Chemical Society." Insert appropriate information in place of the capitalized words.
- One-time permission is granted only for the use specified in your request. No additional uses are granted (such as derivative works or other editions). For any other uses, please submit a new request.

A.1.5 Chapter 6

Adapted with permission from *Inorg. Chem. Front.*, **2020,** *7*, 4805-4812. Copyright 2020 Royal Society of Chemistry.

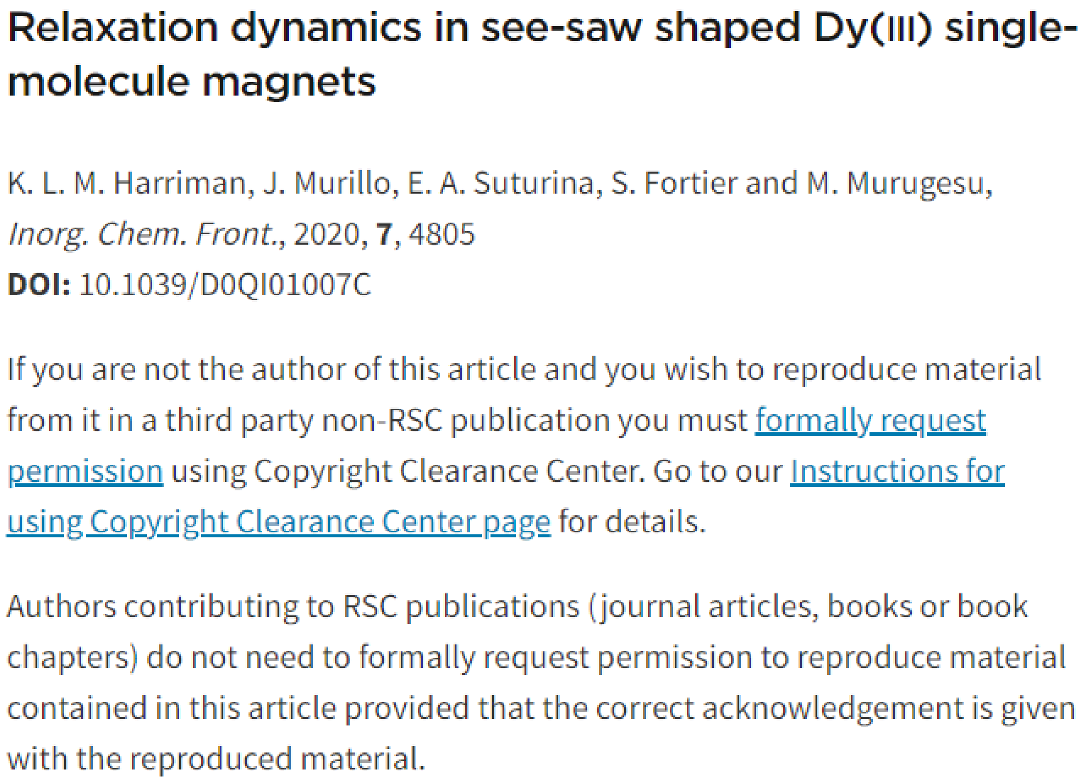

Relaxation dynamics in see-saw shaped Dy(III) single-molecule magnets

K. L. M. Harriman, J. Murillo, E. A. Suturina, S. Fortier and M. Murugesu,
Inorg. Chem. Front., 2020, **7**, 4805
DOI: 10.1039/D0QI01007C

If you are not the author of this article and you wish to reproduce material from it in a third party non-RSC publication you must formally request permission using Copyright Clearance Center. Go to our Instructions for using Copyright Clearance Center page for details.

Authors contributing to RSC publications (journal articles, books or book chapters) do not need to formally request permission to reproduce material contained in this article provided that the correct acknowledgement is given with the reproduced material.